Development of a Simulation Methodology to Predict the Energy Absorption of Composite Structures under Crush Loading

Thomas Feser

Deutsches Zentrum für Luft- und Raumfahrt
Institut für Bauweisen und Strukturtechnologie
Stuttgart

Deutsches Zentrum
DLR für Luft- und Raumfahrt

Forschungsbericht 2022-16

Development of a Simulation Methodology to Predict the Energy Absorption of Composite Structures under Crush Loading

Thomas Feser

Deutsches Zentrum für Luft- und Raumfahrt
Institut für Bauweisen und Strukturtechnologie
Stuttgart

Deutsches Zentrum
DLR für Luft- und Raumfahrt

D 93

Flugzeugcrash, Faserverbundwerkstoffe, Stauchbelastung, Finite Elemente Analyse, Schadensmodellierung, Kontinuumschadensmechanik, Materialmodellierung, Simulationsmethodik

(Veröffentlicht in englischer Sprache)

Thomas Feser
DLR, Institut für Bauweisen und Strukturtechnologie, Stuttgart

Entwicklung einer Simulationsmethodik zur Vorhersage der Energieabsorption von Kompositstrukturen unter Stauchbelastung

D 93 (Dissertation, Universität Stuttgart)

In der vorliegenden Arbeit wird eine stabile Simulationsmethodik entwickelt, die die fortschreitende Schädigung und Energieaufnahme von Faserverbundstrukturen verlässlich vorhersagt. Anhand eines „Building-Block"-Ansatzes wird die Schädigungsausbreitung unter Stauchbelastung untersucht. Die Arbeit liefert wichtige Modellierungsrichtlinien für die erfolgreiche und recheneffiziente Simulation von Verbundwerkstoffen unter axialer Stauchbelastung und trägt dazu bei, den Umfang experimenteller Untersuchungen zu reduzieren. Erstmalig konnte gezeigt werden, dass die Auswirkungen von Diskretisierungs-Optionen vom Anwendungsfall und dem vorherrschenden Versagensmodus abhängen. Insbesondere der Ansatz der Rissbandskalierung der Bruchenergie, ist für die Simulation von progressivem Stauchen nicht anwendbar. Im Rahmen internationaler Forschungskooperationen konnte gezeigt werden, dass diese Simulationsmethodik geeignet ist, verschiedene Materialmodelle in unterschiedlichen FE-Codes zu vergleichen. Haupteffekte lassen sich bereits auf der untersten Ebene des Building Blocks identifizieren. Eine solche Simulationsmethodik ist äußerst hilfreich, um den Ansatz der Zertifizierung ziviler Luftfahrzeuge durch numerische Analyse zu fördern.

Aircraft Crash, Fibre-reinforced composites, Crushing, Finite Element Analysis, Damage Modelling, Continuum Damage Mechanics, Material Modelling, Simulation Methodology

(Published in English)

Thomas Feser
German Aerospace Center (DLR), Institute of Structures and Design, Stuttgart

Development of a Simulation Methodology to Predict the Energy Absorption of Composite Structures under Crush Loading

D93 (Doctoral Thesis, University of Stuttgart)

In the present work, a robust simulation methodology is developed that reliably predicts the progressive damage and energy absorption of composite structures. A building block approach is used to investigate damage propagation under crush loading. The thesis provides important modelling guidelines for the successful and computationally efficient simulation of composites under axial crush loading and contributes to reducing the scope of experimental investigations. For the first time, it was shown that the effects of discretisation options depend on the application case and the prevailing failure mode. In particular, the approach of crack band scaling of fracture energy, is not applicable for the simulation of progressive crushing. Within the framework of international research cooperation, it could be shown that this simulation methodology is suitable for comparing different material models in different FE codes. Main effects can already be identified at the lowest level of the building block. Such a simulation methodology is extremely helpful in promoting the approach of certification of civil aircraft through numerical analysis.

Development of a Simulation Methodology to Predict the Energy Absorption of Composite Structures under Crush Loading

A thesis accepted by the Faculty of Aerospace Engineering and Geodesy of the University of Stuttgart in partial fulfilment of the requirements for the degree of Doctor of Engineering Sciences (Dr.-Ing.)

by

THOMAS FESER

born in Herrenberg, Germany

Main referee: Prof. Dr.-Ing. Heinz Voggenreiter
Co-referee: Reza Vaziri, Ph.D., P.Eng.
Date of defence: November 16th, 2022

Institute of Aircraft Design
University of Stuttgart
2023

Acknowledgements

Contents

Nomenclature

Abbreviations

ACC	NASA Advanced Composite Consortium
AFRP	Aramid Fibre Reinforced Plastic
ASTM	American Society for Testing and Materials
CC	Compact Compression (Test)
CDM	Continuum Damage Mechanics
CFRP	Carbon Fibre Reinforced Plastic
CID	Controlled Impact Demonstration
CLT	Classical Laminate Theory
CMH-17	Composite Materials Handbook
CMH-17 CWG	Crashworthiness Working Group of CMH-17
COH3D8	Cohesive element formulation in Abaqus/Explicit
CPU	Central Processing Unit
CRASURV	Design for Crash Survivability (European Commission funded project)
CS	Certification Specification
CZM	Cohesive Zone Model
DCB	Double Cantilever Beam
DLR	German Aerospace Center - Deutsches Zentrum für Luft- und Raumfahrt e.V.
EA	Energy Absorbed
EASA	European Aviation Safety Agency
ENF	End Notched Flexure
ESIS	European Structural Integrity Society

EU	European Union
FAA	Federal Aviation Administration
FAR	Federal Aviation Regulations
FE	Finite Element
FEA	Finite Element Analysis
FEM	Finite Element Model
FPZ	Fracture Process Zone
FRMM	Fixed-Ratio Mixed Mode
GFRP	Glass Fibre Reinforced Plastic
HEDI	High Energy Dynamic Impact
HL	'Hard' Laminates
HVI	High Velocity Impact
JAR	Joint Aviation Requirements
MAAXIMUS	More Affordable Aircraft through eXtended, Integrated and Mature nUmerical Sizing (EU-funded Project)
MMB	Mixed Mode Bending
NACA	National Advisory Committee for Aeronautics
NASA	National Aeronautics and Space Administration
OCT	Over-height Compact Tension Test
POD	Pin-Opening Displacement
QI	Quasi-isotropic (Laminate)
RVE	Representative Volume Element(s)
S4R	Denotion of Shell Elements in Abaqus/Explicit (4 nodes elements with reduced integration scheme)
SC8R	Denotion of Continuum Shell Elements in Abaqus/Explicit (8 nodes elements with reduced integration scheme)
SDV	Solution Dependent Variable
SEA	Specific Energy Absorbed
SPH	Smooth Particle Hydrodynamics
TTS	Triggered Tube Segment

UBC	The University of British Columbia, Vancouver, Canada
UC	Unit Cell(s)
UD	Uni-Directional (Laminate)
VUMAT	User-Material Model (explicit) in Abaqus/Explicit
WWFE-III	The third World-Wide composite Failure Exercise
XWB	eXtra Wide Body

Superscripts and Subscripts

0	Undamaged
1 or 11	Longitudinal or fibre direction
12	Shear direction
2 or 22	Transverse or matrix direction
abs	Absolute value
$brittle$	Brittle failure
C	Compression
el	Elastic value
EU	Value of EU version of IM7/8552
exp	Exponential softening
f	Fracture
i	Index of load cycle
I, II, III	Mode I, Mode II, Mode III
max	Maximum value
$mean$	Mean value
$peak$	Peak value
pl	Plastic value
sat	Saturation
T	Tension
US	Value of US version of IM7/8552

Symbols

α	Shear-transverse plasticity coupling parameter	-
β	Plasticity hardening law coefficient	-
$\gamma_{12,pl}$	Plastic portion of total shear strain	-
γ_{12}	Shear strain	-
μ	Plasticity hardening law exponent	-
σ_{11}	Longitudinal (fibre) stress	GPa
σ_{22}	Transverse stress	GPa
τ_{12}	Shear stress	GPa
$\tilde{\sigma}_{22}$	Effective transverse stress	GPa
$\tilde{\tau}_{12}$	Effective shear stress	GPa
$\tilde{p}$	Accumulated plastic strain	-
$\underline{Y}_2, \underline{Y}_{12}$	Transverse and shear damage evolution laws	$\sqrt{GPa}$
ε_{11}	Longitudinal (fibre) strain	-
$\varepsilon_{22,pl}$	Plastic portion of transverse strain	-
ε_{22}	Transverse strain	-
a	Crack length	mm
b	Shear-transverse damage coupling parameter	-
d_{12}	Shear damage variable	-
d_1	Fibre damage variable	-
d_2	Transverse damage variable	-
E_{1c}	Longitudinal (fibre) compressive modulus	GPa
E_{1t}	Longitudinal (fibre) tensile modulus	GPa
E_1^0	Initial, undamaged longitudinal modulus	GPa
E_{2c}	Transverse compressive modulus	GPa
E_{2t}	Transverse tensile modulus	GPa
E_2^0	Initial, undamaged transverse modulus	GPa
f	Elastic domain function	
G_{12}	Shear modulus	GPa
G_{12}^0	Initial, undamaged shear modulus	GPa

G_{c1}	Fibre fracture energy	$\frac{kJ}{m^2}$
g_{c1}	Fracture energy density	$\frac{kJ}{m^3}$
G_c	Laminate fracture energy	$\frac{kJ}{m^2}$
l^*	Characteristic element length	mm
p	Effective plastic strain	-
R_0	Plasticity yield stress	GPa
t_{Lam}	Laminate thickness	mm
t_{ply}	Ply thickness	mm
U	Elastic strain energy	kJ
W	Total dissipated energy	kJ
Y_{120}	Shear damage initiation threshold	$\sqrt{GPa}$
Y_{12c}	Shear damage evolution parameter	$\sqrt{GPa}$
Y_{12s}	Shear damage failure threshold	$\sqrt{GPa}$
Y_{20}	Transverse damage initiation threshold	$\sqrt{GPa}$
Y_{2c}	Transverse damage evolution parameter	$\sqrt{GPa}$
Y_{2s}	Transverse damage failure threshold	$\sqrt{GPa}$
Y_2, Y_{12}	Transverse and shear energy release rate functions	$\sqrt{GPa}$

System of Units

Energy	J
Force	kN
Length	mm
Mass	kg
Stress	GPa
Time	ms

Abstract

Due to the high mass specific stiffness and considerably low mass of fibre-reinforced composites, these materials are more and more used in primary structures of civil aircraft. Design guidelines as well as accurate and efficient simulation tools are limited. The development of robust simulation frameworks and numerical approaches which are able to capture the damage mechanics in complex crash events is crucial for crashworthiness research.

In this context, the objective of this dissertation is the development of a robust simulation methodology to reliably predict the progressive damage and energy absorption of composite structures. The research presented in this thesis was performed in the context of the international research collaboration 'DLR@UBC'. The aims are the development of a building block approach and the investigation of damage propagation under crash loading covering a wide range of structural scales from coupons up to the sub-structural level. The simulation methodology shall provide guidelines and best practices on the identification of appropriate input parameters and discretization methods. This effectively supports the design of composite components with reduced reliance on experimental results especially on the more complex sub-structural level.

The methodology follows a building block approach from the definition of material input on ply-level up to the application of progressive crushing. By this, a standard simulation methodology is defined which helps to identify the necessary application levels and required experimental tests for calibration and validation as well as the degree of model detail needed to capture the relevant failure mechanisms. The building block approach is used to investigate the influence of specific damage evolution models and how the effects scale on different levels of complexity as well as failure modes. The simulation methodology developed in this work is based on a meso-scale modelling approach with focus on the intralaminar material behaviour. The research activities include the enhancement of an intralaminar material model in the scope of continuum damage mechanics implemented as a user-material in the framework of the commercial explicit FE-code Abaqus/Explicit. Different fibre softening options based on fracture energies are implemented in the user-material which describe the evolution of fibre damage after damage initiation. The effects of fibre softening options are investigated and shown along the building block up to progressive crushing. To avoid mesh size dependencies, material models in the scope of continuum damage mechanics commonly apply the crack band scaling approach to scale the fracture energy on the element size of the numerical mesh. This approach developed for failure mechanisms where damage is confined into a crack-like narrow band is critically investigated along the building block. The composite material system HEXCEL

IM7/8552 is used consistently throughout the work. Material input parameters required for the simulation are determined from open literature. Missing material parameters are identified and determined in material characterization tests.

In the building block approach, single-element simulations are identified as the fundamental level for verification. The main effects of the material model can be verified and general tendencies valid for the entire building block can be identified at this level. This enables the prediction of failure on higher levels of the building block. The fibre fracture energies are identified as the substantial material parameters of the modelling approach. Calibration and validation of fracture energies are performed using experimental results of fracture tests. The Over-height Compact Tension and Compact Compression tests were found to produce stable and self-similar intralaminar crack growth under tensile and compressive loading. Based on tests results in terms of laminate fracture energies in open literature, the fibre fracture energies are calibrated and used for prediction of progressive crushing. At the level of progressive crushing, the results are validated without further calibration. At this level, it is shown that mesh type and element size significantly influence the predicted crushing force and energy absorption. To reliably predict the complex crushing behaviour with different crushing failure modes, detailed models are required that enable the simulation of the major failure modes fragmentation and splaying.

The simulation methodology shows that the effects of discretization options are dependent on the application case and the predominant failure mode. If damage is confined into a narrow band similar to a crack, crack band scaling of the fracture energies is mandatory to avoid element size dependent results. However in progressive axial crushing, where the volume is successively destructed, crack band scaling results in distinct mesh size dependent results. Finally, it is shown that the effects of different fibre softening options on the global behaviour on all levels of the building block are due to their influence on the fibre damage evolution and ultimate strain on the meso-scale level. Overall, the work contributes to the state of the art and enables the evaluation and selection of simulation approaches to reliably predict the complex failure behaviour of composite structures under crash loading.

Kurzfassung

In Primärstrukturen ziviler Luftfahrzeuge kommen aufgrund von Materialeigenschaften wie hoher massenspezifischer Festigkeiten und Steifigkeiten und der damit verbundenen deutlich geringeren Strukturmassen vermehrt Faserverbundwerkstoffe zum Einsatz. Präzise und effiziente Simulationsmethoden sind jedoch nur begrenzt verfügbar. Entscheidend für die Erforschung der Crashsicherheit von Flugzeugstrukturen ist die Entwicklung stabiler Rahmenbedingungen für die Simulation sowie numerische Vorgehensweisen, die die komplexe Schädigungsmechanik während eines Crashs korrekt abbilden.

Die vorliegende Arbeit untersucht in diesem Zusammenhang die Entwicklung einer stabilen Simulationsmethodik, die die fortschreitende Schädigung und Energieaufnahme von Strukturen aus Verbundwerkstoffen verlässlich vorhersagt und entstand im Rahmen der internationalen Forschungskooperation "DLR@UBC". Ziele sind die Entwicklung eines sogenannten "Building-Block"-Ansatzes und die Untersuchung der Schädigungsausbreitung unter Stauchbelastung, die ein weites Spektrum an Strukturgrößen von Coupon bis zur substrukturellen Ebene abdecken. Die entwickelte Simulationsmethodik definiert Richtlinien und stellt die beste Vorgehensweise für die Bestimmung geeigneter Eingabeparameter und Diskretisierungsmethoden bereit. Dies unterstützt effektiv die Auslegung von Verbundbauteilen mit reduzierter Abhängigkeit von experimentellen Ergebnissen, insbesondere auf der komplexeren substrukturellen Ebene.

Die Methodik folgt dem "Building-Block"-Ansatz von der Definition der Materialeingabeparameter für die Einzellage bis zur Anwendung in progressivem Stauchversagen. Dadurch wird eine Standardsimulationsmethodik definiert, mit deren Hilfe die erforderlichen Anwendungsebenen und benötigten experimentellen Tests für die Kalibrierung und Validierung sowie der Detaillierungsgrad ermittelt werden können, der zur Erfassung der relevanten Versagensmechanismen erforderlich ist. Der "Building-Block"-Ansatz wird verwendet, um den Einfluss unterschiedlicher Modelle des Schädigungsfortschrittes und deren Skalierung auf verschiedene Komplexitätsstufen sowie Versagensmodi zu untersuchen. Die in dieser Arbeit entwickelte Simulationsmethodik basiert auf einem Modellierungsansatz auf meso-skalen Ebene mit Schwerpunkt auf dem intralaminaren Materialverhalten. Die Forschungsaktivitäten umfassen die Weiterentwicklung eines intralaminaren Materialmodells, das auf der Kontinuumsschadensmechanik basiert und als Nutzermaterialmodell im kommerziellen expliziten FE-Programm Abaqus/Explicit implementiert ist. Im Nutzermaterial sind verschiedene Optionen der Faserentfestigung basierend auf Bruchenergien implementiert, die die Entwicklung von Faserschädigung beschreiben. Die Auswirkungen der Entfestigungsoptio-

nen werden entlang des "Building-Block"-Ansatzes bis hin zum progressiven Stauchen auf Substrukturebene untersucht. Um Abhängigkeiten von der numerischen Elementgröße zu vermeiden, kommt in Materialmodellen der Kontinuumsschadensmechanik üblicherweise der Ansatz der Rissbandskalierung zur Anwendung, um die Bruchenergie auf die Elementgröße zu skalieren. Dieser Ansatz, der für Versagensmechanismen entwickelt wurde, bei denen Schädigung auf ein rissartiges, schmales Band beschränkt ist, wird über den gesamten "building block" hinweg kritisch untersucht. In der Arbeit wird konsistent das Verbundmaterial HEXCEL IM7/8552 verwendet. Die für die Simulation erforderlichen Materialeingabeparameter werden aus der Literatur ermittelt. Fehlende Materialparameter werden in Materialcharakterisierungstests ermittelt.

In der entwickelten Simulationsmethodik bilden Einzelelementsimulationen die grundlegende Ebene für die Verifizierung des entwickelten "Building-Block" Ansatzes. Auf dieser Ebene können die Haupteffekte des Materialmodells verifiziert und allgemeine Trends identifiziert werden. Dies ermöglicht die Vorhersage des Versagensverhaltens auf weiteren Ebenen mit steigender Komplexität. Die Faserbruchenergien sind die wesentlichen Materialparameter des Modellierungsansatzes. Die Kalibrierung und Validierung der Bruchenergien erfolgen anhand experimenteller Ergebnisse bruchmechanischer Tests. Sogenannte "Over-height-Compact-Tension"- und "Compact-Compression"-Proben zeigten in Versuchen unter Zug- und Druckbelastung ein stabiles und selbstähnliches interlaminares Risswachstum. Die Faserbruchenergien werden anhand veröffentlichter Testergebnisse kalibriert und für die Vorhersage des Stauchverhaltens verwendet. Anschließend werden die Ergebnisse des progressiven Stauchens ohne weitere Kalibrierung validiert. Auf dieser Ebene zeigt sich, dass die Art des numerischen Netzes sowie die Elementgröße die prognostizierte Stauchkraft und Energieabsorption erheblich beeinflussen. Um das komplexe Stauchverhalten mit den Hauptversagensmodi Fragmentierung und Abspreizung verlässlich vorherzusagen, sind detaillierte Modelle erforderlich.

Die Simulationsmethodik zeigt, dass die Auswirkungen von Diskretisierungsoptionen vom Anwendungsfall und dem vorherrschenden Versagensmodus abhängen. Wenn die Schädigung auf einen schmalen Bereich, ähnlich eines Risses, begrenzt ist, ist die Methode der Rissbandskalierung der Bruchenergie erforderlich, um elementgrößenabhängige Ergebnisse zu vermeiden. Bei progressivem axialen Stauchen, bei dem das Volumen sukzessive zerstört wird, führt die Rissbandskalierung jedoch zu deutlichen Netzgrößenabhängigkeiten der Ergebnisse. Abschließend wird gezeigt, dass die Wirkungen verschiedener Optionen der Faserentfestigung auf das globale Verhalten auf ihren Einfluss auf die Entwicklung der Faserschädigung und maximale Dehnung auf Mesoebene zurückzuführen sind.

Insgesamt trägt die Arbeit zum Stand der Technik bei und ermöglicht die Bewertung und Auswahl von Simulationsansätzen, um das komplexe Versagensverhalten von Verbundstrukturen unter Stauchbelastung zuverlässig vorherzusagen.

1 Introduction

1.1 Background

Composite materials are nowadays used in the transport sector, especially the aerospace industry. Due to superior high mass-specific stiffness and strength, composite materials are widely used in novel commercial transport aircraft. The application of composite materials such as carbon fibre reinforced polymers (CFRP), glass fibre reinforced polymers (GFRP) or aramid fibre reinforced polymers (AFRP) were first limited to secondary aircraft structures like spoilers or air brakes. Due to the improvement of manufacturing processes and gained understanding of mechanical behaviour under various loading conditions, composite materials are more and more replacing metallic alloys in primary aircraft structures such as fuselage and wings. The increasing percentage of composite materials on the structural weight of novel aircraft models such as the Boeing B787 (50%) [1] or Airbus A350 (53%) [2] show the increasing importance of these materials in primary structures. Those primary structures are crucial for the structural integrity of the aircraft since they carry the air and ground loads and in case of the fuselage are pressurized. Crashworthiness requirements of the regulatory authorities like the Federal Aviation Administration (FAA) and the European Union Aviation Safety Agency (EASA) demand sufficient energy absorption capacity and preservation of structural integrity in survivable crash events to ensure an acceptable level of occupant safety [3, 4]. In aircraft with mainly metallic primary structures, energy absorption in a survivable crash scenario such as an emergency landing is achieved mainly through the ductile deformation of the aluminium structure. Figure 1.1 a) shows a drop test of an Airbus A320 metallic rear fuselage section [5]. The generally brittle behaviour of CFRP composites necessitates specific crash concepts and energy absorbing devices to achieve the safety requirements and ensuring the structural integrity of the fuselage in a crash event. Figure 1.1 b) shows a Boeing B787 composite fuselage section. In the sub-cargo floor region where substantial damage is expected in a crash scenario, the imparted crash kinetic energy can largely be absorbed by progressive crushing of the structure due to the high mass-specific energy absorption potential of CFRP materials [6]. In the specific design of the sub-cargo structure, Figure 1.1 c), the imparted impact energy is absorbed by progressive crushing of the c-channel stanchions [7].

The limited airworthiness regulations and design guidelines on composite crashworthiness and energy absorption management as well as the lack of accurate and efficient simulation tools led to the formation of the Crashworthiness Working Group (CWG) of the Composite Materials Handbook
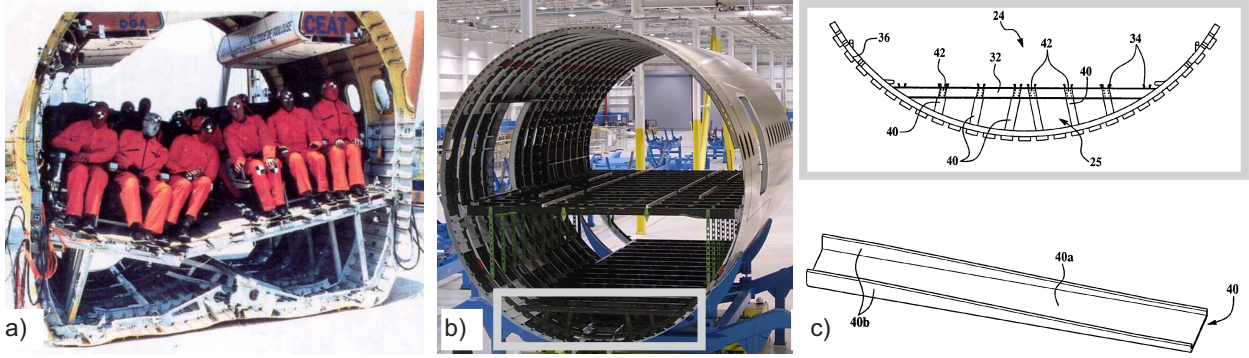
Figure 1.1: a) Drop test of an Airbus A320 rear fuselage section [5]; b) Boeing B787 composite fuselage section with the crash concept in the sub-cargo floor [8]; c) Details of sub-cargo floor structure [7]

(CMH-17) [9]. The CMH-17 CWG is formed by representatives of academia, aircraft and automotive industry and regularization authorities. Through a close interaction with ASTM Committee D-30 [10], the working group addresses the development of guidelines and best practices for the experimental and numerical characterization of the energy-absorbing capability and crash resistance of advanced composite structures. In a concise and comprehensive exercise, the goal is to better understand the complex failure mechanisms, their impact on energy absorbing capabilities, and to derive guidelines and best practice approaches for testing and modelling of composite aircraft structures under crash events.

The development of robust simulation frameworks and numerical approaches which are able to capture the damage mechanics is crucial for crashworthiness research and development [11, 12]. Due to the extensive increase of computational power over the last few years, numerical models became an efficient tool to investigate design optimizations for potential safety improvements. To show fulfilment of the crashworthiness requirements supported by numerical models became an alternative accepted by the regularization authorities. However, the simulation results must be validated only through the comparison with experimental results obtained on previously certified aircraft. Nonetheless, the approach of certification by analysis is important for saving time and cost in the development and authorisation of future composite aircraft [13]. One method would be the improvement of numerical methodologies in order to increase the trust in the predictive capacity of numerical models.

1.2 Objective and Aims

The objective of this dissertation is to contribute to the improvement of numerical modelling methods and to develop a robust simulation methodology to reliably predict the progressive damage and energy absorption of composite structures. The aims are the development of a building block approach and the investigation and simulation of damage propagation under transient-dynamic loading covering a wide range of structural scales from coupons up to sub-structural level. The

goal is to establish a robust simulation framework to support the effective design of crashworthy composite components with reduced reliance on experimental data. The simulation methodology shall also provide guidelines and best practices on the identification of appropriate input parameters and discretization methods.

The methodology is based on a meso-scale modelling approach with focus on the intralaminar behaviour of composite materials. A computationally efficient modelling approach (multi-layered shell approach, also known as single-shell model) will be used for the calibration of material-specific input parameters and investigation of specific material model options. The complexity of the model is increased through a transition to a high-fidelity model (stacked-shell modelling approach) if detailed modelling of complex failure modes is required to reliably predict the crushing behaviour. With the background described above, this leads to the main objectives of this thesis:

1. Review and discussion of the literature available on crushing and energy absorption of composite structures as well as state of the art modelling approaches.

2. The work strictly follows the building block approach from the definition of material inputs on the ply-level up to the application in progressive crushing.

3. The work is based on the material system HEXCEL IM7/8552 [14–16] that is widely used in the aerospace industry and on which several research studies have already been carried out in the open literature. Missing material model specific input parameters are identified and determined in material characterization tests.

4. The research activities requires the improvement of a user-defined composite material model to investigate the influence of different approaches for damage evolution (strain-softening options) and demonstrate the effects on different scales of the building block. The aim is to minimize non-physical parameters in the constitutive model which cannot be calibrated using experimental tests.

5. Influence of discretization options on the prediction of progressive damage (e.g. mesh dependencies, element size dependencies) and alternative approaches to overcome the mesh dependencies. Transition to meso-scale modelling approach with cohesive elements to reliably predict the complex failure behaviour of composite materials.

The work presented in this thesis was performed in the context of the international research collaboration 'DLR@UBC' of the German Aerospace Center (DLR) and the University of British Columbia (UBC), Canada. Objectives of the research topic 'Composite Technologies - Simulation of Crash and HVI' are the improvement of composite material models and modelling approaches used by DLR and UBC and demonstrating their respective applicability at different structural scales from basic coupon tests up to aircraft substructures. This thesis presents the DLR part of the collaborative and objective research work. Results of the DLR@UBC collaboration are published in [17–22].

2 Fundamentals and State of the Art

In this chapter, an overview on the research of composite crushing of structures is presented. The literature review commences with a review on research of crashworthiness of aircraft structures. This is followed by a brief introduction to energy absorption and crushing of composite materials as well as a description of the energy absorption parameters. The second part of this chapter deals with the numerical modelling of composite materials and the simulation of damage and failure of composite materials. This is followed by a detailed review of numerical simulation of progressive crushing. The literature review defines the open questions and outlines the objective of the work. Finally, the structure of the dissertation is given.

2.1 Review on Research of Crashworthiness of Aircraft Structures

In the following sections, a brief overview on aircraft crashworthiness research programmes are given. For a comprehensive review of these programmes, the reader is referred to [23].

2.1.1 Crashworthiness Research Programmes

The research of crashworthiness of commercial aircraft dates back to the 1950s and 1960s were full-scale crash tests of different aircraft types were performed by the National Advisory Committee for Aeronautics (NACA) [24] as well as on behalf of the FAA [25, 26]. However, those tests were performed with mainly horizontal velocity of the aircraft representing potential survivable crash events like hard or emergency landings. The aim of those tests were to generate a dataset of survivable crash cases.

In the 1980s, FAA and NASA performed a test programme where five Boeing B707 fuselage sections of different configurations and lengths of 3 m and 4 m were tested in vertical drop tests [27–29]. The sections were loaded with crash tests dummies, ballast or additionally cargo. The impact velocity of those tests was between 6.1 $\frac{m}{s}$ and 10.4 $\frac{m}{s}$. The research programme peaked in the Controlled Impact Demonstration (CID) full-scale test of a remotely flown Boeing B720 aircraft in 1984. A picture sequence of this test is shown in Figure 2.1. The aim of this test was the acquisition, demonstration and validation of technology for improved crash survivability of transport aircraft occupants. Beneath the investigation of post-crash fire, the objective was to acquire transport aircraft crash structural data [30].

Figure 2.1: Sequence of the Controlled Impact Demonstration (CID) test of a Boeing B720, from [34]

In the European Community funded programme "crashworthiness for commercial aircraft" in the 1990s, quasi-static and dynamic tests were performed on fuselage sections of an Airbus A320. A 6-frame rear fuselage section was drop tested with an initial velocity of 6.7 $\frac{m}{s}$, see Figure 1.1a). This research programme was intended to investigate the failure behaviour of aircraft structures under crash related loads [5, 31, 32]. FAA and NASA also performed vertical fuselage drop tests in the 1990s and beginning of the 2000s. Two Boeing B737 fuselage sections including the cargo door forward of the wing were loaded with luggage as well as an auxiliary fuel tank. Also, the two sections were equipped with overhead compartments to investigate the potential risk of overhead masses. The B737 fuselage sections were drop tested with an initial velocity of 9.1 $\frac{m}{s}$.

The series of FAA and NASA aircraft crash tests culminated in 2019 with a full-scale pendulum crash test of a Fokker F28 MK-1000 [33]. In addition to the previous test programmes with purely vertical velocity drop tests, this horizontal and vertical momentum crash test was intended to contribute to the establishment of new guidelines for commercial transport aircraft certification.

The research on crashworthiness of commercial aircraft contributed to the definition of FAR/JAR/CS 25.562 'Emergency landing dynamic conditions' of FAA and EASA [35]. The requirements also form the 'metallic equivalent' defined in the special conditions for the certification of transport aircraft structures made of composite materials [3, 4].

2.1.2 Research on Crashworthiness of Composite Aircraft Structures

In mainly metallic aircraft, the fuselage is designed in way that the imparted impact energy is absorbed by plastic deformation of the metallic structure below the passenger crossbeam. This also preserves the structural integrity of the cabin and ensures survivable post-crash cabin space and evacuation routes for the occupants. Composite fuselages of modern commercial aircraft must assure the same level of safety in a survivable crash scenario. Due to the generally brittle failure behaviour of composites, the impact energy cannot be absorbed in the same way as in metallic structures. In contrast, CFRP composites provide significantly higher mass-specific energy absorption compared to other materials if a stable progressive crushing process is achieved [36, 37]. This shows the necessity to develop specific crash concepts and implementation of energy absorbing devices in the fuselage structure in order to benefit from the advantages of composite materials.

Different concepts for energy absorptions have been investigated over the past years and are still part of ongoing research. Novel crash concepts use the kinematics and deformation of the fuselage in a crash scenario [23, 38]. Crash devices or plastic hinges implemented in the circumferential frames of the fuselage affect the crash kinematics in a way that the structure fails at a location close to the attachment of the vertical struts [39]. The vertical struts are the connection of the passenger crossbeam and the lower section of the frames and are the support in the vertical direction. In a crash scenario, the vertical struts are loaded in compression and specifically designed attachment elements cut the composite struts into stripes. Additional energy is absorbed by bending of the cut stripes through delamination damage and fragmentation [40, 41].

Energy absorbing devices implemented in the support structures of the overhead compartments prevent their disengagement from the primary structure and ensure the structural integrity of the cabin in severe turbulences or crash. The energy absorption is based on crushing of composite cylinders or composite bearing failure [42–44].

From the energy absorbers in the overhead compartments, the tension-absorbing concept developed by Airbus and the German Aerospace Center (DLR) [45] was derived. Tension loads acting in the cargo crossbeam, or the bolted connection of the passenger crossbeam and frame, are used to absorb energy in a controlled manner by progressive bearing failure. Predictions from full-scale simulations showed that up to 50 % of the overall-absorbed energy could be absorbed by such tension absorbers [46]. In bearing failure, energy is absorbed by crushing of material in front of the bolt. In tension-absorbing joints, high energy absorption is achieved by sustaining the bearing process over long distances. Specially designed washers and notches prevent failure of the bolted connection ensuring the structural integrity. Experimental and numerical studies of this concept using single- and multi-bolt coupons and structural elements have been performed [45–48]. Further studies on the effects of individual material and geometric parameters showed the energy-absorbing capability of the tension-absorbing concept [49–53].

Energy absorber most relevant for this work absorb the impact energy through progressive crushing
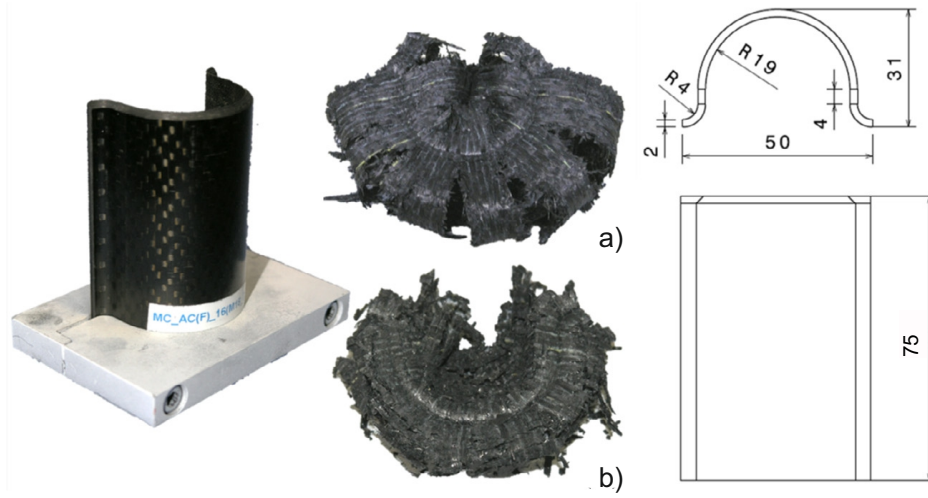
Figure 2.2: DLR segment under axial compression; post-test specimens of a) quasi-static loading, b) dynamic loading, from [64] (with permission from Elsevier)

and high fragmentation of the composite material. Those crash absorbers are mainly located in the sub-cargo floor area in the lower fuselage part. During a crash event, this part is loaded first with large deformation and substantial damage [37, 54].

In the European Commission funded project "Design for Crash Survivability (CRASURV)" [55], the crash zone was located exclusively in the sub-cargo floor region. The complete test pyramid from material tests on coupon level up to drop tests of fuselage sub-floor sections was considered [56–59]. Such a test pyramid, where each level strongly relies on the previous level is called a 'Building Block' [60]. On the coupon level of the CRASURV building block, an omega-shaped tube segment specimen, called 'DLR segment' was used to compare the specific energy absorption (SEA) of different composite materials [56]. Due to its self-stabilising ability without lateral support and reproducible crush failure modes under various loading conditions, the DLR segment was developed as a standard specimen configuration to characterize the crushing performance of composite materials. The DLR segment was used in various test programmes to develop energy absorbing structures of aircraft and helicopter structures [61–63]. The DLR segment is pictured in Figure 2.2 and shows the post-test state after quasi-static a) and dynamic loading b).The DLR segment featured high SEA values [61]. An additional advantage of the DLR segment is the simple test setup.

An attempt to integrate a modified design of the DLR segments as energy absorber in aircraft structures was made in the EU-funded project 'More Affordable Aircraft structure through eXtended, Integrated, and Mature nUmerical Sizing' (MAAXIMUS) [65]. The DLR segments were integrated in an aircraft fuselage structure, with a stiff cargo crossbeam that withstand the crush loads an enables crushing of the sub-cargo structure [66]. In this so-called 'Bend-frame concept', shown in Figure 2.3, modified DLR segments with flanges are bolted on the center framework struts and provide high buckling strength through the self-supporting cross-section. This results
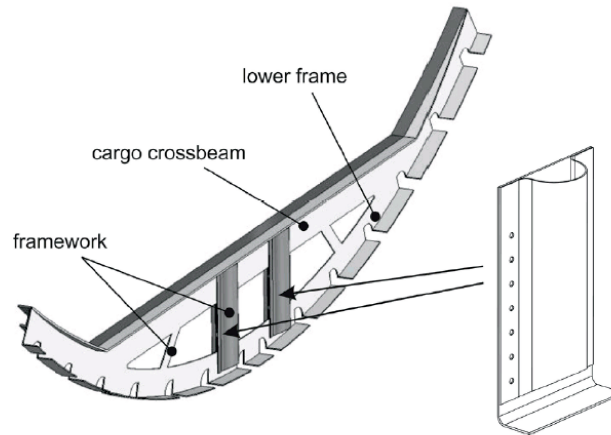
Figure 2.3: Bend-frame concept with DLR segment specimens as energy-absorbing elements, from [66] (with permission from Elsevier)

in progressive crushing instead of instability failure [66] and high mass-specific energy absorption of this highly integrated fuselage section was achieved. The crashworthy aircraft fuselage structure was drop tested and the design worked as intended with progressive crushing of the DLR segments whereas the cargo crossbeam and the structural integrity of the structure remained intact [67]. However, the stiff design of the cargo crossbeam added additional mass to the structure.

The crash concept of the Boeing B787, pictured in Figure 1.1 b), c), is also implemented in the sub-cargo area [7]. CFRP stanchions are supposed to crush in a progressive mode [68]. In this concept, the cargo crossbeam provides much less stiffness compared to the approaches in the CRASURV and MAAXIMUS projects and mass inertia of the loaded cargo maybe intended here to support the crossbeam. Investigation and optimization of the energy absorbing sub-cargo stanchions is objective of the CMH-17 CWG. In this work, the building block approach is followed which includes test procedures for composite energy absorber elements [69] and design analysis methods [70] to predict the crushing behaviour of sub-floor structures.

2.2 Crushing Behaviour and Energy Absorption of Composite Materials

The ability of a composite structure to absorb energy depends on the main failure modes acting during crushing. Two main failure modes of composite energy absorbers were identified: the catastrophic and progressive failure mode whereas the latter absorb a higher amount of energy during the crushing process. Observing the failure modes during a crushing event is a qualitative method to measure the ability of composite structures to absorb energy. A quantitative measurement is by analysing the crush load-crush displacement characteristic. Vast literature is available on crushing of composite materials. Thornton [71] was among the first who investigated the crushing behaviour of composite tubes. By investigating different materials, it was found that specimens made of fibre

composite materials had a higher energy absorption than equivalent components made of metal. Hull [72] investigated composite FRP square tubes and identified two main modes of progressive failure. Progressive folding is the characteristic mode of tubes made from ductile metal and plastic [72]. Progressive crushing is characterised by a zone of micro fractures at one end of the tube that propagates with the same speed as the impact plate [72]. The characteristics of these two failure modes are shown in Figure 2.4. Progressive folding can be subdivided into three phases, clearly visible in the load-displacement characteristic. At the beginning, the load P increases steeply until P_{max} is reached and then likewise drops abruptly (area I in Figure 2.4). This indicates the beginning of the folding process up to the formation of the first complete fold at a displacement of S_i. In the subsequent section II, the force oscillates about a mean value $\overline{P}$ and the tube folds down progressively. By compacting the completely folded tube, the force rapidly increases again in section III [72].

Progressive crushing occurs especially in specimens made of brittle composite materials. To avoid catastrophic failure, progressive crushing can be induced by triggering fracture at the impacted end of the tube [72]. The crush load-crush displacement characteristic as shown in Figure 2.4 b) is similar to the progressive folding. Due to a chamfer trigger at one end of the composite tube, the maximum force P_{max} and the subsequent drop to $\overline{P}$ in section I is lower compared to the progressive folding mode in Figure 2.4 a). Dependent on the chamfer angle, the force drop can be completely avoided [72]. Section II in Figure 2.4 b) is characterized through the constant mean force $\overline{P}$. Compaction of the debris inside the tube results in an increase of force in Section III.

As progressive crushing being the main failure mode of brittle composite materials, Hull further investigated this mode and identified two extreme crushing modes, namely 'splaying' and 'fragmentation' [72]. Hull referenced splaying and fragmentation to research performed on UD glass fibre-polyester resin tubes [73] and woven glass cloth-epoxy tubes [74], respectively. The crushing modes are schematically represented in Figure 2.5. The crushing modes are related to the micromechanics of fracture and are dependent on the distribution of the fibres in the hoop direction of the tube [72]. The first and second stage of both crushing modes are similar and are characterized by crushing down of the 30° chamfer trigger. The differences in the modes in the third and fourth stage are identified in the behaviour of the lamina bundles after the trigger is crushed down. In the splaying crushing mode, Figure 2.5 a), the fibres oriented in axial direction kink and buckle and force the layers oriented in the hoop direction to collapse. A debris wedge of crushed material forms in the middle of the axial layers which is attributed to the friction between the crushed lamina bundles and the impact plate [75]. The wedge forces the axially oriented lamina to the inside and outside. In the fragmentation mode, pictured in Figure 2.5 b), the fibres oriented in the hoop direction are distributed through the wall-thickness in the woven glass cloth tubes reducing the splaying of the axially oriented fibres. The compressive load generates high shear forces and failure in a 30° angle. Hoop restraints produce additional tensile and compressive forces which break the fragments into smaller segments [72]. The likelihood of shear fracture across the tube

a) Progressive folding

b) Progressive crushing
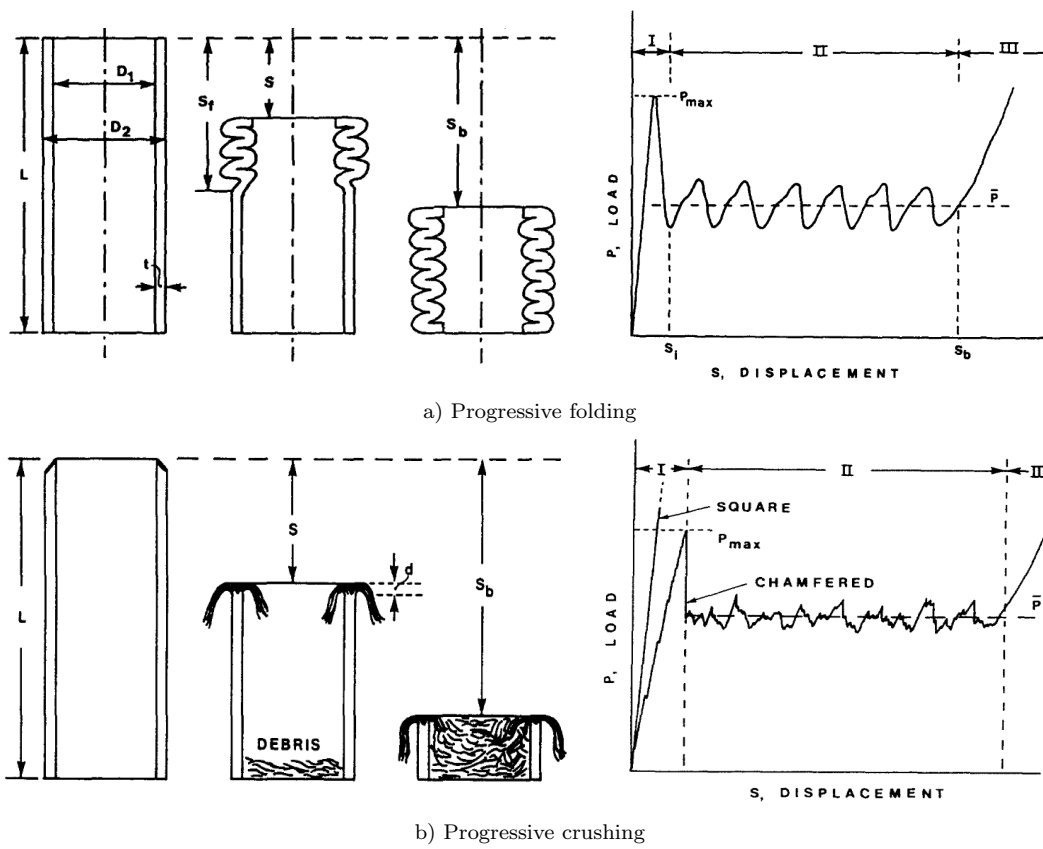
Figure 2.4: Schematic representation of a) progressive folding and b) progressive crushing, from [72] (with permission from Elsevier)

a) Splaying crushing mode

b) Fragmentation crushing mode
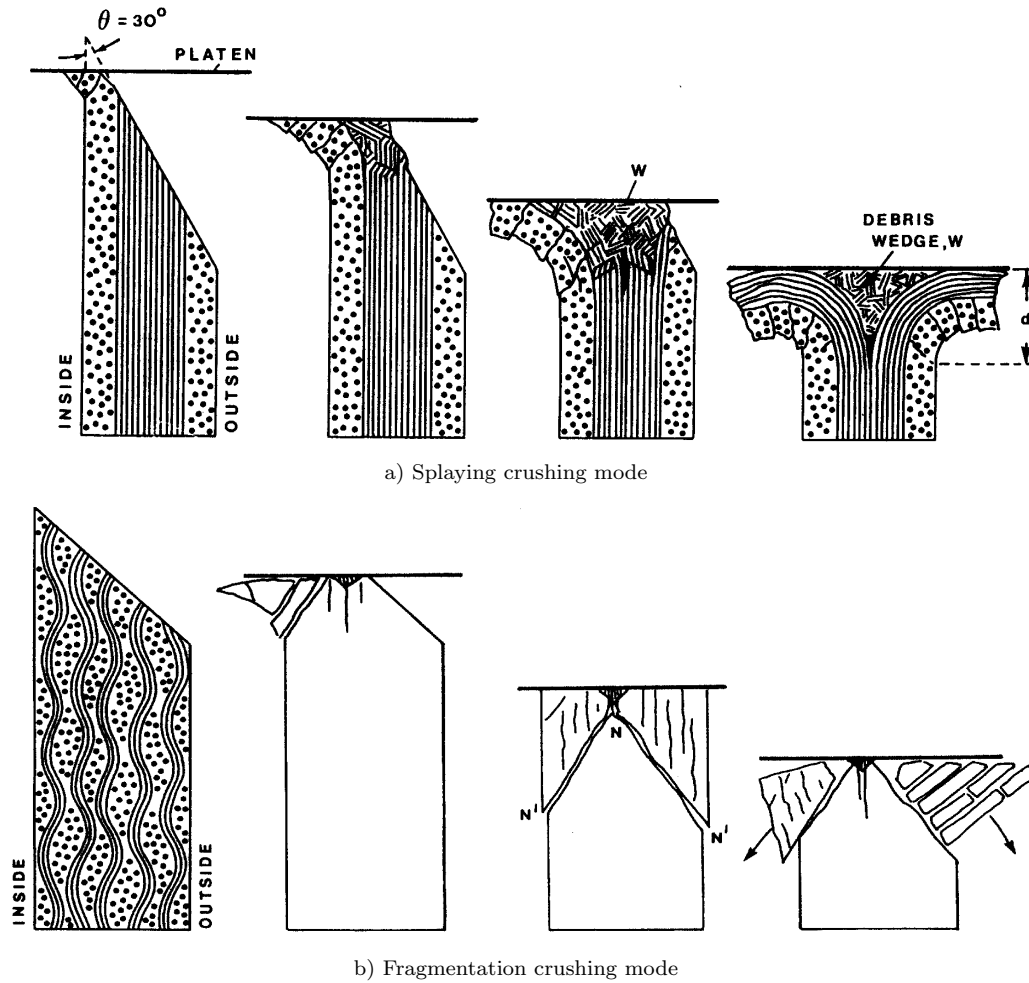
Figure 2.5: Schematic representation of a) splaying crushing mode and b) fragmentation crushing mode, from [72] (with permission from Elsevier)

wall-thickness tends to increased fragmentation. Therefore, the tendency of a composite tube to crush in either splaying or fragmentation depends on the layup. The crush load however is dependent on elastic properties and failure strengths of the fibre, matrix and fibre-matrix interface and therefore of multiple-interacting parameters like temperature and strain-rate.

2.2.1 Detailed Crushing Modes and Failure Mechanisms

Farley [6, 76] and Farley & Jones [77–79] investigated the characteristics of crushing of composite tubes and identified four failure modes: 1) transverse shearing, 2) lamina bending, 3) brittle fracturing and 4) local buckling (or progressive folding). Lamina bending and transverse shearing share similarities with the splaying and fragmentation crushing mode described by Hull [72]. Failure modes 1) to 3) were observed exclusively in composite materials with brittle fibres whereas local buckling can occur in composites with both ductile and brittle fibres [77]. A large percent-
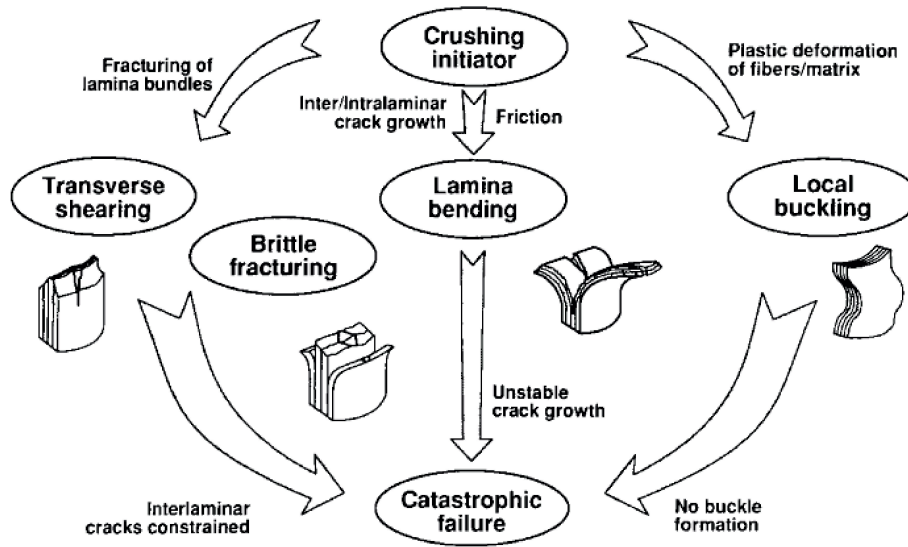
Figure 2.6: Schematic representation of crushing modes and failure mechanisms in composite materials, from [78] (with permission from SAGE Publications)

age of composite materials crush in brittle fracturing. However, brittle fracturing was identified as a unique mode since it is a combination of transverse shearing and lamina bending [78]. The mechanisms resulting in the different failure modes are complex. To avoid catastrophic failure and promote crushing, composite tubes require an intended weakness which triggers the failure process. At the initiation of crushing, local failure of the material occurs in the trigger region. Subsequently, inter- and intralaminar cracks propagate. The length of those cracks as well as the appearance of lamina bundle fracturing is decisive whether the tube fails in transverse shearing, lamina bending or a combination of both, brittle fracturing [78]. In ductile composites and particular brittle composite materials, plastic deformation of the fibres and matrix takes place in the trigger region and the specimen fails in a local buckling mode. The failure modes and the mechanisms that cause them are represented schematically in Figure 2.6. The properties of fibre and matrix, the combination of those two constituents, the layup and the geometry of the composite tube determine whether a composite tube fails in progressive crushing. If the length of interlaminar cracks is less than the laminate thickness of the brittle composite material without appreciable lamina bending, the tube tends to collapse in catastrophic failure [79]. A significant amount of energy can be absorbed in catastrophic failure, however composite materials that tend to fail in a progressive failure mode are preferable for energy absorbing structures since this failure mode retains the structural integrity of the component. The mechanisms that control the failure modes are presented in Figure 2.6.

The failure characteristic of the **transverse shearing** mode is a wedge shaped cross-section and the development of short interlaminar and longitudinal cracks which lead to the formation of lamina bundles. The length of these cracks is normally less than the laminate thickness [79]. Interlaminar cracks initiate through two modes. In mode I there is an opening of the laminates, in mode II the laminates shear-off against each other in the longitudinal direction. In this failure mode, the lamina

bundles resist the impact load and energy is absorbed mainly by fracturing of the lamina bundles [78]. Interlaminar crack growth is influenced by the properties of the matrix, the laminate lay-up as well as the shear strength and the failure strain of the fibres in the hoop direction. The stiffness and strength of the the hoop fibres influence the bending stiffness of the lamina bundles [78]. The impact velocity also affects the energy absorption due to the strain-rate dependent properties of fibre and matrix.

In **lamina bending**, the failure is characterized by the formation of long inter- and intralaminar as well as parallel-to fibre cracks in one or multiple plies with the same fibre orientation. The two failure mechanisms affecting this failure mode are the growth of the inter-, intralaminar and longitudinal cracks and friction. Crack growth is comparable with the transvese shearing mode however, the crack length is one magnitude higher in lamina bending. Energy in the lamina bending failure mode is mainly absorbed by growing of the cracks. The characteristic difference to transverse shearing is an extensive bending without fracturing of the lamina bundles. Due to bending, the lamina bundles slide along the surface of the impact plate as well as adjacent bundles slide against each other. This results in friction as a secondary energy-absorption mechanism [78]. Due to the strain-rate dependent friction coefficient of composite materials, this failure mode is dependent on the loading velocity.

The combination of transverse shearing and lamina bending results in the **brittle fracturing** crushing mode. The majority of composite materials with brittle fibres fail in brittle fracturing [79]. The combination of transverse shearing and lamina bending in the brittle fracturing crushing mode becomes obvious in the crack length which is in the range of one up to ten laminate thicknesses [78]. Further similarities to the transverse shearing and brittle fracturing modes are interlaminar and longitudinal cracks, bending and fracturing of lamina bundles as well as energy absorption mainly through fracturing of the lamina bundles. Progressive crushing develops when the lamina bundles fracture and the force is redistributed within the laminate which results in a recurrence of the failure process.

Failure through **local buckling** consists of the formation of local buckles and occurs in both brittle and ductile fibre composite materials and is comparable to buckling of ductile metals [78]. In ductile composites, plastic deformations occur on the compression side of the buckle. On the tension side, fibre fractures and local delaminations can appear. Due to the plastic deformations of the composite material, the integrity of the specimen is retained, contrary to aforementioned crushing modes. Brittle fibre composite materials only fail in local buckling if the interlaminar stresses are small compared to the matrix strength, the failure stress of the matrix is higher compared to the fibre and the matrix plastically deforms at high stresses [77]. Therefore, brittle composite materials only fail in a local buckling crushing mode if the matrix yields. Strain-rate dependent material properties of matrix and fibre influence the energy absorbing potential of the specimen under high loading rates.

2.2.2 Crush Efficiency and Energy Absorption Performance Parameters

To measure the crushing and energy absorption efficiency of the crushing modes described in the previous section, a variety of performance parameter were defined. A typical crush force-displacement characteristic as shown in Figure 2.4 is used to measure how effective energy is absorbed in a crushing process. The stroke efficiency is the ratio of the stroke length to the initial length of the energy absorber [80, 81]:

$$SE = \frac{S_b}{L} \tag{2.1}$$

S_b is the total crush displacement at the end of progressive folding or progressive crushing in advance to compaction of folds or debris (see Figure 2.4). L is the undamaged length of the crush tube. The closer SE is to 1.0 the higher the efficiency of the crushing process [80, 81]. However, stroke efficiency has to be differentiated for the crushing modes described in the previous section. In transverse shearing, the debris size of the fractured lamina bundles is in between powdery up to the thickness of the lamina. In lamina bending, the debris can reach the length of the tube but both crush modes achieve a stroke efficiency of nearly 1.0 [78]. However, the crushing process is more efficient if more material is crushed. Therefore, a measure using the characteristic length of the debris is more suitable. The smaller the characteristic length the higher the crush efficiency. According to this, transverse shearing has the highest crush efficiency whereas lamina bending has the lowest crush efficiency due to the high characteristic length of the lamina bundles [78].

Bolukbasi [68] introduced the specific sustained crushing stress:

$$SSCS = \frac{\sigma_{sc}}{\rho} \tag{2.2}$$

where ρ is the density of the material and σ_{sc} is the sustained crushing stress defined as:

$$\sigma_{sc} = \frac{\overline{P}}{A} \tag{2.3}$$

$\overline{P}$ is the mean crush force as shown in Figure 2.4. A is the cross-section of the tube. By this definition, the energy absorption potential is solely dependent on the mechanical properties of the material contrary to the stroke efficiency which is primarily dependent on the structure of the specimen and secondarily dependent on the mechanical properties of the material. However, the geometry of the energy absorber also influences the crushing process and energy absorption which is not considered in the aforementioned equation.

Kindervater and Georgi [37] defined additional parameters to measure the crush efficiency of composite materials. The crush force efficiency is the ratio of the mean crush force F_{mean} to the

maximum crush force F_{peak} in the initiation phase of the crushing process.

$$AE = \frac{F_{mean}}{F_{peak}} \tag{2.4}$$

A theoretical crush force efficiency of 1.0 is achieved by ideally-plastic materials with a rectangular-shaped force-displacement curve. AE is also a measurement of the efficiency of the trigger mechanism since the purpose of the trigger is to initiate the failure processes and reduce the peak load.

In the definition of the specific energy E_s, the energy absorbed in the crushing process E_{abs} as the area under the crush force-displacement curve, is related to the mass of the crush absorber. As it takes into account the mass of the whole structure that is required for the energy absorber, e.g. clamping devices, this measure is a criterion especially of interest for lightweight design.

Taking into account the crushed mass of the absorber defines the specific energy absorption:

$$SEA = \frac{E_{abs}}{m_{crushed}} \tag{2.5}$$

The crushed mass $m_{crushed}$ is calculated by multiplying the total crush distance, the cross sectional area and density of the material. Therefore, SEA provides a method to compare the energy absorbing capability of different material systems.

2.3 Modelling of Damage and Failure in Composites

The Classical Laminate Theory (CLT) analytically describes the linear behaviour of composite materials and structures. By considering the elastic mechanical properties Young's moduli, shear modulus and Poission's ratios, CLT effectively calculates the linear stress-strain relationship of the composite laminate up to failure initiation. Even if considered as brittle, most composite materials withstand loads above their initial strengths. The complex failure mechanisms governing the crushing process in composite structures, as described in the previous section, lead to non-linear material behaviour. Finite Element Analysis (FEA) of composite materials and the simulation of highly non-linear crushing processes is an important research field in aerospace engineering. The formulation of realistic damage and failure models as well as modelling the energy absorption mechanism are the focus of this research field. Challenging is the modelling of the material behaviour which occurs on multiple scales with complex interaction as well as the formulation of material models suitable to model larger structural scales with satisfactory accuracy. Therefore, various computational methods to model the structural behaviour of composite materials have been developed over the past years. An overview of commonly used computational methods for the structural analysis of composites is given in [82, 83].

2.3.1 Modelling Methods for Fibre Reinforced Materials

Modelling the complex material behaviour of composite materials is considered at three different scales of spatial resolution, namely micro-, meso- and macro-scale.

Micro-scale Models

Aim of micro-scale models is capturing the interaction of the fibres and matrix with its basic constituents fibre, matrix and fibre-matrix interface. The scale of a few hundred microns is modelled with Unit Cells (UC) or Representative Volume Elements (RVE) where each finite element consists of homogeneous material properties of either fibre, matrix or fibre-matrix interface [84–86]. In UC, the model consists of a centre single fibre surrounded by the matrix [84, 85] and the composite material is modelled by periodic repetition of the UC. In a RVE, the morphology and distribution of the fibre in the ply is considered and the model consists of multiple fibres embedded in the matrix [86]. Micro-scale models were used to successfully predict the elastic properties of the composite material as well as the initiation of damage under various loading combinations. However, micro-scale models are unable to predict damage evolution [82] since the inherently non-local characteristic of damage evolution in composite materials depends on the interaction of material and structural behaviour which cannot be scaled [83].

Meso-scale Models

In meso-scale models, the behaviour of the composite material is numerically modelled at the ply-level. The individual plies of the laminate are represented by several layers of elements with homogeneous material properties of fibre and matrix. The plies of the laminate are modelled either as perfectly bonded or with cohesive interfaces if interlaminar damage is to be considered. Meso-scale modelling has been widely applied to numerically study different load cases including crushing [62, 87–91]. In meso-scale FE-models, the damage behaviour within each ply is assumed to be independent of the surrounding plies and the interaction of damage mechanism is therefore neglected. However, it is accepted that the orientation of the neighbouring layers influences the damage response of the lamina [82, 83]. The material input for the individual plies are determined by characterization tests of unidirectional laminates which often exhibit catastrophic failure. However, this failure mode cannot be transferred to a ply within a multi-directional laminate where neighbouring plies provide structural stability to the damaged ply and provide load redistribution within the laminate. One way to overcome this drawback is the experimental measurement and usage of in-situ strength properties [92]. Due to the detailed modelling of the plies and interfaces, meso-scale FE models are computational costly and therefore are inefficient in modelling large-scale structures.

Macro-scale Models

In macro-scale models, the composite laminate is modelled as a homogeneous material. The overall behaviour is modelled by macro-scale parameters of the laminate and details like damage characteristics and failure interaction in the individual plies are neglected. The focus of macro-scale modelling is the efficient computation of large-scale structures with sufficient accuracy. A drawback of this modelling approach is the necessity to determine the macro-scale parameters individually for each considered laminate since damage depends on the stacking-sequence and thickness of the constituent plies. Macro-scale modelling was used for simulation of composite material including crush simulation in [93–98].

Multi-scale Modelling

Multi-scale modelling is the attempt to combine the benefits of the aforementioned modelling approaches to capture the multi-scale nature of damage in composite structures. In hierarchical multi-scale models, homogenization is used to transfer the constitutive behaviour like the stress-strain response determined at the micro-scale level to a macro-scale model [99, 100]. This enables to reliably predict the elastic macroscopic response of composite materials with complex fibre architectures. However, damage and failure cannot be captured due to the homogenization [83]. In congruent multi-scale models, multiple scales are present simultaneously in the FE-model. The undamaged part of the composite structure is represented by a macro-scale model whereas the resolution of the model is increased in damaged regions to explicitly account for micro-macro features [83]. Disadvantages of congruent multi-scale models are extensive computational costs which makes them impractical in applications.

2.3.2 Intralaminar Damage and Failure Modelling in Composite Materials

Damage and failure in composites takes place at different scales with various interactions of the damage modes as outlined in the previous sections. To numerically model the complex failure mechanisms in composite structures, various modelling approaches and material models were developed over the past years. One distinct modelling approach for damage and failure in composites is the Continuum Damage Mechanics (CDM) approach [101, 102]. Intralaminar damage in multi-directional composites often widely spreads in a diffused pattern, called the Fracture Process Zone (FPZ). In this damage region, the mechanical properties of the damaged material are replaced by homogeneous material properties associated with damage mechanisms and their softening effects on the mechanical material properties. In detail, the loss of stiffness due to damage is described by internal state variables which are governed by damage evolution laws. In composite materials, the in-plane dimensions of plies or laminates are normally a magnitude higher compared to the thickness. Therefore, the stresses in thickness direction are negligible which led to the plane-stress

formulation where the stress vector in the direction perpendicular to the plane is assumed to be zero. In a plane-stress formulation suitable for shell elements, strains are described as:

$$\vec{\varepsilon} = \vec{S}\vec{\sigma} \tag{2.6}$$

where $\vec{\varepsilon}$ represents the strain vector, $\vec{\sigma}$ the stress vector and $\vec{S}$ the compliance matrix. In CDM, strain-softening is applied by introducing scalar damage parameter to the compliance matrix:

$$\vec{S} = \begin{bmatrix} \frac{1}{E_1^0(1-d_1)} & -\frac{\nu_{12}}{E_1^0} & 0 \\ -\frac{\nu_{12}}{E_1^0} & \frac{1}{E_2^0(1-d_2)} & 0 \\ 0 & 0 & \frac{1}{G_{12}^0(1-d_{12})} \end{bmatrix} \tag{2.7}$$

here, d_1, d_2 and d_{12} are the internal damage variables representing damage in fibre, transverse and in-plane shear direction, respectively. In UD-plies which are solely used in this work, the damage variables model the degradation of the elastic Young's moduli of fibre and matrix E_1^0, E_2^0 as well as the elastic in-plane shear modulus G_{12}^0. The values of d_i are in the range $0 \leqslant d_i \leqslant 1$ where $d_i = 0$ represents the undamaged material and $d_i = 1$ fully saturated damage. In CDM it is important to accurately describe damage initiation and damage evolution to formulate the stiffness reduction.

Various composite material models use failure criteria where the onset of failure is related to internal stresses and experimentally measured material strength [103]. Different approaches are used in the various failure criteria. In independent failure criteria such as the maximum stress or maximum strain criterion, the individual stresses or strains of each failure mode are related to the corresponding strength. In interactive criteria, for example Tsai-Wu [104], interaction of the different failure modes is considered to capture the complex failure in composites. In phenomenological interactive criteria like Hashin [105], Chang-Chang [106] and Puck and Schuermann [107], failure is distinguished between fibre and matrix failure under tension and compression [83]. The described failure criteria are suitable to predict the onset of damage in composite materials. However, the reduction of stiffness and dissipation of energy during the failure process cannot be captured. Also, the failure of an elementary ply does not necessarily result in global failure of the laminate. The load is normally redistributed in the undamaged remaining material [83].

To describe the internal damage variables governing the stiffness reduction of the ply or laminate in the damage process (see Equation (2.7)), progressive damage models are required. Those models describe the material behaviour after a failure criterion is satisfied and damage initiates. The reduction of stiffness can occur instantaneous to a fraction of the initial undamaged stiffness or in a gradual manner where the evolution of the damage variables is governed by a field variable such as the fracture energy of the material. Implementations of this approach can be found in [102]. Many material models using different approaches of damage evolution are available in commercial FE-codes. A detailed representation of different approaches for damage initiation and damage evolution for various FE-codes is given in [83]. In the following sections, the relevant theories for

this work are described in detail.

Ladevèze and LeDantec [108] developed a meso-scale, plane-stress damage model in the framework of CDM that predicts the internal stiffness degradation and rupture of UD composite plies. Damage variables and damage evolution laws capture the stiffness reduction due to brittle fibre fracture, fibre/matrix debonding and matrix micro-cracking. The elementary ply is assumed to be homogeneous and orthotropic with a plane-stress damage evolution law suitable for shell elements. The damaged elastic stress-strain relation is written as [108]:

$$\vec{\varepsilon^{el}} = \vec{S}\vec{\sigma} \Leftrightarrow \begin{cases} \varepsilon_{11}^{el} &= \frac{\sigma_{11}}{E_1^0(1+\gamma\langle\sigma_{11}\rangle_-(1-d_1))} - \frac{\nu_{21}\sigma_{22}}{E_2^0} \\ \varepsilon_{22}^{el} &= \frac{\langle\sigma_{22}\rangle_+}{E_2^0(1-d_2)} + \frac{\langle\sigma_{22}\rangle_-}{E_2^0} - \frac{\nu_{12}\sigma_{11}}{E_1^0} \\ \varepsilon_{12}^{el} &= \frac{\sigma_{12}}{2G_{12}^0(1-d_{12})} \end{cases} \tag{2.8}$$

$$\text{with} \begin{cases} \langle\sigma_{ij}\rangle_+ &= \sigma_{ij} \text{ if } \sigma_{ij} \geqslant 0; \text{ else } \langle\sigma_{ij}\rangle_+ = 0 \\ \langle\sigma_{ij}\rangle_- &= \sigma_{ij} \text{ if } \sigma_{ij} < 0; \text{ else } \langle\sigma_{ij}\rangle_- = 0 \end{cases}$$

$\vec{\varepsilon^{el}}$ and $\vec{\sigma}$ are the vectors containing the elastic strains and stresses, respectively and $\vec{S}$ is the stiffness matrix. The damage variables d_i are in the range $0 \leqslant d_i \leqslant 1$ and γ controls the stiffness loss of the fibres under compressive loading. The subscripts '11' and '1', '22' and '2' and '12' represent the directions of fibre, transverse (matrix) and in-plane shear, respectively. Brittle fibre failure is governed by failure limit strains for both tensile and compressive loading at which d_1 becomes one. Transverse and in-plane shear damage evolution is governed by energy release rate functions which are the partial derivatives of the damaged elastic strain energy with respect to d_2 and d_{12} [108]:

$$E_D = \frac{1}{2}\left[\frac{\sigma_{11}^2}{E_1^0} - \frac{2\nu_{12}^0}{E_1^0}\sigma_{11}\sigma_{22} + \frac{\langle\sigma_{22}\rangle_+^2}{E_2^0(1-d_2)} + \frac{\langle\sigma_{22}\rangle_-^2}{E_2^0} + \frac{\sigma_{12}^2}{2G_{12}(1-d_{12})}\right] \tag{2.9}$$

$$Y_2 = \frac{\partial E_D}{\partial d_2} = \frac{\langle\sigma_{22}\rangle_+^2}{2E_2^0(1-d_2)^2} \tag{2.10}$$

$$Y_{12} = \frac{\partial E_D}{\partial d_{12}} = \frac{\sigma_{12}^2}{2G_{12}^0(1-d_{12})^2} \tag{2.11}$$

The evolution of matrix microcracking and fibre/matrix debonding over the time t was described by Ladevèze and LeDantec based on experimental findings as:

$$\underline{Y} = \sup_{\tau \leqslant t}\left(\sqrt{Y_{12}(\tau) + bY_2(\tau)}\right) \tag{2.12}$$

$$\underline{Y_2} = \sup_{\tau \leqslant t}\left(\sqrt{Y_2(\tau)}\right) \tag{2.13}$$

The evolution of the damage parameters is then derived from:

$$d_2 = \frac{\langle \underline{Y} - Y_{20} \rangle_+}{Y_{2c}} \quad \text{if } d_2 < 1 \text{ and } \underline{Y_2} < Y_{2s}; \text{ else } d_2 = 1 \tag{2.14}$$

$$d_{12} = \frac{\langle \underline{Y} - Y_{120} \rangle_+}{Y_{12c}} \quad \text{if } d_{12} < 1 \text{ and } \underline{Y_2} < Y_{2s}; \text{ else } d_{12} = 1 \tag{2.15}$$

Damage in the elementary ply is assumed to be irreversible by means that the damage variables cannot reduce over time t. Brittle failure of the fibre/matrix interface is controlled by the failure threshold Y_{2s}. Evolution of progressive damage is controlled by the parameters Y_{20}, Y_{2c}, Y_{120} and Y_{12c}. Coupling of transverse and shear damage is achieved by the coupling parameter b. A plasticity law to model permanent plastic strains due to internal friction was introduced by Ladevèze and LeDantec with an elastic domain function f and a hardening law $R(p)$ [108]:

$$f = \sqrt{\tilde{\sigma}_{12}^2 + \alpha^2 \tilde{\sigma}_{22}^2} - R(p) - R_0, \quad \text{with} \quad R(p) = \beta p^\mu \tag{2.16}$$

where p is the effective plastic strain, R_0 the yield stress and α the shear-transverse plasticity coupling parameter. $\tilde{\sigma}$ is the tensor of the effective stresses:

$$\tilde{\sigma} = \left[\sigma_{11}, \frac{\langle \sigma_{22} \rangle_+}{(1 - d_2)} + \langle \sigma_{22} \rangle_-, \frac{\sqrt{2}\sigma_{12}}{(1 - d_{12})} \right]^T \tag{2.17}$$

The meso-scale model by Ladevèze and LeDantec [108] was implemented into commercial FE code for woven fabric laminates by Johnson et al. [109] to model and simulate the low velocity impact response of fabric composite structures. David [62] used the fabric ply damage model in the commercial FE-code PAM-CRASH$^{\text{TM}}$ for modelling and simulating of the crushing behaviour of the self-supported DLR segment. Schueler [90] and Schueler et al. [91] implemented the approach by Ladevèze and LeDantec [108] as a user-material model (VUMAT) in the commercial FE-code Abaqus/Explicit$^{\text{TM}}$ to predict the impact behaviour of preloaded composite plates.

To predict low velocity impact, Iannucci et al. [110–112] proposed a progressive damage model in the framework of CDM combined with a fracture mechanics approach to model the damage progression for plane-stress shell elements. The model was implemented for woven composites [110, 111] as well as UD laminates [112]. Damage was accounted for due to normal stresses in fibre and transverse direction and in-plane shear stresses. The internal damage variables were used to reduce the elastic moduli and the Poisson's ratios. The model was extended to differentiate between tensile and compressive damage [111, 112]. Linear elastic behaviour up to damage initiation was assumed for direct stresses and non-linear behaviour for shear loading. After damage initiation, a linear strain-softening approach gradually reduce the stiffness. The evolution of the damage variables in

this bi-linear stress-strain relationship follows the relation:

$$d_i = \frac{\varepsilon_{max,i}}{\varepsilon_{max,i} - \varepsilon_{0,i}} \left[1 - \frac{\varepsilon_{0,i}}{\varepsilon_i} \right] \tag{2.18}$$

The energy dissipating during the damaging process as the area under the stress-strain curve is expressed by the stress at damage initiation σ_0 (the stress at ε_0) and the maximum strain at failure ε_{max} such as:

$$E_f = \frac{1}{2}\sigma_0\varepsilon_{max} \tag{2.19}$$

A crack band model proposed by Bazant and Oh [113, 114] was implemented in the model to prevent mesh dependent solutions during strain-softening due to strain localization problems. In this approach, the strain-softening is related to fracture energies to assure an energy dissipation which corresponds to the energy required for increasing the fracture area. This links continuum damage mechanics to fracture mechanics and relates the specific dissipated energy E_f which is the sum of the elastic energy E_e and the propagation energy E_p, to the material specific intralaminar fracture energy G_f [111]:

$$E_f = E_e + E_p = \frac{G_f}{l_x} \quad \text{with} \quad E_e = \frac{1}{2}\sigma_0\varepsilon_0 \quad \text{and} \quad E_p = \frac{1}{2}\sigma_0(\varepsilon_{max} - \varepsilon_0) \tag{2.20}$$

the characteristic length l_x is related to the size of the finite element and links the volumetric energy E_f to the energy per area G_f. The introduction of l_x assures that the same amount of energy is dissipated in finite elements with different element sizes. Combining Equation (2.19) with Equation (2.20), the failure strain is related to the fracture energy which could be determined from experimental tests:

$$\varepsilon_{max} = \frac{2G_f}{\sigma_0 l_x} \tag{2.21}$$

The approach developed by Iannucci et al. [110–112] was used in a similar way in a model proposed by Maimí et al. [115, 116] for plane-stress shell elements. The LaRC04 failure criterion [117] is based on physical models for each failure mode and taking into account non-linear matrix shear behaviour. Damage evolution in terms of stiffness degradation also uses the crack band model by Bazant and Oh [113, 114] relating the strain energy to the fracture energy. However, the strain-softening behaviour differs to the bi-linear approach proposed by Iannucci et al. The approach by Miami et al. models the strain-softening behaviour with a convex non-linear function.

2.3.3 Interlaminar Damage in Composite Materials

The resin rich interface between plies and interlaminar damage is modelled using different approaches in meso-scale modelling. The connection between individual element layers that represent plies or sub-laminates can be modelled with specific tie-connections with failure behaviour. Such 'tiebreak' connections use fracture mechanics to model the separation of the plies due to inter-

a) Mode I - Opening   b) Mode II - In-plane shear   c) Mode III - Out-of-plane shear
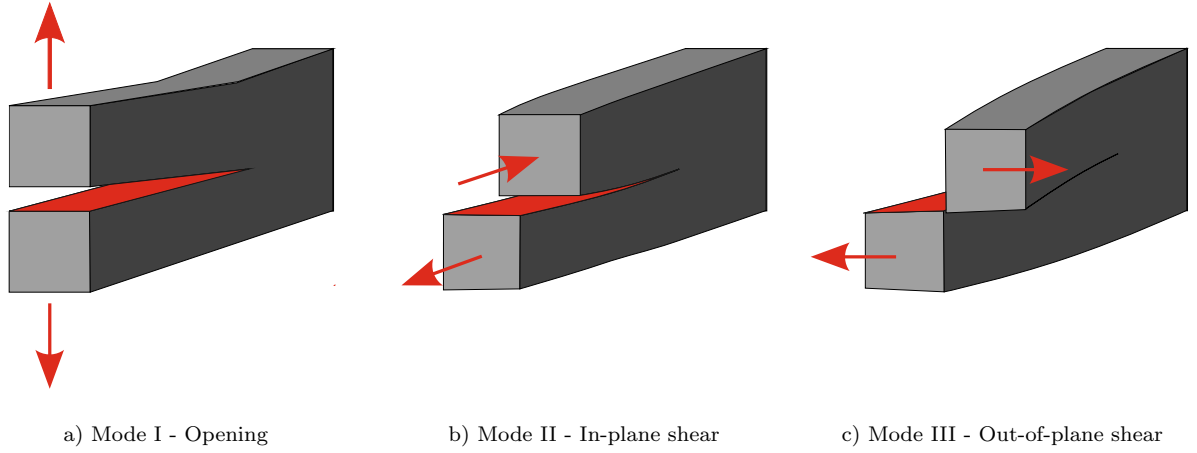
Figure 2.7: Delamination fracture modes; a) Mode I - opening; b) Mode II - In-plane shear (or sliding shear); c) Mode III - Out-of-plane shear (or tearing shear)

laminar damage. Johnson et al. [109] and David [62] followed a slightly different approach originally proposed by Allix and Ladevèze [118] and implemented cohesive contact definitions in their stacked-shell models. The interface is modelled as a solid sheet of zero thickness and introduce traction forces between the nodes of the plies in the stacked-shell model. Other approaches use two-dimensional cohesive surfaces or three-dimensional cohesive interface elements. Delamination damage can be modelled by fracture mechanics formulations describing the characteristic crack front. In the cohesive zone, which is assumed to be a fracture process zone ahead of the crack tip, traction of the cohesive elements is related to the separation and resist further crack propagation until a specific amount of fracture energy is dissipated [119]. This cohesive zone model approach (CZM) goes back to the 1960s [120, 121] and combines continuum damage and fracture mechanics and enables the description of delamination directly by relating the traction to separation and the use of material properties. For a detailed overview of CZM, the reader is referred to [122, 123]. The traction-separation approach is dependent on three different fracture modes that differ in the loading orientation relative to the crack front as shown in Figure 2.7.

Mode I represents opening under tensile loading while mode II and mode III represent in-plane and out-of-plane shearing also called as sliding and tearing shear, respectively. Initially, the traction-separation approach as implemented in the cohesive element formulation shows a linear-elastic behaviour where the slope is represented by the stiffness of the undamaged material in the corresponding loading direction as shown in Figure 2.8 a). After exceeding the strength criterion, damage initiates in the cohesive elements and stiffness is gradually reduced to zero. The work necessary to form the fracture surfaces in the individual fracture modes is represented by the corresponding fracture toughness of each mode G_{Ic}, G_{IIc} and G_{IIIc}. The most common way to model the traction-separation behaviour is by assuming a bi-linear softening law and the enclosed area corresponds to the interlaminar fracture energies. The combination of mode I and mode II mixed-

a) Bi-linear traction-separation behaviour   b) Cohesive mixed-mode behaviour
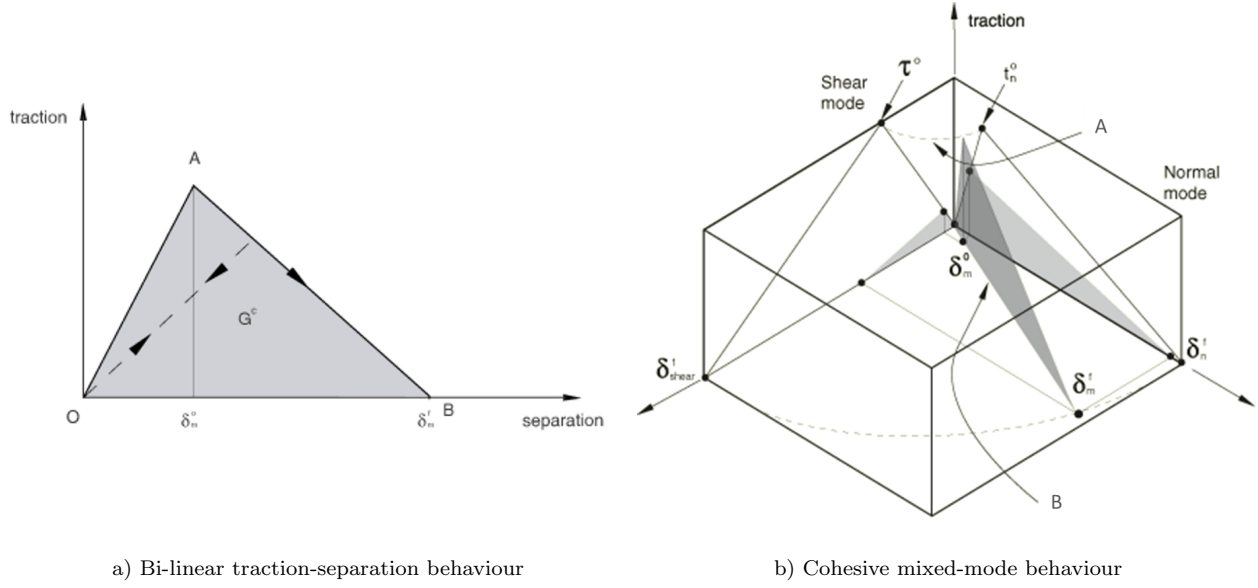
Figure 2.8: Cohesive behaviour; a) Bi-linear traction separation; b) Cohesive mixed mode behaviour; from [130]

mode loading is shown in Figure 2.8 b). Mixed-mode behaviour can be modelled by either coupling the tractions at damage initiation of mode I and mode II [124] or the fracture toughness of the modes [125]. Mode-mix by coupling damage initiation takes the form:

$$\left(\frac{\langle t_I \rangle}{t_I^0}\right)^2 + \left(\frac{t_{II}}{t_{II}^0}\right)^2 + \left(\frac{t_{III}}{t_{III}^0}\right)^2 = 1 \tag{2.22}$$

where t_{I-III} are the tractions at damage initiation in the corresponding loading directions and t_{I-III}^0 are the damage initiation tractions at pure mode I to mode III loading. Camanho et al. [125] presented a mixed-mode formulation where coupling of the fracture toughness of the modes is defined by:

$$\left(\frac{G_I}{G_{Ic}}\right)^\eta + \left(\frac{G_{II}}{G_{IIc}}\right)^\eta + \left(\frac{G_{III}}{G_{IIIc}}\right)^\eta = 1 \tag{2.23}$$

η is the mode-mix power law parameter. Benzeggagh and Kenane [126] proposed an alternative mode-mix failure criteria which assumes that the critical fracture energies for mode II and mode III are the same. The mixed mode behaviour is given by:

$$G_{Ic} + (G_{IIc} - G_{Ic})\left(\frac{G_S}{G_T}\right)^\eta = G_C \quad \text{with} \quad G_S = G_{II} + G_{III} \quad \text{and} \quad G_T = G_I + G_S \tag{2.24}$$

The required material parameter for this mixed-mode failure criteria are $G_{Ic}, G_{IIc} = G_{IIIc}$ and η. To model delamination using the CZM and correctly discretise the fracture process zone, the length of the cohesive zone has to be determined. Different formulations to define the length of the cohesive zone exist in literature [127–129]. Within the framework of CDM, general constitutive laws are formulated for the interfaces and propagation of delamination damage is modelled through

the degradation of the elastic properties following a stress-displacement model based on fracture energies. This approach drastically reduced the computational costs due to the significantly lower number of elements compared to a model with cohesive interface elements. Johnson et al. [109] reported good results for the prediction of impact damage as well as David [62] for the simulation of progressive axial crushing. However, Heimbs [131] compared cohesive contact and cohesive element approaches in the simulation of bird strike impact and found the cohesive contact to be much more computationally expensive.

2.3.4 Numerical Approaches

The numerical work described in the later chapters are performed in the commercial explicit FE-code Abaqus/Explicit. The numerical approaches described in the next sections therefore contain code-specific formulations. Especially, the element formulations are specific to Abaqus/Explicit. However, similar element formulations are also available in other commercial FE-codes.

Explicit Solving Algorithms

Finite element methods, implemented in commercial FE-codes are used to solve the equations of motion for each node in the model:

$$M\ddot{u} + C\dot{u} + Su = F(t) \tag{2.25}$$

where M denotes the matrix of masses, C the damping matrix, S the stiffness matrix and $F(t)$ the vector of the external nodal forces. To solve Equation (2.25) for the displacement u, two different algorithms exist in finite element codes, the implicit and the explicit method. In the implicit method, the displacement u, velocity $\dot{u}$ and acceleration $\ddot{u}$ are evaluated and the solution for the current step is based on the solution of the previous step $t - \delta t$. Geometrical and material non-linearities lead to changes in the stiffness matrix and in the implicit method, the stiffness matrix has to be inverted for each time increment which is numerically highly expensive especially for large models. Therefore, the implicit method is mainly used for linear and moderately non-linear models in which the solutions are unconditionally stable and permit larger time steps. In events with a dynamic equilibrium as well as highly non-linear problems, explicit methods solve the dynamic equation of motion for the acceleration $\ddot{u}$ at the time t to find the solution for the velocity $\dot{u}$ and displacement u at $t + \delta t$. The mass matrix is considered as a lumped diagonal matrix and therefore only the diagonal terms have to be inverted. Equation (2.25) can be rearranged as:

$$\ddot{u} = M^{-1} \left[F(t) - C\dot{u} - Su \right] \tag{2.26}$$

by replacing Su with the nodal elastic forces, no assembly of the stiffness matrix is necessary. The time step in an explicit finite element analysis has to be smaller than the time required for

a dilatational wave to pass through the stiffest element. Since the critical time step is in the range of microseconds to nanoseconds, the explicit method is efficient for simulation of crash or impact where the event time is a few milliseconds. The critical time step can be increased by adding artificial mass to the elements. With this mass-scaling, explicit methods can be used to simulate quasi-static events with high event times as long as the kinetic energy is less than 5% of the internal energy. The explicit time integration is solely used throughout this work due to the transient dynamic loading resulting in event times in the range of milliseconds as well as the highly non-linear behaviour in crushing.

Element Formulations in Abaqus/Explicit

Shell elements and continuum shell elements are using the plane-stress formulation and are implemented in the commercial FE-code Abaqus/Explicit. Continuum shell elements are an enhancement of conventional shell elements in order to remedy some of the disadvantages of the shell element formulation. The nodes of conventional shell elements have three translational and three rotational degrees of freedom. This results in problems while connecting shell elements to other elements with only translational degrees of freedom [132]. To account for this disadvantage Hauptmann and Schweizerhof [132] proposed continuum shell elements which combine the plane-stress formulation and kinematics of conventional shell elements with the thickness definition of solid elements. Therefore, continuum shell elements have at least six nodes with only three translational degrees of freedom. The comparison is shown in Figure 2.9. Using conventional shell elements, the geometry of the body to be modelled is defined by the reference surface and thickness is a section property. In continuum shell elements, a full 3D geometry is specified and thickness is defined by the definition of the nodes. This enables a contact definition by use of the continuum shell surfaces. In Abaqus/Explicit, contact for conventional shell elements, is formulated by definition of the contact height. In composite plies, the in-plane dimensions of shell elements are commonly much larger than the thickness resulting in a high length-to-thickness ratio. In Abaqus/Explicit this results in a reduced contact height and complicates the correct modelling of contacts. Continuum shell elements on the other hand are numerically more expensive since the stable time increment is dependent on the thickness of the continuum shell elements. Detailed modelling of composite plies with conventional shell elements results in small element thickness and stable time increments. Both types of shell elements show numerical stiffening called shear-locking. To overcome this, reduced integration is used where the number of integration points in the elements are reduced. However, the usage of reduced integration may result in hourglass modes. Quadrilateral shell elements and continuum shell elements with reduced integration in Abaqus/Explicit have the formulation S4R and SC8R, respectively.

Cohesive elements are used in Abaqus/Explicit to model adhesives between two components, bonded interfaces, gaskets as well as interfaces between two plies in composite laminates. The interface is discretized by cohesive elements through which connect the two adjacent ply layers. If
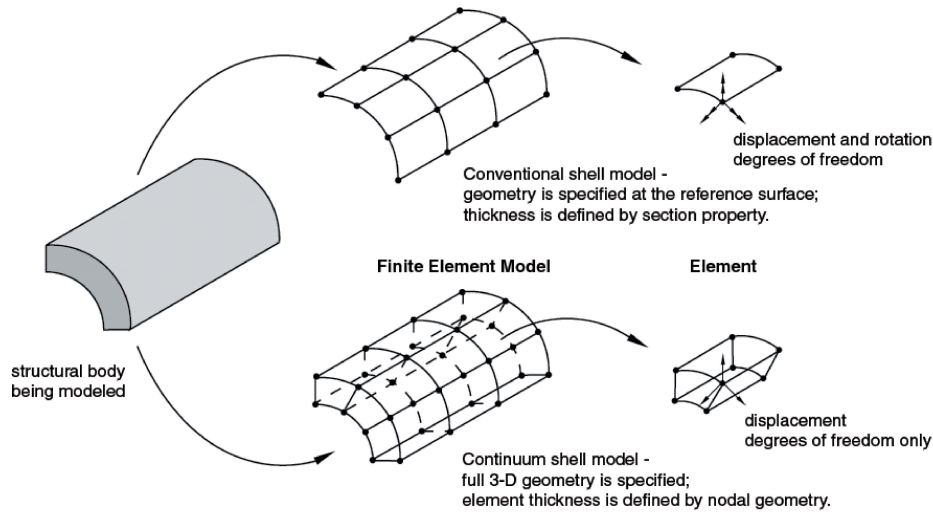
Figure 2.9: Comparison of conventional and continuum shell elements in Abaqus/Explicit, from [130]

cohesive elements are supposed to represent an adhesive material with finite thickness, the continuum material properties can be used directly to model the constitutive response of the adhesive zone. If the cohesive elements represent an infinitesimal thin layer in composites, the interface response can be defined directly by traction versus separation. At least one of the cohesive surfaces must be tied to another component and it is advised to constrain both the top and bottom surface. Since the membrane stiffness of cohesive elements is not defined, the cohesive elements exhibit one or more singular modes of deformation when only one surface of the cohesive element is constraint whereas the other surface is free. Cohesive elements may share nodes with the neighbouring elements which is easy to implement. However, depending on the element size of the neighbouring components, result in a coarse discretization of the cohesive zone. A cohesive mesh with smaller element size compared to the surrounding mesh can be realized by using tie connection to other components. Also, a contact definition has to be defined for the components connected by the cohesive elements. The element formulation in Abaqus/Explicit for three-dimensional cohesive elements with eight nodes is COH3D8.

Multi-layered Shell and Stacked-shell Modelling of Composite Materials

The multi-layered shell model is an efficient modelling approach where the composite laminate is discretized by a single layer of shell elements. Each ply of the composite laminate is represented by one or multiple integration points through the thickness of the shell elements. Both conventional shell and continuum shell elements can be used in the multi-layered shell model. The thickness of conventional shell elements is defined as the sum of the thickness properties of the individual layers in the multi-layered shell model. The thickness of continuum shell elements is specified by the nodal definition. The thickness of individual layers is defined similar to conventional shell elements. Based on the thickness and the fibre orientation of the individual layers, the material

properties of the laminate are calculated internally using the classical laminate theory. The multi-layered shell approach is efficient especially for large scale models and is most suitable for purely intralaminar modelling. Interlaminar damage cannot be modelled in detail with the multi-layered shell approach.

In the stacked-shell modelling approach, the composite laminate is discretized by multiple shell layers which are stacked together. Both conventional and continuum shell elements connected with tie-connections or by shared nodes in case of the continuum shell elements can be used in this modelling approach. In a stacked-shell model, multiple plies of the laminate can be represented within one shell layer in the same way as in the multi-layered shell approach. In a detailed stacked-shell modelling approach, each ply of a composite can be discretized by a single shell layer. However, this increases the number of elements and therefore the computational costs significantly. The advantage is the ability to capture transversal through-thickness tensions [133]. In combination with interface models such as cohesive zone models, tiebreak connections or other types of elements, the stacked-shell approach is capable of modelling interlaminar damage. As described in the previous section, cohesive elements can be implemented as connection elements between the individual shell layers. Modelling the cohesive interface with a finite thickness results in an increased total thickness of the stacked shell model and a change of the laminate properties which has to be considered. Modelling the cohesive elements with zero thickness resulted in numerical instabilities as shown in previous works [46, 134, 135]. To obtain the real thickness of the composite laminate, the geometrical shell element thickness has to be reduced accordingly. The influence of the cohesive element thickness on the moment of inertia dependent on the number of shell layers is shown in [134].

2.4 Numerical Simulation of Progressive Crushing

Numerical simulation of fibre composite materials under crush loading is subject of various research [62, 64, 79, 89, 94–97, 109, 134–146]. Especially, the numerical prediction of the complex material behaviour, crushing modes and failure mechanisms described in Section 2.2 pose challenges for the available FE-codes. Due to the efficient modelling approach and relatively small number of elements, multi-layered shell models were used mainly in previous research. The models were able to predict fragmentation dominated failure reasonably well, however, due to the lack to model delamination damage, multi-layered shell models were not capable to capture failure modes like splaying. As a reason of the steadily increasing computational performance, much more complex models could be simulated and stacked-shell models with a large amount of elements were used to model complex structures. In combination with cohesive interface models, the stacked-shell approach can model both the fragmentation and splaying mode which is mandatory to reliably predict the energy absorbing capabilities of composite structures. Therefore, the stacked-shell approach is the state of the art in simulating progressive crushing of composite materials. In the

following sections, the development of various numerical models is discussed in a detailed literature review on the research of numerical simulation of progressive crushing in chronological order. The focus is on material models, modelling approaches for the laminate, trigger mechanisms as well as meshing and element size effects.

Farley and Jones [79] numerically investigated the crushing of composite tubes to predict the energy absorption capability. The finite element code 'Engineering Analysis Language' was used and the laminate was modelled using the stacked-shell approach where each of the four composite plies was modelled by a single shell layer. The congruent element nodes were connected with spring elements. After reaching the critical energy release rate G, interlaminar damage initiates and the spring elements are deleted from the mesh. To reduce the number of elements in the model, only a quarter of the circular tube was modelled and symmetry boundary conditions were used. The energy absorption of the simulations was about 25% higher for kevlar-epoxy tubes but could capture the local buckling failure mode. In the simulation of graphite-epoxy tubes, the simulation differ for all three investigated ply orientations and where either 28% higher, 20% lower or only 22% of the experimentally determined value. Reasons for these discrepancies were found in an incorrect prediction of the failure modes and unrealistic low allowable compressive strains determined from compression tests which produce overly conservative results [79]. Suggested improvements were the use of constituent material properties and refining the FE-mesh.

In the European Community funded programme 'CRASURV - Design for Crash Survivability', high effort was raised to develop improved formulations for composite materials [136]. The verification was performed on different scale levels from coupon up to fuselage section level. Kohlgrueber and Kamoulakos [137] numerically investigated the crushing of the self-supported DLR segment as well as helicopter sub-floor structures. The multi-layered shell approach with conventional shell elements was used in the FE-code PAM-CRASH. A specially developed fabric material model with damage evolution based on equivalent strains was used in the simulations. Due to the inability of the model to capture all failure modes that contribute to the energy absorption, the average crushing stresses and specific absorbed energies were about 10% to 30% lower than in the experimental tests. A stacked-shell model of the half-tube segment with solid elements and tie connections using a maximum force failure criterion was able to model the separation of the composite plies. This led to improved agreement with the test results. However, the numerically determined crush force was lower than the reported experimental crush force.

Johnson et al. [109] used the stacked-shell approach in the simulation of low velocity impact on composite plates. In this approach, the interlaminar layers and the reduction of strength due to delamination was modelled. A fabric material model implemented in PAM-CRASH and based on the model by Ladevèze and LeDantec [108] was used. The model contains elastic damage along the principal fibre directions and elastic-plastic damaging under in-plane shear loading. Damage evolution was based on simple linear or log-linear forms and power-law functions for plastic hardening. Due to relatively large time increments which depends on the element size rather than the

inter-ply thickness, the stacked-shell model was found to be an efficient approach to model both delamination and intralaminar failure in composites. The composite laminate consisting of eight UD-plies was modelled on the meso-scale level by two layers of multi-layered shell elements where each shell layer contain four UD plies. The shell layers were connected through cohesive interface elements that enabled splitting of the laminate into sublaminates when failure of the interface occur [109]. The model gave encouraging results in predicting the failure modes but showed limitations in predicting the delamination damage in low velocity impact. The stacked-shell approach as well as the fabric material model in PAM-CRASH was also used by David [62] and David and Johnson [64] to simulate the crushing behaviour of woven fabric DLR segments. The layup of the DLR segment, containing nine plies of woven fabric and UD plies, was modelled with four multi-layered shell layers and three layers of interface elements in between. Key feature of the model was a numerical wedge as trigger for the splaying crush mode which modelled the behaviour of the debris wedge at the crush front. This effect was identified using high-resolution computer tomography scans in the experiments. By varying the contact height of the numerical debris trigger in accordance to the modes observed in CT-scans of the experimental tests, the different crush failure modes of quasi-static and dynamic tests could be modelled [62]. The dominant failure modes and main energy absorption mechanisms splaying and fragmentation as well as friction could be captured with good correlation.

Aktay [138], Aktay and Johnson [139] and Aktay et al. [140] modelled the damage phenomena under crush [138, 140] and impact loading [138, 139] using the meshless Smooth Particle Hydrodynamics (SPH) method. SPH was used in PAM-CRASH as an alternative that replaced the conventional finite elements by a set of particles. In the numerical models, the failure region, especially the debris in the propagating crush front, was modelled either using a direct coupling with a discrete particle formulation or a semi-adaptive coupling where the FE mesh was converted into discrete particles [138]. The applicability of SPH was demonstrated in crush simulations of aluminium [138, 140] and composite [138] energy absorbers. The multi-layered shell modelling approach was used to model the aluminium tube walls. The polystyrene foam filler was modelled with the discrete and coupled FE/discrete element method. The crush response, predicted SEA and deformation patterns of the numerical simulations showed good agreement with the experimental results [138, 140] which was contributed to the closed domain of the foam-filled tubes and the well-known standard material parameters [138]. The seven layers of the composite DLR segment were modelled using a combination of the multi-layered and stacked-shell approach where three, respectively four plies were modelled with single shell layers. The resin material of the composite material was modelled with discrete particles and an elastic-plastic material model [138]. Bonding and delamination was modelled with tied-contact algorithm [138]. The initiation of splaying due to the chamfer trigger in the quasi-static crush tests was introduced in the model by offsetting the upper element rows of the two shell layers [138]. Compared to the experimental crush test results, the simulations showed satisfactory agreement [138]. Differences were identified due to limitations in the material models in PAM-CRASH. Also, it was recommended to further study the effect of element size, number of

particles and element elimination strain [138]. Besides these limitations, the presented results indicated the potential of SPH methods to model the crushing behaviour of composite energy absorbers [138].

McGregor and co-workers [94–96, 147] and Xiao et al. [97] experimentally tested [147] and numerically simulated [94–97] the axial crushing of triaxially braided composite tubes. A physically-based macromechanical approach was used where the damage growth in the plies of a laminate or sublaminate was smeared over a representative volume element. The finite element code LS-DYNA was used with a composite damage model in the framework of CDM called CODAM proposed by Williams and Vaziri [93]. The material model was modified and enhanced by McGregor et al. [94] to capture the response under compressive loading. The mechanical response of matrix cracking, fibre breakage, delamination and fibre kinking are represented in the model. The material properties were determined for the representative volume element and damage development within the RVE was modelled by progressive degradation of the elastic moduli dependent on the strain-state. The stress vs. effective strain response is determined from damage versus effective strain and normalized modulus versus damage characteristics. The enclosed area corresponds to the specific energy absorbed in the framework of the crack-band approach [113, 114]. The braided tube was modelled with a multi-layered shell approach [94] and a stacked-shell approach in further work [95, 96]. Plugs on the impact plate were modelled as crushing triggers. In the multi-layered shell approach, the main failure mode in the plug-initiated simulation, was tearing in the corners of the squared tube. In the simulation of crushing without plug, the failure mode was longitudinal compressive damage along the perimeter. For both types of crush initiation, the force-displacement characteristic, peak force and SEA mean values were predicted reasonably well compared to the test results. The stacked-shell model [95] contains layers representing sublaminates connected through tie-break interfaces which model delamination based on a mixed-mode failure criterion. The main feature of this work was a debris wedged fixed on the impact plate to initiate and propagate the splaying mode of crushing [95]. Due to this rigid debris wedge, crushing was predicted with high qualitative conformity to the experimental tests. Also the comparison of experimental and predicted force-displacement characteristics showed good agreement.

Boria et al. [141] investigated the impact behaviour of composite frontal crash structures of a Formula SAE racing car both experimentally and numerically. Simulations of a tube and impact attenuator were performed using the commercial FE-code LS-DYNA using both 2D shell as well as 3D solid elements to capture the stresses in the thickness direction. A mesh size study was performed with element sizes of $1.0\,mm$, $2.5\,mm$ and $5.0\,mm$ in the shell model and $2.5\,mm$ and $5.0\,mm$ in the solid model. The progressive failure model MAT054 was used for the simulations. In order to reduce the calculation time in the solid model, the laminate of the crush tube was modelled with two layers. Since it was observed in the experiments that the same amount of plies bend inwards and outwards during progressive crushing, the effect was modelled by connecting the solid layers with cohesive elements. In the impact attenuator model, up to four solid layers were

modelled which resulted in high computation times [141]. The mesh size study of the three element sizes in the shell model and two mesh sizes in the solid model revealed no differences in the force-displacement curves. However, it should be noted that MAT054 in LS-DYNA does not consider fracture energies and therefore does not use the crack band scaling approach. The comparison of the shell and solid modelling approach revealed that it is more reasonable to adopt the shell modelling approach in structures where splaying is not evident in order to reduce computation times. On the other hand, when interlaminar damage is a significant failure mode, a solid approach with cohesive elements lead to a detailed reproduction of the physical phenomenon [141].

Waimer et al. [89], Siemann [134] and Feser [135] used the stacked-shell approach to model the complex layup of a CFRP absorber of the bend frame concept (as pictured in Figure 2.3) containing braided fabric, non-crimp fabric, UD-plies and ply drop-off. A stack of up to eight continuum shell layers representing the smeared intralaminar material behaviour and cohesive elements to model the interfaces were used in the detailed model. The built-in user-material for fabrics, 'ABQ_PLY_FABRIC' [130], was selected for intralaminar modelling due to comprehensive options to describe the failure mechanisms by energy-based damage evolution and plasticity. The model provides an orthotropic linear elastic material with formulations for damage initiation and damage propagation. Damage initiated after surpassing the defined maximum stress. The evolution of the internal fibre damage variables which control the exponential softening of the stiffness was based on fracture energies and ensured correct energy dissipation for different element sizes. The material behaviour in shear direction was similar to the model proposed by Johnson [109] and contained damage evolution and plasticity. Interlaminar damage modelled by the cohesive elements was based on the cohesive zone model with bi-linear traction-separation law. Challenges were identified in the definition of cohesive stiffness to avoid numerical instabilities. The modelling methodology presented an application-oriented procedure to calibrate the required material model input parameters from experimental coupon tests. Especially the intralaminar fracture energy parameters were identified to be important in modelling progressive crushing of composite materials. Drawbacks were missing material characterization tests on the coupon level for the specific composite materials in the absorber structure. Therefore, similar fabric materials with available test data had to be used for calibration of the material input. Further modelling aspects were discussed to avoid mesh dependency in the crushing simulation but also to model the cohesive zone appropriately. The validation of the simulations methods without adapting the simulation model or input parameters on the structural level was performed with a classical building block approach in order to show the applicability and robustness on different levels. A comprehensive test programme considering a wide range of design and loading parameters was used for validation. All relevant effects were sufficiently captured both qualitatively and quantitatively. A few detailed failure effects could not be captured and the steady state crush force was partly lower in the simulations compared to the tests.

Cherniaev et al. [142] investigated the progressive axial crushing of CFRP tubes using three CDM

constitutive models in LS-DYNA. The widely used composite material models MAT054, MAT058, MAT262 were compared and their predictive capabilities were shown with respect to progressive axial crushing. The numerical results were compared to experimental results of axial crush tests of tubes made from HEXCEL IM7/8552. Single shell layer (multi-layered shell) modelling has been used and the capabilities and limitations in modelling progressive crushing have been identified. It was concluded that interlaminar failure in general is an important mechanism in crushing. Therefore, stacked-shell models should be preferred over single shell layer models [142]. However, the main intent of the work was the comparison of the three intra-ply model's applicability for simulation of crushing. Since modelling of delamination significantly influence the simulation and disguise the effects of intralaminar material models, it was decided to select only laminates with intralaminar dominated failure. Therefore, the single shell layer modelling approach was selected. In the numerical model, structured meshes with an element size of $5\,mm$ were selected without further investigation of the mesh type or element size. In selecting the element size, it was referred to [141]. However, it should be noted that MAT262 uses fracture energy and crack band scaling. Material input for IM7/8552 was derived from [148]. However, due to the lack of experimental data, assumptions were taken for the fracture energies of IM7/8552 [142]. From the comparison of the three considered material models, it was concluded that all models required extensive calibration to achieve correlation with experimental data. Especially, non-physical parameters in the models were identified to have a severe influence on the simulation results. Moreover, it was recommended for future studies to develop a robust material model with a minimum of unknown parameters requiring calibration [142]. In terms of the modelling approach, it was concluded that the single shell layer approach is not applicable to scenarios when splaying is a dominant mode of crushing. It was reported that the approach can lead to significant underestimation of energy absorption and therefore a stacked-shell modelling approach should be used for more accurate predictions when the failure mode is unknown in advance.

Zhu et al. [143] and Ren et al. [144, 145] simulated the crushing behaviour of composite tube sections [143] and corrugated plates [144, 145], respectively. The multi-layered shell and stacked-shell modelling approach were compared in this work. Zhu et al. [143] used a user-material in Abaqus/Explicit to predict the crushing behaviour of woven-fabric composite tubes of different cross-sectional shapes. For the single-shell model the selected element size was $1.0\,mm$ and a structured mesh type was used. However, no element size study or mesh type study was performed. The results of the single-shell model showed distinctive force spikes in the force-displacement characteristic as well as force drops indicating catastrophic failure. From the results of single shell model simulations it was concluded that this modelling approach is not able to capture the failure mechanisms and energy absorption capacity of the experimental tests [143]. In the stacked-shell modelling approach, different number of shell layers were investigated. In the simulation with 3 and 5 shell layers, no delamination failure mode occurred [143]. The stacked-shell model with 9 layers however was able to predict the damage progression [143]. Ren et al. [144, 145] predicted the crushing behaviour of corrugated composite plates using different single- and stacked-shell models

[144]. Structured meshes with $0.1\,in$ x $0.1\,in$ element size were used. Results of the single-shell model showed distinctive force spikes ranging from nearly $0\,kN$ to $35\,kN$. No study of the element size or mesh type was performed. It was concluded that the single-shell model could simulate the impact load curve without the ability to simulate delamination damage [144]. Stacked-shell models with 12 layers were investigated were the interlaminar damage is represented by tiebreak contacts, spot weld beam element, cohesive elements or contact-based cohesive elements. Those models were able to simulate the delamination failure during crushing and better predicted the impact load compared to the single-shell model [144].

Dalli et al. [146] presented a numerical methodology to simulate the crushing behaviour of a composite side impact structure of a Formula One racing car. In a macro-scaled modelling approach, the Abaqus/Explicit in-built orthotropic composite damage model 'ABQ_PLY_FABRIC' [130] suitable for modelling 2D woven fabrics was coupled with the CZone add-on to capture the crushing behaviour. The CZone add-on is an energy absorbing contact formulation available for Abaqus/Explicit. The built-in material model was based on continuum damage mechanics that uses fibre fracture energies for damage evolution in the two main directions. Crack band scaling is implemented in this model to regularize the dissipated energy. The CZone add-on was used to model the behaviour of the element at the crush front. The structure was modelled using a single shell layer through the thickness without considering interlaminar damage. The study referred to mesh size insensitivity due to the implied crack band scaling approach. However, a mesh size study was not performed. Also no information on the mesh types were given. The numerical results showed good agreement with the experiments in the deceleration of the sled impactor. In the crush-force vs. displacement characteristics, the numerical results correlated well with the experimental results in the early stage crushing but over-estimated the experimental results as the crushing processed further [146]. Splaying and lamina bending was reported in the experiments which resulted in lower energy absorption. However, the overestimation of the numerical results was not contributed to the single shell modelling approach since it was unable to capture this failure mode.

2.5 Conclusion and Open Questions

The energy absorption capability of composite materials is of special interest for the design of crashworthy aircraft structures. The crushing behaviour of composite structures is a complex failure process with interacting failure modes which has been studied in numerous research work. The different failure modes identified in crushing have been studied in detail and their contribution to the energy absorption capability has been identified. The two main failure modes of crushing which influence the energy absorption capability are fragmentation and splaying. Multiple approaches to measure the crushing performance and energy absorption have been defined whereas the specific energy absorption was identified to be suitable to compare the crushing performance of different materials and structures.

Various numerical models have been proposed over the last years to predict the complex behaviour of composite materials. The level of discretization range from detailed consideration of the composites main constituents fibre and matrix to smeared approaches where the laminate was modelled in its entirety. Initiation of damage in the composite was either considered independently for fibre and matrix following different initiation criteria or in a complex interaction of different failure modes. Propagation of damage in most of the reported numerical approaches was in the framework of continuum damage mechanics where internal damage variables govern the reduction of the elastic material properties. However, the underlying theories for evolution of the damage variables differ and no clear conclusion on the influence of the shape of the softening behaviour was given in literature. Fracture mechanics was used in many numerical approaches with the fracture energies being the driving force of damage evolution. To avoid strain localizations and mesh dependencies, the fracture energy was scaled by the size of the element to assure a constant energy dissipation in the damaging process. However, crack band scaling has been developed to model fracture mechanics, where damage was confined into a narrow band. The validity of this approach on crushing was not investigated.

In finite element codes, a wide spectrum of element types and modelling approaches for composite materials is given. Due to the nature of composite plies with low ratios of thickness to in-plane dimension, two-dimensional elements with plane-stress formulation have been used which represented the intralaminar behaviour of the plies. Interface elements were implemented to model the interlaminar behaviour. The modelling methodologies which were used for the simulation of progressive crushing of composite structures have shown that it is crucial to accurately capture all failure modes which contribute to the crushing process in order to reliably capture the energy absorption. In post-test simulations, the driving mechanisms of crushing were numerically modelled in detail and the experimental results were accurately reproduced on the laboratory scale. However, due to the detailed modelling, those methodologies were inapplicable on the structural scale. A large effort in calibration of material parameters and non-physical parameters was necessary to match the experimental results. Also, the question of the predictability and robustness of those methodology arises when used on varying loading conditions. The stacked-shell modelling approach was identified as the modelling methodology to capture the main crushing modes accurately. However, often no building block approach was defined providing guidelines what level of detail is required on the individual levels. Influence of discretization options like mesh type and element size were insufficiently investigated in progressive crushing.

Based on the identified challenges presented in this section, the following research questions can be formulated:

- What levels of the building block are required to predict crushing of composite structures and which level requires experimental tests for calibration and validation of the methodology?

- How influence fibre softening options the damage process on different structural scales?

- How do discretization options influence the damage behaviour and how can mesh dependencies be avoided on different scales of the building block?

- What level of detail in the model is required throughout the building block? Which modelling approach is required to reliably predict the complex failure behaviour of progressive crushing?

By answering these research questions, the aim of this work is the development of a robust simulation framework to reliably predict the progressive damage and crushing of composite materials. The developed simulation framework will enable the evaluation and selection of simulation approaches suitable for the respective case. The simulation methodology shall provide guidelines and best practices for the selection of discretization methods and identification of appropriate input parameters which are calibrated on the lower levels using experimental results whereas non-physical parameters are minimized in the model.

2.6 Detailed Objectives and Thesis Structure

In order to answer the research questions presented in the previous section, the detailed objectives of this work imply:

Chapter 3 Summary of HEXCEL IM7/8552 Material Properties

For modelling of failure and damage of composite materials and the prediction of crushing behaviour, a consistent set of material input data on all levels of the building block is required. The material used in this work is HEXCEL IM7/8552. In this chapter, a summary of literature data of both intra- and interlaminar IM7/8552 material parameter is given. Missing material properties required for the numerical analysis are identified and material characterization tests to determine model-specific parameters were carried out. Complete material data sets for two version of IM7/8552 are defined. Also, parameters which have to be numerically calibrated are identified.

Chapter 4 Numerical Modelling of Composite Materials

In this chapter, the implementation of a user-defined material model which is used to predict the energy absorption of composite materials is described in detail. Implementation of a user-material model is required to answer the previously defined research questions. Access to the source code provides the ability to adapt model specific definitions such as softening laws. The composite damage model on meso-scale level in the framework of continuum damage mechanics contains assumptions for the damage behaviour of the fibre based on fibre fracture energies and different fibre softening options are implemented. The damage behaviour of the matrix is based on the theory proposed by Ladevèze and LeDantec [108]. A failure criterion for transverse compressive loading is implemented as well. The model is verified on single-element simulations. The influence

of the implemented softening options, fibre fracture energy and element size is shown in stress-strain curves and the evolution of damage parameters.

Chapter 5 Behaviour on Laminate Level

The first level of the building block contains multi-layered shell, single-element simulation of quasi-isotropic composite laminates. In this chapter, the influence of fibre fracture energies, fibre softening options and mesh discretization on the fundamental laminate behaviour under tensile and compressive loading is investigated. Also, the influence of boundary conditions is shown which becomes essential in meso-scale modelling.

Chapter 6 Numerical Analysis of Fracture Mechanic Tests

The prediction of progressive damage in fracture tests is described in this chapter. Progressive damage under tensile and compressive loading is investigated with 'Over-height Compact Tension Test' (OCT) and 'Compact Compression Tests' (CC), respectively. The influence of fibre fracture energies, different fibre softening options and mesh discretization on progressive damage is investigated. The fibre fracture energies for the simulation of progressive crushing are calibrated on this level of the building block with experimental data of OCT and CC tests available in literature. At this building block level, the material input data set is fixed and is used for prediction on the higher levels.

Chapter 7 Numerical Analysis of Progressive Crushing

In this chapter, the simulation methodology is developed for prediction of progressive axial crushing. The influence of discretization options using different mesh types and element sizes is investigated in detail based on simulations of the self-supported DLR segment. Identified mesh size dependencies are traced back to the crack band scaling approach. The influence of fibre softening options are shown on the DLR segment. Results of flat coupon crush tests were used for validation of the simulation methodology. It is shown that the multi-layered shell approach is not suitable to accurately predict the crushing modes whereas the stacked-shell modelling approach is capable to capture the main crushing modes and also predicts the influence of different layups on the crush response.

Chapter 8 Conclusion and Outlook

The final chapter presents a summary of the main conclusions and contributions from this dissertation and gives an outlook on future research based on the limitations encountered in this thesis.

The research presented in this thesis was performed in the context of the DLR@UBC research collaboration. In Chapter 4 to Chapter 8 solely the results of the author of this work are presented. For an overall representation of the results of the DLR@UBC research topic 'Composite Technologies - Simulation of Crash and HVI', the reader is referred to [17–22].

3 Summary of HEXCEL IM7/8552 Material Properties

The selected material system in the scope of this work is HEXCEL IM7/8552 by Hexcel Corporation. The material system is a UD prepreg of a HexTow IM7 continuous, high performance, 12k filament count tows fibre [14] in a HexPly 8552 epoxy matrix [15, 16]. The material was chosen due to its wide use and amount of available material data in literature. The purpose of this chapter is the definition of consistent material data sets for the numerical analysis on all levels of the building block. A literature survey for both intra- and interlaminar material parameters is given and missing material properties required for the material model are identified. Material characterization tests to determine the missing material properties are described in the appendix of this chapter (see Appendix A.1). Consistent material data sets for both material versions are presented at the end of this chapter.

3.1 Summary of Literature Data of HEXCEL IM7/8552

HEXCEL IM7/8552 has been used, among other material systems, in the third world-wide composite failure exercise (WWFE-III) [149]. The WWFE was introduced in the mid 1990s with the aim to close the gap between the academic and the design world of numerical modelling of composite materials. Objectives of WWFE-III were damage evolution under uniaxial, biaxial, bending, and loading/unloading load cases in combination with thermal effects as well as interacting failure modes. The key findings and recommendations for designers are outlined in [150]. For the third edition of the WWFE, parameters needed to calibrate damage and failure models for material IM7/8552 have been extensively characterised [148, 151].

In the scope of the CMH-17 CWG, the material system IM7/8552 is used in the current round-robin exercise. This ongoing simulation effort with support by experimental testing is following a building block approach consisting of coupon tests up to the sub-structural level with composite components of crash absorbing structures. The aim of this work is to support the development and use of composite structures through the definition of reliable guidelines and standards. Material data of the US-Version of IM7/8552 have been characterized by the National Center for Advanced Materials (NCAMP) for the simulation work of the current round-robin exercise and are outlined in [152].

For material system IM7/8552, the two versions are defined by different properties of the HexPly 8552 epoxy matrix and prepreg plies. In the EU-Version of the HexPly 8552 matrix [15], the areal density of the prepreg plies defined as the mass per unit area is given as $134\,\frac{g}{m^2}$ with a nominal thickness of $0.125\,mm$. For the US-Version, the areal density is given as $190\,\frac{g}{m^2}$ and a nominal ply thickness of $\sim 0.187\,mm$ [16]. The HexTow IM7 carbon fibre however is reported to be unique and is assumed to be identical in both versions of the material [14]. The EU-Version was used and characterised in the WWFE-III and was also used in various experimental test programmes [52, 53, 153–156]. No comparison of the two version was reported in literature and the effects of the different matrix versions is not clear. Therefore, two material data sets are defined in the next sections. Both material data sets are used in the scope of this work and are chosen depending on the material version of the corresponding experimental tests. This means, in the scope of the building block approach, the available experimental data on the level of fracture mechanics tests are on basis of the EU-Version of IM7/8552. The effects of the material versions are identified and presented on the individual levels of the building block. The US-Version of IM7/8552 is used on the level of progressive crushing since the validation tests have been performed on this version in the CMH-17 CWG. Details of the source of each material parameter are given in the next sections.

3.1.1 Intralaminar Material Properties

The elastic material properties of the EU-Version of IM7/8552 were documented by Kaddour et al. [148]. The material data were provided to the 12 participants of WWFE-III and contain all elastic constants, ultimate strains and strengths of a IM7/8552 unidirectional laminate. The elastic material and strength properties selected for the EU-Version of IM7/8552 are presented in Table 3.1.

Lee and Soutis [153] measured the notched compressive strength and size effects of composite laminates made of IM7/8552 (EU-Version). The compressive in-plane stiffness and strength properties obtained from standard strength tests performed by the material's manufacturer were reported in this work. The compressive strength properties in longitudinal compressive loading reported in [153] are chosen for the IM7/8552 EU-Version material data set in this work.

One approach within the 12 leading theories of damage and failure in composites used in WWFE-III, was an enhanced meso-scale model for laminates presented by Daghia and Ladevèze [151] based on the original theory by Ladevèze and LeDantec [108]. However, the material data provided in the WWFE-III could not be used for determining material model specific parameters and assumptions had to be made based on published data or results obtained from similar materials [151]. The material properties are presented in Table 3.1 (line 'Ladevèze Parameter'). Due to the lack of loading/unloading shear data, the initial damage threshold Y_0 was defined as zero which enables the identification of Y_{12c}, R_0 and the hardening law $R(p)$ [151]. However, setting $Y_0 = 0$ means that matrix damage initiates directly when the load is applied and no elastic behaviour is modelled

in the transverse stress-strain or shear stress-shear strain characteristic.

In the scope of the CMH-17 CWG, a fixed material data set for IM7/8552 (US-Version) is defined and provided to the participants. The elastic and strength properties are reported in [152]. Isotropic behaviour under tension and compression was reported with identical longitudinal Young's moduli and strength properties. Only material-model specific parameters should be characterized individually by the participants in the CMH-17 CWG. Therefore, material characterization tests were carried out at DLR Institute of Structures and Design to determine the material parameters required for the meso-scale model based on the theory by Ladevèze and LeDantec [108]. The material characterization procedure is outlined in Appendix A.1. The mechanical properties of the US-Version of IM7/8552 are reported in Table 3.1

A wide range of longitudinal fibre fracture energies for IM7/8552 for both tensile and compressive loading is reported in the literature. For tensile loading, the reported fracture energies range from 81.5 [157], 94.1 [158], 112.7 [159] up to 134.7 $\frac{kJ}{m^2}$ [158]. For compressive loading, the reported fibre fracture energies range from 25.9 [159, 160], 47.5 [161], 79.9 [162], 101.6 [163], 106.3 [157] up to 165.6 $\frac{kJ}{m^2}$ under dynamic loading [163]. Due to this wide range of reported fracture energies, it is decided to calibrate the fibre fracture energies for the numerical simulation by the use of experimental results on the same material system. Zobeiry [154] and Zobeiry et al. [155, 164] characterized the fracture energies of a quasi-isotropic laminate made of IM7/8552 (EU-Version) under tensile and compressive loading by the use of non-destructive testing with digital image correlation [154, 155] as well as the tensile fracture energy numerically by the use of machine learning algorithms [164]. Over-height compact tension (OCT) specimen proposed by Kongshavn & Poursartip [165] and compact compression (CC) specimen were experimentally tested. The fracture energies of the quasi-isotropic laminate were determined to be in the range of 95 $\frac{kJ}{m^2}$ [154, 155] to 136 $\frac{kJ}{m^2}$ [164] under tensile loading and 85 $\frac{kJ}{m^2}$ [154] under compressive loading.

3.1.2 Interlaminar Material Properties

Strain energy release rates used in numerical models to simulate the interlaminar behaviour of interface elements (e.g. cohesive elements, cohesive zone, tie-break) are commonly measured using Double Cantilever Beam (DCB) and End Notched Flexure (ENF) tests. Test standards ASTM D5528 [166] and ASTM D7905 [167] define DCB and ENF tests. The following section contain a literature survey of interlaminar material properties of IM7/8552 as part of the DLR contribution to the CMH-17 CWG. A detailed literature review of the interlaminar energy release rates for IM7/8552 is provided in Appendix A.1.2. The elastic properties and fracture toughness data used for the interlaminar and interface model are listed in Table 3.2 and Table 3.3, respectively. The elastic interlaminar material properties are also achieved from literature [168, 169]. However, it should be noted that the cohesive interface stiffness in mode I and mode II/III are non-physical penalty parameters. For guidelines in calibrating these parameters, the reader is referred to [89,

135]. The mode I and mode II/III damage initiation tractions correspond to the transverse tensile strength and in-plane shear strength of IM7/8552, respectively.

3.2 Overview of Material Input Data for Numerical Analysis

The following section presents the intralaminar material data for both the EU- and US-Version of IM7/8552. The literature source of each parameter is given whereas the entry 'Test' refer to material data determined in experimental tests and the entry 'Sim.' refers to material properties calibrated in numerical simulations. The two material data sets are used in the following sections of this work:

- **Chapter 4**: The single-element simulations in this chapter are performed using both the EU-Version and US-Version of IM7/8552. However, stress-strain characteristics of the material characterization tests of IM7/8552 (US-Version) are presented to verify the single-element simulation with experimental results.

- **Chapter 5**: The numerical work on the single-laminate element level is performed on the EU-Version of IM7/8552. This is due to the comparison of the results of fracture mechanic tests in chapter 6 on the identical quasi-isotropic laminate. The two versions are compared to identify the effects on this level.

- **Chapter 6**: The fracture mechanic tests of OCT and CC tests were performed on the EU-Version of IM7/8552. The fibre fracture energies are calibrated and validated for both material versions.

- **Chapter 7**: The simulation of progressive crushing is performed in the scope of the CMH-17 CWG. Experimental validation tests were performed with specimens made of the US-Version of IM7/8552.

Table 3.1: Mechanical properties of Hexcel IM7/8552 - Properties of EU and US-Version

Intralaminar Material Properties							
Description	Parameter	Value		Source		Unit	
		EU	US	EU	US		
Elastic Parameters							
Longitudinal Tensile Modulus	E_{1T}	165.0	154.58	[148]	[152]	GPa	
Longitudinal Compressive Modulus	E_{1C}	150.0	154.58	[153]	[152]	GPa	
Transverse Tensile Modulus	E_{2T}	9.0	8.96	[148]	[152]	GPa	
Transverse Compressive Modulus	E_{2C}	11.0	8.96	[153]	[152]	GPa	
In-plane Shear Modulus	G_{12}	5.6	4.69	[148]	[152]	GPa	
Major Poisson's Ratio	ν_{12}	0.34	0.316	[148]	[152]	$-$	
Minor Poisson's Ratio	ν_{21}	0.0185	0.0183			$-$	
Strength Parameters							
Longitudinal Tensile Strength	X_T	2.56	2.50	[148]	[152]	GPa	
Longitudinal Compressive Strength	X_C	1.69	1.714	[153]	[152]	GPa	
Transverse Tensile Strength	Y_T	0.073	0.064	[148]	[152]	GPa	
Transverse Compressive Strength	Y_C	0.25	0.285	[153]	[152]	GPa	
In-plane Shear Strength	S_{12}	0.09	0.09	[148]	[152]	GPa	
Ladevèze Parameters							
Shear Damage Initiation Threshold	Y_{120}	0.0	5.31	[151]	Test	MPa	
Shear Damage Evolution Parameter	Y_{12c}	12.0	110	[151]	Test	MPa	
Shear Damage Failure Threshold	Y_{12s}	57.9	57.9	Test	Test	MPa	
Transverse Damage Initiation Threshold	Y_{20}	0.0	2.97	[151]	Test	MPa	
Transverse Damage Evolution Parameter	Y_{2c}	12.0	128.0	[151]	Test	MPa	
Transverse Damage Failure Threshold	Y_{2s}	16.2	16.2	Test	Test	MPa	
Shear-Transverse Damage Coupling Parameter	b	0.5	0.465	[151]	Test	$-$	
Plasticity Parameter							
Plasticity Yield Stress	R_0	60.0	32.5	[151]	Test	MPa	
Plasticity Hardening Law Coefficient	β	1.0	680	[151]	Test	MPa	
Plasticity Hardening Law Exponent	μ	0.54	0.45	[151]	Test	$-$	
Shear-Transverse Plasticity Coupling Parameter	α	0.67	0.75	[151]	Test	$-$	
Fibre Fracture Energies							
Tensile Fibre Fracture Energy	G_{c1}^T	120.0		Sim.		$\frac{kJ}{m^2}$	
Compressive Fibre Fracture Energy	G_{c1}^C	60.0 − 80.0		Sim.		$\frac{kJ}{m^2}$	

Table 3.2: Elastic properties of the cohesive traction-separation behaviour

Interlaminar Material Properties				
Description	Parameter	Value	Unit	Source
Cohesive Interface Stiffness - Mode I (penalty)	K_{nn}	467.0	$\frac{kN}{mm^3}$	[168]
Cohesive Interface Stiffness - Mode II/III (penalty)	$K_{ss} = K_{tt}$	167.0	$\frac{kN}{mm^3}$	[168]
Mode I Damage Initiation Traction	σ_I^0	60.0	MPa	[169]
Mode II/III Damage Initiation Traction	$\sigma_{II}^0 = \sigma_{III}^0$	90.0	MPa	[169]

Table 3.3: Interlaminar fracture toughness data

Fracture Toughness Parameters of the Matrix			
Description	Parameter	Value	Units
Mode I Fracture Toughness of Matrix	G_{Ic}	0.277	$\frac{kJ}{m^2}$
Mode II Fracture Toughness of Matrix	G_{IIc}	0.788	

Fracture Toughness Parameters of the Matrix					
Description	Parameter	Value	Parameter	Value	Units
Mixed Mode Toughness of Matrix	$\frac{G_{II}}{G_{tot}}$	0.33	G_c	0.298	$\frac{kJ}{m^2}$
		0.66	G_c	0.374	

For IM7/8552 Interfaces: Fracture Toughness Parameters			
Interface	Mode I Fracture Toughness	Mode II Fracture Toughness	Units
0°/0°	0.22	0.63	$\frac{kJ}{m^2}$
0°/45°	0.22	0.94	
0°/90°	0.22	0.73	
45°/ − 45°	0.22	1.3	

4 Numerical Modelling of Composite Materials

This chapter describes in detail the implementation of the intralaminar damage model used for the simulation of crushing of composite materials. The composite material model uses theories from the literature and describes the behaviour of fibre and matrix independently of each other. To investigate the research questions outlined in Section 2.5, a user-material model is required which enables access to the source code in order to adapt and extend. This possibility is not given for material models implemented in commercial FE codes since full access to the source code is not granted. Modification of the user-material includes the adaptation for modelling of unidirectional plies, a fracture mechanics based damage behaviour in fibre direction, different fibre softening options, as well as the implementation of a failure criterion in transverse compressive loading.

4.1 Intralaminar Damage Model - ABQ_DLR_UD

The meso-scale material model 'ABQ_DLR_UD' is implemented as an explicit user-material 'VU-MAT' in the framework of the commercial FEA code Abaqus/Explicit. ABQ_DLR_UD is based on the material model proposed by Schueler [90] and Schueler et al. [91] and uses the theories of Ladevèze and LeDantec [108]. The main differences to the model in [90, 91] are the damage behaviour in longitudinal (fibre) direction as well as a failure criterion for transverse compressive loading, as outlined in the following section. The elementary ply is modelled as a homogeneous, orthotropic material with a plane-stress formulation where the two constituents fibre and matrix govern the behaviour in longitudinal and transverse direction, respectively. A linear elastic behaviour is assumed until a damage initiation criterion is met (longitudinal direction) or the yield stress is exceeded and plastic flow initiates (transverse direction). The framework of CDM is used where internal state variables govern the stiffness degradation controlled by damage evolution equations. The material model is suitable for plane-stress element types in Abaqus/Explicit. In detail, conventional shell elements (element formulation: 'S4R') and continuum shell elements (element formulation: 'SC8R'). To model the laminate or sublaminates in a multi-layered shell or stacked-shell modelling approach, shell sections are defined that uses through-thickness integration points, called section points. The orientation of the ply representing the material orientation is defined for each shell section. Simpson's integration rule with three section points for each shell section is used to calculate the cross-sectional behaviour. The material response at each section point is calculated within the VUMAT with respect to the defined material orientation. ABQ_DLR_UD consists of a
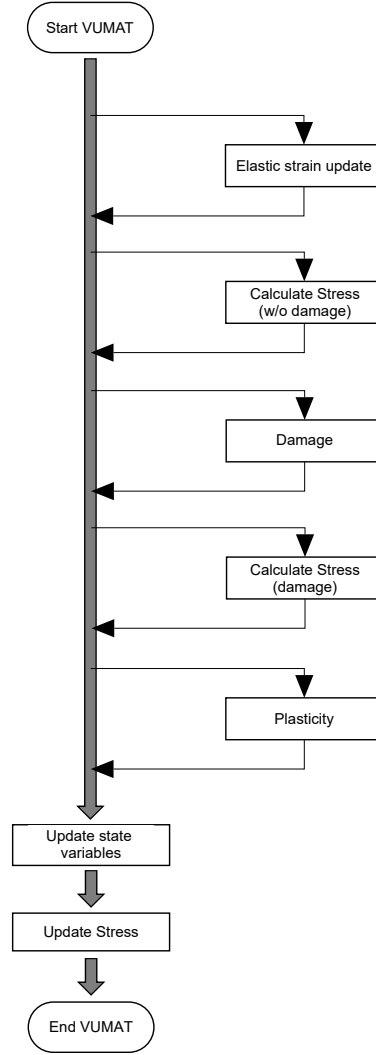
Figure 4.1: Flow chart of VUMAT ABQ_DLR_UD

set of subroutines and the programme flow chart is shown in Figure 4.1. For each section point, the FE-code passes the strain increments of the current time step t together with the strains and solution dependent variables (SDV) from the previous time step $t - \delta t$, with δt being the stable time increment. For $t = 0$, the initial strains and SDVs are set to zero. The initial strain vector of the actual time step is assumed to be purely elastic and is calculated with the strain vector of the previous time step and the strain increments. From this, the corresponding stresses are calculated assuming no further damage from the elastic strains. If the stresses exceed the limit at which damage initiates, evolution of fibre damage under tensile and compressive loading, matrix damage under tensile loading and shear damage as well as matrix failure under compressive loading is calculated in the subroutine 'Damage'. The equations governing the damage evolution are described in detail in the following sections. With the updated damage variables, the tensor of the effective stresses is calculated using the damaged stiffness matrix. A plasticity law describing permanent

plastic strains in the matrix as proposed by Ladevèze and LeDantec [108] was implemented in the model of Schueler [90, 91] and is used in this work with adaptations. Coupling of plasticity and damage is considered in the model by using the tensor of the effective stresses to calculate the elastic domain function and the damaged stiffness matrix which is then used to update the stresses in the plasticity algorithm. The SDVs containing the damage variables, elastic and plastic strains and failure flags amongst others are updated. A list of the SDVs of ABQ_DLR_UD is shown in Table B.1 in Appendix B.2. Finally, the stress tensor is updated for time t and returned to the solver. The described procedure is repeated for each stable time increment δt until the termination time of the simulation is reached. In the following sections, the implementation of fibre and matrix behaviour is described in detail. The material behaviour is then verified in terms of stress-strain characteristics of UD single-element simulations.

4.2 Material Behaviour of Fibre and Matrix

The Ladevèze based meso-scale UD-model implemented by Schueler [90, 91] in Abaqus/Explicit was applied to simulate high-velocity impact on transport aircraft fuselage bay sized plates [91]. The focus of this model was the linkage of intra-ply matrix damage with the initiation of delamination damage. In the present work, the Ladevèze based UD-model is adapted by defining fracture mechanics based damage evolution laws with different softening options for the fibre behaviour in longitudinal loading. This extension involves the crack band method [113]. Fibre fracture energies are implied to address the mesh dependency with regard to the dissipated damage energy during crack propagation. Compared to the UD-model implemented by Schueler [90, 91] which used a strain-based damage evolution law for fibre damage.

4.2.1 Damage Initiation and Damage Evolution in Longitudinal Direction

The material behaviour in longitudinal direction is governed by the constitutive behaviour of the fibre. Initially, a linear-elastic behaviour of the fibre is assumed. The stress-strain relation is defined as:

$$\vec{\varepsilon^{el}} = \vec{S}\vec{\sigma} \Leftrightarrow \begin{cases} \varepsilon_{11} & = \frac{\sigma_{11}}{E_1^0(1-d_1)} - \frac{\nu_{21}\sigma_{22}}{E_2^0} \\ \varepsilon_{22}^{el} & = \frac{\langle\sigma_{22}\rangle_+}{E_2^0(1-d_2)} + \frac{\langle\sigma_{22}\rangle_-}{E_2^0} - \frac{\nu_{12}\sigma_{11}}{E_1^0} \\ \varepsilon_{12}^{el} & = \frac{\sigma_{12}}{2G_{12}^0(1-d_{12})} \end{cases} \qquad (4.1)$$

The indices '11'/'1' describe the longitudinal or fibre direction, '22'/'2' the transverse or matrix direction and '12' the shear direction. Tensile and compressive anisotropy is considered by implementing different Young's moduli of elasticity and damage variables for both fibre and matrix in the model. In the VUMAT, distinction between tension and compression is made using [130]:

$$\text{if} \quad tr(\vec{\varepsilon}) \geqslant 0 \quad \text{then} \quad E_1^0 = E_{1T}, E_2^0 = E_{2T} \quad \text{else} \quad E_1^0 = E_{1C}, E_2^0 = E_{2C} \qquad (4.2)$$

Fibre damage in fibre direction is initiated in ABQ_DLR_UD when a maximum stress criterion is met which relates the longitudinal stress to the fibre tensile or compressive strength values, respectively. The maximum stress criterion is met when:

$$\frac{\sigma_{11}}{X_T} \geqslant 1 \quad \text{or} \quad \frac{\sigma_{11}}{X_C} \leqslant -1 \tag{4.3}$$

with X_T, X_C being the tensile and compressive strength of the fibre, respectively. When the stress at a section point exceeds the tensile or compressive strength, damage in fibre direction evolves. Fibre damage evolution in the framework of CDM is governed by the scalar damage parameters for tensile and compressive damage d_1^T and d_1^C, respectively. An exponential softening approach is chosen and defined as the baseline configuration throughout this work. The scalar damage parameter for exponential softening are defined as:

$$d_1^{T/C} = 1 - \frac{X_{T/C}}{E_{1T/C}} \frac{\exp\left(\Phi\left(\frac{X_{T/C}}{E_{1T/C}} - |\varepsilon_1|\right)\right)}{|\varepsilon_1|} \tag{4.4}$$

with ε_1 denoting the longitudinal strain. To define a physical foundation of the softening behaviour, the softening coefficient Φ takes into account the fracture energies G_{c1}^T, G_{c1}^C such as:

$$\Phi = \frac{2 \cdot (1-k) X_{T/C} \cdot l^*}{2 \cdot G_{c1}^{T/C} - \frac{X_{T/C}^2 \cdot l^*}{E_{1T/C}}} \tag{4.5}$$

In CDM approaches, the experimentally determined fracture energies are typically distributed over the volume of an element in order to avoid strain localizations by considering a characteristic element length l^*. The characteristic element lengths are determined within Abaqus/Explicit and are provided as input parameters to ABQ_DLR_UD. The characteristic element length l^* of an element is defined as the square root of the in-plane area:

$$l^* = \sqrt{A_{ele}} \tag{4.6}$$

Equation (4.5) can be formulated in terms of the fracture energy densities:

$$g_{c1}^{T/C} = \frac{G_{c1}^{T/C}}{l^*} \tag{4.7}$$

If the characteristic length of an element is too large, the energy density becomes less than the elastic strain energy. Therefore, a maximum characteristic length is defined for the fibre fracture energies:

$$l_{max}^* = \frac{2 \cdot G_{c1}^{T/C} \cdot E_{1T/C}}{X_{T/C}^2} \tag{4.8}$$

if $l^* > l^*_{max}$ the fibre fracture energies are artificially increased until Equation (4.8) is met. Due to the formulation of $d_1^{T/C}$ in Equation (4.4), the stress is exponentially reduced after damage initiation and converges asymptotically to zero. Based on the approach presented by Maimí et al. [115] and adopted by Ehrich [170], a strain can be defined at which the damage is assumed to be saturated as:

$$\varepsilon_{sat,exp} = \frac{X_{T/C}}{E_{1T/C}} - \frac{ln(k)}{\Phi} \tag{4.9}$$

at this saturation strain, the stress becomes less than $k \cdot X_{T/C}$ where k is a factor chosen to be sufficiently small (here: $k = 0.01$) such that the energy dissipated due to damage propagation is negligible for $\varepsilon \geqslant \varepsilon_{sat}$.

Implementation of additional fibre softening options

To investigate the influence of strain-softening approaches, different formulations are implemented in ABQ_DLR_UD which govern the evolution of the fibre damage variables and therefore the shape of the strain-softening. The softening options considered in this work contain a linear softening approach, a brittle failure with residual stress level and a combination of both, a linear softening up to a certain stress level which is kept constant until the saturation strain is reached. A schematic representation of the strain-softening approaches is shown in Figure 4.2. All softening options are based on fibre fracture energies. The softening options can be selected independently for tensile and compressive loading.

In the **linear softening** approach, the slope of strain-softening from damage initiation to the point of saturation is linear. The linear fibre damage variables in tension and compression are defined as:

$$d_{1,linear}^{T/C} = \frac{\frac{2 \cdot G_{c1}^{T/C}}{X_{T/C} \cdot l^*}}{\frac{2 \cdot G_{c1}^{T/C}}{X_{T/C} \cdot l^*} - \frac{X_{T/C}}{E_{1T/C}}} \left(1 - \frac{\frac{X_{T/C}}{E_{1T/C}}}{\varepsilon_1} \right) \tag{4.10}$$

and the saturation strain is calculated such as:

$$\varepsilon_{sat,lin} = (1 - k) \left(\frac{2 \cdot G_{c1}^{T/C}}{X_{T/C} \cdot l^*} - \frac{X_{T/C}}{E_{T/C}} \right) + \frac{X_{T/C}}{E_{1T/C}} \tag{4.11}$$

The **brittle failure with residual stress** approach assumes brittle failure after the fibre tensile/compressive strength is reached resulting in a sudden drop to a certain stress level defined as a fraction of the strength, $soft \cdot X_{T/C}$. This stress level is kept constant until the fibre fracture energy is dissipated in the damaging process. The tensile and compressive damage variables are defined as:

$$d_{1,brittle}^{T/C} = 1 - \left(\frac{soft \cdot \frac{X_{T/C}}{E_{1T/C}}}{\varepsilon_1} \right) \tag{4.12}$$

a) Exponential softening

b) Linear softening

c) Brittle failure with residual stress

d) Linear softening with residual stress
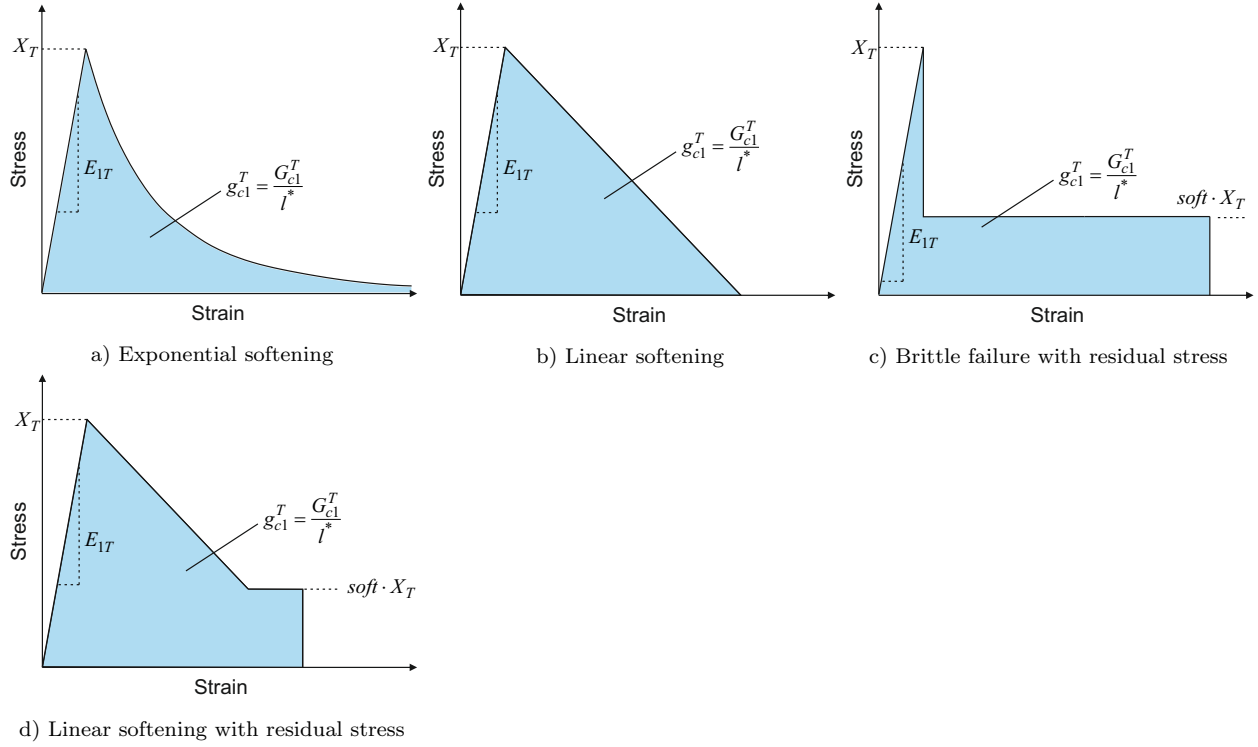
Figure 4.2: Schematic representation of fibre softening options implemented in ABQ_DLR_UD. a) Exponential softening; b) Linear softening; c) Brittle failure with residual stress; d) Linear softening with residual stress

After damage initiates at $\varepsilon_1 = \frac{X_{T/C}}{E_{1T/C}}$, the damage variables jump from zero to $1 - soft$ and slightly increase to keep the stress level of $soft \cdot X_{T/C}$. To reach the correct amount of energy that dissipates during damage, the saturation strain is defined as:

$$\varepsilon_{sat,\,brittle} = \frac{G_{c1}^{T/C}}{soft \cdot X_{T/C} \cdot l^*} - \frac{X_{T/C}}{2 \cdot E_{1T/C} \cdot soft} + \frac{X_{T/C}}{E_{1T/C}} \tag{4.13}$$

The combination of **linear softening with residual stress** results in the fourth softening approach. The evolution of the damage variables is defined in Equation (4.10). Different stress levels are defined by setting $k = soft$ in the definition of the saturation strain in Equation (4.11). The same procedure can also be applied to the exponential softening approach in Equation (4.5) and Equation (4.9). However, this is not considered in the scope of this work.

4.2.2 Material Behaviour in Transverse Direction

Matrix damage under transverse tensile and shear loading in ABQ_DLR_UD, is described by the formulations of Ladevèze and LeDantec [108] as described in Section 2.3.2 and the modifications to the original formulations by Schueler [90, 91]. The scalar damage variables are functions of the damage-energy release rate Y defined as the partial derivative of the strain-energy potential φ with

respect to the transverse tensile and shear damage variables d_2^T and d_{12}, respectively such as:

$$\varphi = \frac{1}{2}\left[\frac{\sigma_{11}^2}{E_1^0} - \frac{2 \cdot \nu_{12}^0}{E_1^0}\sigma_{11} \cdot \sigma_{22} + \frac{\langle\sigma_{22}\rangle_+^2}{E_2^0(1-d_2)} + \frac{\langle\sigma_{22}\rangle_-^2}{E_2^0} + \frac{\sigma_{12}^2}{2 \cdot G_{12}(1-d_{12})}\right] \tag{4.14}$$

$$Y_2 = \frac{\partial\varphi}{\partial d_2} = \frac{\langle\sigma_{22}\rangle_+^2}{2 \cdot E_2^T(1-d_2)^2} \tag{4.15}$$

$$Y_{12} = \frac{\partial\varphi}{\partial d_{12}} = \frac{\sigma_{12}^2}{2 \cdot G_{12}(1-d_{12})^2} \tag{4.16}$$

where $\langle\cdot\rangle_+$ implies Macauley brackets which indicate that only transverse tensile stresses are accounted. Damage in transverse compressive loading was not considered in the original theory of Ladevèze and LeDantec since they argue that micro-cracks close up under compressive loading [108]. Experimental results of Ladevèze and LeDantec [108] showed that the evolution of transverse damage, in detail matrix microcracking and fibre/matrix debonding can be approximated by the quantities $\underline{Y}$ and $\underline{Y}_2$, respectively such as:

$$\underline{Y} = \sup_{\tau \leqslant t}\left(\sqrt{Y_{12}(\tau) + bY_2(\tau)}\right) \quad \text{and} \quad \underline{Y}_2 = \sup_{\tau \leqslant t}\left(\sqrt{Y_2(\tau)}\right) \tag{4.17}$$

with $\sup_{\tau \leqslant t}$ describing that $\underline{Y}$ and $\underline{Y}_2$ can only increase throughout the load history. From this, the damage variables d_2^T and d_{12} are defined as:

$$d_2^T = \begin{cases} 0, & \underline{Y}_2 < Y_{20} \\ \frac{\underline{Y}-Y_{20}}{Y_{2c}}, & \underline{Y} < Y_{12s} \,\text{and}\, \underline{Y}_2 < Y_{2s} \\ 1 - \frac{soft \cdot \frac{Y_T}{E_2^T}}{\varepsilon_{22}}, & \text{else} \end{cases} \tag{4.18}$$

$$d_{12} = \begin{cases} 0, & \underline{Y} < Y_{120} \\ \frac{\underline{Y}-Y_{120}}{Y_{12c}}, & \underline{Y} < Y_{12s} \,\text{and}\, \underline{Y}_2 < Y_{2s} \\ 1 - \frac{soft \cdot \frac{S_{12}}{G_{12}}}{\varepsilon_{12}}, & \text{else} \end{cases} \tag{4.19}$$

where Y_T is the transverse tensile strength and S_{12} the in-plane shear strength. The parameters Y_{20}, Y_{2c}, Y_{120}, Y_{12c} govern the progressive damage propagation whereas the quantities Y_{2s} and Y_{12s} where defined by Schueler [90, 91] and are damage threshold parameters to control brittle failure at which d_2^T and d_{12} are set to the maximum values. The experimental determination of the damage evolution and failure threshold parameters is described in Appendix A.1. A residual stress level is implemented in transverse and shear direction in the same way as for the longitudinal direction. The residual stress level is a fraction of the transverse or in-plane shear strength, respectively. However, the softening parameter is chosen to be $soft \ll 1$ in the scope of this work. Even if damage evolution under transverse compressive loading is not considered in the original formulation of Ladevèze and LeDantec [108], a damage variable d_2^C is defined in ABQ_DLR_UD. After exceeding the transverse

compressive strength Y_C, the damage variable jump to a value defined as:

$$d_2^C = 1 - \frac{soft \cdot \frac{Y_C}{E_2^C}}{\varepsilon_{22}} \tag{4.20}$$

To model plasticity in terms of permanent transverse and shear strains, Schueler [90, 91] implemented the plasticity law of Ladevèze and LeDantec [108] in Abaqus/Explicit. The approach is also implemented in ABQ_DLR_UD. The procedure is described in detail in [90]. The plasticity algorithm uses an elastic domain function and a hardening law to determine the permanent strains on the basis of internal friction. A backward Euler scheme and an iterative Newton solver which could be interpreted as an elastic predictor and plastic corrector algorithm is used [90]. The elastic domain function is defined as:

$$f = \sqrt{\widetilde{\sigma}_{12}^2 + \alpha^2 \cdot \widetilde{\sigma}_{22}^2} - R(p) - R_0 \quad \text{with} \quad R(p) = \beta \cdot p^\mu \tag{4.21}$$

with $\widetilde{\sigma}_{12}$, $\widetilde{\sigma}_{22}$ being the effective stresses, α is the material dependent transverse and shear coupling parameter, R_0 the yield stress and $R(p)$ the isotropic hardening law as a function of the plastic strain (p). Determination of the material's plasticity parameters is outlined in Appendix A.1. Coupling of damage and plasticity is considered by the definition of the effective stresses as:

$$\widetilde{\sigma}_{12} = \frac{\sigma_{12}}{1 - d_{12}} \quad \text{and} \quad \widetilde{\sigma}_{22} = \frac{\langle \sigma_{22} \rangle}{1 - d_2^T} + \langle \sigma_{22} \rangle_- \tag{4.22}$$

4.2.3 Material Failure and Element Erosion

Failure of the fully damaged material is modelled using an Element Elimination Technique (EET) where elements that have met an elimination criterion are deactivated in the numerical model. By setting all stresses and moduli of the finite element to zero, the elements no longer contribute to the structural response of the modelled part. However, for the simulation of crushing, the response of debris in the crush front influence the crushing behaviour for example due to frictional effects and inertial masses. Therefore, even if fully damaged elements without stiffness don't provide resistance, those elements represent physical effects and a removal can influence the crushing result. On the other hand, elements with a low stiffness tend to extreme distortion and cause error terminations of the simulation. An elimination criterion is defined which models the post-failure behaviour in a smeared manner. A criterion based on elimination strains is chosen for this work. After the material is fully damaged by reaching the saturation strains for the fibre direction or the damage threshold parameters for transverse and shear direction, the residual stress level is defined to keep the value of $(1 - d)$ times the strength. By further increasing the damage variables, the residual stress level is kept constant until the erosion strain is reached and the elements are deactivated in the mesh. Elimination strains and maximum damage are numerical parameters which cannot be determined in material characterization tests. The approach in this work to select the elimination

strains is by defying:

$$\varepsilon_{1,\,max} \geqslant \varepsilon_{sat,\,1}; \quad \varepsilon_{2,\,max} \geqslant \varepsilon_2(Y_{2s}); \quad \varepsilon_{12,\,max} \geqslant \varepsilon_{12}(Y_{12s}) \tag{4.23}$$

and choosing the maximum values to be sufficiently small to avoid distorted elements. Since $\varepsilon_{sat,\,1}$ is dependent on the fibre fracture energies and element sizes, no uniform saturation strain is defined. However, as a rule of thumb, the erosion strain of the matrix is selected to be the same as the fibre erosion strain for the corresponding loading to avoid too early elimination of elements which are not fully damaged in fibre direction. For softening approaches with residual stress plateau the stress plateau is implemented to model the response of the debris in the crush front, as outlined in Section 4.2.1. Therefore, the erosion strains are equal to the saturation strains as defined in Equation (4.13). When the elimination strain is reached at a section point, the SDV variable *status* is set to zero. In Abaqus/Explicit, different criteria are available which defines whether a fully damaged element is deactivated. In this work, a last-ply failure criterion is used where the element is deactivated when $status = 0$ is reached at all section points.

4.2.4 Single-Element Simulations - Verification of the Implemented User-material Model

The stress-strain characteristics of longitudinal tensile and compressive loading of a UD-single element are presented in Figure 4.3 a) and b), respectively. The results are presented for uni-directional $1.0\,mm \times 1.0\,mm$ single-elements ($l^* = 1.0\,mm$) obtained with the material data sets of both IM7/8552 versions as outlined in Table 3.1. The boundary conditions represent uni-axial stress. The input of the fibre fracture energy is chosen as $G_{c1}^T = G_{c1}^C = 120\,\frac{kJ}{m^2}$. It is shown, that the different material properties have no significant influence on the fibre tensile and compressive behaviour. Fibre tensile and compressive damage is zero in the initial linear elastic region until the tensile/compressive strength is reached. Afterwards, damage develops and the damage variables increase following Equation (4.4). The area enclosed by the stress-strain curves corresponds to the fracture energy densities $g_{c1}^{T/C}$. The fracture energy densities are slightly higher compared to the input values of the fracture energies $G_{c1}^{T/C}$ due to the constant stress level $k \cdot X_{T/C}$ for $\varepsilon_1 \geqslant \varepsilon_{sat}^{T/C}$. The additional energy due to this constant stress level depends on the selected erosion strain which is chosen here as $\varepsilon_{1,\,max} = 0.35$ for both tension and compression. However, the additional fracture energy is less than 4% and assumed to be negligible. It is shown that the selected erosion strain is higher than the saturation strain in accordance to Equation (4.23).

Evolution of the matrix damage variables for both material versions are presented in Figure 4.3 a). The matrix damage variables contain both the transverse tensile and shear damage variable d_2^T and d_{12}, respectively. Here, the influence of the different matrix properties of the IM7/8552 versions are seen. Transverse damage in the EU-Version initiates at load application due to the assumption of $Y_{20} = Y_{120} = 0$ and the coupled transverse tensile and shear damage energy release
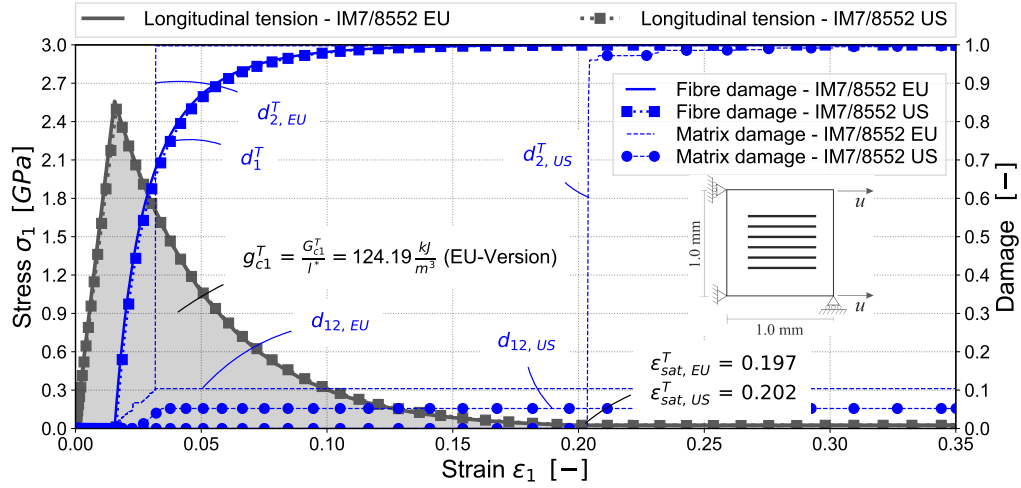
a) Longitudinal tensile loading
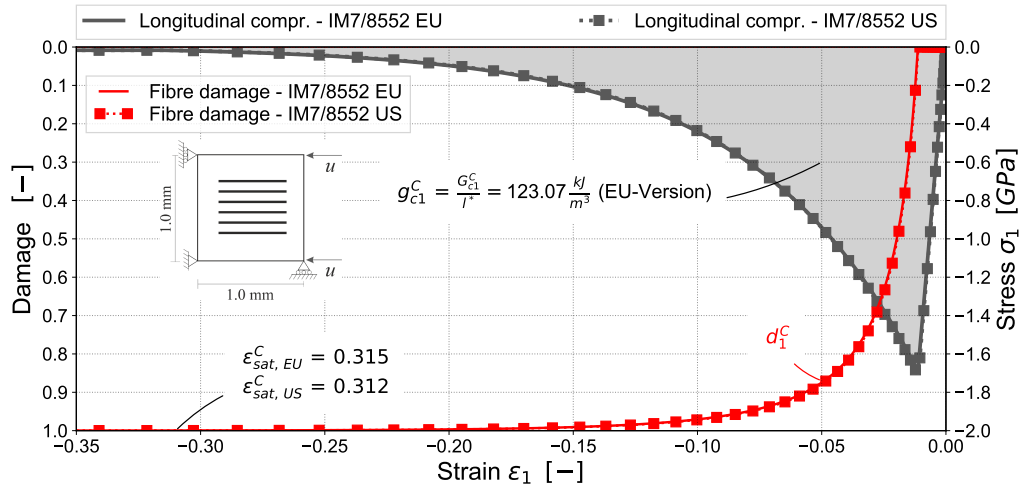
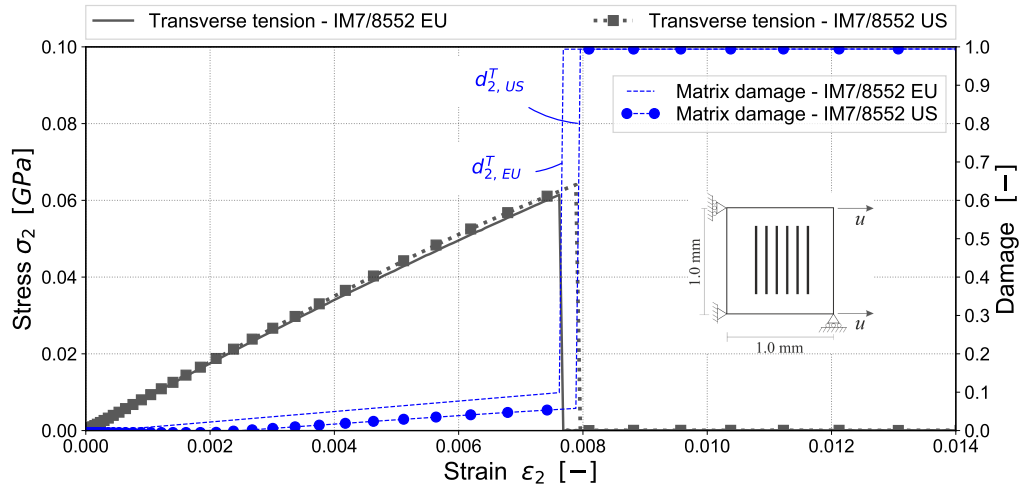b) Longitudinal compressive loading

Figure 4.3: Longitudinal stress-strain characteristic of a) tensile loading, b) compressive loading. Evolution of fibre tensile and compressive damage variables d_1^T, d_1^C and a) transverse tensile damage d_2^T and shear damage d_{12} variables; Material properties of IM7/8552 EU-Version and IM7/8552 US-Version

rate reaches $\underline{Y} \geqslant Y_{2s}$ at $\varepsilon_1 = 0.032$ which result in maximum transverse tensile damage. This shows the necessity to carefully define the erosion strain based on fibre damage since an erosion strain based on transverse tensile damage would have triggered the element erosion at a point at which fibre damage is not fully saturated and the complete fibre fracture energy is absorbed. On the other hand, for the US-Version of IM7/8552, transverse damage initiates as shear damage at $\varepsilon_1 = 0.032$ and the energy release rate $\underline{Y}$ does not exceed $\underline{Y}_{2s}$ or $\underline{Y}_{12s}$ until the fibre saturation strain is reached. In longitudinal compressive loading, Figure 4.3 b), also no significant influence of the material version is identified. The saturation strains are higher compared to longitudinal tensile loading with the same fibre fracture energy due to the lower fibre compressive strength. Matrix damage is omitted in Figure 4.3 b) since matrix compressive damage is not implemented and transverse contraction is not sufficient to initiate (transverse) tensile loading.

The material behaviour of the matrix in transverse and shear loading is shown in Figure 4.4. Results for both material versions are shown and the boundary conditions represent uni-axial stress in all three loading cases. Figure 4.4 a) presents the matrix behaviour under tensile loading. The stress-strain characteristics for the two material version show minor differences with a slightly higher maximum stress value obtained for the US-Version of IM7/8552. It is noticeable that the maximum stress of the EU-Version is lower compared to the transverse tensile strength of $Y_T = 0.073\,GPa$ found in literature and listed in Table 3.1. This is due to the assumption for transverse tensile damage initiation threshold $Y_{20} = 0$ in the EU-Version. Whereas the strength of $Y_T = 0.064\,GPa$ is predicted reasonably well by the material model for the US-Version of IM7/8552. By comparing the characteristics of the damage variables in Figure 4.4 a), it is shown that $d_{2,\,EU}^T$ increases from the origin whereas $d_{2,\,US}^T$ is zero until $\varepsilon_2 \approx 0.002$, the point at which $\underline{Y}_2 \geqslant Y_{20}$. The stress-strain characteristics show a slightly non-linear behaviour which is affected by both the evolution of damage as well as plastic flow after exceeding the yield stress.

Figure 4.4 b) presents the matrix behaviour under transverse compressive loading. For this loading case, the influence of the parameters of the two material version is obvious. Due to the 14 % increase in transverse compressive strength of IM7/8552 US, the saturation strain increases by 114 %. Since no damage evolution is implemented for transverse compressive loading, this increase is the result of permanent plastic strains. More plastic strain is accumulated until the higher compressive strength and the failure criterion is met. Also, the yield stress determined for the US-Version of IM7/8552 is 50 % less compared to the assumed yield stress of the EU-Version which result in an earlier development of plastic strain and therefore a higher accumulated plastic strain at failure.

Figure 4.4 c) shows the shear response of a $[\pm 45]_s$ single-element under uni-axial tensile stress. The shear stress-shear strain characteristics of both material versions are shown along with the experimentally determined stress-strain curve of test sample '45_5 (US-Version)' (see Appendix A.1). The simulation of IM7/8552 EU is performed with monotonic loading whereas the single-element of the US-Version is cyclically loaded and unloaded. It is shown that the shear stress-shear strain characteristic of the simulation of IM7/8552 US correlates well with the experimental results.

a) Transverse tensile loading
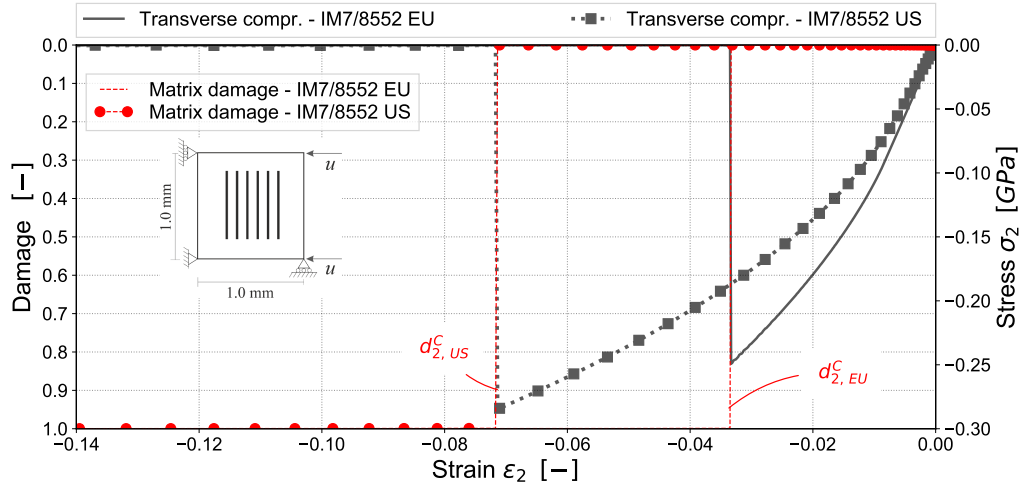
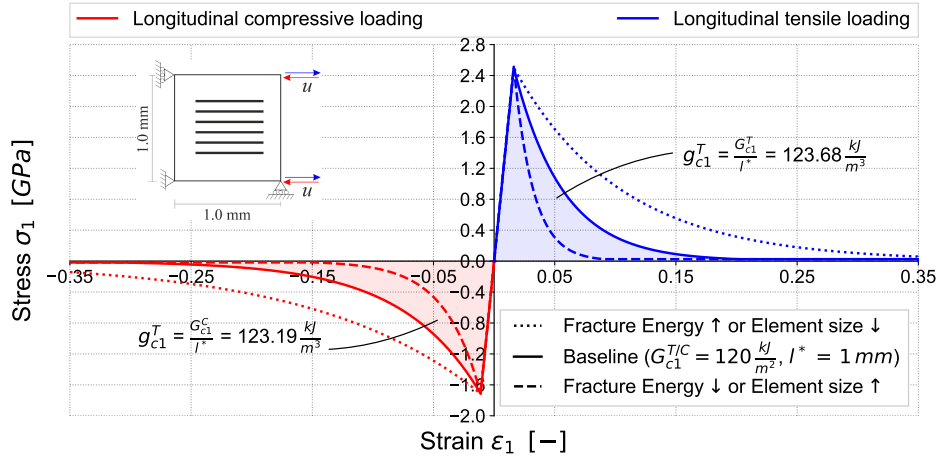b) Transverse compressive loading
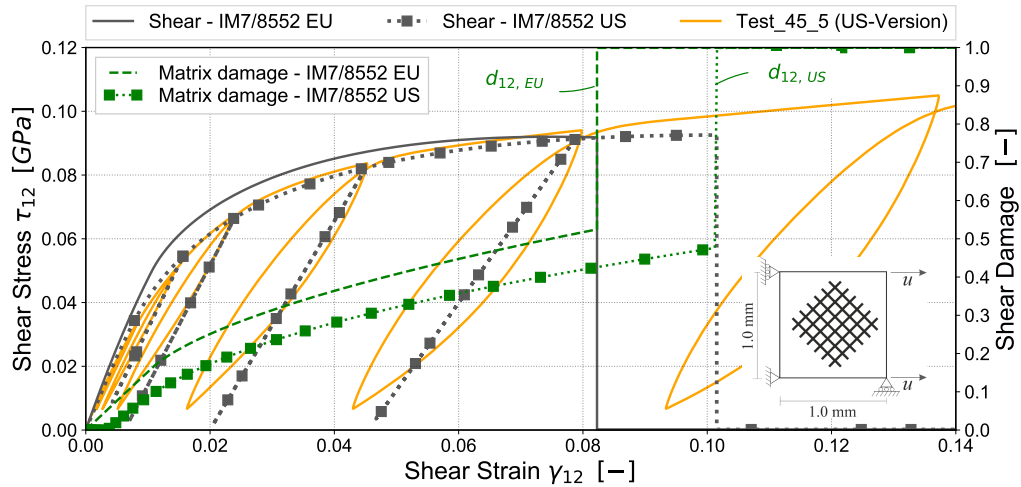
c) Shear loading

Figure 4.4: Transverse stress-strain characteristic of a) tensile loading, b) compressive loading c) shear loading. Evolution of matrix tensile and compressive damage variables d_2^T, d_2^C and d_{12}

This is expected since the material input parameter were determined from the experimental tests. Deviations between simulation and test can be identified in the loading/unloading slopes. The loading/unloading slopes of the simulation are steeper compared to the experimental results. One reason might be a reduced damage evolution in the simulation which results in higher damaged shear modulus $(1 - d_{12})G_{12}$ compared to the experimental results. The hysteresis effect which is seen in the experimental tests also has an influence since this effect is not modelled in the simulation. Comparing the two material versions in Figure 4.4 c) shows that the shear stress - shear strain characteristic predicted in the simulation of IM7/8552 EU is higher compared to IM7/8552 US up to a shear strain of ≈ 0.08. The reasons are mainly identified in the different elastic properties and yield stresses. Due to the higher shear modulus of the EU-Version compared to the US-Version, the initial elastic slope is higher. Shear damage develops initially at load application due to the assumption of $Y_{120} = 0$. This results in an initial non-linear stress-strain behaviour for IM7/8552 EU. The non-linearity increases due to plastic flow after exceeding the yield stress. The yield stress is reached at $\sigma_{12} = R_0(1 - d_{12})$ which is lower as R_0 outlined in Table 3.1 due to initial damage. In the simulation of IM7/8552 US, damage initiates later due to $Y_{120,US} > Y_{120,EU}$. Therefore, the non-linearity in the shear stress-shear strain curve initiates when $\sigma_{12} = R_0 = 32.5\,MPa$. The element is fully damaged when $\underline{Y} = Y_{12s}$, the point at which d_{12} instantly becomes maximum. However, this point does not necessarily correspond to the in-plane shear strength S_{12} since this property is not considered in the Ladevèze theory. The in-plane shear strength is used after failure of the element to defined the residual stress level until the shear erosion strain is reached (see Equation (4.19)).

The results presented in the previous section are part of a wide verification process on single-element level. The results verified the user-material model in the baseline configuration with exponential softening. The material properties of the two versions of IM7/8552 are correctly modelled by the user-material model ABQ_DLR_UD. In the following sections, the user-material model ABQ_DLR_UD is further verified with different fibre fracture energies and element sizes as well as fibre softening approaches.

4.3 Influence of Fibre Fracture Energy and Element Size

In ABQ_DLR_UD, the material behaviour in fibre direction takes into account the crack band method [113] where fibre fracture energies are implied to address the mesh dependency. The experimentally determined fracture energies are distributed over the volume of an element with characteristic element length l^*. As outlined in the previous section, the fracture energies and characteristic element lengths are considered in the damage evolution equation of the fibre to avoid strain localisations and mesh dependencies. The influence of both the fracture energy and characteristic element length on the longitudinal stress-strain characteristics is shown in Figure 4.5. The area under the stress-strain curves corresponds to the fracture energy density which is defined

Figure 4.5: Single-element simulation - Stress-strain characteristic of longitudinal tensile and compressive loading. Influence of fibre fracture energy and element size. Material properties of IM7/8552 US-Version

in Equation (4.7) as the ratio of the fibre fracture energies to the characteristic element length. The fracture energy density is increased by either increasing the fracture energies or by reducing the characteristic element length. In addition to the baseline configuration in Figure 4.5 (same as in Figure 4.3), stress strain characteristics are shown where either the fracture energies are increased/reduced by factor 2, or l^* is reduced/increased by factor 2, respectively. An increased fibre fracture energy (or reduced characteristic element length) results in higher saturation strain (see Equation (4.9)) and vice versa. Therefore, the elimination strains have to be adapted when the fracture energies are increased (or characteristic lengths are reduced). Distributing the fracture energy over the volume of the element by using the characteristic element length in the crack band method assures that the same amount of energy dissipates in crack propagation independently of the mesh. This is shown in Figure 4.6. A quadratic 2.0 mm x 2.0 mm tension/compression specimen is discretised with characteristic element lengths ranging from $l^* = 0.5\,mm$ to $l^* = 2\,mm$. The discretisation of the specimens is schematically shown in Figure 4.6 a) and c). The same fibre fracture energies of $G_{c1}^T = G_{c1}^C = 120\,\frac{kJ}{m^2}$ are assumed in the simulations of the specimens. With increasing characteristic length of the elements, the fracture energy density of each element is reduced following Equation (4.7) and as shown in Figure 4.5. Loading the specimen in longitudinal tension or compression, the elements in the model fail following the stress-strain behaviour in Figure 4.5 and the same amount of energy is dissipated independently of the mesh as shown in the stress-strain characteristics in Figure 4.6 b). To investigate a potential mesh size dependency in transverse direction, the 2.0 mm x 2.0 mm tension/compression specimen with 90° fibre orientation (see Figure 4.6 c)) is investigated. The behaviour under transverse tension and compression is shown in Figure 4.6 d). The stress-strain behaviour is identical for transverse tension for all element sizes and for transverse compression for element sizes of 0.5 mm and 1.0 mm. Failure in the 2.0 mm element occurs at a higher strain in compression due to a slightly higher plastic strain. This shows

the mesh independent behaviour of the material model ABQ_DLR_UD on the level of single element simulation with unidirectional fibre orientation. The results without crack band scaling are shown in Figure 4.7. Scaling of the fracture energy density by the element length is deactivated by increasing or reducing the fracture energy input in order that the fracture energy density corresponds to $l^* = 1.0\,mm$, $g_{c1,\,l^*=1.0\,mm}^{T/C} = 120\,\frac{kJ}{m^3}$. In longitudinal loading, Figure 4.7 a), it is shown that without crack band scaling of the fracture energies, the stress-strain characteristics are different for different element sizes. This means that the dissipated energy in a crack is dependent on the element size and therefore results in mesh dependencies. In transverse loading, Figure 4.7 b), the crack band method has no effect since no fracture energies are used for the calculation of damage evolution.

4.4 Influence of Strain-Softening Options

Single-element simulation with different fibre strain-softening behaviour is presented in this section. The different strain-softening approaches model linear softening (Equation (4.10)), brittle failure with residual stress (Equation (4.12)) and linear softening with residual stress, a combination of the first two options. Stress-strain characteristics of the 1.0 mm x 1.0 mm single UD-element loaded in longitudinal tension and compression are shown in Figure 4.8. Material properties of IM7/8552 US are used for the simulation. The initial linear-elastic behaviour up to the maximum stress is defined by the tensile/compressive Young's moduli and is independent of the softening options in ABQ_DLR_UD. The selected fibre fracture energies in tension and compression are $G_{c1}^T = G_{c1}^C = 120\,\frac{kJ}{m^2}$ for all simulations. The stress-strain characteristic of the linear softening approach is shown in Figure 4.8 a). In this bi-linear behaviour, the slope of the stress from damage initiation to the saturation strain (see Equation (4.11)) is linear. The fracture energy density as the area under the bi-linear stress-strain curve is $g_{c1}^T = 126.35\,\frac{kJ}{m^3}$ in tension and $g_{c1}^C = 126.15\,\frac{kJ}{m^3}$. In a quadratic element with $l^* = 1.0\,mm$, the fracture energy densities should be equal to the fibre fracture energies. The reason for the discrepancies seen here are due to the constant stress level $k \cdot X_{T/C}$ for $\varepsilon_1 \geqslant \varepsilon_{sat}^{T/C}$ as outlined for the exponential softening approach in Section 4.2.4. The reason for a higher fracture energy density for linear softening compared to exponential softening with the same fibre fracture energies is $\varepsilon_{sat,lin} < \varepsilon_{sat,exp}$ and therefore the energy added due to the constant stress level in the range from $\varepsilon_{sat,lin}$ to $\varepsilon_{1,max} = 0.35$ is higher. However it is assumed that the added energy still is in an acceptable range.

The stress-strain curves of brittle failure with residual stress are presented in Figure 4.8 b). For tensile and compressive loading, simulations with four residual stress levels are shown. Different stress levels are selected by setting the parameter $soft$ in Equation (4.12) to a value of $0 \leqslant soft \leqslant 1.0$ whereas $soft = 0$ would result in purely brittle failure without energy absorption due to damage and $soft = 1.0$ in a plateau with a residual stress level corresponding to $X_{T/C}$. In the scope of this work, the residual stress plateaus are selected in the range $0.2 \leqslant soft \leqslant 0.8$ which result
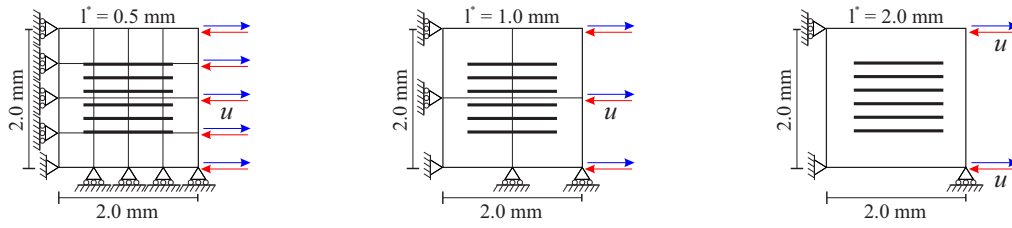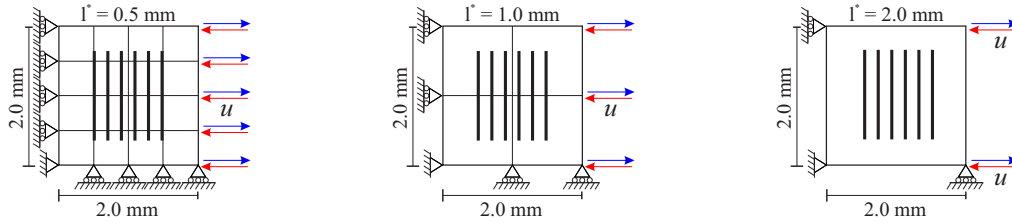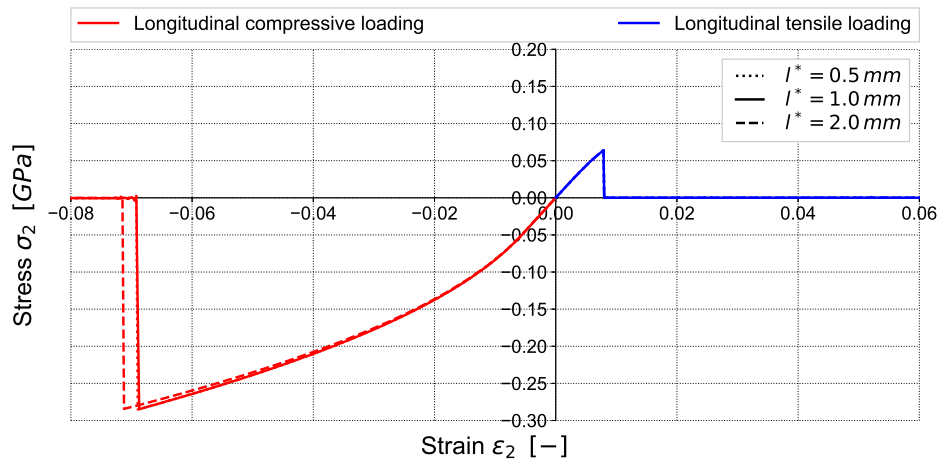
a) Schematic presentation of the 2.0 mm x 2.0 mm specimen discretised with varying characteristic lengths - Longitudinal loading
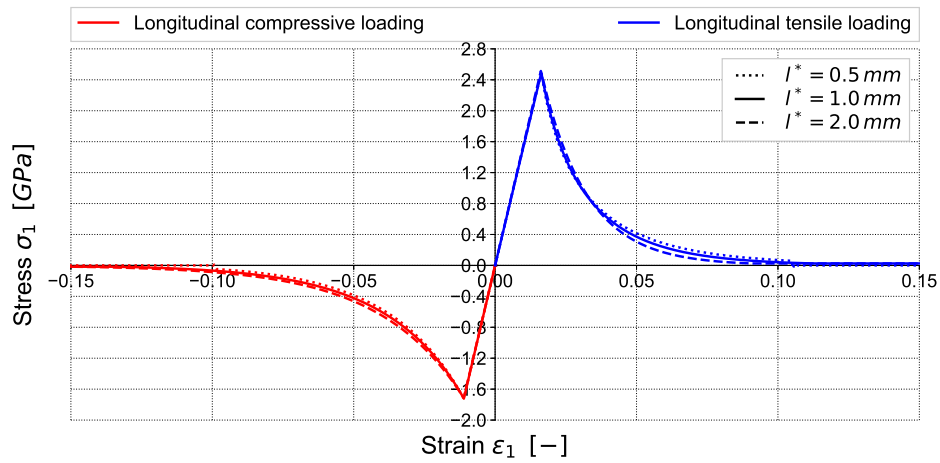
b) Longitudinal Stress-strain characteristics with varying discretisation. The implemented crack band theory results in mesh-independent stress-strain characteristics


c) Schematic presentation of the 2.0 mm x 2.0 mm specimen discretised with varying characteristic lengths - Transverse loading
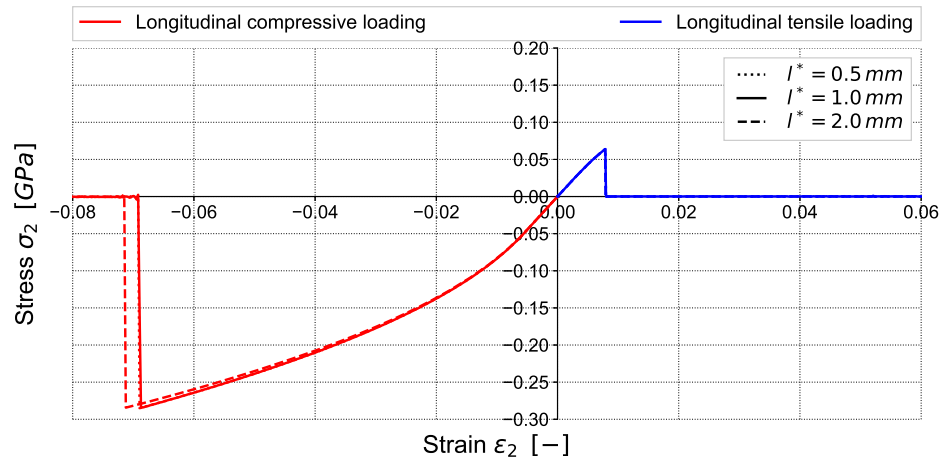

d) Transverse stress-strain characteristics with varying discretisation

Figure 4.6: Stress-strain characteristics of a 2.0 mm x 2.0 mm specimen with element sizes ranging from 0.5 mm to 2.0 mm under tension and compression. Material properties of IM7/8552 US-Version
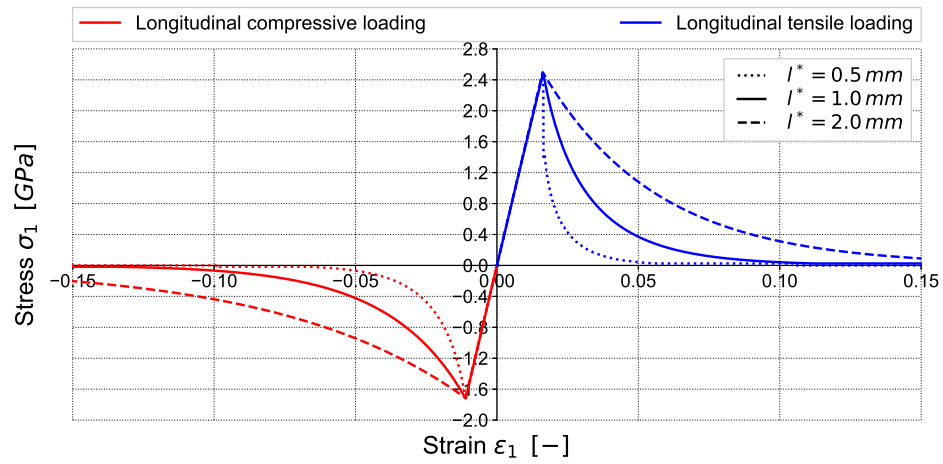
a) Longitudinal Stress-strain characteristics

b) Transverse Stress-strain characteristics

Figure 4.7: Stress-strain characteristics of a 2.0 mm x 2.0 mm specimen with element sizes ranging from 0.5 mm to 2.0 mm under tension and compression. Disabling the crack band scaling of the fracture energy results in mesh-dependent stress-strain characteristics in longitudinal direction. Material properties of IM7/8552 US-Version

in stress levels of 20% to 80% of the tensile/compressive strength. For the material properties of IM7/8552 US, this results in stress levels ranging from $0.5\,GPa$ to $2.0\,GPa$ in tension and $0.34\,GPa$ to $1.37\,GPa$ in compression. In order to assure the same fracture energy densities for each residual stress level, the elimination strains are set to the saturation strains defined in Equation (4.13). With increasing residual stress plateau, the saturation strains decrease and the fracture energy densities correspond to the fibre fracture energies from the material input. The physical meaning of the stress plateau can be interpreted as the resistance of damaged material in the crush front.

Linear-softening with residual stress is shown in Figure 4.8 c). Damage evolution follows the linear softening as shown in Figure 4.8 a). When the stress corresponding to $soft \cdot X_{T/C}$ is reached on the softening slope, the stress level is kept constant until the saturation strain as defined in Equation (4.11) is met and the element is eroded from the numerical mesh. The same values of $soft$ are used for the stress plateaus in Figure 4.8 b) and c). However, the saturation strains are significantly lower for the linear softening with residual stress compared to the brittle failure approach. This is seen especially for the configuration $soft = 0.2$ in both tensile and compressive loading with $\varepsilon_{sat}^{T} = 0.09$, $\varepsilon_{sat}^{C} = 0.13$ versus $\varepsilon_{sat}^{T} = 0.22$, $\varepsilon_{sat}^{C} = 0.33$ in the brittle failure approach.

The different fibre softening approaches have no influence on the matrix behaviour under transverse loading. The evolution of the damage parameters of the different softening options are presented in Appendix B.3.

4.5 Conclusion of Numerical Modelling of Composite Materials

A plane-stress, meso-scale material model in the framework of continuum damage mechanics was implemented as an explicit user-material in the commercial FEA code Abaqus/Explicit. The material model ABQ_DLR_UD describes the behaviour of the fibre and matrix which govern the behaviour in longitudinal and transverse direction of the elementary ply. Fibre damage is based on fracture mechanics with a maximum stress criterion and damage evolution based on fibre fracture energies. The crack band method is implemented to scale the fracture energy densities and assure that the same amount of energy dissipates in the damage process independent of the element size. Beneath exponential softening, additional strain-softening approaches also based on fibre fracture energies were implemented in the material model and contain linear softening, brittle failure with residual stress and linear softening with residual stress where the stress levels are a fraction of the fibre strengths. Material behaviour of the matrix is based on the theory proposed by Ladevèze and LeDantec [108] where coupled energy release rates under tension and shear govern the damage behaviour. Plasticity in terms of permanent transverse and shear strains is active in the model. A maximum stress failure criterion was implemented for transverse compressive behaviour. The material model was verified on singe-element simulations. From this, the following conclusions are drawn:
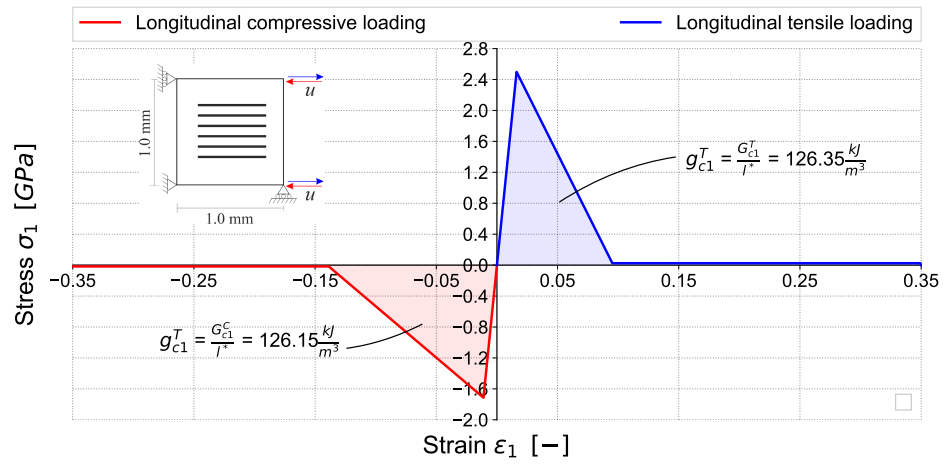
a) Linear softening
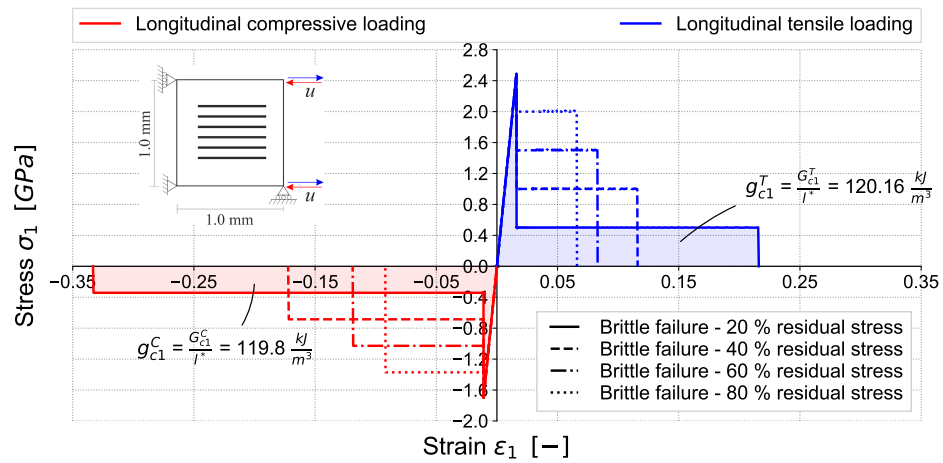
b) Brittle failure with residual stress
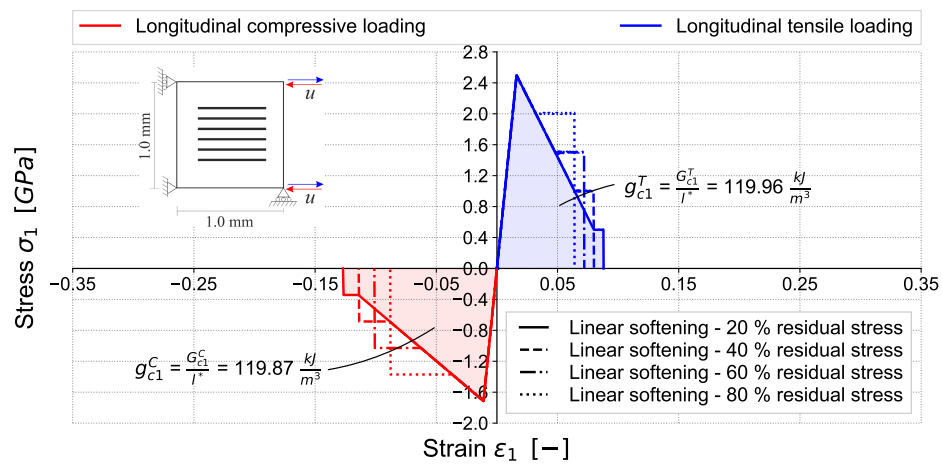
c) Linear softening with residual stress

Figure 4.8: Single-element simulation - Stress-strain characteristic of a) linear softening, b) brittle failure with residual stress c) linear softening with residual stress; Material properties of IM7/8552 US-Version

- Simulations with both material versions of IM7/8552 showed no significant differences in longitudinal direction. In transverse direction however, the higher transverse compressive strength of the IM7/8552 US-Version resulted in significant higher transverse compressive failure strain. This was due to plasticity in transverse direction which resulted in higher non-linearity in the stress-strain curve and a higher strain at maximum stress. This showed that the transverse compressive strength has a substantial influence on the material response whereas deviations of other material properties in a typical range of material characterization are negligible.

- Both the element size and fibre fracture energy scale the longitudinal stress-strain curve due to the implemented crack band theory. Simulations of a quadratic tension/compression UD specimen discretized with different element sizes showed identical stress strain curves in longitudinal and transverse loading with active crack band scaling in the model. With disabled crack band scaling, the results became sensitive on the element size. This showed that the crack band method has to be used in order to obtain mesh size insensitive results on this level of the building block.

- Single-element simulations with different strain-softening options verified that the implemented softening options obtained the same fibre fracture energies.

5 Behaviour at the Laminate Level

The simulation of multi-layered, single-shell elements of composite laminates is defined as the fundamental level of the building block approach. A quasi-isotropic laminate with stacking sequence $[90/45/0/-45]_{4s}$ is investigated in this chapter. The laminate on this level of the building block is identical to the one considered on the subsequent level of fracture mechanic tests. Aim of the single-laminate element simulations presented in this chapter is the verification of the meso-scale modelling approach on the macro-scale laminate level and investigating the laminate behaviour determined from ply-based input. At this basic level of the building block, meso-scale damage models at the ply-level, like ABQ_DLR_UD, can be compared with macro-scale damage models which model the laminate as a homogeneous material.

For the single-laminate element simulations, both material input data sets are used and show the influence of varying IM7/8552 material parameters and the robustness of the material model on the macro-scale laminate level. Simulations with uni-axial strain are compared to uni-axial stress and show the effects of boundary conditions which become relevant in meso-scale modelling. The influence of element size and fibre softening options on the laminate level is presented as well.

5.1 Single-Element Simulations at the Laminate Level

This fundamental study investigates the stress-strain relation of a quasi-isotropic $[90/45/0/-45]_{4s}$ laminate under uni-axial tension and compression. The $1.0\,mm$ x $1.0\,mm$ multi-layered shell element is build up on ply-level with unidirectional material input data at the through-thickness section points. The fibre orientation of the individual plies are defined at the section points and each ply of the laminate is modelled with three section points. A nominal ply thickness of $0.125\,mm$ (laminate thickness: $4\,mm$) is defined at the section definition. Material input at ply-level is identical to in Chapter 4. The load is applied with a velocity boundary condition and a constant velocity of $1.0\,\frac{m}{s}$.

5.1.1 Comparison of Material Input Data of IM7/8552 - Influence on Laminate Level

Material input data of both IM7/8552 material versions (as shown in Table 3.1) are used. The stress-strain characteristics are compared to show the influence of the material input data on the laminate level. The fibre fracture energies in tension and compression are $G_{c1}^T = G_{c1}^C = 120\,\frac{kJ}{m^2}$.

Figure 5.1 a) presents the tensile and compressive stress-strain relations. In addition, Figure 5.1 b) and c) show the ply-based damage evolution in the fibre and matrix direction predicted by ABQ_DLR_UD. At first, the results of tensile loading are discussed shown on the right of Figure 5.1 b) and c). Afterwards, the results of compressive loading shown on the left of Figure 5.1 b) and c). Under tensile loading, the overall response of the single-laminate element is about equal for both material data sets. The stress-strain characteristics behave linear up to the ultimate strength which is predicted as $895\,MPa$. Each kink in the stress strain curve of the laminate is related to damage initiation or damage saturation in one of the individual plies as shown in the evolution of damage parameters in Figure 5.1 b) and c). Matrix tensile failure initiates in the $90°$ plies soon after load application with ultimate failure strain of ~ 0.009 as shown on the right of Figure 5.1 b) and c). However, matrix failure of the $90°$ plies shows no visible influence on the stress-strain characteristic. At the point of maximum stress, fibre damage initiates in the $0°$ plies as shown in Figure 5.1 b) and c). Evolution of fibre damage is equal for both material data sets which is the same tendency identified for UD single-elements in Section 4.2.4. A cascade is identified at a strain of 0.02 due to ultimate matrix damage in the $\pm45°$ plies. A plateau of constant stress follows until fibre compressive damage initiates in the $90°$ plies due to lateral contraction of the element. With reducing stiffness of the laminate due to damage in the $90°$ plies, lateral contraction increases and the load is redistributed in the remaining plies of the laminate. This results in transverse compressive loading of the $0°$ plies until ultimate compressive failure of the matrix occurs at a strain of 0.054 for IM7/8552 EU, see Figure 5.1 b). Due to a higher transverse compressive strength of IM7/8552 US, ultimate transverse compressive failure of the $0°$ plies takes place at a higher strain of 0.088, see Figure 5.1 c). The effect of a higher transverse compressive strength is discussed in Section 4.2.4 on basis of single-UD elements. Afterwards, the $0°$ and $90°$ plies carry the load until ultimate fibre failure is reached. The overall fracture energy of the laminate of unit length can be determined by calculating the area under the stress-strain curves. The predicted tensile laminate fracture energies for IM7/8552 EU and US are $63.07\,\frac{kJ}{m^2}$ and $64.87\,\frac{kJ}{m^2}$, respectively. This is a deviation of 3% and shows that the differences in the material input parameters of the IM7/8552 material versions are small in tensile loading on laminate level.

Under compressive loading, similar effects can be identified in the stress-strain characteristics. Each kink in the stress-strain characteristic of the single-laminate simulation can be clearly linked to damage initiation or ultimate damage in one of the individual plies. The stress-strain curve is linear up to $\sim 650\,MPa$ compressive stress for both material versions. At this stress, compressive fibre damage initiates in the $0°$ plies, see Figure 5.1 b) and c). Ultimate compressive strength of the laminate is predicted as $869\,MPa$. The maximum compressive strength coincides with the onset of fibre compressive damage in the $\pm45°$ plies. For IM7/8552 EU, this is combined with ultimate matrix compressive failure in the $90°$ plies at a strain of 0.035. This is shown in a kink of the stress strain curve, see Figure 5.1 b). This is followed by ultimate matrix compressive failure of the $\pm45°$ plies at a strain of 0.076. Same as in tensile loading outlined in the previous paragraph, the different transverse compressive strengths are identified as the main reason for differences in the
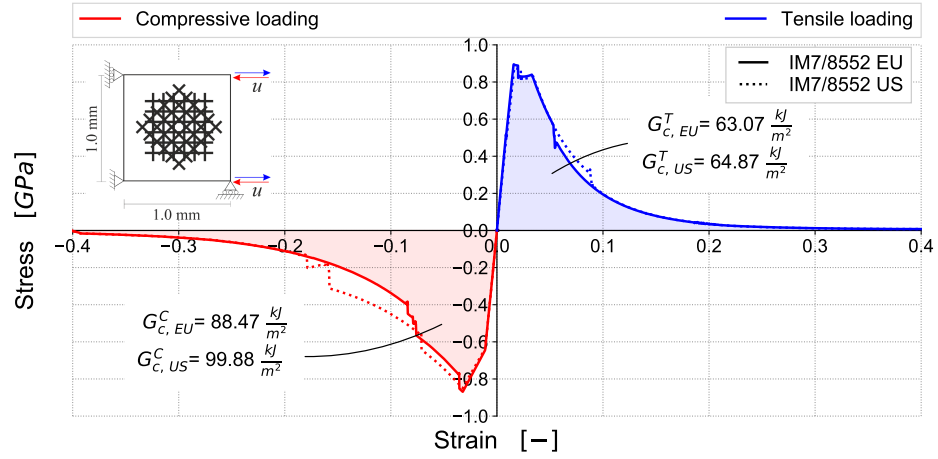
a) Tensile and compressive stress-strain characteristic
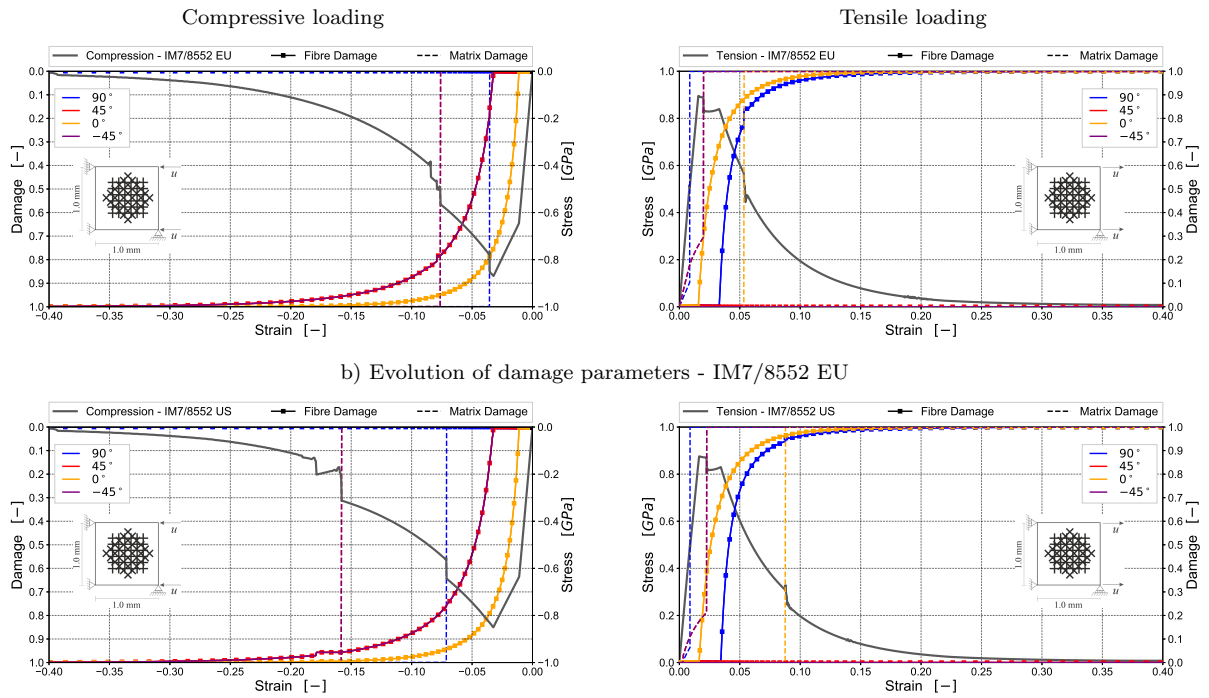
b) Evolution of damage parameters - IM7/8552 EU
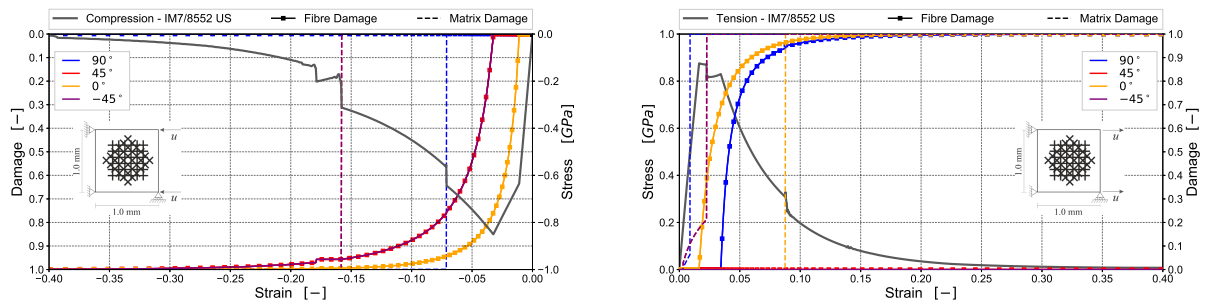
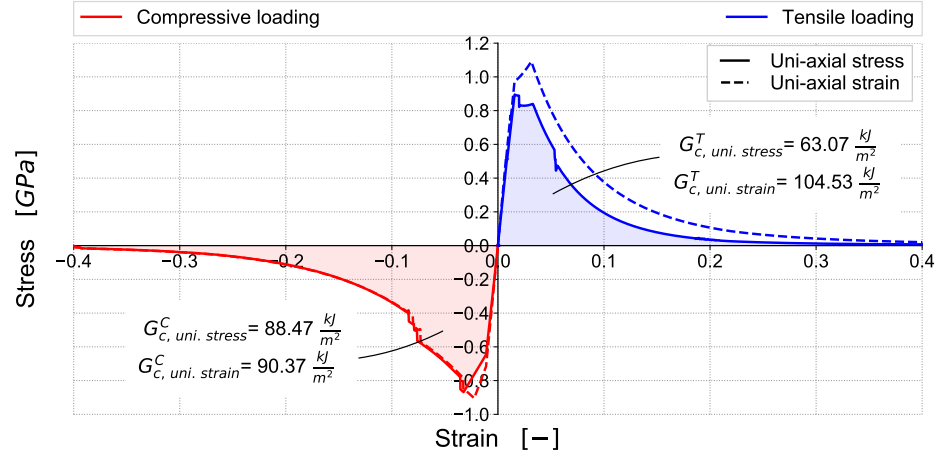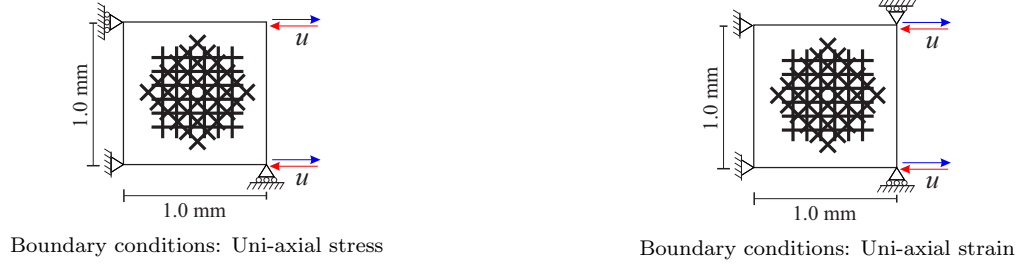c) Evolution of damage parameters - IM7/8552 US

Figure 5.1: Tensile and compressive loading of $1.0\,mm$ x $1.0\,mm$ single-laminate element with layup $[90/45/0/-45]_{4s}$ under uni-axial stress; a) Stress-Strain characteristics; Evolution of damage parameters in the individual plies, b) IM7/8552 EU-Version, c) IM7/8552 US-Version
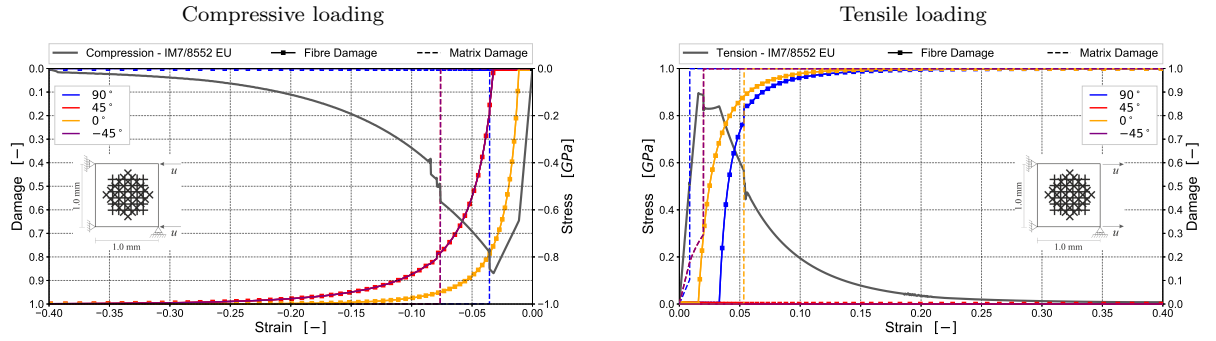
stress-strain curves of the EU and US-Version of IM7/8552. Ultimate matrix compressive failure of the 90° and ±45° plies of IM7/8552 US is predicted by ABQ_DLR_UD at strains of 0.071 and 0.158, as shown in Figure 5.1 c). This is twice the ultimate strains in these plies compared to the predictions for the EU-Version of IM7/8552. This means, that the contribution of the 90° and ±45° plies to the overall energy absorption of the laminate is higher. The effect of an increased transverse compressive strength on the overall response of the laminate is reflected in the predicted laminate fracture energy. For the EU-Version of IM7/8552, a compressive laminate fracture energy of $G_{c,EU}^C = 88.47 \frac{kJ}{m^2}$ is predicted. For IM7/8552 US, the laminate compressive fracture energy is $G_{c,US}^C = 99.88 \frac{kJ}{m^2}$ which is an increase of 12%. Contrary to tensile loading, the material input data of the IM7/8552 material versions and especially the transverse compressive strength show an influence on the overall laminate response. The simulations in the further course of this chapter are based on the material data IM7/8552 EU.

5.1.2 Influence of Boundary Conditions - Uni-axial Strain vs. Uni-axial Stress

To investigate the influence of boundary conditions on the single-laminate element level, simulations with boundary conditions representing uni-axial stress are compared to uni-axial strain. In uni-axial stress, the nodes are fixed in a way that the element can freely deform longitudinally in load direction and transversely due to lateral contraction and the stress tensor is oriented in the loading direction. In uni-axial strain, the nodes are fixed to suppress lateral contraction which results in lateral stresses and the strain tensor is oriented in load direction. The influence of these boundary conditions on the stress-strain characteristic of the laminate is presented in Figure 5.2. The stress-strain characteristics in Figure 5.2 b) are identical to Figure 5.1 b) and shown here for comparability. Under tensile loading, the boundary conditions show a significant influence on the stress-strain characteristic of the laminate. The effects of an uni-axial strain boundary condition are identified in an increased ultimate laminate strength and a higher ultimate failure strain of the laminate. This results in a significantly increased laminate fracture energy. Ultimate laminate strength in uni-axial strain is $1090.8\,MPa$ and 29% higher compared to uni-axial stress. The predicted tensile laminate fracture energy under uni-axial strain is $G_{c,\,uni.\,strain}^T = 104.53 \frac{kJ}{m^2}$. This is an increase of 65.7% compared to the predicted laminate fracture energy in uni-axial stress. The reason for this increase in laminate fracture energy is identified in the damage behaviour of the 90° and ±45° plies. The damage evolution of the individual plies for uni-axial stress and uni-axial strain is shown in Figure 5.2 b) and c), respectively. In the laminate with stacking sequence $[90/45/0/-45]_{4s}$ the percentage of 0°, ±45° and 90° plies is 25%, 50% and 25%, respectively. In uni-axial stress, the load carried by the fibres of the ±45° plies is less than the fibre tensile strength. This is shown as no fibre damage initiates in the ±45° plies throughout the load history. Therefore, the fibres in the ±45° plies, as the main load carrying constituent of the ply, do not contribute to the predicted overall fracture energy of the laminate. Only the matrix contribute to the overall stress-strain behaviour of the laminate. This is shown as ultimate matrix failure in these plies

Boundary conditions: Uni-axial stress

Boundary conditions: Uni-axial strain

a) Tensile and compressive stress-strain characteristic

Compressive loading   Tensile loading

b) Evolution of damage parameters - Uni-axial stress
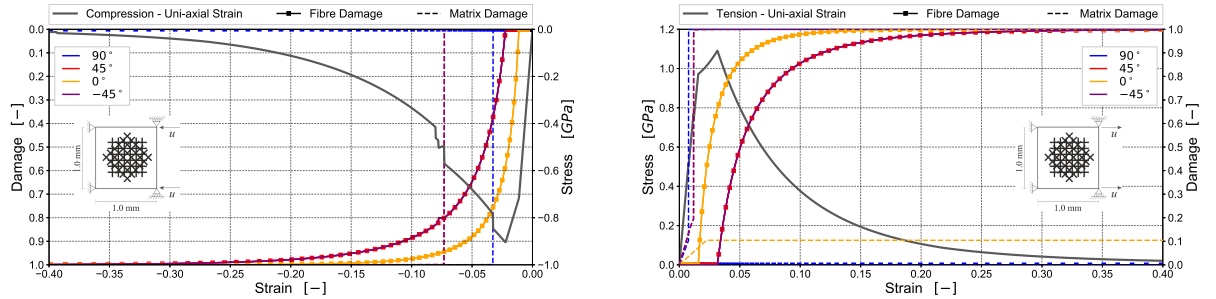
c) Evolution of damage parameters - Uni-axial strain

Figure 5.2: Tensile and compressive loading of $1.0\,mm$ x $1.0\,mm$ single-laminate element; a)Stress-Strain characteristics; Evolution of damage parameters in the individual plies, b) boundary condition of uni-axial stress, c) boundary condition of uni-axial strain; IM7/8552 EU

results in a distinct response in the stress-strain characteristic, see Figure 5.2 b). For uni-axial strain, Figure 5.2 c) shows that after fibre tensile damage initiates in the 0° plies, resulting in the first kink in the stress-strain curve, the stress further increases up to the ultimate strength of the laminate. Reaching the ultimate strength coincides with initiation of fibre tensile damage in the ±45° plies. On the other hand, no fibre compressive damage initiates in the 90° plies. However, the contribution of the ±45° plies to the overall stress strain response and fracture energy of the laminate is higher.

Under compressive loading, the effects of the boundary condition are less distinctive. Loading in uni-axial strain results in a slightly higher ultimate strength of $904.4\,MPa$ (+4% compared to uni-axial strain) and therefore a higher predicted compressive fracture energy of $G^C_{c,\,uni.\,strain} = 90.37\,\frac{kJ}{m^2}$ (+2% compared to uni-axial stress). The reason for the higher ultimate compressive strength is again identified in the ±45° plies. Up to the initiation of fibre compressive damage in the 0° plies, the stress-strain curves are identical for both boundary conditions. In uni-axial strain, fibre damage in the ±45° plies initiates at a lower strain of 0.0224 compared to 0.032 in uni-axial stress. This shows that the contribution of the ±45° plies to the overall load carrying capacity of the laminate is higher in uni-axial strain than in uni-axial stress. However, compared to tensile loading, this effect is less distinctive and the influence of boundary condition is negligible in compressive loading.

From the investigation of boundary conditions, it is concluded that an distinctive influence on the predicted laminate fracture energy is shown under tensile loading. Therefore, the boundary conditions have to be considered when the predicted laminate fracture energies are compared to experimentally determined fracture energies or the numerical results of different damage models or modelling approaches are compared. Moving up the building block approach, it is assumed that the behaviour of elements which are embedded and surrounded by other elements rather corresponds to uni-axial strain than uni-axial stress. Therefore, uni-axial strain is considered in the further course of this chapter.

5.2 Influence of Element Size and Fibre Fracture Energy on Laminate Level

Purpose of this section is the investigation of element size effects and the influence of fibre fracture energy on laminate level. In UD single-element simulations in Section 4.3, both element size and fibre fracture energy showed an influence on the stress-strain characteristic due to the implemented crack band approach for fibre damage in ABQ_DLR_UD. In how far this influences are also effective on the laminate level is investigated in this chapter.

5.2.1 Element Size Effects

To investigate the influence of element size on laminate level, single-laminate elements with characteristic lengths of $l^* = 0.5\,mm, 1.0\,mm$ and $2.0\,mm$ are loaded in tension and compression in uni-axial strain. The stress-strain characteristics are shown in Figure 5.3. Under both tensile and compressive loading, the predicted laminate fracture energy as the area under the stress-strain curve reduces with increasing characteristic length. This is the same effect as seen in UD single-element simulations in Figure 4.5. Due to the crack band scaling approach in fibre damage evolution, the input of fibre fracture energy is scaled to the element size. The ultimate tensile strength of the laminate reduces with increasing element length. From $1195\,MPa$ for $l^* = 0.5\,mm$ and $1090\,MPa$ for $l^* = 1.0\,mm$ to $971\,MPa$ for $l^* = 2.0\,mm$. The point of the characteristic kink after the initial linear slope in the stress-strain curve, representing damage initiation in the $0°$ plies, does not change with element size due to the maximum stress based damage initiation in fibre direction which is independent of the element size. However, after damage initiates in the $0°$ plies, fibre damage evolution is dependent on the element size. This means that with increasing element size, fibre damage grows faster and the strain-softening slope is steeper (see Figure 4.5). Transferred to laminate level, higher damage evolution in the $0°$ plies results in reduced laminate stiffness and therefore reduced ultimate strength of the laminate. A reduced ultimate strength with increasing element size is also identified in compressive loading. However, the effect is less distinctive compared to tensile loading. The difference of the damage initiation strains in the $0°$ and $\pm 45°$ plies is less. Therefore the distance from the damage initiation kink (indicating fibre damage initiation in the $0°$ plies) to ultimate compressive strength (initiation of fibre damage in the $\pm 45°$ plies) in the stress-strain characteristic. However, in uni-axial stress, the effect of increasing ultimate strength with reducing element size would be more distinctive due to the higher strain difference of fibre damage initiation in the $0°$ and $\pm 45°$ plies (see Figure 5.2). After reaching the ultimate compressive strength, the laminate behaviour is governed by fibre damage in the $0°$ and $\pm 45°$ plies. Due to the crack band approach, the fracture energy densities in tension and compression are higher for smaller elements resulting in higher stress level and higher laminate fracture energies. The predicted laminate fracture energies in tension are $G_c^T = 49.61\,\frac{kJ}{m^2}$ for $l^* = 2.0\,mm$, $G_c^T = 104.53\,\frac{kJ}{m^2}$ for $l^* = 1.0\,mm$ and $G_c^T = 220.14\,\frac{kJ}{m^2}$ for $l^* = 0.5\,mm$. The compressive laminate fracture energies are $G_c^C = 51.27\,\frac{kJ}{m^2}$ for $l^* = 2.0\,mm$, $G_c^C = 90.37\,\frac{kJ}{m^2}$ for $l^* = 1.0\,mm$ and $G_c^C = 155.57\,\frac{kJ}{m^2}$ for $l^* = 2.0\,mm$. This shows that the laminate fracture energies are scaled with a factor of 2.1 for tensile loading and 1.7 for compressive loading with reducing element size. Analogous to the investigation on single-element level shown in Figure 4.6, a quadratic 2.0 mm x 2.0 mm tension/compression specimen is discretised with single-laminate elements of characteristic lengths ranging from $l^* = 0.5\,mm$ to $l^* = 2\,mm$, see Figure 5.4 a). The stress-strain characteristics under tension and compression are shown in Figure 5.4 b). Under tensile loading, an influence of the discretisation on the ultimate strength of the specimen is identified. With increasing element size, the ultimate strength reduces. This is due to the effects described above. However, the strain softening slopes are nearly the same and inde-
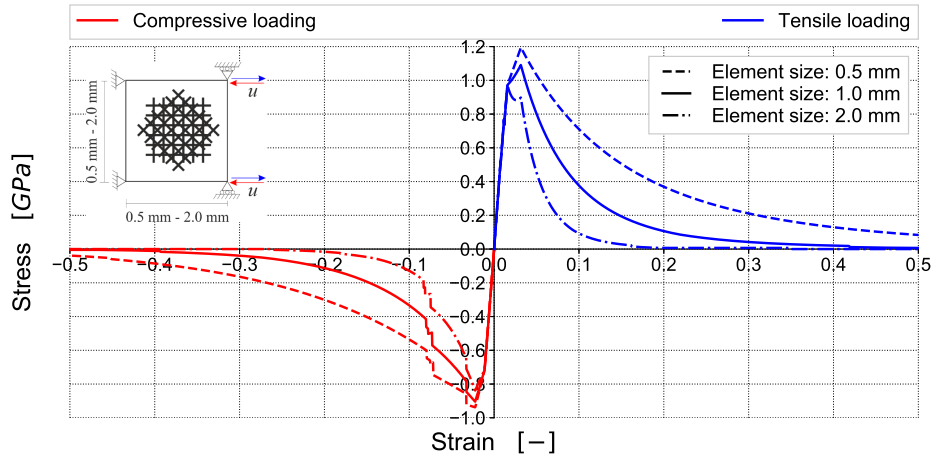
Figure 5.3: Single-element simulation - Stress-strain characteristic under tensile and compressive loading. Influence of element size. Material properties of IM7/8552 EU-Version

pendent of the discretisation. The predicted laminate tensile fracture energies are $G_c^T = 49.61 \frac{kJ}{m^2}$ for $l^* = 2.0\,mm$, $G_c^T = 55.83\,\frac{kJ}{m^2}$ for $l^* = 1.0\,mm$ and $G_c^T = 59.8\,\frac{kJ}{m^2}$ for $l^* = 0.5\,mm$. In compressive loading, the effects resulting in higher ultimate compressive strength on single-laminate level as described above show only minor influence on the compression specimen. However, an influence of the discretisation is identified in the strain-softening slope. The kink which correlates with matrix compressive failure in the $\pm45°$ plies (see Figure 5.2 c)) is shifted to higher strains with increasing element size. Since matrix compressive damage is governed by a maximum stress criterion, it is concluded that the transverse stresses in the $\pm45°$ plies reduce with increasing element size. The predicted compressive laminate fracture energies are $G_c^C = 51.27\,\frac{kJ}{m^2}$ for $l^* = 2.0\,mm$, $G_c^C = 46.95\,\frac{kJ}{m^2}$ for $l^* = 1.0\,mm$ and $G_c^C = 41.52\,\frac{kJ}{m^2}$ for $l^* = 0.5\,mm$. Contrary to tensile loading, the fracture energy of the specimen increases with increasing element size. This shows that under compressive loading, the matrix behaviour has an influence on the overall response of the laminate. These effects are due to the meso-scale modelling approach of the laminate. In a macro-scale modelling approach it is expected that these effects, especially the increased ultimate laminate strength, do not occur. This has to be kept in mind when comparing the results obtained from meso- and macro-scale models. However, it is reasoned that this is the result of modelling the specimen with multiple elements rather than a mesh size dependency in the damage model since the stress-strain curves are scaled equally in single-laminate element simulations with varying element size. The effects without crack band scaling are shown in Figure 5.4 c). As described in the single-element studies in Section 4.3, the crack band method is disabled by scaling the fracture energies that the fracture energy densities of different element sizes corresponds to the value of $l^* = 1.0\,mm$. Contrary to the effects described above, it is shown that the ultimate strength of the laminate is the same for different element sizes whereas the post-peak slope reduces with the element size under both tensile and compressive loading.
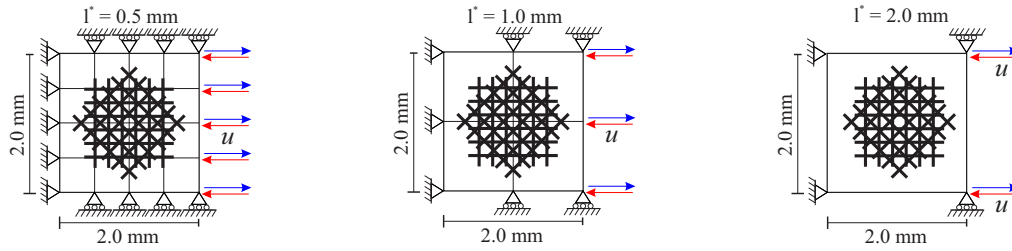
a) Schematic presentation of the 2.0 mm x 2.0 mm specimen discretised with single-laminate elements with varying characteristic lengths loaded in uni-axial strain
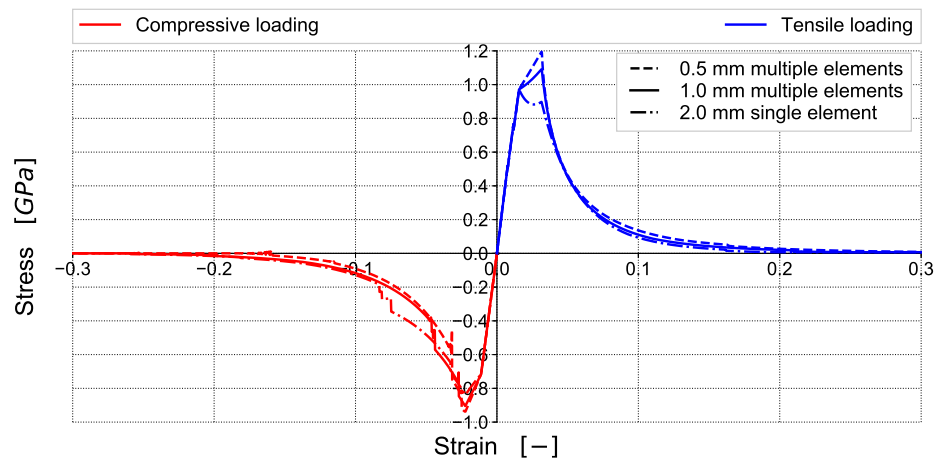
b) Laminate stress-strain characteristics with varying discretisation
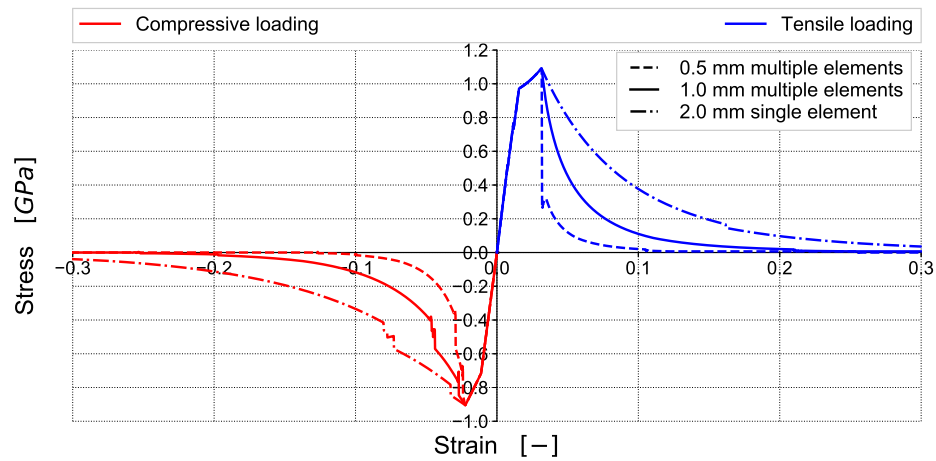
c) Laminate stress-strain characteristics with varying discretisation - Crack band scaling of the fracture energy disabled

Figure 5.4: Stress-strain characteristics of a $2.0\,mm$ x $2.0\,mm$ specimen with stacking sequence $[90/45/0/-45]_{4s}$ with element sizes ranging from 0.5 mm to 2.0 mm under tension and compression

5.2.2 Influence of Fibre Fracture Energy

To investigate the influence of fibre fracture energies on the response of the laminate, tensile and compressive fibre fracture energies are varied in a range reported in literature for material IM7/8552 (see Section 3.1.1) between $G_{c1}^{T/C} = 60 - 160 \frac{kJ}{m^2}$. The stress-strain characteristics of single-laminate element simulation with varying fibre fracture energies in uni-axial strain are shown in Figure 5.5. It is shown that the effects of increasing fibre fracture energies are the same as for reducing element size. The reason is that both the fibre fracture energy and characteristic length scale the fracture energy density which governs fibre damage evolution as discussed in Section 4.3 and shown in Figure 4.5. In tensile loading, the ultimate tensile strength of the laminate increases with increasing fibre fracture energy. Due to a reduced fibre damage evolution with increasing fracture energy, the stiffness reduction in the 0° plies is lower. The ultimate tensile strength ranges from $971\, MPa$ for $G_{c1}^T = 60 \frac{kJ}{m^2}$ to $1142\, MPa$ for $G_{c1}^T = 160 \frac{kJ}{m^2}$. The ultimate tensile strength for $G_{c1}^T = 60 \frac{kJ}{m^2}$ is the same as the value determined for a characteristic element length $l^* = 2.0\, mm$, this shows that both the fibre fracture energy and characteristic length equally scale the ultimate tensile strength by scaling the fracture energy density in fibre direction. The same effect is identified in compressive loading. However, the increase in ultimate compressive strength with increasing fibre compressive energy is less distinctive compared to tensile loading. This is the same effect as identified and discussed for the influence of element size.

Due to the increased fracture energy density with increasing fibre fracture energy which mostly affects the behaviour of the 0° and ±45° plies, the total laminate fracture energy increases equally. This is shown in Figure 5.6. The laminate fracture energies increase linearly from $G_c^T = 55.74 \frac{kJ}{m^2}$, $G_c^C = 53.29 \frac{kJ}{m^2}$ for $G_{c1}^{T/C} = 60 \frac{kJ}{m^2}$ to $G_c^T = 139.14 \frac{kJ}{m^2}$, $G_c^C = 113.09 \frac{kJ}{m^2}$ for $G_{c1}^{T/C} = 160 \frac{kJ}{m^2}$. Zobeiry [154] and Zobeiry et al. [155] determined the fracture energies for the same laminate as $G_f^T = 90.4 - 125.6 \frac{kJ}{m^2}$ and $G_f^C = 85 \frac{kJ}{m^2}$. On single-laminate level, these laminate fracture energies are predicted for fibre fracture energies in the range of $G_{c1}^{T/C} = 100 - 120 \frac{kJ}{m^2}$

5.3 Influence of Fibre Softening Options

This section presents the influence of different fibre softening options on laminate level. Fibre damage evolution in the individual plies follows the stress strain characteristics of linear softening, brittle failure with residual stress and linear softening with residual stress as discussed in Section 4.4 and shown in Figure 4.8. The input of fibre fracture energy is $G_{c1}^{T/C} = 120 \frac{kJ}{m^2}$ for all softening options and the characteristic length of the single-laminate element is $l^* = 1.0\, mm$. The boundary condition is uni-axial strain. For comparison of results obtained with the baseline exponential softening, the reader is referred to the previous sections, in particular the stress-strain characteristic shown in Figure 5.2 a). The stress-strain characteristics of the additional softening options are shown in Figure 5.7. The reader is also referred to Appendix C.1. Here, the evolution of damage
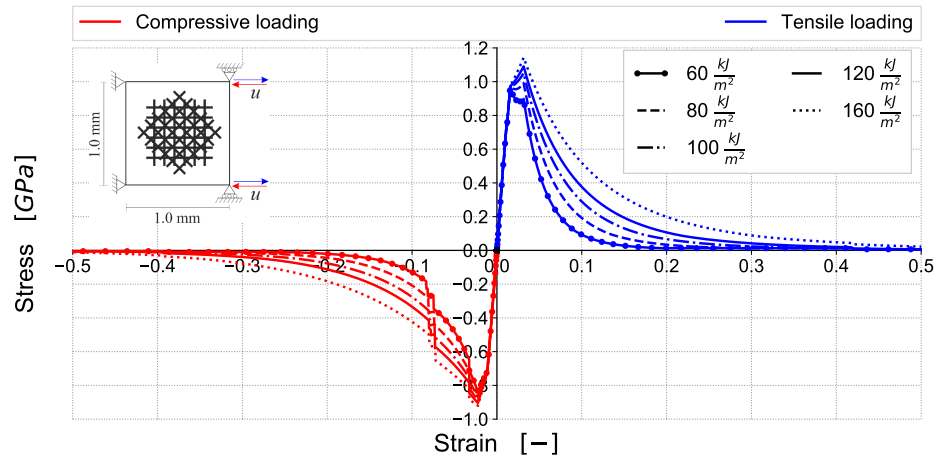
Figure 5.5: Single-element simulation - Stress-strain characteristic of tensile and compressive loading. Influence of fibre fracture energies on the stress-strain characteristic of the laminate with layup $[90/45/0/-45]_{4s}$. Material properties of IM7/8552 EU-Version
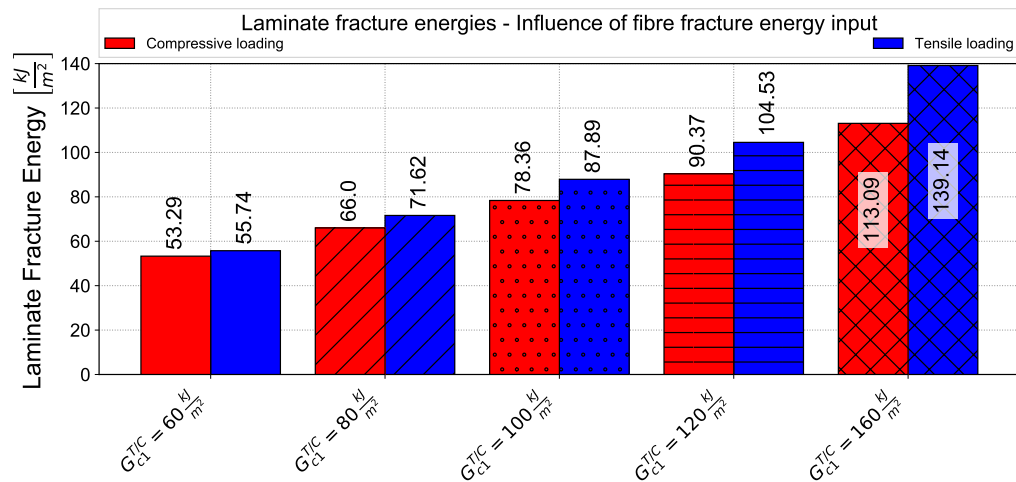

Figure 5.6: Single-element simulation - Predicted laminate fracture energies under tensile and compressive loading of the laminate with layup $[90/45/0/-45]_{4s}$. Influence of fibre fracture energy. Material properties of IM7/8552 EU-Version

in the individual plies is shown for the three softening options.

The response of the laminate for **linear softening** in the fibre direction of the individual plies is shown in terms of tensile and compressive stress-strain characteristics in Figure 5.7 a). Under both tensile and compressive loading, each kink in the stress-strain curve is related to damage initiation or damage saturation in one of the individual plies, whereas the first kink in the stress strain curve is associated with fibre damage initiation in the 0° plies, as previously discussed. Fibre damage initiation is independent of the softening option. Therefore, the strain of the first kink in the stress-strain curve does not change with the softening option and has a value of ∼ 0.016. Up to this strain, the response is independent of the fibre softening option. The slope of the subsequent linear section and the ultimate strength of the laminate is governed by damage evolution in the 0° plies and therefore influenced by the softening option, as previously discussed. The ultimate tensile strength for linear softening is 1172.5 MPa which is slightly higher compared to exponential softening (1090.8 MPa). This result was also reported by Zobeiry [154] for a laminate with the same layup ($[90/45/0/-45]_{4s}$). This effect will be further discussed in Section 6.2.3. After reaching the point of ultimate strength, a bi-linear strain-softening up to ultimate failure of the single-laminate element is shown. The kink at a strain of 0.1 is associated with damage saturation in the 0° plies (see also Figure C.1). The basic findings and effects of the fibre softening option in tension are also valid in compression. The ultimate compressive strength for linear softening is 934.7 MPa compared to 904.4 MPa for exponential softening. During strain-softening, the segments are linear rather than exponential. The predicted laminate fracture energies are shown in Figure 5.8. For both tensile and compressive loading, the fracture energies predicted by linear fibre softening are slightly higher compared to the baseline exponential softening approach. As discussed on single-element level in Section 4.4, the explanation for this is a lower fibre damage saturation strain for linear softening compared to exponential softening in combination with a residual stress plateau of $k \cdot X_{T/C}$ (with $k = 0.01$) until reaching the fibre erosion strain. However, the differences are small (< 4%). The influence of fibre **brittle failure** approach with different residual stress levels in the individual plies on laminate level is shown in Figure 5.7 b). For both tensile and compressive loading a zig-zag behaviour is shown up to ultimate tensile or compressive strength. This is due to the jump in the fibre damage function after fibre damage initiation. The fibre damage variable $d_1^{T/C}$ jumps from zero to a value defined by the selected stress plateau. This results in a sudden stiffness reduction in the 0° plies. Afterwards, part of the load is redistributed among the remaining plies. Since the matrix of the 90° and ±45° plies fails very early in the load history, the load is carried only by the already damaged fibres of the 0° and undamaged fibres of the ±45° plies. After fibre damage initiates in the ±45° plies, another distinctive jump in the stress-strain characteristic is shown. In tension, a residual stress plateau is kept constant until saturation strain is reached in the 0° plies. Afterwards, only the ±45° plies carry the load in the laminate which is indicated by a lower stress plateau until damage saturation in the ±45° plies results in ultimate failure of the laminate. In compression, matrix compressive failure in the 90° and ±45° plies results in additional cascades in the stress-strain characteristic. When only the fibres of the 0° and ±45° plies carry
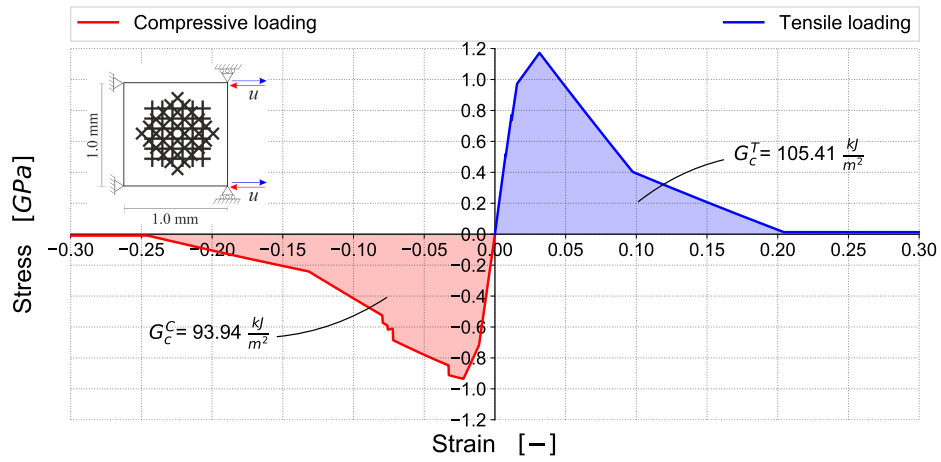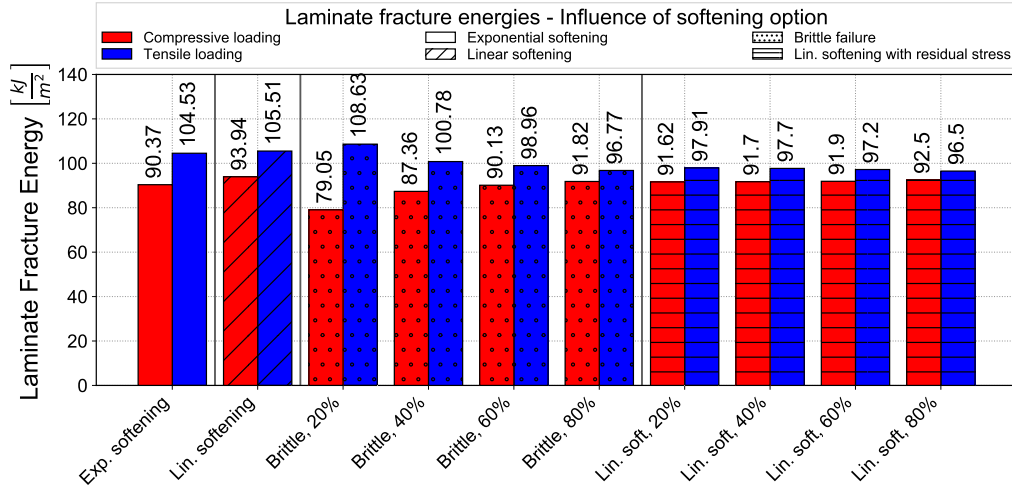
a) Linear softening
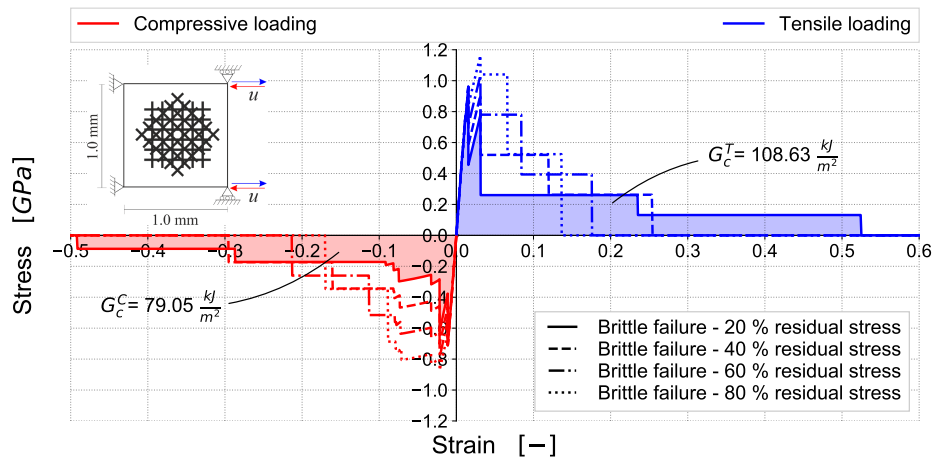
b) Brittle failure with residual stress
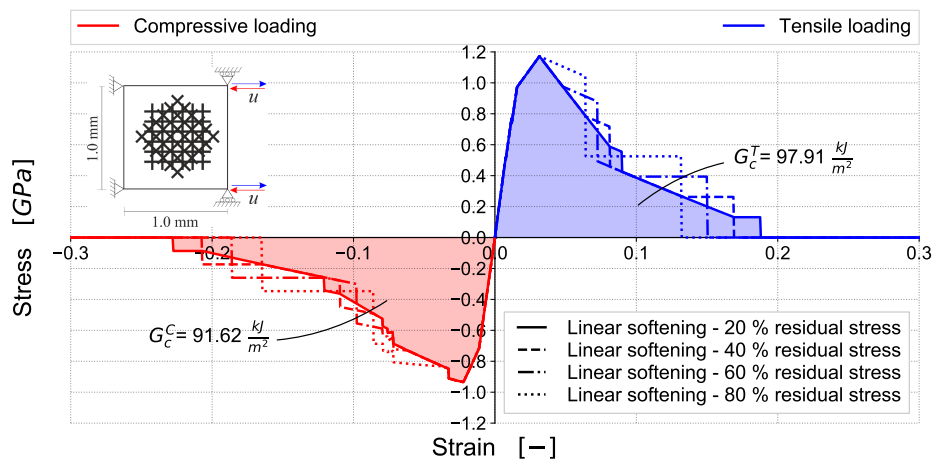
c) Linear softening with residual stress

Figure 5.7: Single-laminate element simulation - Stress-strain characteristic of a) linear softening, b) brittle failure with residual stress c) linear softening with residual stress; Material properties of IM7/8552 EU-Version

Figure 5.8: Predicted laminate fracture energies for different fibre softening options. Material properties of IM7/8552 EU-Version

the load in the laminate, the same behaviour up to ultimate failure as seen in tensile loading is shown. Two main effects of the residual stress levels on the response of the laminate are identified. First, for higher stress levels ($\geq 60\%$ of $X_{T/C}$), the ultimate strength of the laminate increases with the stress plateau and second, the ultimate failure strain reduces with increasing stress plateau. The reason for an increased ultimate strength is reduced fibre damage with increasing stress level. Maximum fibre damage in the $0°$ plies is lower for higher residual stress levels resulting in a higher stiffness of the laminate. Ultimate strength is reached when fibre damage initiates in the $\pm 45°$ plies. Due to lower fibre damage saturation strains for higher stress levels, the ultimate failure strain of the laminate is lower. Contrary effects of the stress level on the laminate fracture energy are identified under tension and compression. As shown in Figure 5.8, the predicted laminate tensile fracture energy of the laminate reduces with increasing residual stress level from $108.36 \frac{kJ}{m^2}$ for 20% to $96.77 \frac{kJ}{m^2}$ for 80% of X_T. In compressive loading on the other hand, the predicted compressive fracture energy increases from $79.05 \frac{kJ}{m^2}$ for 20% to $91.82 \frac{kJ}{m^2}$ for 80% of X_C. Here, the average tensile laminate fracture energy is in range of the predicted energies with exponential and linear softening whereas only the compressive laminate fracture energies of 60% and 80% of X_C are in the range of exponential and linear softening.

The stress-strain characteristics for fibre **linear softening with residual stress** is shown in Figure 5.7 c). It is clearly seen that this softening approach is a combination of linear-softening and brittle failure with residual stress. Up to the ultimate strength in both tension and compression, the laminate shows the same stress-strain characteristic as for linear softening in Figure 5.7 a). This is due to the fact that for the range of residual stresses from 20% to 80% of $X_{T/C}$, the slope of fibre damage evolution is initially the same as in the linear softening approach. After reaching the residual stress level in the $0°$ plies, damage evolution is the same as in the brittle failure approach

described in the previous paragraph. This is shown in the laminate stress-strain characteristic in a shift in the strain-softening slope. Damage is nearly kept constant until the fibre damage saturation strain is reached which results in cascades in the laminate stress-strain characteristic. Two effects are identified for increasing residual stress levels. The ultimate tensile and compressive failure strain is lower and the stress at which the strain-softening slope changes is shifted to lower strains. Also, the constant stress levels in the laminate stress-strain characteristic increase with the residual stress level. The predicted laminate fracture energies are about equal for different residual stress levels for both tension and compression. As shown in Figure 5.8, the predicted tensile fracture energies slightly reduce with increasing residual stress level from $97.91 \frac{kJ}{m^2}$ for 20% to $96.5 \frac{kJ}{m^2}$ for 80% of X_T whereas the compressive fracture energy slightly increases from $91.62 \frac{kJ}{m^2}$ to $92.5 \frac{kJ}{m^2}$. Compared to the baseline exponential softening, the tensile fracture energies are lower whereas the compressive fracture energies are higher. Figure 5.8 shows that a modification in the fibre strain-softening, for example changing the residual stress level, mainly affects the laminate fracture energy when the laminate behaviour after damage initiation is affected by the changes. Linear softening with residual stress shows no significant differences in the predicted laminate fracture energy for a change of the residual stress level from 20% to 80%.

5.4 Summary and Conclusion of Single-laminate Element Simulation

In this chapter, simulations of multi-layered single-laminate elements were carried out to verify the meso-scale damage model on the macro-scale laminate level. A quasi-isotropic laminate with stacking sequence $[90/45/0/-45]_{4s}$ was considered. The single-laminate element was identified as the fundamental level of the building block to compare the numerical results of meso- and macro-scale material models. The following conclusions on laminate level can be drawn:

- The stress-strain characteristic of a quasi-isotropic laminate with stacking sequence $[90/45/0/-45]_{4s}$ under tension and compression is dominated by the fibre behaviour of the $0°$ and $±45°$ plies.

- The influence of material input data for the two versions of IM7/8552 was seen in both tensile and compressive loading of the laminate. The higher transverse compressive strength of the US-Version of IM7/8552 resulted in an increased matrix compressive failure strain in the $0°$ plies in tension and $±45°$ and $90°$ plies in compression.

- A significant influence of the boundary condition on the single-laminate element was identified in tension. Both the predicted ultimate tensile strength (+29%) and fracture energy (+65.7%) of the laminate were significantly higher under uni-axial strain compared to uni-axial stress. The reasons for this were identified mainly in the $±45°$ plies. The fibres of these plies were damaged in uni-axial strain but not in uni-axial stress. This significantly influenced the contribution of these plies to the energy dissipation and fracture energy of the laminate.

From this it is concluded that the boundary conditions play an important role on laminate level and therefore have to be considered when comparing results from different numerical models.

- The influence of the element size on laminate level was identified in increased ultimate strengths and fracture energies under both tensile and compressive loading. This was attributed to the implied crack band scaling on ply level. With increasing element size, fibre damage grows faster which resulted in a reduced stiffness of the 0° plies and therefore lower ultimate strength of the laminate. An identical behaviour in the ±45° plies then resulted in less laminate fracture energy with increasing element size. The discretization of a quadratic 2.0 mm x 2.0 mm tension/compression specimen showed also a reduced ultimate strength with increasing element size but identical post-peak slopes under tension. In compression, the post-peak slopes varied and the predicted laminate fracture energy increased with the element size. This was attributed to matrix compressive failure in the ±45° plies. However, it was reasoned that this is due to modelling of the specimen with multiple elements rather than a mesh dependency in the damage model. When the crack band scaling was disabled, the ultimate strengths were the same for different element sizes. However, distinctive mesh sensitivities were observed in the post-peak stress characteristics and predicted laminate fracture energies. This leads to the conclusion that the crack band scaling of the fracture energy densities on ply level is required to avoid mesh sensitivities on the laminate level.

- Both the ultimate strength and predicted laminate fracture energy increased with the fibre fracture energy in tension and compression. The laminate fracture energy increased linearly due to a higher fracture energy density in the 0° and ±45° plies.

- With the implementation of different fibre softening options in ABQ_DLR_UD it was possible to investigate the influence of strain-softening approaches on the laminate within the same material model. Different fibre softening options at ply level showed a significant influence on the stress-strain characteristic of the laminate. Linear softening, brittle failure with residual stress and linear softening with residual stress influenced the ultimate strength and strain-softening slope of the laminate. The reasons were identified in the damage growth of the fibres. A low fibre damage increment in the 0° plies resulted in a higher ultimate strength. This effect was also identified for increasing residual stress level along with a reduced ultimate failure strain. Compared to exponential fibre softening, linear softening showed a higher ultimate strength and laminate fracture energy. Brittle failure with residual stress resulted in increased ultimate laminate strengths as well as increased compressive and decreased tensile laminate fracture energies with increasing residual stress level. In linear softening with residual stress level, both the ultimate strength and predicted laminate fracture energies did not significantly change with residual stress level.

- The simulations in this chapter were performed on a single quasi-isotropic laminate with

stacking sequence $[90/45/0/-45]_{4s}$. Changing the layup and increasing or reducing the number of $0°$ and $\pm 45°$ plies in the laminate may increase the effects. Increasing the $0°$-plies in the laminate would result in an increased ultimate laminate strength. The stress-strain characteristic of a UD $0°$- laminate, the extreme of this extrapolation, is shown in Figure 4.3 in Section 4.2.4.

6 Numerical Analysis and Validation of Fracture Mechanic Tests

Following the fundamental investigation on single element level in the previous chapters, the simulation of fracture mechanic tests on the coupon level is intended to investigate the global behaviour of the ABQ_DLR_UD damage model and how the findings on single-element level translate into larger scale test cases. Over-height Compact Tension (OCT) specimen [20, 154, 155, 165, 171] and Compact Compression (CC) specimen [154] were found to produce stable and self-similar intralaminar crack growth under tensile and compressive loading, respectively. Experimental data of OCT and CC tests performed on the EU-Version of IM7/8552 published by Zobeiry [154] and Zobeiry et al. [155] are used for calibration of the fibre tensile and compressive fracture energies, respectively as well as the fibre softening options. The stacking sequence of the laminate is $[90/45/0/-45]_{4s}$ for both OCT and CC simulations and is the same stacking sequence used in the previous chapter on single-laminate element simulations. Therefore, the findings of the macro-scale single-laminate level can be directly transferred. The first part of this chapter focuses on damage propagation and validation under tension by the use of OCT models. This is followed by validation under compressive loading on CC models in the second part of this chapter. The chapter concludes with validation of the fibre fracture energies on a stacked-shell modelling approach which will be used for the simulation of progressive crushing. Outcomes of this chapter are calibrated and validated fibre fracture energies as well as a selection of fibre softening options.

6.1 Numerical Model Description and Data Reduction

The geometry of the OCT and CC test specimens and finite element models are shown in Figure 6.1 a) and b), respectively. The dimensions of the numerical model correspond to the nominal dimensions of the test specimens. The width of the initial notch is modelled with $2\,mm$ in the OCT and $1\,mm$ in the CC model. The multi-layered shell approach is used to model the laminate. Each ply of the $[90/45/0/-45]_{4s}$ layup is modelled with three section points through the ply-thickness of $t_{ply} = 0.125\,mm$ resulting in a laminate thickness of $t_{Lam} = 4.0\,mm$. Shell elements with reduced integration scheme (type 'S4R') are used. The 0°- direction is oriented in loading direction and the 90°-direction perpendicular and in direction of the notch. The region of the expected damage zone ('test area' - grey) is meshed with a regular mesh and elements with uniform characteristic lengths

a) Over-height Compact Tension specimen (OCT)   b) Compact Compression specimen (CC)
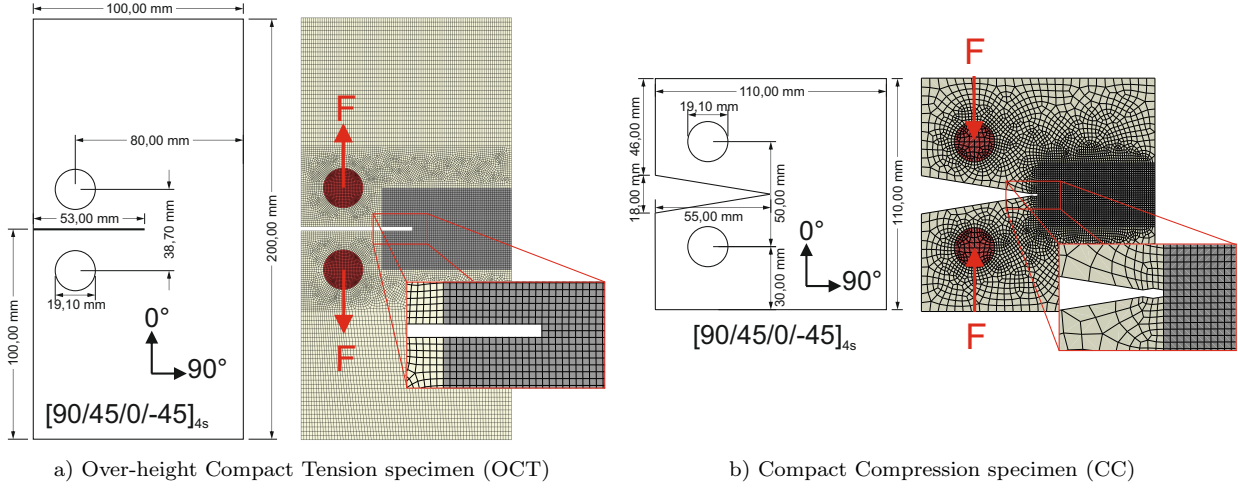
Figure 6.1: Geometry and numerical models of OCT and CC specimens

of $0.5\,mm \leq l^* \leq 2.0\,mm$ in the OCT model and $0.5\,mm \leq l^* \leq 1.0\,mm$ in the CC model. The baseline element size is $l^* = 1.0\,mm$ which is mainly used in the simulations of this chapter. The remaining area of the model is meshed with varying element sizes. Except for the elements of the loading pins (red) ABQ_DLR_UD is used to model the material behaviour. Material input of the IM7/8552 EU-Version (Table 3.1) is used as the baseline material input in this chapter. The loading pins are modelled as purely elastic steel. A prescribed velocity boundary condition with $v = 0.1\,\frac{m}{s}$ is applied on the centre nodes of the loading pins in opposite vertical direction. Additionally, the translational degrees of freedom except the vertical direction (DOF 1) and rotational degrees of freedom except the rotation around the pin-axis (DOF 6) are locked at the center nodes of the pins. No further boundary conditions are active in the numerical model. The displacement of both pin centre nodes relatively to each other is referred to as the pin-opening displacement (POD). Modelling of contact is not relevant in the OCT model and is therefore omitted. In the CC simulations, contact becomes relevant for higher crack lengths and smaller element sizes. Therefore, contact is considered and its influence is investigated in the following sections. Self contact is modelled in the test area with a coefficient of friction of $\mu = 0.4$. The numerical results are validated by the use of force vs. pin-opening displacement and the evolution of the crack length vs. pin-opening displacement as well as by determining and comparing the laminate fracture energies. However, no evolution of the experimental crack lengths was provided by Zobeiry [154] for the CC tests and therefore only the force vs. pin-opening displacements and laminate fracture energies are used for validation. Force and pin-opening displacement are recorded with $\Delta t = 0.01\,ms$ and the crack lengths determined from field outputs with $\Delta t = 0.25\,ms$. Since no strain-rate model is active in the simulations, there is no difference of the material properties between quasi-static and dynamic loading. Therefore, dynamic loading is used in the simulations instead of quasi-static loading in the tests in order to reduce computation times. This produces a noisy numerical force signal. The force signal is filtered using a Butterworth low-pass filter with $20\,kHz$ cut-off frequency without filtering

out significant information. The force vs. pin-opening data and crack length measurements are combined to calculate the laminate fracture energy G_c as:

$$G_c = \frac{W - U}{t_{Lam}a} \tag{6.1}$$

where W is the total dissipated energy corresponding to the area under the force vs. pin-opening displacement curve, U is the elastic strain energy, t_{Lam} is the thickness of the laminate (here $t_{Lam} = 4.0\,mm$) and a the crack length. It should be noted that the smallest increment of crack growth corresponds to the element size in the test area. The laminate fracture energies are determined in the simulation up to $POD = 2.5\,mm$ for both OCT and CC simulations. Multiple options are available to define the crack length in the numerical simulation. In the scope of this work, the crack length is determined by fibre tensile or compressive damage. Two definitions of the crack length based on fibre damage are used. In the first definition, crack growth is assumed when fibre tensile/compressive damage initiates in the $0°$ plies. In the second definition, crack growth is defined when fibre damage is saturated meaning that the total fibre fracture energy is dissipated in the $0°$ plies. By this, a range of predicted laminate fracture energies is defined with the lower bound is the laminate fracture energy based on fibre damage initiation and the upper bound based on fibre damage saturation. Matrix damage is not considered in the crack growth definition for the prediction of the laminate fracture energy since matrix damage initiates early in the model which would result in an under-prediction of the laminate fracture energy. The initial fibre fracture energies for tension and compression are $G_{c1}^T = G_{c1}^C = 120\,\frac{kJ}{m^2}$.

6.2 Calibration and Validation of Tensile Fibre Fracture Energy with Over-height Compact Tension Tests

Calibration of the fibre fracture energy and fibre softening option under tensile loading is performed in this section. At the beginning, mesh size dependencies and the influence of crack band scaling of the fibre fracture energies are investigated. This is followed by the validation of the tensile fibre fracture energy input for the baseline configuration with exponential softening. Afterwards, effects of fibre softening options on the damage propagation in OCT models are investigated. Finally, the influence of varying material parameters is shown by comparing the two material versions of IM7/8552.

6.2.1 Influence of Mesh Size on Fracture Mechanic Tests

The test area in the OCT model is uniformly meshed with three characteristic element lengths of $l^* = 0.5\,mm$, $l^* = 1.0\,mm$ and $l^* = 2.0\,mm$. Figure 6.2 presents the results of the simulations with varying element sizes. The force vs. pin-opening displacement characteristics of the simulations

are shown in Figure 6.2 a) and compared to the experimental results published by Zobeiry [154] and Zobeiry et al. [155]. The experimental data show load-unload cycles which are not considered in the simulations. The stiffness of the laminate as the slope of the force vs. pin-opening displacement curve in the pre-peak domain is predicted well by the meso-scale modelling approach of ABQ_DLR_UD. The slopes of the simulations become non-linear when fibre damage initiates in the 0° plies. With increasing element size, damage in the 0° plies initiates at higher POD. This is shown in Figure 6.2 b). The dotted lines represent the crack length determined from fibre damage initiation in the 0°-plies. The POD of fibre damage initiation increases from $POD = 0.65\,mm$ for $l^* = 0.5\,mm$ and $POD = 0.75\,mm$ for $l^* = 1.0\,mm$ to $POD = 0.9\,mm$ for $l^* = 2.0\,mm$. In the experiments, the cracks initiated at $POD = 0.78\,mm$ and $POD = 0.9\,mm$. For higher POD, the force level of the experiments only slightly increases whereas the simulations over-predict the strength of the OCT specimen. With increasing element size, the predicted ultimate strength of the laminate decreases. This is in agreement with the findings on single-laminate element level with identical element sizes shown in Figure 5.3 and Figure 5.4. On single-laminate level, it was concluded that the slope of the fibre strain-softening curve, which is dependent on the element size, effects the ultimate strength of the laminate. For increasing characteristic lengths, the strain softening slope is steeper resulting in higher damage growth as well as lower damage saturation strains (see Figure 5.3). This combination results in lower ultimate strength in the main load-carrying 0° plies. The POD of ultimate strength coincides with the initiation of crack growth based on fibre damage saturation. The cracks based on damage saturation initiate at $POD = 1.2\,mm$ for $l^* = 1.0\,mm$ and $l^* = 2.0\,mm$ and at $POD = 1.25\,mm$ for $l^* = 0.5\,mm$. After reaching the point of ultimate strength, a sharp drop is identified in the force characteristics of the simulation which is due to a sudden crack growth of both fibre damage initiation and saturation. Subsequent, the force level is equal for the different element sizes with a slightly higher force for $l^* = 0.5\,mm$. This is also in agreement with observations on single-laminate level in Figure 5.4. From this it is concluded that the shape of the fibre strain-softening slope influences the ultimate strength of the laminate on coupon level in the same way as on single-laminate level. As reported by Zobeiry [154], a steeper strain-softening slope results in lower ultimate strength whereas identical fibre fracture energies result in similar post-peak force levels. This will be further investigated in the following sections on different fracture energies and strain-softening options. In comparison with the experiments, the simulations are not able to predict the post-peak force level accurately. Comparing the experimental and numerical crack lengths in Figure 6.2 b), the crack length based on fibre damage initiation predicts the onset of the crack growth well but over-predicts the crack length for increasing POD. If fibre damage saturation is considered, the POD of crack initiation is over-predicted by the simulations but the growth of the crack length correlates well with the experimental results. The fracture energy of the laminate is determined from the force vs. pin-opening displacement and crack length following Equation (6.1). The predicted laminate fracture energies for the varying element sizes as well as the minimum and maximum fracture energies of the experiments [154, 155] are shown in Figure 6.3. Using fibre damage initiation to define the crack length, the predicted

laminate fracture energies are lower as the experimental results. Using damage saturation for the definition of the crack length, the predicted laminate fracture energies are in the range of the experimental results. With increasing element size, the predicted fracture energies reduce due to two reasons. The reducing ultimate strength results in lower dissipated energy. Additionally, the crack length increases with the element size. This results in slight deviations of the results with different element sizes. However, the differences are marginal and the laminate fracture energies are in the range of the experimental results for all three investigated element sizes due to the implemented crack band scaling approach in the model. In Figure 6.2 c), results are shown for simulations of different element sizes without crack band scaling of the fibre fracture energy densities. The crack band approach is disabled in the model by scaling the fibre fracture energies input to achieve the fracture energy density of $l^* = 1.0\,mm$, which in this case is $g_{c1,\,l^*=1.0\,mm}^{T/C} = 120\,\frac{kJ}{m^3}$. It is shown that both the ultimate laminate strength and the post-peak force level and therefore the dissipated energy during crack propagation significantly increase with the element size. This shows the necessity to use the crack band scaling to achieve mesh size independent results in order to validate the laminate fracture energy. In the further course of this section, results are discussed which are obtained for a uniform element size of $l^* = 1.0\,mm$ and using the crack band scaling approach.

6.2.2 Validation of Tensile Fibre Fracture Energies

With an assumed fibre tensile fracture energy input of $G_{c1}^T = 120\,\frac{kJ}{m^2}$ the predicted laminate fracture energy is in the range of experimental results, as shown in the previous section. To validate this, fibre tensile fracture energies in the range of $80\,\frac{kJ}{m^2} \leqslant G_{c1}^T \leqslant 160\,\frac{kJ}{m^2}$ are investigated in this section. The force vs. pin-opening displacement scale uniformly with the fibre fracture energy as shown in Figure 6.4 a). Both the ultimate laminate strength and post-peak force increase with the fracture energy. However, the post-peak force level of the experiments is not accurately predicted for the range of fibre tensile fracture energies. The increasing ultimate strength are again traced to the slope of the strain-softening curve in the $0°$ plies where a steeper strain-softening curve results in lower ultimate strength. This is in agreement with the findings on single-laminate level (see Figure 5.5). The effect of the tensile fracture energy on the crack growth is shown in 6.3 b). Since fibre damage initiation is independent of the fracture energy, the initiation of the crack based on fibre damage initiation does not change with the fracture energy. However, the crack growth is higher for lower tensile fracture energies. Two main effects of the fibre fracture energy are identified for the crack length based on damage saturation. The POD of crack initiation increases with fracture energy due to the increased fibre damage saturation strains with increasing fracture energy. Also, the crack growth reduces with increasing fracture energy which is traced to the slope of the strain-softening curve and relating thereto the fibre tensile damage growth which is less for higher fracture energies. From this, it is concluded that a varying fibre fracture energy influences both the ultimate laminate strength and the post-peak force level due to the changing strain-softening slopes. The influence of these identified effects on the predicted laminate fracture energy is shown in Figure 6.5. The
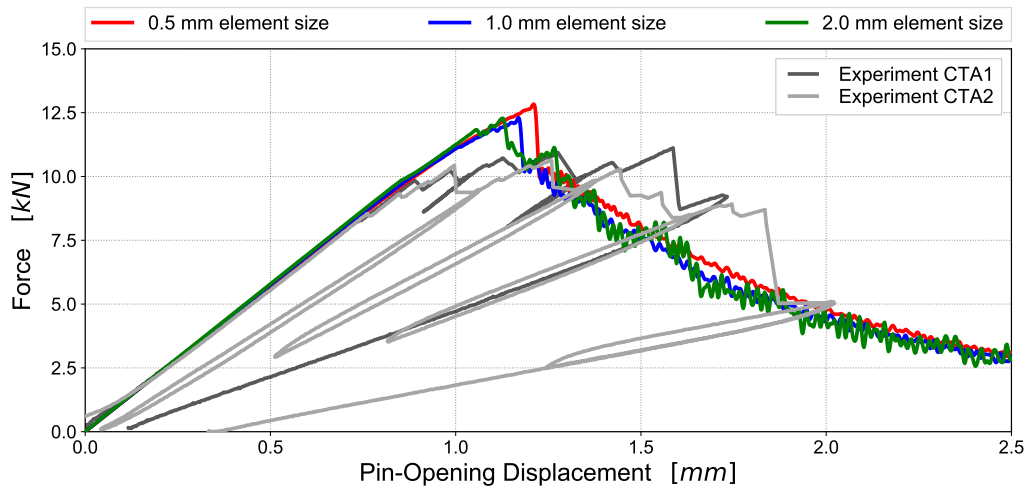
a) Force vs. pin-opening displacement characteristic
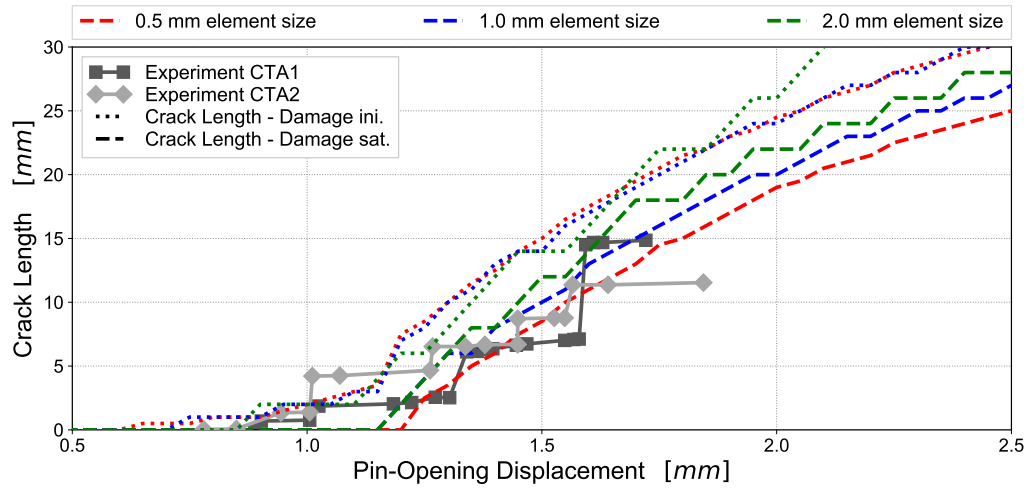
b) Crack length vs. pin-opening displacement
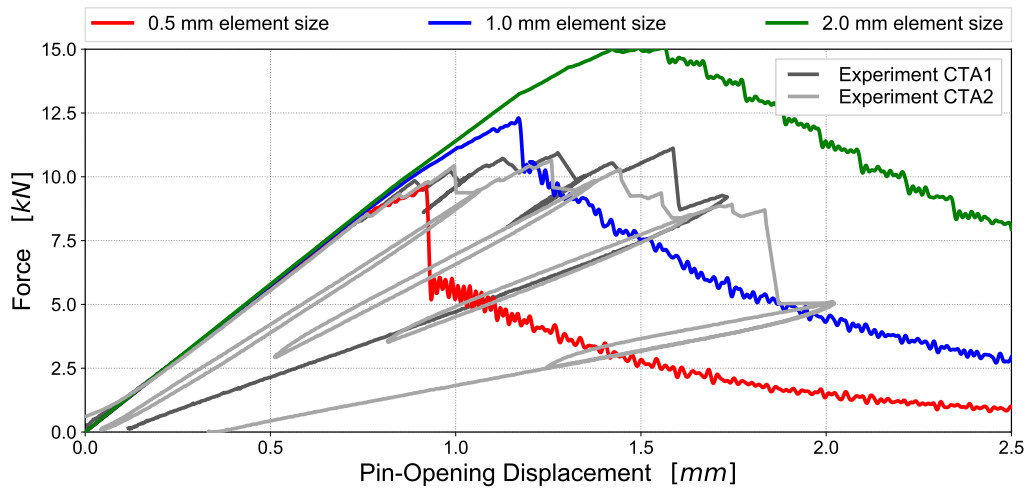
c) Force vs. pin-opening displacement characteristic without crack band scaling

Figure 6.2: OCT simulation - Influence of element size; a) Force vs. pin-opening displacement, b) crack length vs. pin-opening displacement, c) force vs. pin-opening displacement without crack band scaling
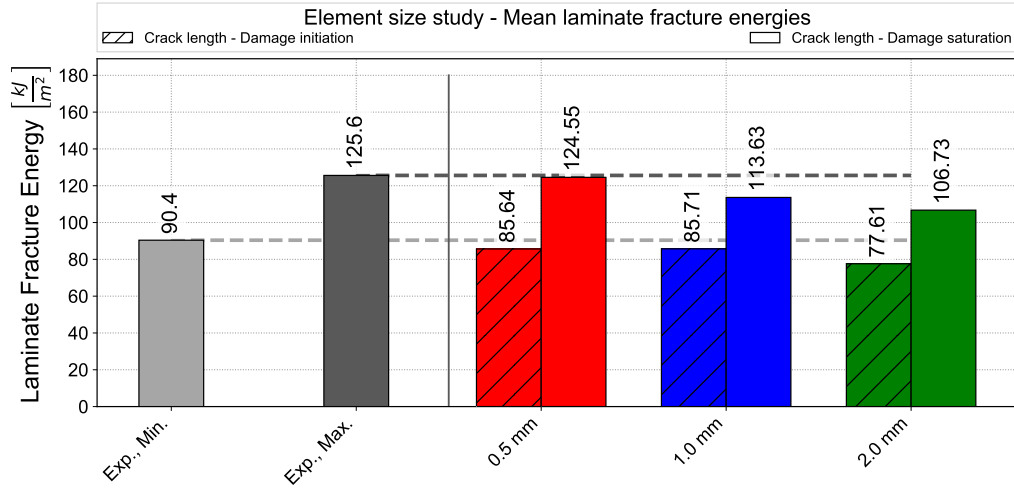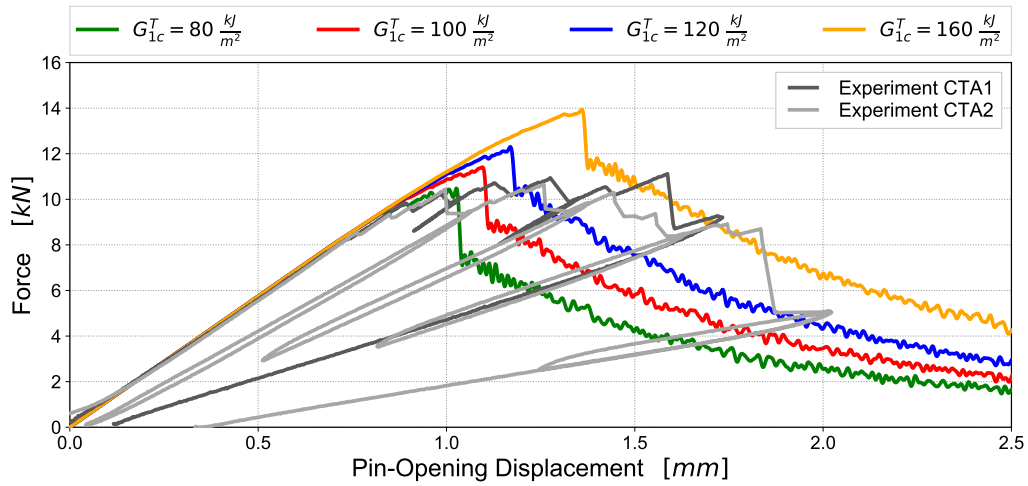
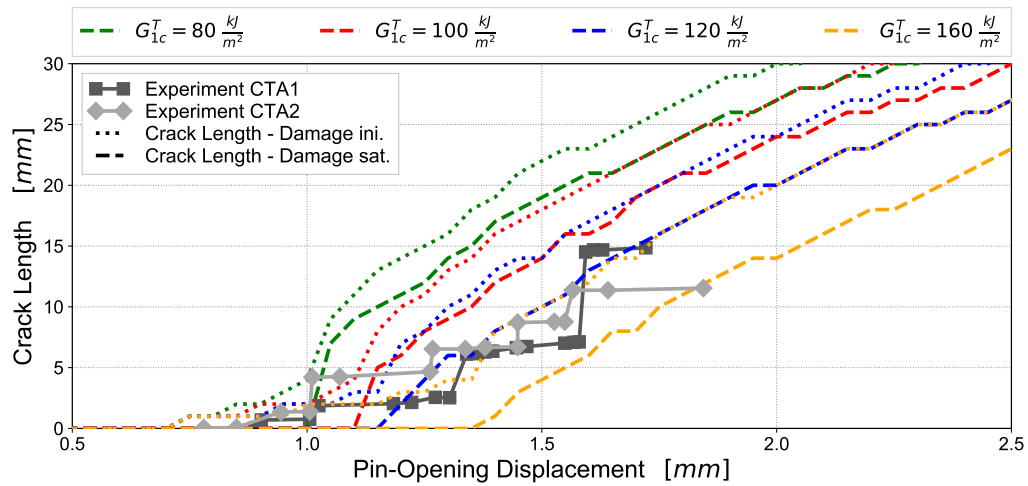**Figure 6.3:** Laminate fracture energies predicted from OCT simulations using different element sizes

predicted laminate fracture energies increase uniformly with the tensile fibre fracture energy for both approaches of the crack length. Comparing the laminate fracture energy predicted from the crack length based on fibre damage initiation, only the result for $G_{c1}^T = 160 \frac{kJ}{m^2}$ is in the range of the laminate fracture energy of the experiments. For damage saturation, the predicted laminate fracture energies of $G_{c1}^T = 100 \frac{kJ}{m^2}$ and $G_{c1}^T = 120 \frac{kJ}{m^2}$ are in the range of the experiments whereas $G_{c1}^T = 80 \frac{kJ}{m^2}$ and $G_{c1}^T = 160 \frac{kJ}{m^2}$ under- and over-predict the experimental results, respectively. Comparing the crack-lengths of damage saturation in Figure 6.4 b), the results of $G_{c1}^T = 120 \frac{kJ}{m^2}$ correlates well with the crack length of the two experiments whereas for $G_{c1}^T = 100 \frac{kJ}{m^2}$, the crack length is higher. Compared to the findings on single-laminate level, the predicted laminate fracture energies for $G_{c1}^T = 120 \frac{kJ}{m^2}$ are slightly higher in the OCT simulations. It is concluded that this difference is due to the sensitivity of the laminate fracture energy on the crack length. From these findings, a fibre tensile fracture energy of $G_{c1}^T = 120 \frac{kJ}{m^2}$ is validated and therefore used for the simulation in this chapter as well as the simulation of progressive crushing in the following chapter. No further refinement of the fibre fracture energy is made.

6.2.3 Effects of Fibre Softening Options on the Crack Propagation in OCT Models

As outlined in the previous sections, the shape of the fibre strain-softening slope is identified as the main factor influencing the force-displacement characteristic of OCT specimen. In a sensitivity study on macro-scale level, Zobeiry [154] investigated the effect of parameters defining the slopes of an optimised trilinear softening response on the OCT force characteristic. To further investigate this thesis, different strain-softening options on the meso-scale are used in the simulation of the OCT specimen. The fibre strain-softening approaches and parameters are the same as in Section 5.3. Therefore, direct comparison between the effects on laminate level and the level of fracture mechanic
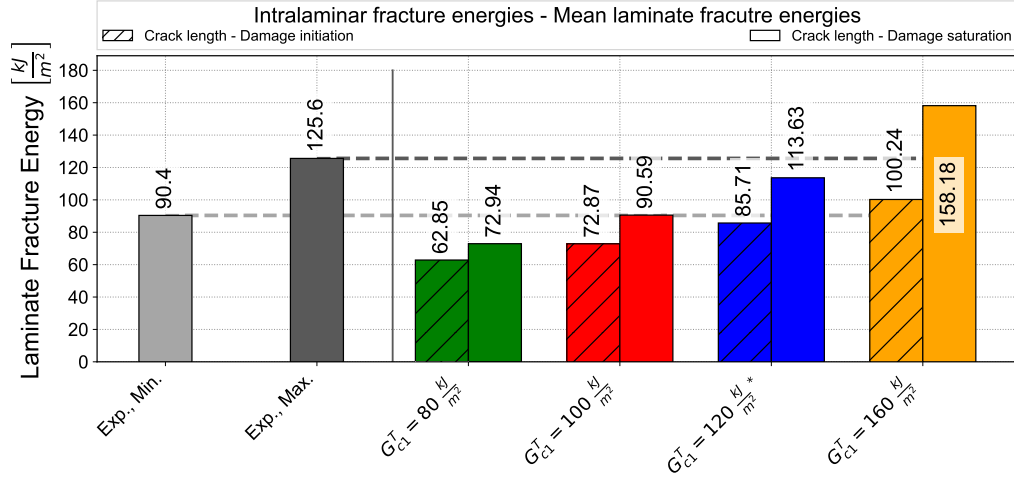
a) Force vs. pin-opening displacement characteristic

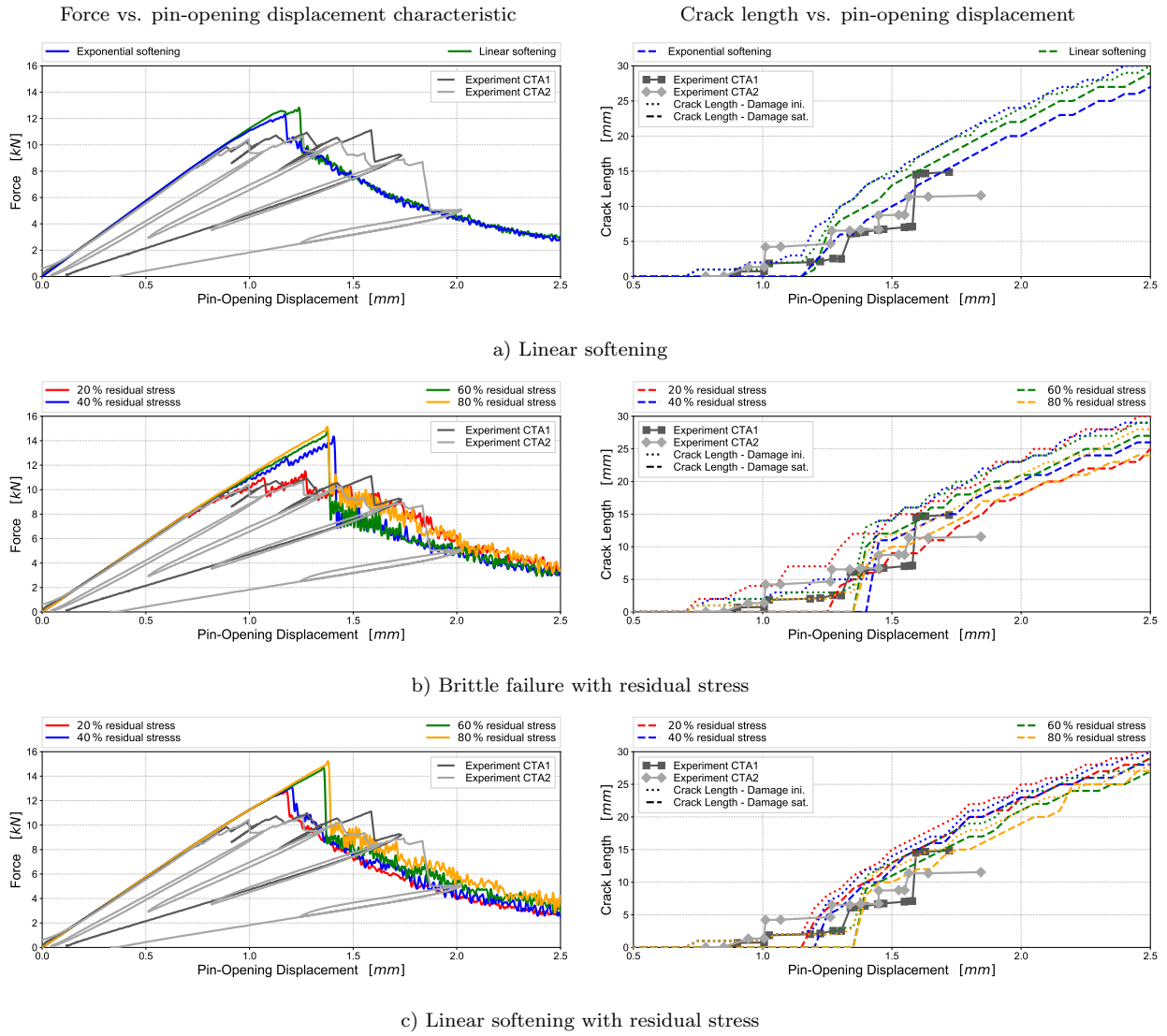b) Crack length vs. pin-opening displacement

Figure 6.4: OCT simulation - Validation of tensile fibre fracture energy; a) Force vs. pin-opening displacement characteristic, b) crack length vs. pin-opening displacement

Figure 6.5: Laminate fracture energies predicted from OCT simulations using different fibre fracture input

tests can be made. The strain-softening options in this work affect the shape of the laminate stress-strain characteristic. Their influence can be directly compared to the effects of changing the slopes in an optimised trilinear softening response investigated by Zobeiry [154]. The force vs. pin-opening displacement characteristics and the development of the crack length of the fibre softening approaches are shown in Figure 6.6. The fibre softening approaches in addition to the baseline exponential softening are linear softening, brittle failure with residual stress and linear softening with residual stress levels ranging from 20% to 80% of the fibre tensile strength. The fibre tensile fracture energy is the same for all softening approaches. Figure 6.6 a) presents the results of the **linear softening** approach. The exponential softening is shown for comparison and corresponds to the results shown in the previous section. As shown on single-UD element simulation in Section 4.4 and on single-laminate level in Section 5.3, the steeper initial post-peak slope of exponential softening is the result of higher fibre damage that results in less global strength of the laminate. This correlates well with the findings of Zobeiry [154] where increasing the first slope in the trilinear softening response, the slope following the peak stress, results in an increased peak load of the laminate [154]. The force vs. pin-opening displacement characteristics of both linear and exponential softening start to diverge at approx. $POD = 1.0\,mm$. At the peak force of exponential softening, the force characteristic of linear softening shows a kink. At this point, the crack based on fibre damage saturation initiates in both softening approaches. However, the crack length of fibre damage initiation is already higher for the exponential softening approach which results in a distinct force drop. The force predicted by linear softening further increases until the crack length of both damage initiation and damage saturation rapidly increase at $POD = 1.25\,mm$. Afterwards, the crack length of damage saturation is higher for linear softening whereas the crack length of fibre damage initiation is about equal, as shown in the right graph in Figure 6.6 a). For higher POD, the force levels of both softening approaches are equal. Due to the higher ultimate

Force vs. pin-opening displacement characteristic   Crack length vs. pin-opening displacement

a) Linear softening

b) Brittle failure with residual stress


c) Linear softening with residual stress

Figure 6.6: OCT simulation - Effects of fibre softening options; Left: Force vs. pin-opening displacement characteristic; Right: crack length vs. pin-opening displacement. a) Linear softening, b) brittle failure with residual stress, c) linear softening with residual stress

strength, more strain energy is released at crack initiation resulting in a higher crack propagation in linear softening. Afterwards, the increment of crack length is about equal for exponential and linear softening. In Figure 6.7, the laminate fracture energies predicted by the different softening options are shown in comparison with the minimum and maximum experimental results obtained by Zobeiry [154] and Zobeiry et al. [155]. The predicted laminate fracture energy based on damage initiation is higher for linear softening as the result of the higher total dissipated energy due to the higher ultimate strength. The laminate fracture energy based on damage saturation is higher for exponential softening due to the smaller crack length for higher POD. However, the effect on the predicted laminate fracture energy is small and the fracture energies are in the range of the experimental results.

The results of **brittle failure** with different residual stress levels are shown in Figure 6.6 b). Compared to exponential softening, the ultimate strength of the laminate is significantly lower for 20% residual stress without a significant peak force. The reasons are identified in the effects of the brittle failure softening on the laminate stress-strain response. The effects on laminate level compared to exponential softening correspond to a reduction of the first slope according to Zobeiry [154]. This was reported to reduce the ultimate strength of the laminate. Increasing the residual stress levels significantly increases the maximum force and results in a explicit force peak. Zobeiry [154] also reported this effect when increasing the plateau stress in the trilinear softening response of the laminate. The post-peak force characteristics for increasing residual stress levels show contrary effects. This is due to the evolution of fibre damage in the 0°-plies. The force curve of 20% residual stress correlates well with the experimental results. The slope becomes non-linear at $POD \approx 0.75\,mm$ when fibre damage initiates in the 0°-plies. Fibre damage increases instantaneously after damage initiation which is characteristic for this softening option. With increasing stress level, the maximum fibre tensile damage reduces, see Figure B.2 in Appendix B.3. As a result, the residual stiffness of the main load carrying 0°-plies increases with residual stress affecting the slope in the pre-peak region. This effect is also seen in a lower crack length based on damage initiation for increasing residual stress levels as shown in the evolution of the crack length on the right of Figure 6.6 b). With increasing residual stress level up to 60%, the post-peak force level is lower compared to 20% residual stress. This is due to a large growth of the crack length based on damage saturation. With increasing stress level, the fibre tensile saturation strain reduces resulting in higher crack lengths. However, for 80% residual stress, the post-peak force is higher compared to 40% and 60% and is on the same level as for 20% residual stress. This contrary tendency is due to a lower crack length based on damage saturation for 80% residual stress compared to the crack lengths of 40% and 60% residual stress. This seems to be an outlier since it is expected that the increasing amount of strain energy prior to the force drop would results in a larger increase of the crack length and therefore a lower force level. However, due to the high residual stress of 80% fibre tensile strength, damaged elements in the test area still have a high residual stiffness slowing down the crack propagation.

The effects described above are also identified for **linear softening with residual stress** shown in Figure 6.6 c). The main outcomes are an increased ultimate laminate strength with residual stress level, a force drop which becomes more distinctive for increasing residual stress levels as well as an increasing post-peak force level with increasing residual stress level. The reason for the higher ultimate laminate strength is the more gradual post-peak slope in combination with a lower maximum fibre damage value for increasing residual stress levels (see Figure C.3 in Appendix C.1). The more distinctive force drop is attributed to the increased strain energy that is released at crack propagation for higher residual stress level and an initiation of the damage saturation crack at higher POD. The higher post-peak force level is the result of a lower crack length based on damage saturation. The crack length based on fibre damage initiation has no visible effect on the global force vs. pin-opening displacement characteristic since the post-peak softening slope is identical until the residual stress level is reached.

The effects of different residual stress level in the fibre softening approach on the predicted laminate fracture energy are shown in Figure 6.7. The tendencies identified on the force characteristic are also seen on the laminate fracture energies. For brittle failure, the predicted laminate fracture energy reduces with increasing residual stress level up to 60% but is highest for 80% for both definitions of the crack length. For linear softening with residual stress level, the predicted laminate fracture energies increase with the residual stress level. For most of the softening options, the predicted laminate fracture energies are in the range of the experimental results expect for brittle failure with 20% and 80% residual stress which over-predict the laminate fracture energy due to high force levels in combination with a relatively low crack length based on damage saturation.

From the investigation of strain-softening options on OCT specimens it is concluded that the influence is due to different shapes of the strain-softening slopes which influence the ultimate strength of the laminate as well as the crack propagation based on damage saturation. With increasing ultimate strength, the strain energy increases that is released with initiation of the damage saturation crack. Therefore, a high strain energy results in a large increase in crack length. High level of residual stress result in increased post-peak force levels and reduce the crack propagation. From the predicted laminate fracture energies which covers the complete damage process, it is concluded that the influence of increased residual stress level is due to its effects on the crack length based on damage saturation. However, compared to the effect of increased fibre fracture energies in Section 6.2.2 it is concluded that the fracture energy has a more distinctive influence on the predicted laminate fracture energy. This correlates with the findings of Zobeiry [154]. Zobeiry et al. [155] concluded that an optimised trilinear softening-response for the laminate reasonably represents the real behaviour of the material. Even when the differences between bi- and trilinear softening responses were reported to be small in FE-simulations, it was stated that a more complex softening response of the laminate might better average the real behaviour [155]. As shown in Chapter 5 for layup $[90/45/0/-45]_{4s}$, an exponential fibre softening approach on the meso-scale level results in an exponential softening response on the macro-scale level which
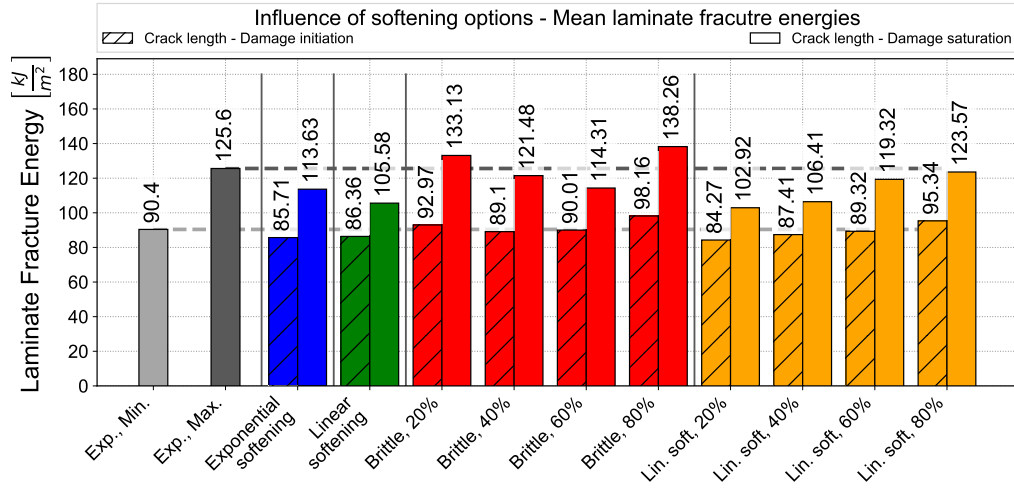
Figure 6.7: Laminate fracture energies predicted from OCT simulations using different fibre softening options

can be seen as an extension of a multi-linear softening response. Even if the exponential softening approach is not able to capture the post-peak force characteristic of the tests, the crack length and predicted laminate fracture energy based on damage saturation are reliably predicted. Therefore, exponential softening is used for the fibre tensile behaviour in the prediction of progressive crushing in the following chapter. OCT-simulations with the material parameters of the US-Version of IM7/8552 (Table 3.1) are conducted to validate that the findings obtained for the EU-Version of material system IM7/8552 are also valid for the US-Version. In the scope of the building block approach in this work, this comparison is made to show that the fracture energy is valid for both material systems and findings made on the EU-Version can be used on the following level of the building block to predict progressive crushing which is performed on the US-Version of IM7/8552. The results of the simulation with exponential softening and a fibre tensile fracture energy of $G_{c1}^T = 120 \frac{kJ}{m^2}$ are shown in Figure 6.8. The differences in the force vs. pin-opening displacements are explained directly by the variations of the fibre tensile material properties. The lower tensile modulus of the US-Version results in slightly lower pre-peak force slope. The slightly lower peak value is due to the lower fibre tensile strength. The POD of the force drop which indicates crack initiation based on damage saturation is higher for the US-Version and can be traced to a higher fibre damage saturation strain, as shown in Figure 4.3. The post-peak force levels as well as crack lengths for higher PODs are identical for both material versions. The predicted laminate fracture energies for the US-Version based on damage initiation are $80.54 \frac{kJ}{m^2}$ and $112.32 \frac{kJ}{m^2}$ based on damage saturation, respectively. This shows that a fibre tensile fracture energy of $G_{c1}^T = 120 \frac{kJ}{m^2}$ is valid also for the US-Version of IM7/8552 and will therefore be used as the tensile fibre fracture energy for the prediction of progressive crushing.
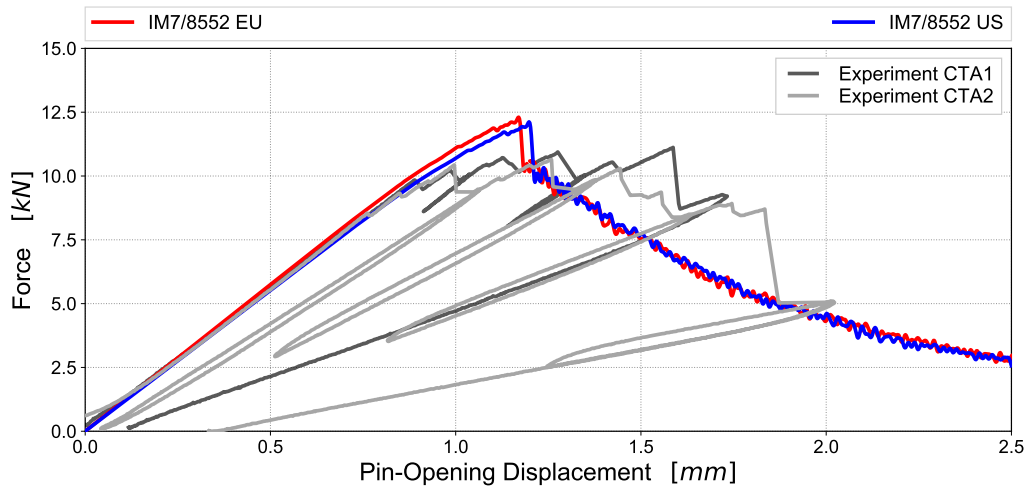
a) Force vs. pin-opening displacement characteristic
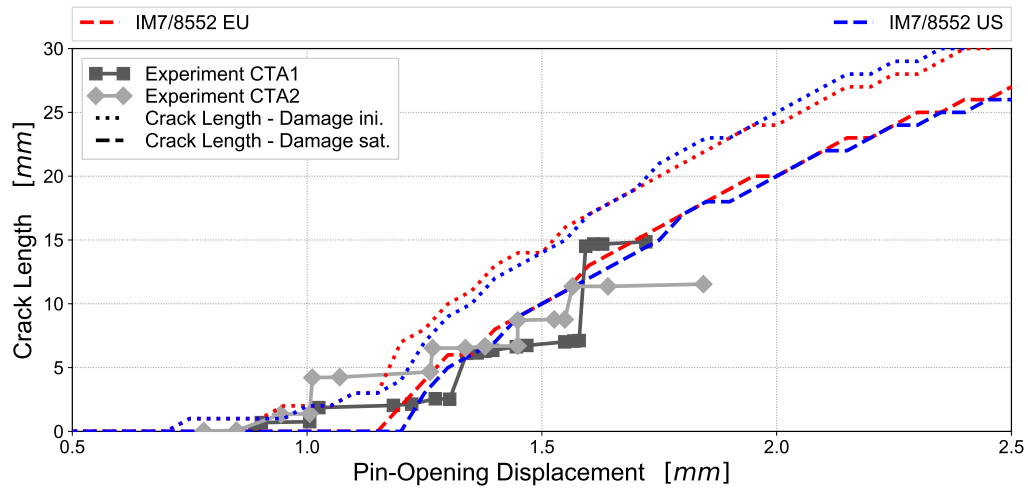
b) Crack length vs. pin-opening displacement

Figure 6.8: OCT simulation - Comparison of IM7/8552 material versions; a) Force-displacement characteristics, b) crack length vs. pin-opening displacement

6.3 Calibration and Validation of Compressive Fibre Fracture Energy with Compact Compression Tests

Calibration of the fibre fracture energy and fibre softening option under compressive loading is performed on Compact Compression (CC) simulations. At the beginning of this section, it is shown that the experimental results have to be scaled in the initial displacement to obtain a comparison with the numerical results. This is followed by a discussion of the influence of the mesh size and modelling of contact. By variation of the compressive fibre fracture energies, the fracture energy input is validated. A brief discussion of the fibre softening options shows the influence of the strain-softening approach under compressive loading. A comparison of the two IM7/8552 material versions shows the influence of varying material input parameters and validates the compressive fracture energy for both material versions.

Figure 6.9 a) presents the initial simulation results of the CC specimen in terms of force vs. pin-opening displacement characteristics. The results are obtained for a characteristic length of $l^* = 1\,mm$ and compressive fibre fracture energy of $G_{c1}^C = 120\,\frac{kJ}{m^2}$. The experimental results published by Zobeiry [154] and Zobeiry et al. [155] labelled 'CCA1' and 'CCB2' are used for comparison. It is shown that the numerical results significantly diverge from the experimental results in three major points. The initial slope of the force vs. pin-opening displacement curve, representing the stiffness of the specimen, the ultimate strength and the post-peak force level are over-predicted by the simulation. The higher post-peak force level is due to a high initial fibre compressive fracture energy which will be calibrated in the following section. An increased stiffness of the specimen could be due to a higher fibre compressive modulus or a lower initial notch length in the simulation compared to the experiments. Zobeiry [154] published an elastic laminate modulus of $E_x = 54.2\,GPa$ obtained from FE-simulations of the optimized constitutive response [154]. In the single-element simulation on laminate level in Chapter 5, an elastic compressive modulus of $64.4\,GPa$ is predicted for the same laminate stacking sequence. In an initial step, the fibre compressive modulus was reduced in order to obtain the same stiffness as in the tests. However, the fibre compressive modulus would have to be decreased to a non-physical value to reduce the laminate stiffness close to the experimental results. Increasing the notch length also did not result in a significant reduction of the stiffness. From this and from discussion with a co-author of [155] it is concluded that the test setup might has an influence on the measured stiffness. Due to the unknown compliance of the test setup and in order to be consistent with the results obtained in the previous section, it was decided to scale the experimental results of Zobeiry [154] whereas the numerical results are not scaled. Scaling of the experimental results follows the assumption of a linear-elastic spring that represents the compliance of the test setup. Hence, scaling of the measured displacement is force dependent. The pin-opening displacements of the experimental results are scaled using:

$$POD_{true} = POD_{exp} - F_{exp}/k \tag{6.2}$$

with F_{exp} being the experimental force and k the assumed stiffness of the test fixture. The assumed stiffness k is calibrated to fit the initial linear-elastic slope of the experiments to the numerical simulation. Figure 6.9 b) presents the scaled results. Scaling of the force vs. pin-opening displacement curve also affects the laminate fracture energy. Assuming that the crack length is not affected by the compliance of the test setup, the laminate fracture energy is scaled by a factor j defined as the ratio of the unscaled vs. scaled total dissipated energy W. The factor is determined to be $j = 1.4$. This scales the laminate compressive fracture energy of $G_f = 85 \frac{kJ}{m^2}$ as reported by Zobeiry [154] to $G_{f,scaled} = 60.7 \frac{kJ}{m^2}$ which is further used to validate the simulation results in this chapter.

6.3.1 Influence of Mesh Size and Contact Modelling on Compact Compression Tests

In the CC models, the test area is uniformly meshed using characteristic element lengths of $l^* = 0.5\,mm$ and $l^* = 1.0\,mm$. A characteristic element length of $l^* = 2.0\,mm$ is omitted in this investigation due to the specimen design with tapered notch (see Figure 6.1). Figure 6.10 presents the results of the two element sizes. The simulation results are compared to the scaled experimental results. The numerical results are shown without contact modelling on the left of Figure 6.10, as well as including contact in the model on the right of Figure 6.10. In contrast to the OCT specimen, contact is relevant in the CC test. As reported by Zobeiry [154], the damaging process under tension and compression differs significantly. Under compressive loading, load can be transferred across the edges of the crack and damage propagates in the undamaged material, contrary to tensile loading [154]. Zobeiry [154] called this effect of damage growth in the vicinity of the crack 'damage band broadening'. Modelling this effect with continuum damage mechanics and element erosion to delete completely damaged elements is challenging. By eroding fully saturated elements, the notch propagates through the model and load cannot be transferred across the edges of the notch. For increasing pin-opening displacements, the notch closes starting at the point of crack initiation due to the global deformation of the CC specimen. In the simulation without contact the elements interpenetrates without interacting, as shown on the left of Figure 6.10 b). However this does not influence the force vs. pin-opening displacement characteristic. As shown on the left of Figure 6.10 a), the post-peak force constantly decreases. However, when contact is modelled, the elements on both side of the notch are getting in contact and load is transferred across the notch representing the crack as described in the experiments, resulting in an additional damage zone. This effect is shown in the contour plot of fibre compressive damage on the left of Figure 6.10 b). Modelling contact has a significant influence on the force response of the model. When the notch in the model closes and the elements are getting in contact, a secondary damage zone establishes. This results in an increase of the force response. A second effect of contact modelling is a reduced crack growth at the crack tip. As shown in the evolution of the crack length in Figure 6.10 a) the crack growth reduces when an additional contact zone establishes. However, the crack growth is about constant in the model without contact. The POD at which contact becomes active in the model is dependent on the width of the notch defined by the element size as the notch width is defined here by one
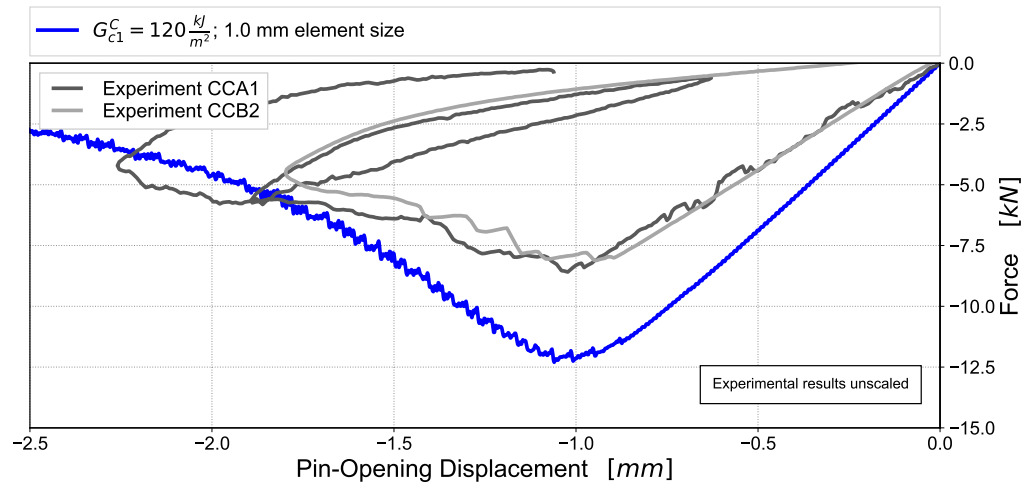
a) Unscaled experimental results
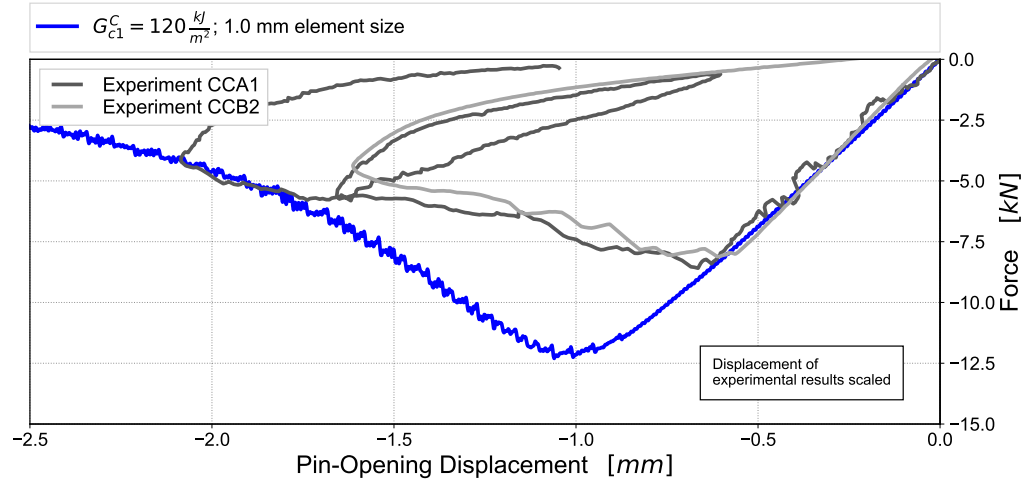

b) Scaled experimental results

Figure 6.9: Compact compression - Scaling of the experimental displacement

element row. Reducing the element size results in the establishment of additional damage zones. This is the reason for differences in the post-peak force characteristics of different element sizes, as shown on the right of Figure 6.10 a). In the experiments, load is transferred across the edges over the complete crack length. To model this effect would require an infinitesimal small element size which would result in extremely small time steps in the explicit simulation and therefore high computational costs. Influence of the mesh size is also identified in the simulations without contact, shown on the left of Figure 6.10 a). The peak force is lower for a characteristic element length of $l^* = 0.5\,mm$ than for $l^* = 1.0\,mm$. The reason for this is identified in a crack initiation based on saturated fibre compressive damage at lower POD for $l^* = 0.5\,mm$. This shows the sensitivity of the CC force characteristic to the crack length. However, it is concluded that this effect is not due to the crack band scaling. In Figure 6.11, the results are shown with disabled crack band scaling in the simulation. A distinctive sensitivity on the element size is identified in significantly reduced ultimate strength, post-peak force level and dissipated energy when reducing the element size. Therefore, the crack band scaling approach has to be used in order to reduce the mesh size sensitivity on the level of fracture mechanic tests. In the following sections, results will be shown for simulations with element size of $l^* = 1.0\,mm$ and contact modelling. All simulation results without contact modelling are shown in Appendix D.2.

6.3.2 Validation of Compressive Fibre Fracture Energies

The results of the previous sections showed that an initial fibre compressive fracture energy of $G_{c1}^C = 120\,\frac{kJ}{m^2}$ resulted in higher post-peak force level compared to the scaled experimental results. To calibrate the compressive fibre fracture energy under compression, a range of $60\,\frac{kJ}{m^2} \leqslant G_{c1}^C \leqslant 160\,\frac{kJ}{m^2}$ is investigated whereas fibre fracture energies $\geq 120\,\frac{kJ}{m^2}$ are presented for completeness. The results are shown in Figure 6.12. The force vs. pin-opening displacement characteristics are shown in comparison with the scaled experimental results in Figure 6.12 a). The evolution of the crack lengths based on fibre compressive damage initiation and damage saturation in the $0°$-plies is shown in Figure 6.12 b). No evolution of crack length was reported by Zobeiry [154]. However, Zobeiry [154] reported a fibre breakage/bending zone with a length of $31\,mm$ which was obtained from the post mortem specimen 'CCB1'. Whereas no information was given on the maximum POD that results in this crack length. Therefore, this value is used as a maximum reference. With increasing fibre fracture energy the force vs. pin-opening displacement increases uniformly. A higher fibre fracture energy results in an increase of both the ultimate strength and post-peak softening response of the laminate. The results shown here are in agreement with the findings on single-laminate level in Section 5.2.2. For the range of fibre fracture energies, the peak-forces of the simulations are higher compared to the experimental results. The post-peak force predicted by the simulation with $G_{1c}^C = 60\,\frac{kJ}{m^2}$ correlates well with the scaled experimental results. The post-peak force decreases slower in the experimental results due to the damage band broadening described in the previous section. This effect can be partially reproduced by the simulation due to
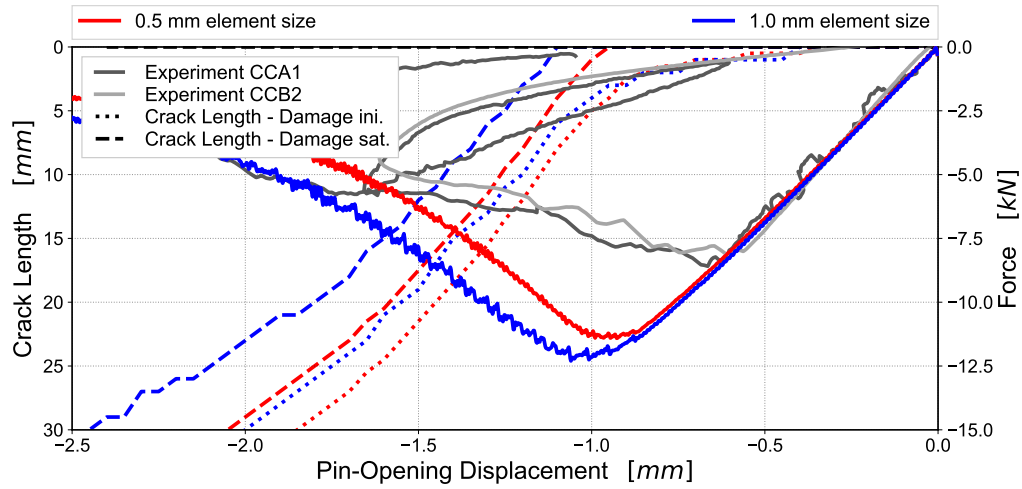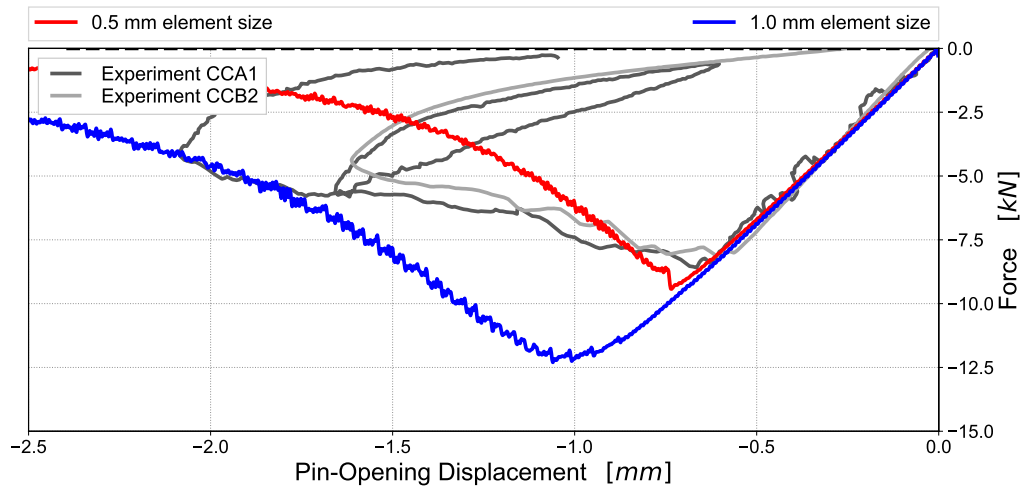
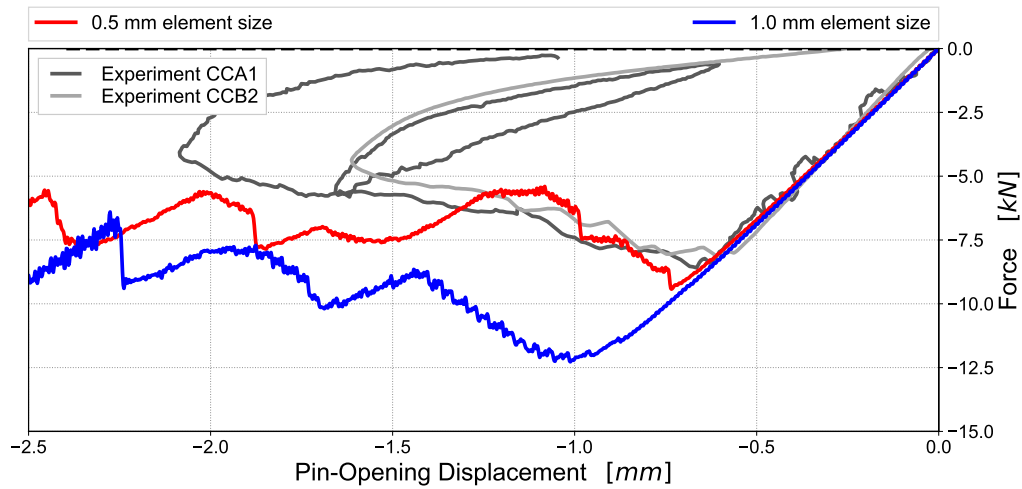a) Force vs. pin-opening displacement - Simulation without contact
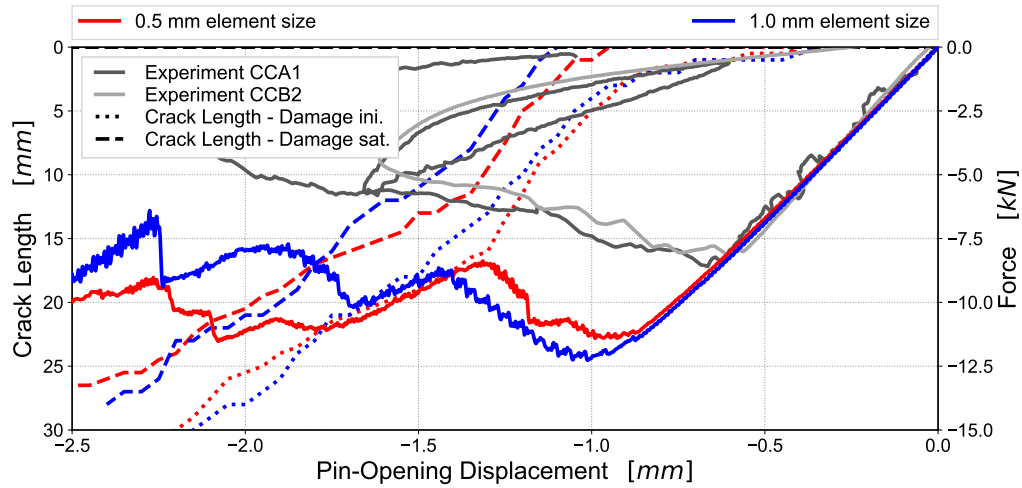
b) Force vs. pin-opening displacement - Simulation with contact
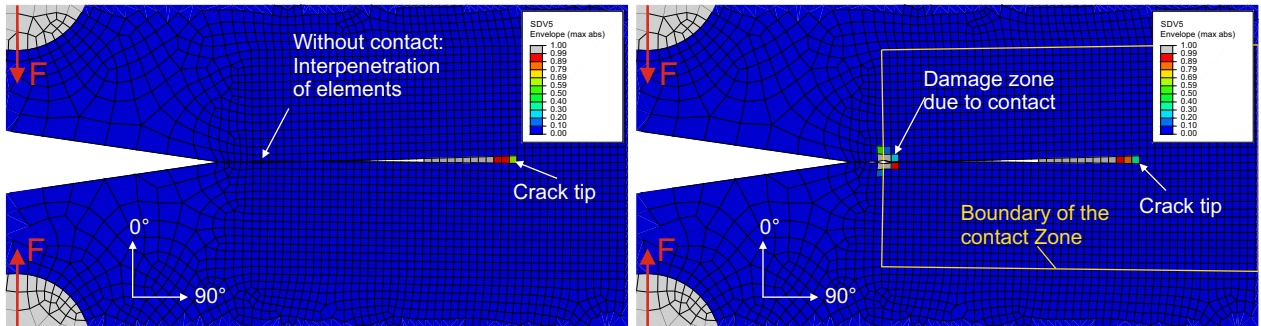
c) Contour plot of fibre compressive damage (SDV5), envelope of all plies; $1\,mm$ element size at $POD = -2.25\,mm$

Figure 6.10: Compact compression - Influence of contact modelling; a) Force vs. pin-opening displacement without contact; b) Force vs. pin-opening displacement with contact; c) Contour plot of fibre compressive damage - Left: Simulation without contact; Right: Simulation with contact (Note: Simulation results with initial fibre fracture energies)

a) Simulation without contact

b) Simulation with contact

Figure 6.11: Force vs. pin-opening displacement without crack band scaling for $0.5\,mm$ element size. Simulation without and with contact modelling (Note: Simulation results with initial fibre fracture energies)

contact modelling resulting in a good agreement in the post-peak force. As stated in the previous section, the predicted peak force of the simulation is sensitive to the initiation of the crack based on damage saturation. The peak force of the experiments is reached at a POD (scaled) of approx. $-0.66\,mm$. It is assumed that damage of the laminate is substantially advanced at this POD. As stated in the section of tensile loading, the crack lengths based on damage initiation and damage saturation define the lower and upper bound of damage, respectively. The crack based on fibre damage initiation starts to grow at $POD = -0.45\,mm$ independently of the fibre fracture energy. The crack based on damage saturation initiates at $POD = -0.8\,mm$ for a fibre fracture energy of $G_{1c}^C = 60\,\frac{kJ}{m^2}$ and increases with the fibre fracture energy, as shown in Figure 6.12 b). The scaled POD at peak force of the experiments is between the PODs of crack initiation based on damage initiation and damage saturation of the simulation with $G_{1c}^C = 60\,\frac{kJ}{m^2}$. The crack lengths increase with the POD and the maximum damage length of the experiments is reached at $POD = 1.7\,mm$ for damage initiation and $POD = 1.95\,mm$ for damage saturation. For increasing fibre fracture energies, the experimental crack length of $31\,mm$ [154] is only reached for $G_{1c}^C = 80\,\frac{kJ}{m^2}$ whereas for higher fracture energies, the maximum crack length based on damage saturation is lower for the range POD. From this it is assumed that the fibre fracture energy is in the range of $G_{1c}^C = 60-80\,\frac{kJ}{m^2}$. The laminate fracture energy of the CC simulations are predicted using Equation (6.1). Again, both the crack length based on damage initiation and damage saturation are used to predict a range of laminate fracture energies. The predicted fracture energies are shown in Figure 6.13 in comparison with the scaled fracture energy of the experiments. It is shown that the predicted laminate fracture energy increases with the fibre fracture energy for both definitions of the crack lengths. However, the crack length based on damage initiation underestimates the laminate fracture energy for the investigated fibre fracture energies. For the crack length based on damage saturation, the predicted laminate fracture energy with $G_{1c}^C = 60\,\frac{kJ}{m^2}$ is slightly lower compared to the experimental results. For $G_{1c}^C = 80\,\frac{kJ}{m^2}$, the predicted laminate fracture energy exceeds the scaled experimental results.

From the results of the force vs. pin-opening displacement characteristic, the maximum crack length and the predicted laminate fracture energies it is concluded that the optimized fibre compressive fracture energy for IM7/8552 is in the range of $G_{1c}^C = 60 - 80\,\frac{kJ}{m^2}$.

6.3.3 Effects of Fibre Softening Options on Compressive Loading

Validation of the fibre softening option under compressive loading is performed with CC simulations. For this study, a fibre compressive fracture energy of $G_{1c}^C = 60\,\frac{kJ}{m^2}$ is used. The main effects of fibre softening options on fracture mechanic tests under tensile loading are also identified under compressive loading. The results are shown in Figure 6.14.

Figure 6.14 a) presents the results of **linear softening**. The results are shown and compared to exponential softening and the scaled experimental results. The force vs. pin-opening displacement characteristic of linear softening shows no significant difference to the exponential softening result.
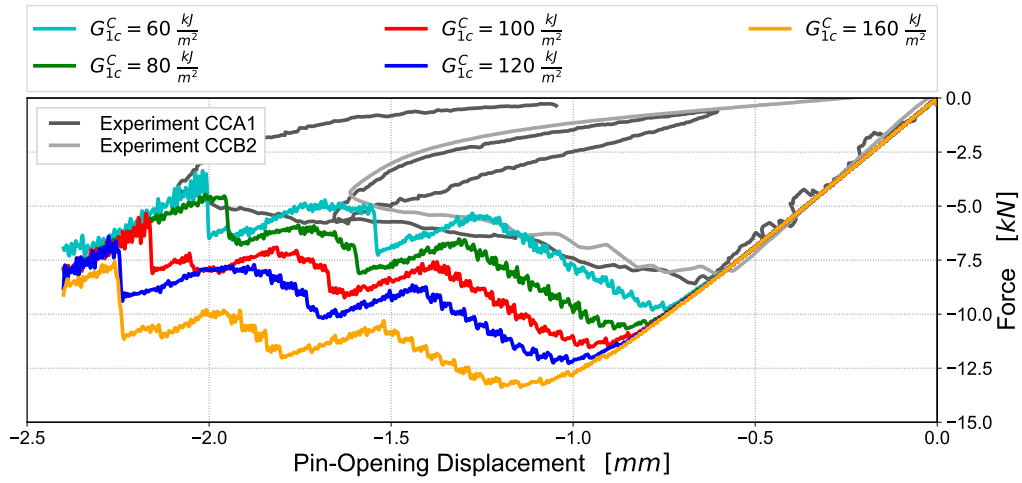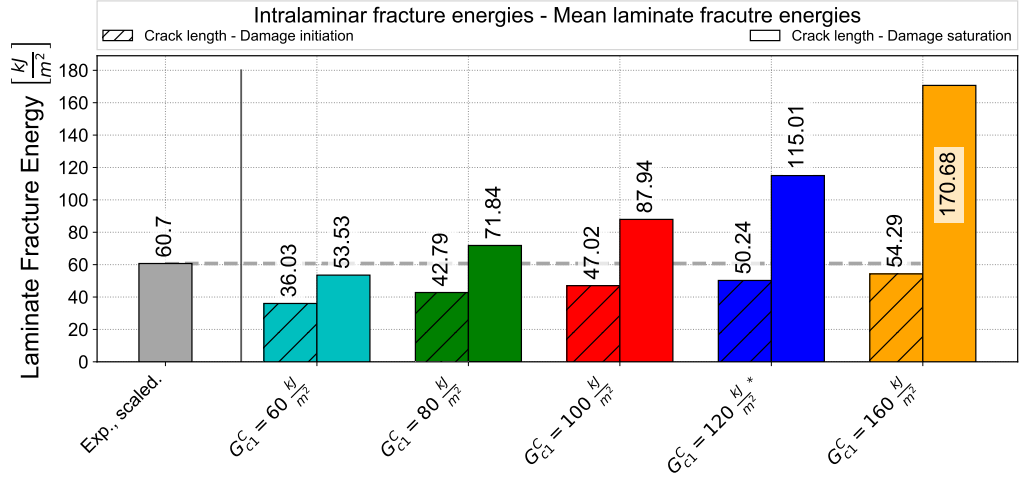
a) Force vs. pin-opening displacement characteristic
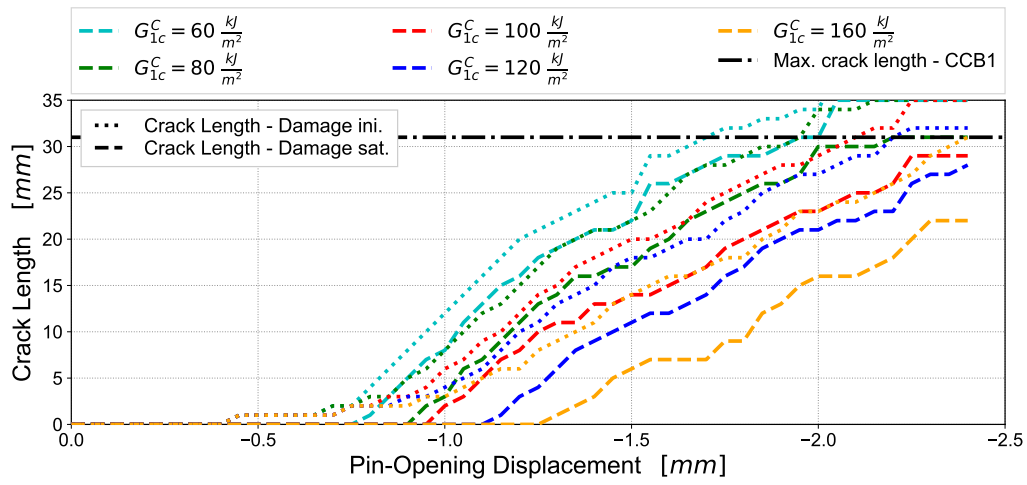
b) Crack length vs. pin-opening displacement

Figure 6.12: CC simulation - Validation of compressive fibre fracture energy; a) Force-displacement characteristics, b) crack length vs. pin-opening displacement

Figure 6.13: Laminate fracture energies predicted from CC simulations using different fibre compressive fracture energies

Minor differences are a higher peak force as well as slightly higher PODs of the secondary force drops in linear softening. The secondary force drops are the result of the additional damage zone due to contact. The reason for these differences is the lower post-peak stress-strain slope in linear softening which results in a higher strength of the laminate. This correlates with the findings of tensile loading on OCT specimens and the single-laminate element under compression in Section 5.3. A lower post-peak slope as the result of less damage increase and therefore a lower stiffness reduction in the elements. This affects the damage propagation of both the initial damage zone and the secondary damage zone due to contact. The evolution of the crack lengths in Figure 6.14 b) shows only minor differences between linear and exponential softening. The growth of the crack based on damage saturation is slightly higher for linear softening due to a lower damage saturation strain for the linear softening approach (see Figure 4.3 and Figure B.1).

The results of **brittle failure with residual stress** are shown in Figure 6.14 b). The effects of an increasing residual stress level are identified in a higher peak load and increased post-peak force level. This is more pronounced for increasing the residual stress up to 60% whereas no significant differences are shown for a further increase to 80% residual stress. This is contrary to the findings identified under tensile loading. However, the effects leading to these results are the same for both loading conditions. The increasing peak force for higher residual stress levels is due to a lower maximum fibre damage and therefore a higher stiffness of the elements prior to damage saturation and element erosion. The peak load of 20% residual stress level correlates well with the experimental results. A flattened force curve for lower residual stress levels was also reported by Zobeiry [154] under tensile loading. The flattened force curve is explained by a reduced propagation of the crack based on damage saturation for 20% residual stress as shown on the right of Figure 6.14 b). This is due to a higher saturation strain for 20% residual stress level compared to the other investigated
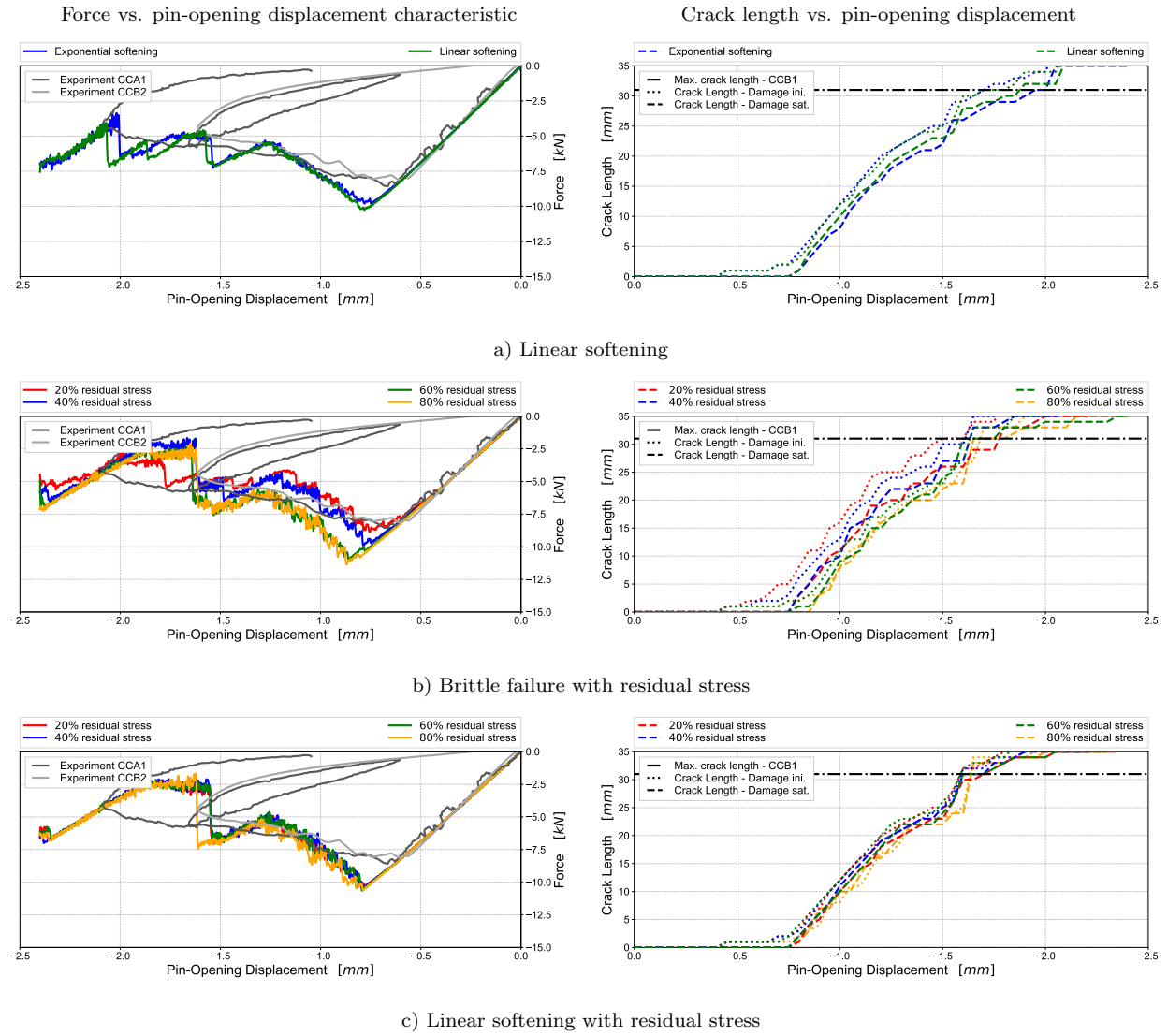
residual stress levels. Increasing the stress level to 40% results in a steeper force curve. However, this effect is less pronounced for further increase of the stress level. For higher POD, the force level of the simulation with 20% residual stress is lower compared to experimental results. Whereas for 60% and 80% residual stress, the post-peak force is higher up to the distinctive force drop indicating the initiation of the second damage zone. The force drop is more pronounced for higher force level due to the higher strain energy that is released with crack propagation in both damage zones.

Figure 6.14 c) presents the effects of **linear softening with residual stress** under compressive loading. For this softening option, an increasing residual stress level has only minor influence on both the peak load and the post-peak force level. The peak load does not significantly change with the residual stress level. The post peak force level is slightly higher for 80% residual stress than for 20%. This is contrary to the findings identified in tensile loading where an increasing residual stress level results in a significantly higher peak force and higher post-peak force level. In compression, the main influence of the residual stress level is a higher POD of the distinctive force drop for 80% residual stress. The same tendency is also shown in the evolution of the crack length in Figure 6.14c). The effect of an increased residual stress level is identified only for 80% residual stress level.

The predicted compressive laminate fracture energies for different softening options are shown in Figure 6.15. The predicted fracture energies reflect the tendencies described in the previous sections. The numerical results are compared with the scaled experimental results of Zobeiry [154]. It is shown that the differences of the predicted laminate fracture energies are moderate for different softening options. For the softening options with residual stress level, it is shown that the laminate fracture energy increases with the residual stress level and this tendency is more pronounced for brittle failure than for linear softening with residual stress. Here, the fracture energy increases by 20 % when the residual stress level increases from 20 % to 80 % of the compressive fibre strength. This effect is contributed to the higher laminate strength for increasing residual stress level. However, for linear softening with residual stress, the effect is less distinctive and the increase in laminate fracture energy from 20 % to 80 % residual stress level is less than 2 %. These tendencies are the same as the effects identified on the single laminate element under compression. This shows once more, that effects of damage evolution have the same effects on different levels of the building block.

From the validation of softening options on fracture mechanics tests under compression it is concluded that the major effect is seen on the peak force due to the different underlying damage propagation behaviour of different softening options. Whereas the influence on the predicted laminate fracture energy is less pronounced compared to the effects of the compressive fibre fracture energy.

The influence of material input on the Compact Compression is investigated in order to validate the compressive fibre fracture energy also for the US-Version of IM7/8552 as the material used for

Force vs. pin-opening displacement characteristic

Crack length vs. pin-opening displacement

a) Linear softening

b) Brittle failure with residual stress


c) Linear softening with residual stress

Figure 6.14: CC simulation - Effects of fibre softening options; Left: Force-displacement characteristics; Right: Crack length vs. pin-opening displacement; a) Linear Softening, b) Brittle failure with residual stress, c) Linear softening with residual stress
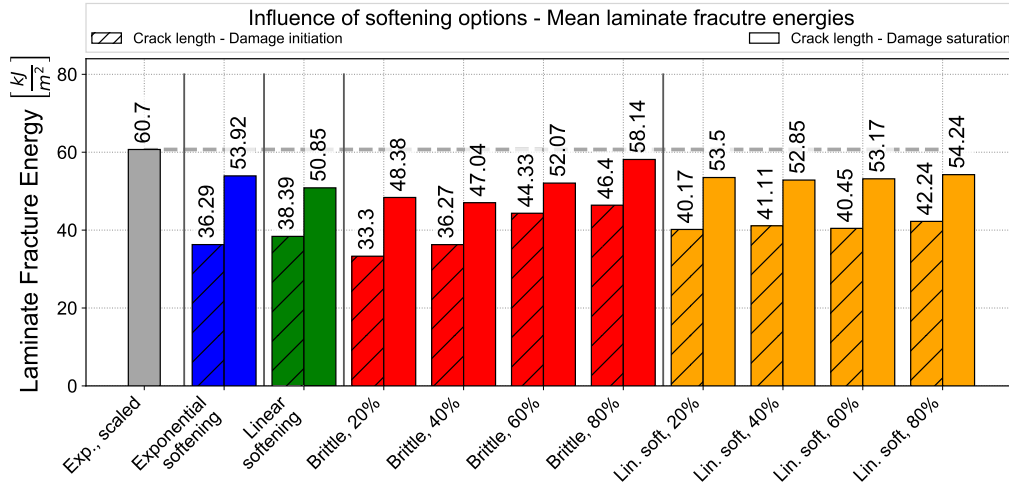
Figure 6.15: Laminate fracture energies predicted from CC simulations using different fibre softening options

progressive crushing. The results of the simulation with the two material versions of IM7/8552 are presented in Figure 6.16. In the force vs. pin-opening displacement characteristic, Figure 6.16 a), it is shown that the peak force and post-peak force level are higher for the US-Version of IM7/8552. The reason for this is identified in the higher transverse compressive strength of the US-Version. This also results in a higher post-peak force level. A higher post-peak force level correspond to the effects identified on single laminate level (see Figure 5.1). On the other hand, the crack length for both damage initiation and damage saturation are higher for the US-Version compared to the counterparts of the EU-Version. The predicted laminate fracture energies are approx. 20 % higher for the US-Version. This shows how distinctive the matrix behaviour under compression affects the results on the level of fracture mechanic tests. The fracture energy based on damage saturation is in the range of the scaled experimental results. Therefore, a compressive fibre fracture energy input of $G_{c1}^C = 60 \frac{kJ}{m^2}$ is validated to be suitable for the US-Version of IM7/8552.

6.4 Validation of the Stacked-Shell Modelling Approach

In the previous sections, the fibre fracture energies were validated using multi-layered shell models. This modelling approach was selected as a numerical efficient procedure to investigate and validate intralaminar damage models on the level of fracture mechanic tests. The stacked-shell approach with cohesive elements representing the interfaces is used on the level of progressive crushing where splaying and fragmentation are the major crushing modes. In order to validate the intralaminar fibre fracture energies for the stacked-shell approach, the OCT and CC specimens are modelled in detail with cohesive interfaces. In the stacked shell models, each layer of continuum shell elements represents a single ply of the laminate. The thickness of each cohesive layer is $0.01\,mm$ connecting the adjacent continuum shell layers through shared nodes. The in-plane meshes of both the shell
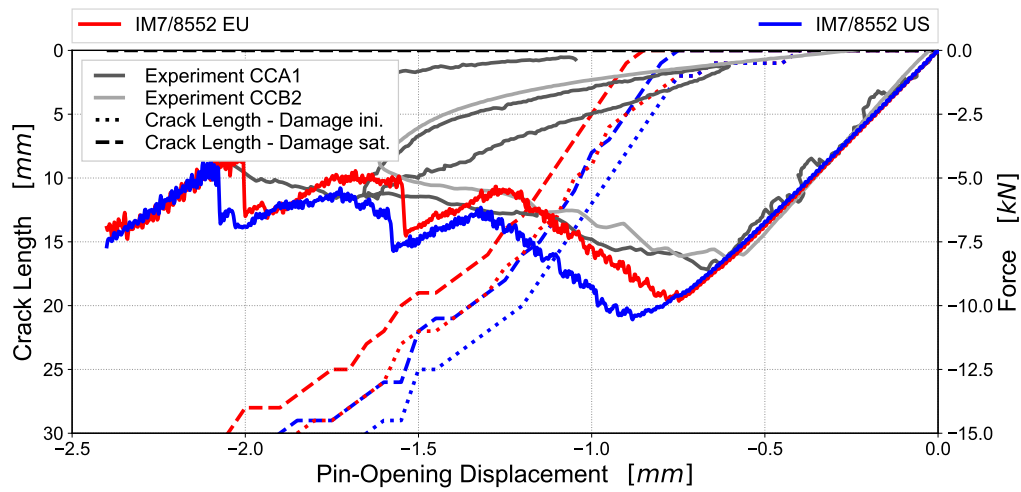
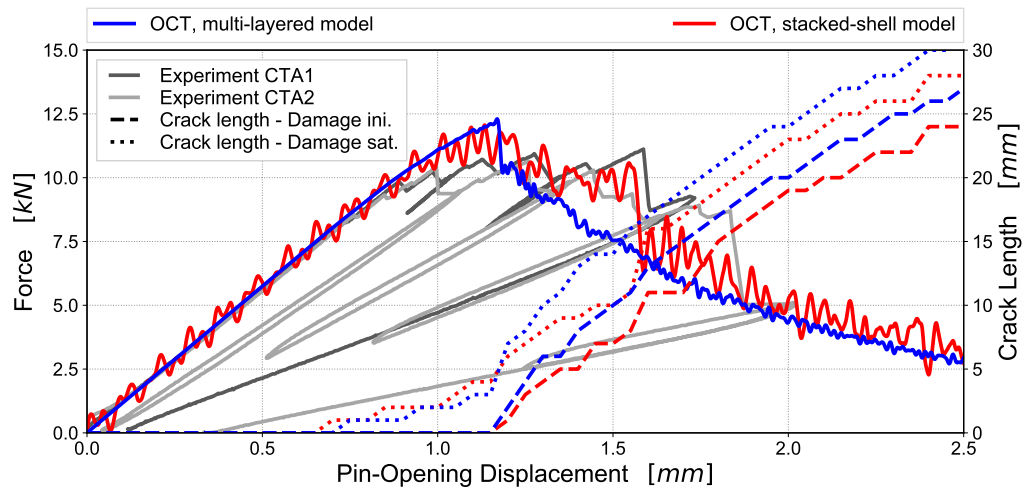a) Force vs. pin-opening displacement characteristic
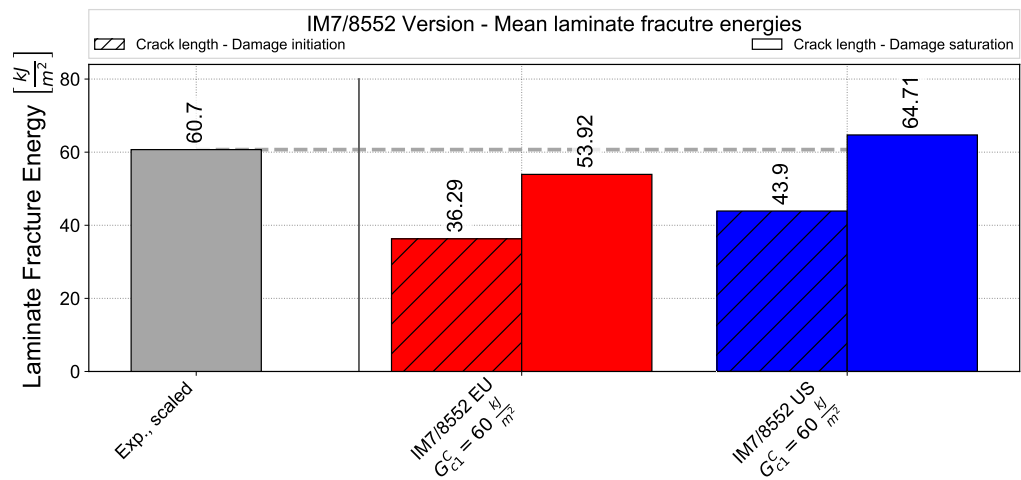
b) Predicted laminate fracture energies

Figure 6.16: CC simulation - Comparison of IM7/8552 material versions; a) Force-displacement characteristics, b) predicted laminate fracture energies

and cohesive layers corresponds to the meshes shown in Figure 6.1 a) and b) for OCT and CC models, respectively. One quarter of the laminate stacking sequence is modelled to avoid excessive computation times and the results are scaled to the full laminate thickness. A bi-linear traction-separation behaviour is used to model the interlaminar material behaviour. The material properties of the cohesive interface elements are listed in Table 3.2. The interlaminar fracture toughness is dependent on the represented interface as shown in Table 3.3. The fibre fracture energies are $G_{c1}^T = 120 \, \frac{kJ}{m^2}$ and $G_{c1}^C = 60 \, \frac{kJ}{m^2}$ and the EU-Version of IM7/8552 is used.

Figure 6.17 and Figure 6.18 present the force vs. pin-opening displacement characteristics and predicted laminate fracture energies of the OCT and CC stacked-shell simulations, respectively. The results of the multi-layered shell models of the previous sections are shown in comparison. Figure 6.17 shows that for OCT simulations the force vs. pin-opening displacement characteristics of both modelling approaches are similar. Especially the pre-peak force is the same for both modelling approaches. From this, it is concluded that modelling of the interlaminar behaviour with cohesive material parameters reported in literature has no significant influence on the stiffness in the linear-elastic region of the OCT specimen. The ultimate laminate strength is slightly lower for the stacked-shell model whereas the post-peak force level is higher compared to the multi-layered shell model. The cracks of both damage initiation and damage saturation start to grow at the same POD for both modelling approaches. Crack growth is higher in the multi-layered shell model compared to the stacked-shell model. This results in higher predicted laminate fracture energies for the stacked-shell model. The predicted laminate fracture energy based on damage saturation is slightly higher than the maximum fracture energy reported from the experiments. However, the difference is marginal with less than 2 %.

The results of the CC-simulations are presented in Figure 6.18. In the elastic domain of the force vs. pin-opening displacement characteristic, the stacked-shell model predicts a slightly lower stiffness compared to the multi-layered shell model. This might be due to early matrix damage in the 90° plies in the stacked-shell model resulting in early element erosion in these plies. The ultimate compressive strength and post-peak force level are marginally higher in the stacked shell model. Differences in the force characteristics are visible starting at $POD \approx 1.3 \, mm$. The force in the multi-layered shell model increases whereas the force in the stacked-shell model continuously reduces until the establishment of the secondary contact zone due to contact at $POD \approx 1.8 \, mm$. The reason for this discrepancy is identified in the contact modelling algorithm. The definition of the search radius in the contact algorithm identifying contact is dependent on the modelled ply thickness. In the multi-layered shell model, the total laminate thickness is modelled in the single shell element layer. In the stacked-shell model, each ply is modelled by an individual shell layer. This results in a larger search radius in the multi-layered shell model and therefore contact at a lower POD. As a result, the force is artificially increased leading to a higher predicted laminate fracture energy. On the other hand, the contact softens the mesh-dependent effect of the notch width. This effect has to be kept in mind when comparing the force vs. pin-opening displacement characteristics of
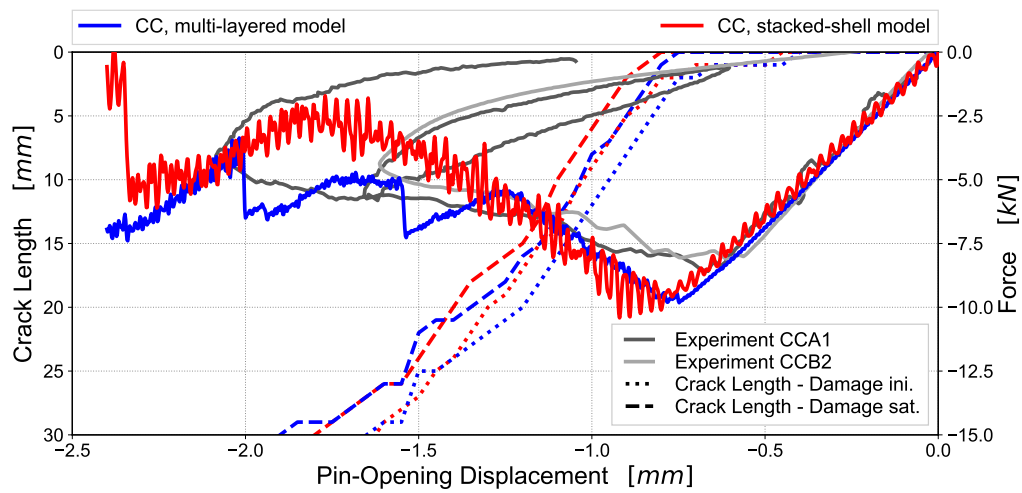
a) OCT - Force vs. pin-opening displacement characteristic and crack length
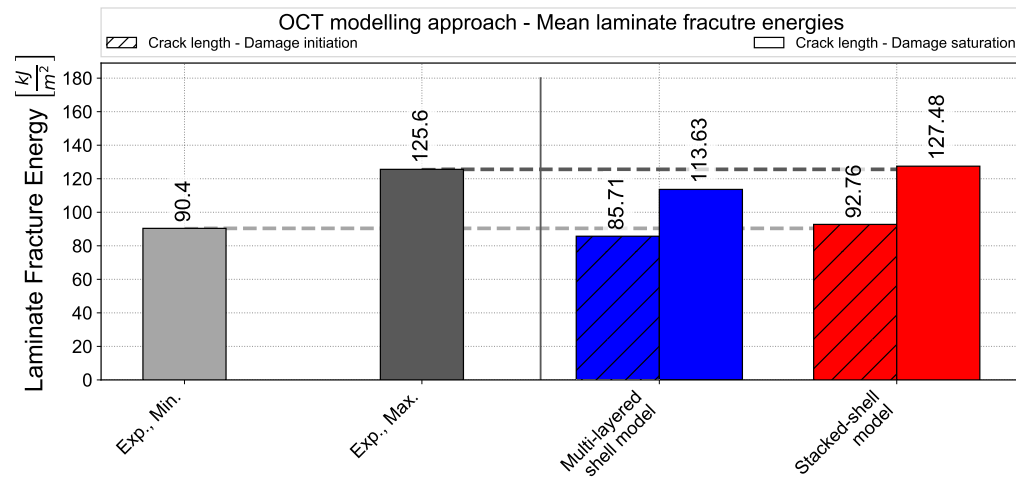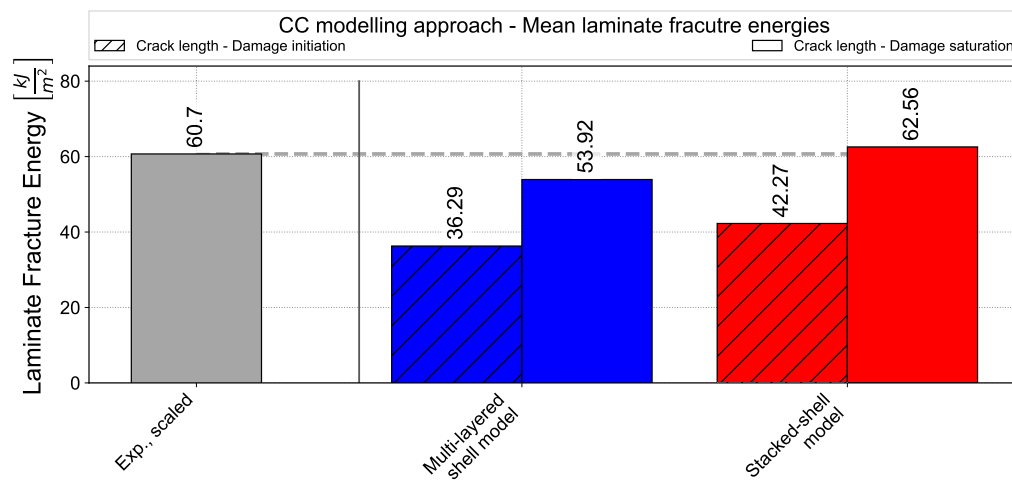

b) OCT - Predicted laminate fracture energies

Figure 6.17: Comparison of OCT results obtained with multi-layered shell and stacked shell models

a) CC - Force vs. pin-opening displacement characteristic and crack length

b) CC - Predicted laminate fracture energies

Figure 6.18: Comparison of CC results obtained with multi-layered shell and stacked shell models

the two modelling approaches. Comparing the predicted laminate fracture energies shows that the stacked-shell model predicts a higher fracture energy compared to the multi-layered shell model. A compressive fibre fracture energy of $G_{c1}^C = 60\,\frac{kJ}{m^2}$ seems to be suitable for the stacked-shell modelling approach whereas for the multi-layered shell model, the predicted laminate fracture energy is less than the scaled experimental result. In Figure D.5 in Appendix D.2, the results are shown without contact modelling. Here, similar results are obtained for the two modelling approaches for both the force vs. pin-opening displacement characteristic and predicted laminate fracture energies.

By comparing the two modelling approaches, it is shown that the validated fibre fracture energies obtained from computational efficient multi-layered shell models are also valid in stacked-shell models with cohesive interfaces for the investigated laminate. However, it should be noted that changing the laminates stacking sequence could result in differences of the modelling approaches. In laminates where interlaminar failure is more pronounced, e.g. in blocked laminates where plies with the same fibre orientation are stacked together, the ability of the model to predict interlaminar damage might result in differences of the modelling approach [20].

6.5 Summary and Conclusion of Validation on Fracture Mechanics Test

In this chapter, the global behaviour of the ABQ_DLR_UD progressive damage model was investigated in tension and compression by the simulation of Over-height Compact Tension (OCT) and Compact Compression(CC) specimens. As reported in literature, these specimens were found to produce stable and self-similar intralaminar crack growth under tensile and compressive loading, respectively. Experimental test data published in literature were used for validation. The stacking sequence of the laminate was identical to the level of single-laminate element simulations. Therefore, correlations between the effects identified on fracture mechanic tests and the laminate behaviour on macro-scale level were identified. The numerical results were validated qualitatively with force vs. pin-opening displacement characteristics and the evolution of crack-length vs. pin-opening displacement. A quantitative validation was performed by the determination of the laminate fracture energies which took into account the dissipated energy during the progressive damage process and the crack length. For OCT and CC simulations, the crack length was defined on fibre damage and included both fibre damage initiation and fibre damage saturation. With these two definitions, a range of potential crack lengths and predicted laminate fracture energies was defined and used for validation. Following the research questions of this work, the influence of discretization options in terms of element size as well as different fibre softening options were investigated. The main outcome of the study on the level of fracture mechanic tests is the calibration of the fibre fracture energies and fibre softening options for the simulation of progressive axial crushing. The multi-layered shell approach was used for validation of the OCT and CC specimens. The comparison of the experimental and numerical results of the CC-specimen showed discrepancies in the initial stiffness of the specimen. These were attributed to compliance of the test setup which was not

modelled in the simulation. To compare the results, the displacement of the experimental results was scaled to match the numerical results in the pre-peak regime. From this, a factor was determined to scale the reported laminate fracture energies which were used for validation. The fibre fracture energies were also validated for the stacked-shell approach.

The following conclusions of the simulation of fracture mechanic tests are drawn:

- The shape of the laminate stress-strain characteristic dominated by the fibre behaviour was identified as the main factor influencing the force vs. pin-opening displacement characteristic of the OCT and CC simulations. The stress-strain response of the laminate directly influenced both the force characteristic and crack propagation of the OCT and CC specimen. Effects of element size, fibre fracture energies and fibre softening options on the global response of the fracture mechanic tests were traced back to their influence on the stress-strain response on meso- and macro-scale level. In detail, the influence on the ultimate strength and/or the post-peak behaviour of the laminate.

- The effects of discretization options on fracture mechanic tests were investigated with crack band scaling as well as in models with disabled crack band scaling. In simulations of the OCT specimen with crack band scaling, an influence of element size on the maximum force was identified whereas the post-peak force characteristics showed no significant changes with the element size. In simulations with disabled crack band scaling in the model, the maximum force and post-peak force characteristic as well as the predicted laminate fracture energy showed a significant dependency of the element size. In simulations of CC-specimen with crack band scaling, the maximum force and post-peak force was lower for the smaller element size. However, without crack band scaling, this effect became more pronounced. It was concluded that crack band scaling is mandatory on the level of fracture mechanic tests of the building block to avoid mesh dependent results.

- The fibre fracture energies showed a major impact on the global response of both OCT and CC specimens. With increasing tensile and compressive fibre fracture energy, the maximum force, post-peak force level and predicted laminate fracture energy increased. The reasons were identified in an increase of both the ultimate laminate strength and post-peak stress slope on macro-scale level. As a result, the crack growth based on fibre damage saturation was reduced with increasing fibre fracture energy.

- The main impact of different fibre softening options was identified on the maximum force obtained in the OCT and CC simulations. Only minor influences were identified on the post-peak force level. The effects of fibre softening options were traced back to the macro-scale level and were identified due to an increased ultimate strength of the laminate and variations of the post-peak strain-softening slope. The influence of the fibre softening options on the predicted laminate fracture energy is mainly due to variations of the maximum force. From this, it was concluded that fibre softening options mainly influence the maximum force of OCT and CC

simulations. Compared to the influence of fibre fracture energies which influence both the maximum and the post-peak force.

- The tensile fibre fracture energy was validated as $G_{c1}^T = 120 \frac{kJ}{m^2}$ for both material versions of IM7/8552 as well as for both multi-layered shell and stacked shell models. The compressive fibre fracture energy was validated to be in the range of $G_{c1}^C = 60 \frac{kJ}{m^2}$ to $G_{c1}^C = 80 \frac{kJ}{m^2}$ depending on the material version of IM7/8552 and the modelling approach.

- The level of fracture mechanic tests of the building block approach was identified as a suitable level for calibration and validation of meso-scale continuum damage models. Experimental results of OCT and CC tests were used to calibrate the tensile and compressive fibre fracture energies, respectively. Numerically efficient multi-layered shell models can be used to calibrate the fibre fracture energy input and fibre softening approach. With the calibration of fibre fracture energies, the material input data set is fixed, and no further calibration on higher building block levels is necessary.

7 Numerical Analysis of Progressive Crushing

This chapter describes the building block level of progressive crushing. A numerical study of the self-supported DLR segment is performed with the objective to investigate the finite mesh- and element size dependency. The influence of different fibre softening options on the crushing behaviour is performed on the DLR segment. The second part of this chapter considers the contribution of DLR to the CMH-17 CWG Round Robin 3 simulation campaign. The simulation methodology developed in this work is validated for progressive crushing using flat coupon specimens with experimental results provided to the CHM-17 CWG. With splaying as a major crushing mode identified in flat coupon crush tests, the influence of the modelling approach is shown by comparing the results of a computational efficient multi-layered shell approach and the stacked-shell modelling approach.

7.1 CMH-17 Crashworthiness Working Group

The work presented in this chapter is the contribution of the author to the numerical Round Robin phase 3 campaign of the CMH-17 CWG. DLR is contributing to the working group as one of the analysis teams. One of the main objectives of the CMH-17 CWG is to generate guidelines and best practices for the numerical prediction of crashworthy structures in commercial FE codes [9]. Due to the wide range of commercial FE-codes, material models and modelling approaches, an agreement is required for regulatory approval of certification by analysis. In previous Round Robin phases 1 and 2, structures at coupon to sub-structural level of different geometry and failure behaviour were experimentally tested and numerically modelled. Phase 1 consists of a corrugated plate specimen [70] which was stable against buckling and behave similar to the DLR segment [62]. In phase 2, three coupon specimens, a small corner segment, a C-channel specimen and a square tube specimen were considered. The C-channel specimen of phase 2 was considered as a combination of two corner segments and a flat segment whereas the square tube was an extension of the C-channel specimen with four corner segments and four flat coupon segments. In the scope of the Round Robin 3 simulation campaign, a flat coupon and C-channel crush specimen with a slightly different cross-sectional geometry and different CFRP material compared to phase 2 were experimentally tested. The C-channel specimen consists of three flat segments and two small corner segments. Multiple analysis teams using different finite element codes, material models and modelling approaches are tasked to predict progressive crushing of flat coupon and C-channel specimens made of the US-Version of IM7/8552. The C-channel specimen has a similar cross-section

as the C-channel stanchions in the Boeing B787 sub-cargo floor structure [7] (see Figure 1.1). Experimental results of the flat coupon crush tests in terms of force-displacement characteristics and SEA-values are provided to the analysis teams for validation of the numerical models. The simulation methodology developed in this work is used for prediction and validation of the flat coupon crush specimen. Experimental results of the C-channel crush tests are not provided and therefore, the C-channel blind predictions are not presented in this work. Guidelines and best practices are derived from the simulation methodology and submitted to the CMH-17 CWG for consideration in the CMH-17 handbook.

7.2 Numerical Study of the DLR Crush Segment

At the building block level of progressive crushing a numerical study of the self-supported DLR segment is performed. In the scope of the CMH-17 CWG, self-supported specimens were discussed, tested and simulated already in Round Robin phase 1 and 2. In the past, the self-supported DLR segment has been investigated in various studies [62–64, 89] both experimentally and numerically and proved to be suitable to investigate composite materials. The transient-dynamic crush behaviour of the self-supported DLR segment was identified in the past as mainly intralaminar fragmentation. Due to the intralaminar dominated failure mode, the DLR segment is identified as a helpful intermediate validation step between the building block level of fracture mechanic tests and the simulation of progressive crushing of flat coupon and C-channel specimen which provide a more complex crush response including fragmentation, splaying and partly also tearing in the corner sections. Self-supported crush segments are also suitable for comparison of numerical damage models, modelling approaches and finite element solvers, as the test boundary conditions are simple and allow precise representation on the numerical models.

The numerical study carried out on the DLR segment considered the investigation of discretization options, in detail, the finite mesh- and element size dependency. The investigation of the fibre softening on the level of progressive crushing is also performed on the DLR segment. Even though the self-supported DLR segment has been investigated in various studies in the past, no experimental results are available for material system IM7/8552.

7.2.1 Model Description

The numerical study carried out on the DLR segment is performed on numerical efficient multi-layered shell models. The model is shown in Figure 7.1. The geometry corresponds to the DLR segment tested by David [62], David et al. [63, 64] and Kohlgrueber [56] (see Figure 2.2), with the length of the model corresponding to the free length of the tested specimens and laminate thickness of $t_{lam} = 2.0\,mm$. The single shell layer represents a quasi-isotropic laminate with stacking sequence $[90/\pm 45/0]_{2s}$ which is the same layup as laminate 'QI-1' in the flat coupon

test programme described in Section 7.3. The material system of this study is the US-Version of IM7/8552 (see Table 3.1). Conventional shell elements with reduced integration (type 'S4R') are used to model the DLR segment. The impact plate is modelled as a rigid body with the reference node located in the center of gravity. The bottom nodes of the DLR segment are fixed in all degrees of freedom. A velocity boundary condition with constant velocity of $2.0 \frac{m}{s}$ is applied to the rigid body reference node of the impact plate. With these simple boundary conditions the test setup is precisely modelled. The 45° chamfer trigger is modelled in a simplified manner: The modelled thickness of the laminate is increased over the first three element rows, as shown in the rendered view in Figure 7.1. Contact is modelled between the impact plate and the DLR segment with a coefficient of friction of $\mu_{plate} = 0.2$ as well as self-contact of the DLR segment with $\mu_{segment} = 0.4$. The simulation time is $t_{sim} = 10.0 \, ms$. Field output is written every $0.25 \, ms$ and history output every $0.01 \, ms$. A Butterworth low-pass filter with $20 \, kHz$ cut-off frequency is used to filter the numerical results. The investigation of discretization options considers three mesh types and three element sizes. The mesh type variations are shown in Figure 7.1. A structured mesh, a skewed mesh with 10° inclined element edges and an unstructured mesh are investigated. Elements with characteristic lengths of $0.5 \, mm$, $1.0 \, mm$ and $2.0 \, mm$ are considered. The structured mesh is a uniform mesh with identical element sizes. In the skewed mesh model, the middle part of the DLR segment is modelled with inclined element edges whereas the region at the top and bottom are meshed in an unstructured manner. In all three mesh type variations, the impact plate is meshed with a structured mesh and a uniform element size of $2.0 \, mm$.

7.2.2 Mesh Type and Element Size Study

Following the research question of this work, the investigation of discretization options on the level of progressive crushing is performed on the DLR segment. Two types of discretization options are investigated. In addition to the investigation of the mesh size dependency, which was also performed on the lower levels of the building block, the influence of the mesh types described in the previous section is investigated. Each mesh type is meshed with three characteristic element lengths of $0.5 \, mm$, $1.0 \, mm$ and $2.0 \, mm$. In the unstructured mesh, the characteristic element length varies around the mean selected element length due to the approach of calculating the characteristic length from the area of the elements in Abaqus/Explicit (Equation (4.6)) and the randomized meshing. The discretization options are investigated in terms of their influence on the force-displacement characteristic and absorbed energy. The force-displacement characteristics are determined with the contact force acting on the impact plate plotted over the displacement of the impact plate reference node. The absorbed energy is the external work extracted from the history output of the simulation. The results of the study on discretization options are shown in 7.2.
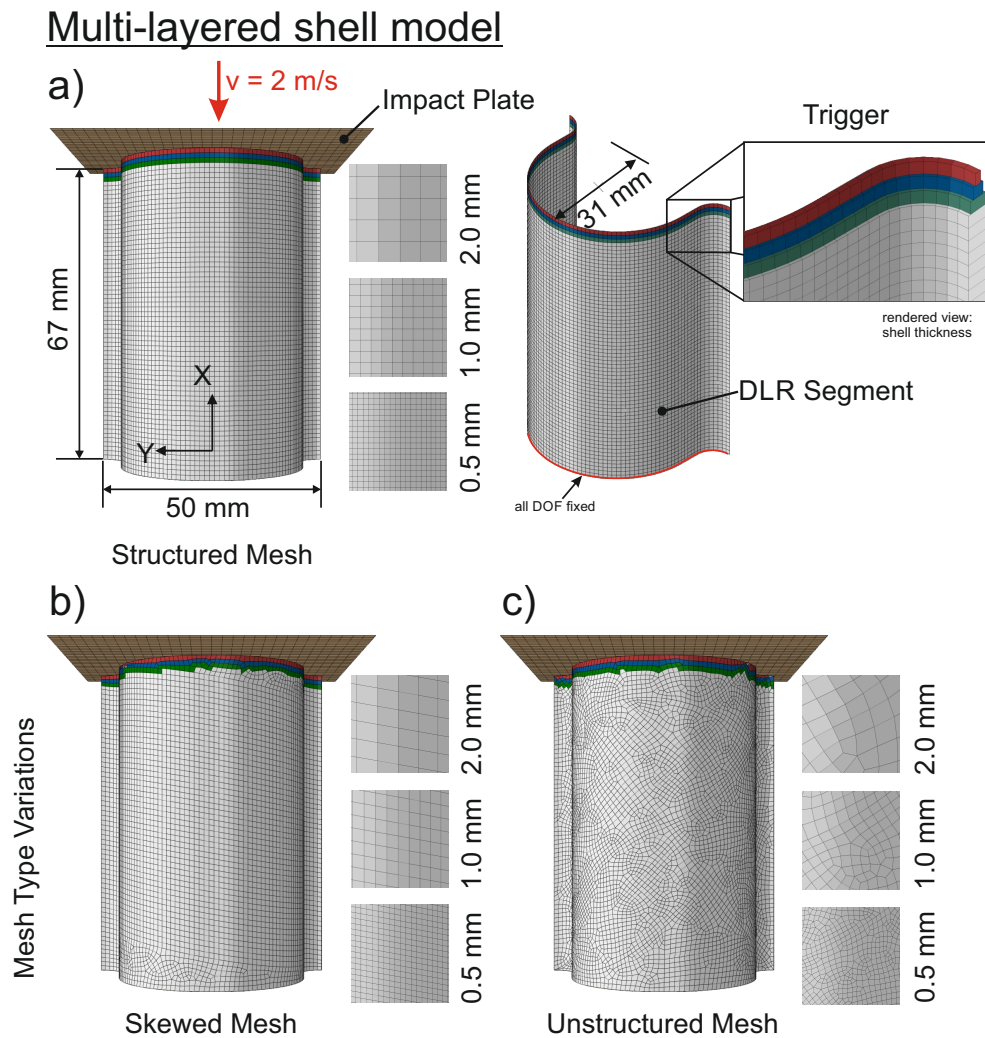
Figure 7.1: Numerical model of the self-supported DLR segment - Multi-layered shell model to study the influence of discretization options. a) Structured mesh; b) Skewed mesh; c) Unstructured mesh

a) Structured mesh

b) Skewed mesh

c) Unstructured mesh
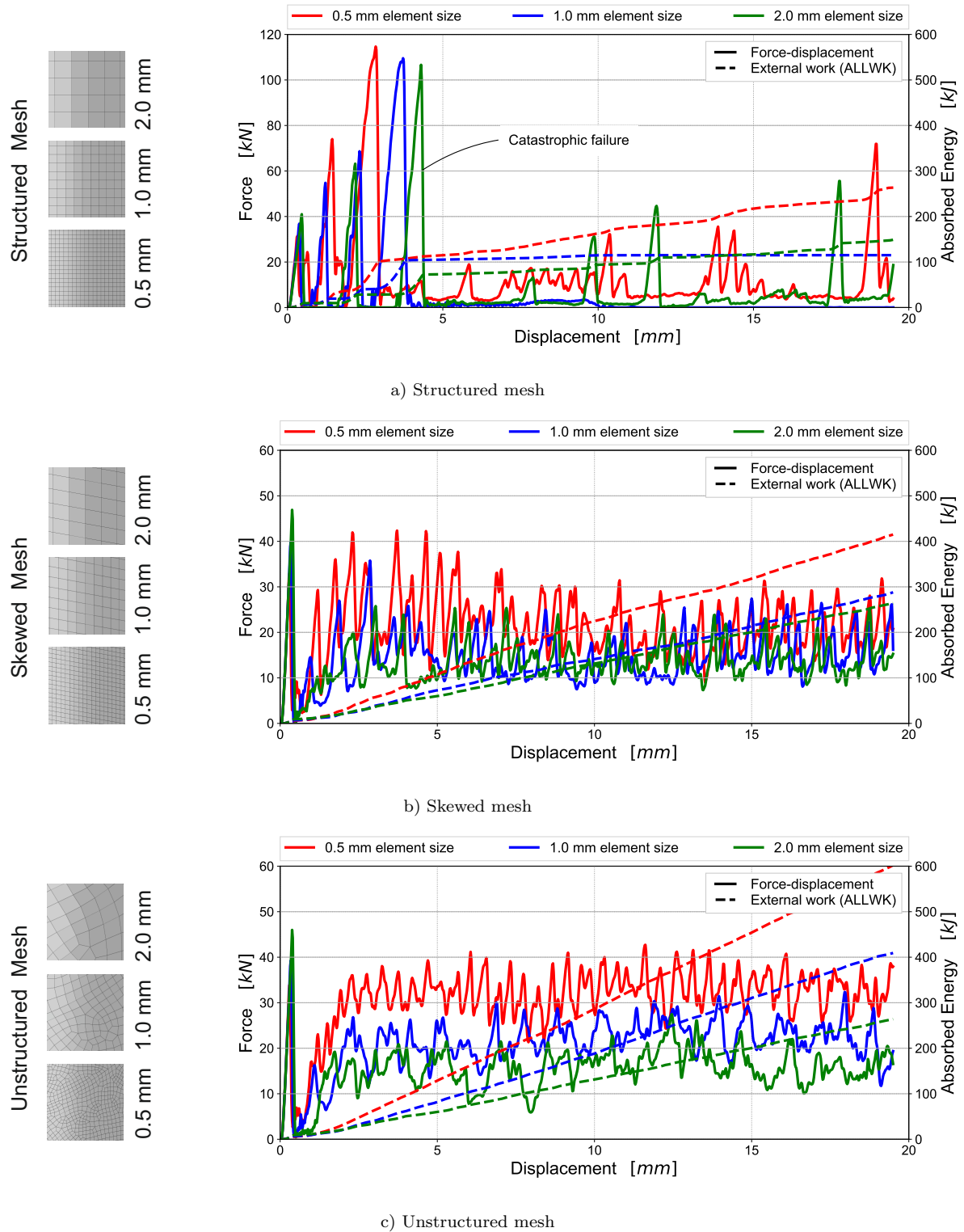
Figure 7.2: Numerical study of a self-support crush segment - Influence of discretization options. Investigation of three mesh types: Structured mesh, skewed mesh and unstructured mesh and three element sizes, $0.5\,mm$, $1.0\,mm$ and $2.0\,mm$. Force-displacement characteristic and evolution of absorbed energy

Influence of the Mesh Type

Figure 7.2 presents the results of the three different mesh types and three element sizes. At first, the influence of the mesh type on progressive crushing is discussed. In the simulations with structured meshes, Figure 7.2 a), the typical force-displacement characteristics driven by significant force spikes [89] are identified for all element sizes. Simultaneous failure and element deletion of entire element rows lead to force drops and subsequent unrealistic high force spikes when the next undamaged element row gets in contact with the impact plate. In this way, the force spikes reach force levels which are significantly higher than the failure initiation force of the triggered specimen. This is shown in Figure 7.2 a) where the initial force spikes increase to a maximum value of over $100\,kN$ after the trigger region is crushed down and the impact plate contacts the full-thickness element rows. Every force spike represents failure of one element row. As a consequence, the excessive force spikes lead to catastrophic failure of the specimen. This is shown in a distinctive force drop followed constantly low force levels. Also, the absorbed energy remains nearly constant (for $1.0\,mm$ and $2.0\,mm$ element size) after the maximum force spike. Additional force spikes are identified due to self-contact of the failed parts of the DLR segment.

In contrast, the skewed and the unstructured mesh provide continuous damage, failure and erosion of elements in the crush zone as shown in Figure 7.2 b) and c), respectively (note the different scales of the force axes in Figure 7.2 b) and c) compared to Figure 7.2 a)). The force increases during the crushing of the trigger and remains nearly constant through the crushing process. As a result, the absorbed energies constantly increase. This shows that a progressive crushing behaviour is achieved in the simulations.

The different crushing behaviour dependent on the mesh type is also shown in Figure 7.3. The contour plot of the fibre compressive damage (SDV5) is shown for the models with $1.0\,mm$ element size at a crush distance of $\approx 4.0\,mm$. In the structured mesh, damage spreads over the complete length and catastrophic failure is identified in the middle and at the bottom of the segment. The crush distance of this contour plot coincides with the maximum force spike in the force-displacement characteristic. For skewed and unstructured mesh types, elements are damaged in a defined crush zone on top of the specimen. The vast majority of elements are undamaged. Due to the inclined or unstructured orientation, elements of the crush segment are subsequently damaged while the impact plate is consistently in contact with elements of the crush segment as shown in the detailed view. The elements are successively damaged which results in the establishment of a progressive crushing behaviour and a constant crush force. This results in a more realistic representation of the crushing processes as the behaviour of the structured mesh. This mesh study showed the influence of the mesh type on the predicted crushing behaviour. A progressive damaging of the elements is mandatory to achieve a progressive crushing behaviour. Also, in an application at larger structural scales, the high load spikes observed for the structured mesh may result in unrealistic damage in the structure.
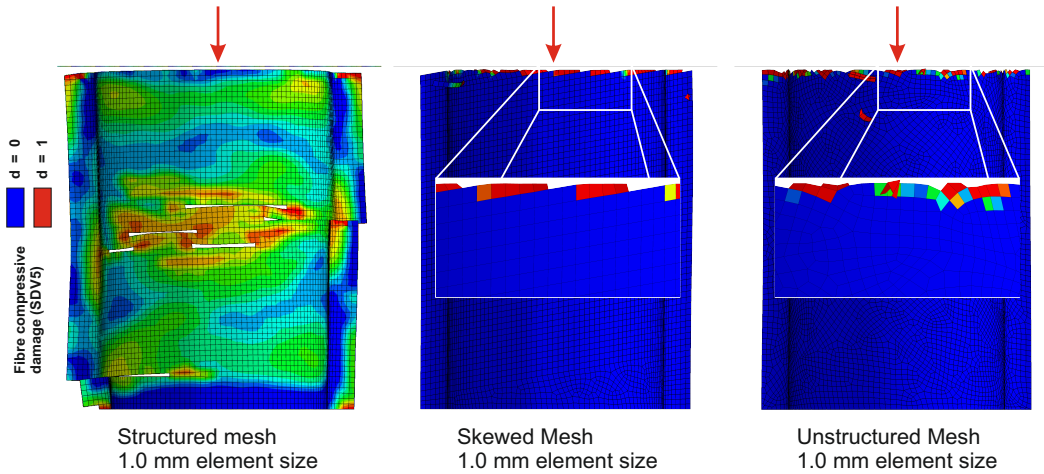
Figure 7.3: Contour plot of fibre compressive damage (SDV5) on the DLR segment - Influence of mesh type on the damage behaviour. Characteristic element length of the three mesh types is $1.0\,mm$. Contour plot at a crush distance of $\approx 4.0\,mm$

Influence of the Element Size

The second study of discretization options contains the investigation of the mesh size. The results of the three element sizes for each mesh type are shown in Figure 7.2. The main conclusion drawn from this study is that the force and absorbed energy decrease with increasing element size from $0.5\,mm$ to $2.0\,mm$. However, the influence of the element size is dependent on the mesh type. In the structured mesh, Figure 7.2 a), it is shown that the force spikes reduce with increasing element size and the maximum force spikes are identified in the mesh with $0.5\,mm$ elements. Due to the catastrophic failure behaviour of the structured mesh, investigating the influence of the element size over the complete crushing distance is difficult. After crushing down the trigger region, failure and deformation of the model and contact of different parts of the element influence the force characteristic and the absorbed energy in a higher degree than the element size. Therefore, the influence of element size is further investigated for the skewed and unstructured meshes where a progressive crushing behaviour is obtained.

In the simulations with skewed mesh, Figure 7.2 b), both the force level and as a consequence the absorbed energy decrease with increasing element size. This effect is more pronounced for increasing the element size from $0.5\,mm$ to $1.0\,mm$ than for further increase to $2.0\,mm$. In the simulations of the unstructured mesh type, Figure 7.2 c), the same tendency is identified. However, the effect of decreased force and absorbed energy with increasing element size is about linear over the range of investigated mesh sizes. Increasing the element size from $0.5\,mm$ to $1.0\,mm$ reduces the absorbed energy from $602.25\,kJ$ to $409.21\,kJ$ (-32.1%). Further increase of the element size to $2.0\,mm$ results in a decrease of the absorbed energy to $302.5\,kJ(-26.1\%)$. The explanation of this effect is identified in Bazant's crack band scaling approach implied in the continuum damage mechanics model ABQ_DLR_UD. Moreover, this effects all damage models using the crack band
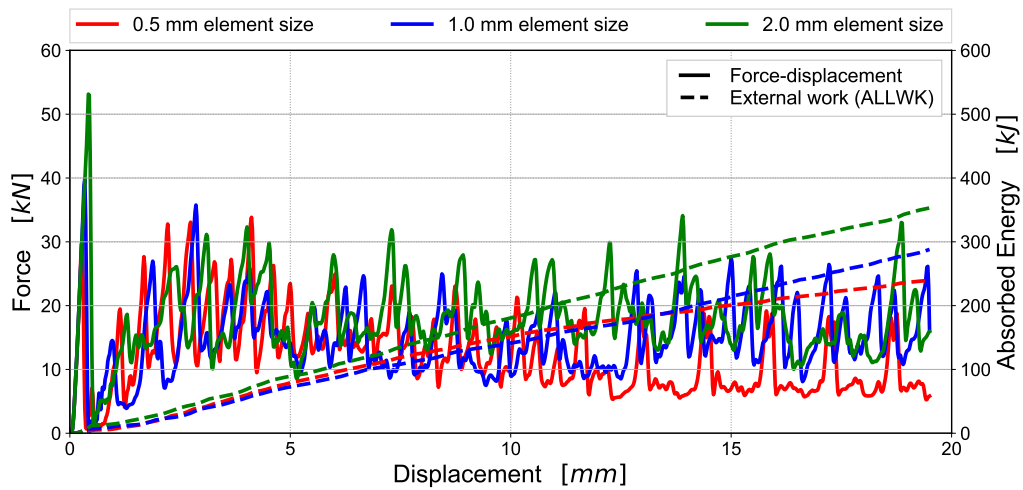
a) Skewed mesh with variable element size
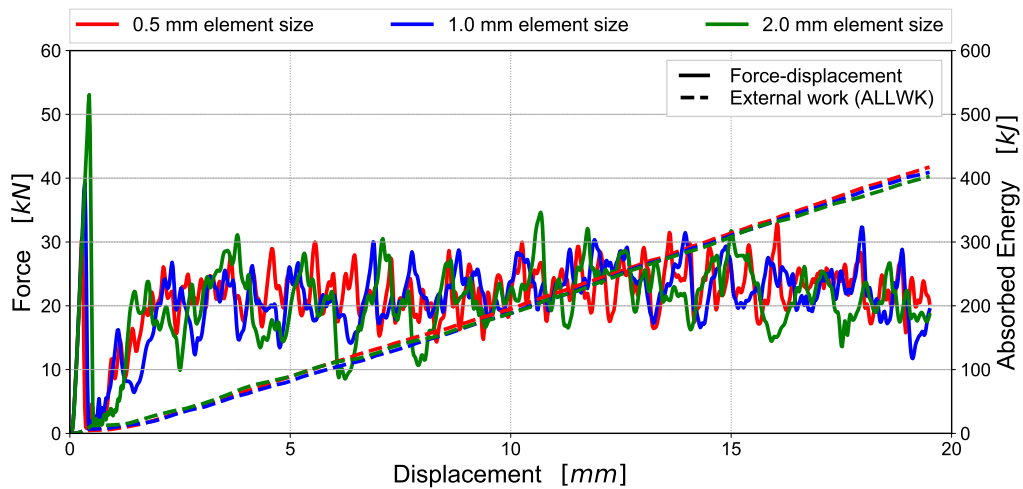
b) Unstructured mesh with variable element size

Figure 7.4: Force-displacement characteristic and evolution of absorbed energy for a) skewed mesh and b) unstructured mesh type with variable element size. Crack band scaling is disabled in the models

scaling approach independent of the FE-code as shown in the work of Reiner, Feser and co-workers [22]. The results of the simulations of fracture mechanic tests in Section 6.3.1 as well as on single laminate level in Section 5.2.1 proofed that Bazant's crack band scaling approach can be applied to simulate damage evolution in composites. The reason is that the damage zone is confined to a narrow band similar to a single crack proceeding through the laminate. Investigation of the element size effects in OCT and CC simulations demonstrated that activating crack band scaling resulted in similar results for different element sizes. Also on single-laminate level shown in Figure 5.4, activating crack band scaling resulted in mesh independent results assuming that failure of the single laminate is crack-like. In contrast, the simulation of progressive axial crushing where fragmentation is the major failure mode clearly indicate that the application of crack band scaling results in mesh dependent behaviour. Figure 7.2 shows that the application of crack band scaling leads to severe mesh-dependent predictions of the crush force as well as absorbed energy. In Figure 7.4, the results of the skewed mesh and unstructured mesh with variable element size are shown when crack band scaling is disabled in the model. The crack band approach is disabled by scaling the fibre fracture energy input to achieve the fracture energy density of $l^* = 1.0\,mm$. For $l^* = 1.0\,mm$ the fracture energy density corresponds to the fracture energy of the material. Without crack band scaling, the results of progressive axial crushing become independent of the element sizes. This effect is more pronounced for the unstructured mesh than the skewed mesh. However, the effect is clearly visible for both mesh types. The effect leading to this significant finding is illustrated in Figure 7.5. Here, a volume with a cross-sectional area of $2.0\,mm$ x $2.0\,mm$ is discretized with different characteristic element lengths ranging from $l^* = 0.5\,mm - 2.0\,mm$. The top edge of the volume is loaded in compression to achieve axial crushing. If crack band scaling based on the element length l^* is applied, the dissipated energy in each row of crushed elements is equal to the material fracture energy G_f. This is reasonable in fracture mechanics if damage is crack-like and confined to a narrow band. However, in progressive crushing, this effect is repeated for each element row until the total volume is crushed down. If each element row is scaled by the crack band approach, the fracture energy adds up. The total dissipated energy therefore becomes a multiple of the materials fracture energy G_f. On the other hand, if crack band scaling is disabled in the model, the dissipated energy in each element row is reduced with the element size. This results in mesh-dependent energy dissipation in the crack-like damage progress however assures that the total dissipated energy of a fixed volume remains constant for different element sizes. This shows the main difference of single crack propagation and progressive crushing. In fracture mechanics, a crack is modelled which propagates within one element row. In progressive crushing, a damage zone is modelled which propagates through the element rows in the crushing process. Since crack band scaling is implied in ABQ_DLR_UD in the same way as for many different continuum damage mechanics models, it is strongly assumed that this finding generally applies to all CDM material models based on fracture energies independent of the FE-code.
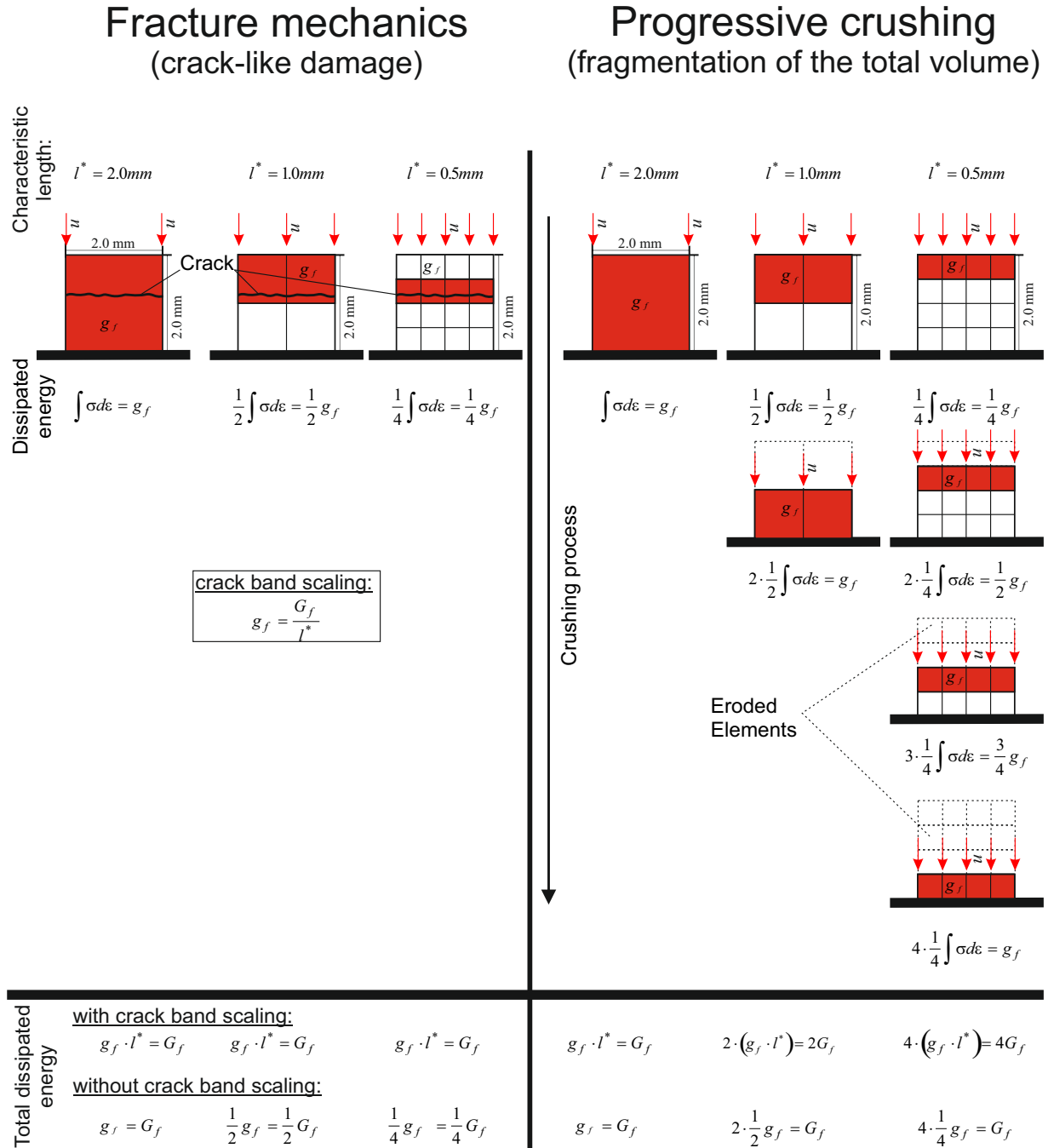
Figure 7.5: Schematic representation of the effect of crack band scaling on the calculation of the total dissipated energy in progressive crush simulations discretizing the mesh with different element sizes
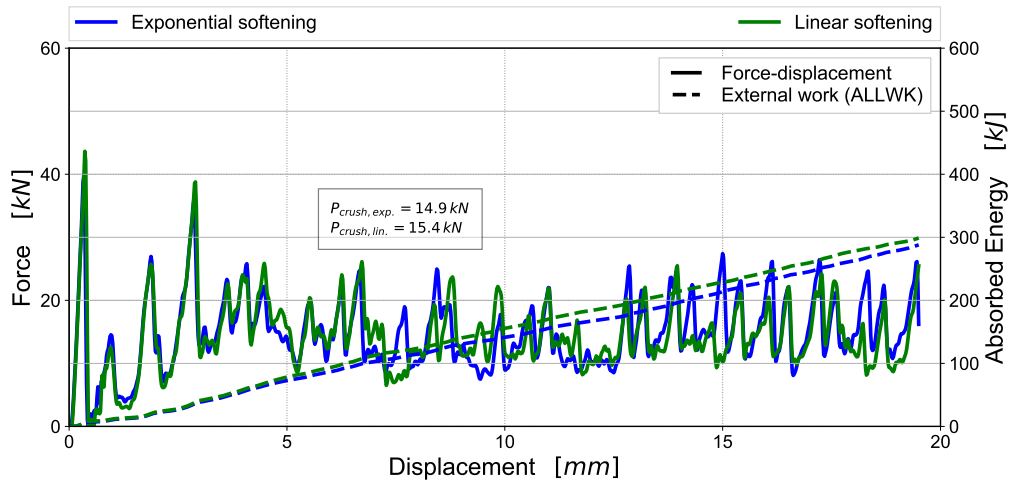
7.2.3 Influence of Fibre Softening Options on Progressive Crushing

The investigation of the influence of different fibre softening options on the level of progressive crushing is performed on the DLR crush segment. The skewed mesh type with $1\,mm$ element size is used for this study. The effects of linear fibre softening on the crush force in comparison with exponential softening is shown in Figure 7.6 a). The effects of brittle failure and linear softening with different residual stress levels are shown in Figure 7.6 b) and c), respectively. Comparing linear and exponential softening, the effects are small with a slightly higher absorbed energy and mean crush force (P_{crush}) for the linear softening determined between $\delta_0 = 5.0\,mm$ and $\delta_f = 20.0\,mm$ crushing distance. This effect correlates with the findings on the level of fracture mechanic tests and single laminate level. The effect of brittle failure, Figure 7.6 b), shows that the highest mean crush force and absorbed energy for this softening option is obtained for 20% residual stress level, followed by 80% residual stress being second highest for both mean crush level and absorbed energy. However, both quantities of this softening option are lower compared to the continuous softening options linear and exponential softening. This main tendency again correlates with the effects identified on fracture mechanic tests and single laminate element simulations. Linear softening with residual stress level, Figure 7.6 c), showed the lowest mean crush forces and absorbed energies of all softening options. Both quantities reduce with increasing residual stress level. This tendency is different compared to the behaviour identified on the other levels of the building block. This shows again the different failure behaviours of progressive crushing and fracturing. In crushing, the early erosion of the elements due to the lower erosion strains for higher residual stress levels results in reduced number of elements in the crushing zone which are in contact with the impact plate. Therefore, the contact force reduces. Whereas, in the simulation of fracture mechanic tests, the lower maximum fibre damage resulted in higher laminate stiffness and strength which delays initiation of the crack in the element row leading to higher force level.

7.2.4 Conclusion of Numerical Study of the DLR Crush Segment

Finally, before describing the validation of the simulation methodology in the following section, the results of the numerical study of the DLR crush segment are summarized.

- The selected mesh type in the numerical model of the DLR segment significantly influences the crushing behaviour, force-displacement characteristic, and therefore the predicted absorbed energy. A structured mesh resulted in significant and unrealistic high force spikes followed by catastrophic failure. The skewed and unstructured mesh provided continuous damage, failure and erosion which resulted in a constant force level and progressive crushing behaviour.

- The investigation of different element sizes showed significant mesh size dependencies in the models with skewed and unstructured meshes. Both the force level and as a consequence, the absorbed energy decreased with increasing element size. This effect was traced back to the
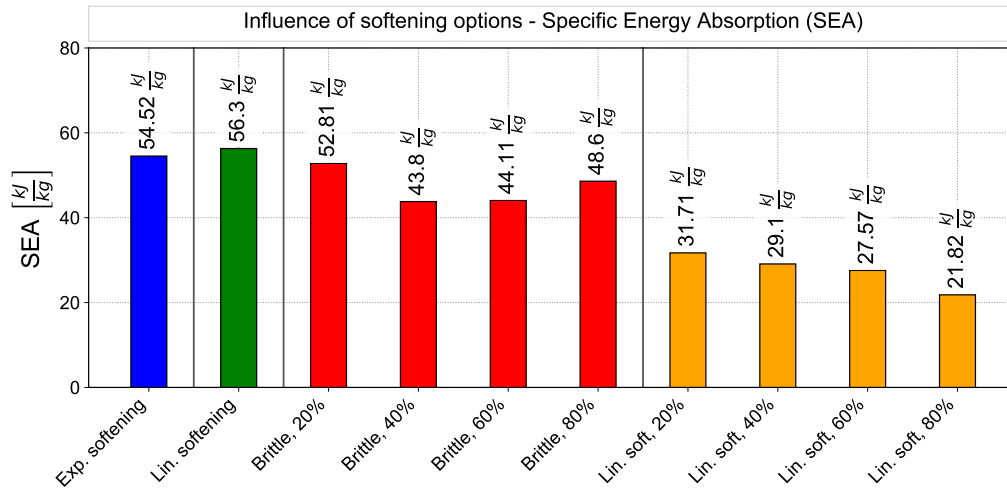
a) Linear softening
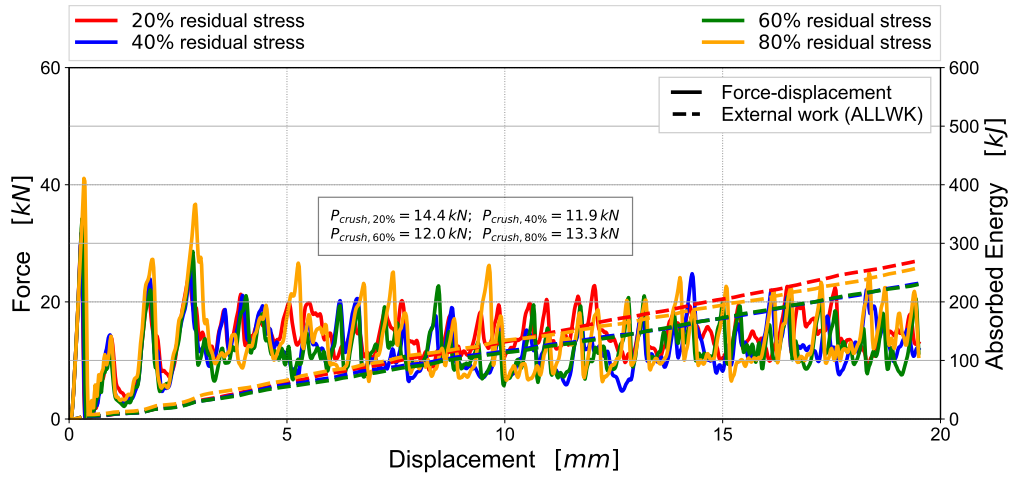
b) Brittle failure with residual stress
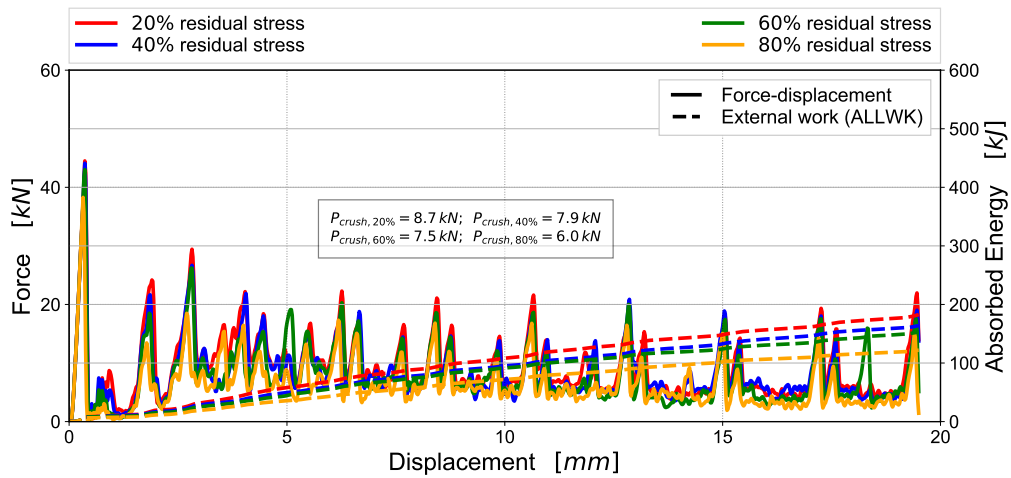
c) Linear softening with residual stress

Figure 7.6: Numerical study of a self-support crush segment - Influence of fibre softening options in progressive crushing; Force-displacement characteristic and evolution of absorbed energy

Figure 7.7: DLR crush segment - Predicted Specific Energy Absorption (SEA) for different fibre softening options

implemented crack band scaling approach which is implemented in the user-material model ABQ_DLR_UD as well as in other material models using continuum damage mechanics. It was shown that crack band scaling is applicable only in crack-like damage processes to achieve mesh-independent results. In progressive crushing however, the opposite effect was observed and the use of crack band scaling resulted in mesh dependent results and should therefore not be used in the simulation of progressive crushing.

- The investigation of different fibre softening options showed that exponential and linear softening predicted the highest specific energy absorption. This was in agreement with the results on the other levels of the building block. Linear softening with residual stress level predicted the lowest SEA in the simulation of progressive crushing. This effect was different compared to the other building block levels and was contributed to the different failure behaviour in progressive crushing and fracturing.

7.3 Validation of the Simulation Methodology - Flat Coupon Crushing

Up to this building block level, a meso-scale multi-layered shell approach was used where the composite laminate is discretized through-thickness by one single shell element layer. Each ply of the composite laminate was represented by three integration points through the thickness of the shell element (ply-based modelling approach). In contrast to the self-supported DLR crush segment described in the previous section, flat coupon specimens generally tend to locally buckle when applied to crush loading [172]. As a consequence, the failure phenomena in the crush zone are no longer driven solely by intralaminar failure modes but additionally by interlaminar failure in terms of large delamination resulting in splaying which needs to be considered in the simulations.

Table 7.1: Laminate definition of flat coupon specimens tested for validation [173, 174]

Quasi-isotropic laminates			
Laminate	QI-01	QI-02	QI-03	QI-04
Stacking sequence	$[90/\pm 45/0]_{2s}$	$[90_2/(\pm 45)_2/0_2]_s$	$[(\pm 45)_2/90_2/0_2]_s$	$[\pm 45/90/0]_{2s}$
Gap height	$8.6\,mm$	$15\,mm$	$15\,mm$	$7.5\,mm$
Hard laminates			
Laminate		HL-01	HL-02
Stacking sequence		$[90_2/0_2/\pm 45/0_2]_s$	$[90/+45/0_2/90/-45/0_2]_s$
Gap height		$14.5\,mm$	$14.5\,mm$

To reliably capture this complex failure mode, the extended meso-scale stacked-shell approach can be used where the composite laminate is discretized through the thickness by a stack of multiple shell element layers representing the individual plies - or stacks of plies with the same fibre orientation. Cohesive elements are modelled between the individual shell element layers and enable the separation of the shell layers, hence represent inter-laminar failure.

The experimental tests used for validation were performed at the University of Utah and results were provided to the author [173, 174]. A large variety of stacking sequences was investigated and optimized in terms of energy absorption under progressive axial crushing. The laminates are classified as quasi-isotropic ('QI') with equally distributed $0°/\pm 45°/90°$ ply orientations and 'hard' laminates ('HL') with 50% $0°$-plies. Force-displacement characteristics and SEA-values of four quasi-isotropic and two 'hard' laminates were provided. Gap heights ranging from $7.5\,mm$ to $15\,mm$ were used in the tests [173, 174], see Figure 7.8. The stacking sequence of the laminates are shown in Table 7.1.

For validation of the simulation results, fibre compressive fracture energies of $G_{c1}^C = 60\,\frac{kJ}{m^2}$ and $G_{c1}^C = 80\,\frac{kJ}{m^2}$ are used as material input. This range of fibre fracture energies is the result of the calibration on the level of fracture mechanic tests described in Chapter 6. No further calibration of material input data is performed on the building block level of progressive crushing.

7.3.1 Model Description

The flat coupon models are shown in Figure 7.8. Both the multi-layered shell and stacked-shell approach are considered to identify their capabilities and limitations. The boundary conditions in the numerical models are derived from the test setup including the support plates as well as the resin embedded clamping in the upper $20\,mm$ of the flat coupon specimen [173]. In this clamped region, the lateral, translational DOF are fixed in Y and Z direction (DOF2 and DOF3). In the stacked-shell model, this boundary condition is active solely in the nodes of the surface of the flat coupon specimen. Additionally, in both models, all nodes of the top edge of the specimen are fixed

in the translational DOF2 and DOF3 as well as all rotational DOF (DOF4 - DOF6). The velocity boundary condition in x-direction (DOF1) with a constant velocity of $v = 4.0 \frac{m}{s}$ is applied to these nodes. An initial velocity of $v_{initial} = 4.0 \frac{m}{s}$ is applied to all nodes of the flat coupon specimen. The gap height of the experimental tests is selected dependently of the layup and is modelled in a range of $h_{gap} = 7.5 \, mm - 15.0 \, mm$ according to the gap heights selected in the experiments [174]. The gap height of each layup is listed in Table 7.1. A saw tooth trigger at the impacted end of the flat coupon specimen is implemented in the model. The support plate as well as the impact plate are modelled as rigid bodies. In the multi-layered shell model, the support plates have to be placed carefully and dependent on the modelled laminate thickness. In the implemented contact algorithm in Abaqus/Explicit, the contact height is reduced if the ratio of element length to modelled thickness undercut a certain value. This issue is not relevant in the stacked-shell model since the ratio of element length to ply thickness is higher. Here, the support plates are modelled to be initially in contact with the outer surfaces of the flat coupon specimen. Friction is modelled between the flat coupon specimen and the impact plate with a coefficient of friction of $\mu = 0.2$. Self-contact of the specimen is modelled with $\mu = 0.4$ whereas contact of the flat coupon specimen and the support plates is assumed to be frictionless. The skewed mesh element type is selected for the flat coupon model with $10°$ inclination angle of the element edges. The characteristic length of the elements is $l^* = 1.0 \, mm$. In the multi-layered shell model, the intralaminar plies are modelled by a single layer of conventional 4-node elements (element type S4R). The laminate thickness is modelled via section properties in the model definition. In the stacked-shell model, identical mesh types and element sizes are used for the intralaminar shell layers and cohesive layers. However, 8-node continuum shell elements (element type SC8R) are used here. The thickness of the cohesive elements (element type COH3D8) is selected as $t_{coh} = 0.01 \, mm$. Field output is written every $0.25 \, ms$ and history output every $0.01 \, ms$.

In this applied modelling approach, fragmentation as an intralaminar dominated failure mode is represented by the material model ABQ_DLR_UD. The US-Version of IM7/8552 is used for the intralaminar material. Splaying as a major interlaminar failure mode is modelled with cohesive elements using a bi-linear traction-separation law. The inter-laminar material parameters are listed in Table 3.2 and Table 3.3 in Section 3.2.

A mesh type and mesh size study identical to the self-supported DLR segment is performed on the flat coupon specimen using the multi-layered shell approach. The mesh types and mesh sizes in this study are identical to the ones used in the study of the DLR segment in Section 7.2.2. The tendencies and results are the same as identified on the DLR segment and confirmed the conclusions. The results of the flat coupon study on discretization options are shown in Figure E.1 in Appendix E.
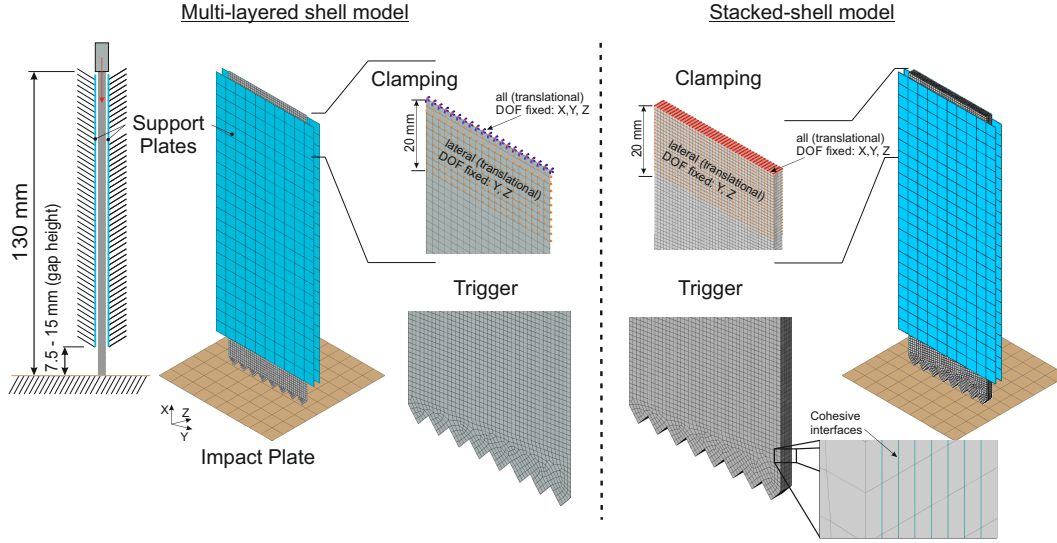
Figure 7.8: Numerical model of the Flat coupon specimen - Multi-layered shell and stacked-shell model

7.3.2 Multi-layered Shell Model Results

The simulation results of the multi-layered shell model are presented in Figure 7.9. The contact force vs. displacement of the impact plate is shown for the quasi-isotropic layup 'QI-01'. Figure 7.9 presents the results of the multi-layered shell model simulation with compressive fibre fracture energies of $G_{c1}^C = 60 \frac{kJ}{m^2}$ and $G_{c1}^C = 80 \frac{kJ}{m^2}$ as well as the experimental results obtained from the University of Utah. Unfiltered and filtered numerical results using a Butterworth low-pass filter with $20\,kHz$ cutoff frequency are shown. The presented experimental results are unfiltered. However, high masses in the test fixture resulted in low-frequency force signals. Therefore, comparison of the experimental and numerical results is quantitatively performed based on the mean crush force P_{crush} and the specific energy absorption (SEA), defined as:

$$SEA = \frac{P_{crush}}{\rho A} \tag{7.1}$$

Where ρ is the density of the material and A the cross-sectional area of the flat coupon specimen. P_{crush} and SEA are determined for the displacement range between $5.0\,mm - 30.0\,mm$ which is in the range of steady state crushing. By comparing the force-displacement characteristic it is identified that the multi-layer shell approach predicts a higher steady-state crush force level for both fracture energy inputs compared to the experimental results. The mean-crush forces of the simulations are $P_{crush,60} = 15.9\,kN$ and $P_{crush,80} = 18.3\,kN$ for $G_{c1}^C = 60 \frac{kJ}{m^2}$ and $G_{c1}^C = 80 \frac{kJ}{m^2}$, respectively. This is nearly twice as high as the average mean crush force of the three experimental results of $P_{crush,QI01} = 8.7\,kN$. The same tendency is identified for the SEA, where $SEA_{60} = 92.9 \frac{kJ}{kg}$, $SEA_{80} = 113.6 \frac{kJ}{kg}$ are twice as high as the average experimental result $SEA_{QI01} = 46.6 \frac{kJ}{kg}$. The multi-layered modelling approach is capable to capture the fragmentation failure mode whereas ply interface failure, such as splaying cannot be captured. This is in agreement with the conclusions
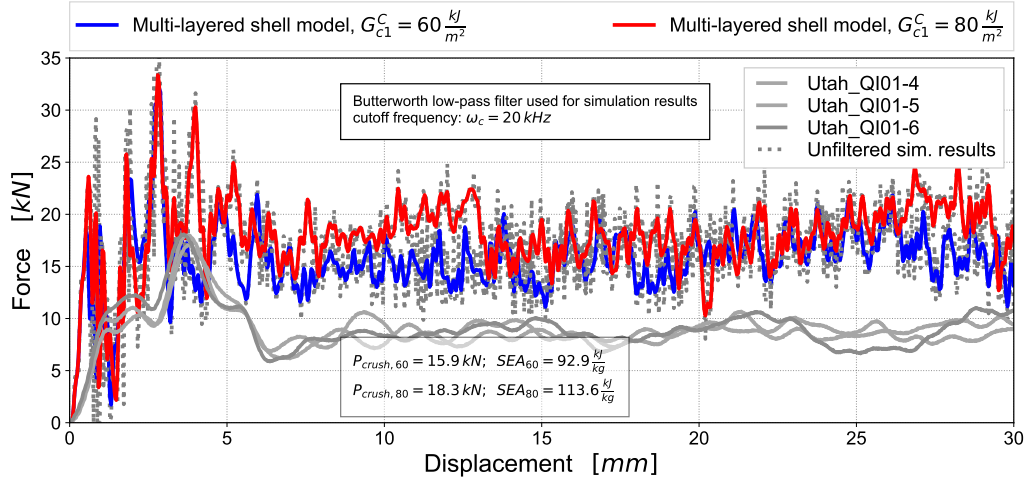
Figure 7.9: Force-displacement characteristic of the flat coupon simulation of laminate 'QI-01' $[90/\pm45/0]_{2s}$ using multi-layered shell models with different compressive fibre fracture energy

of Cherniaev et al. [142]. However, the opposite effect on the absorbed energy is observed here. Cherniaev et al. [142] argued that the multi-layered shell approach underestimates the energy absorption since it does not consider splaying as an additional failure mode [142]. However, the contrary is argued in the present work. The multi-layered shell approach captures only fragmentation as a failure mode with high energy absorption due to full fragmentation of the entire material. Therefore, the total energy is absorbed in fragmentation and the specific energy absorption is generally over-predicted. Splaying as a 'low-energy' failure mode as large portions of the material just separate by delamination without getting damaged has significant influence on the crush response and furthermore depends on the laminate layup. In the flat coupon crush tests of different quasi-isotropic and 'hard' laminates it has been shown that different layups result in different crushing behaviour with varying extend of splaying. Dependent on the ratio of fragmentation and splaying failure, the specific absorbed energy of the layups varies [173].

7.3.3 Stacked-shell Model Results

The results of the stacked-shell modelling approach are shown in Figure 7.10. Comparing the force-displacement characteristics shows good correlations between the stacked-shell simulations with both fibre fracture energies and the experimental results in terms of the steady-state force level. The mean crush force of the stacked-shell simulations between $5.0\,mm$ and $30.0\,mm$ crush displacement is $P_{crush,60} = 7.7\,kN$ and $P_{crush,80} = 8.3\,kN$. This results in $SEA_{60} = 43.6\,\frac{kJ}{kg}$ and $SEA_{80} = 47.0\,\frac{kJ}{kg}$ (vs. a mean SEA of $46.6\,\frac{kJ}{kg}$ of the experiments).

Moving from the multi-layered shell to the stacked-shell modelling approach, no further calibration of the intralaminar model is performed. Solely the cohesive interface model is additionally imple-
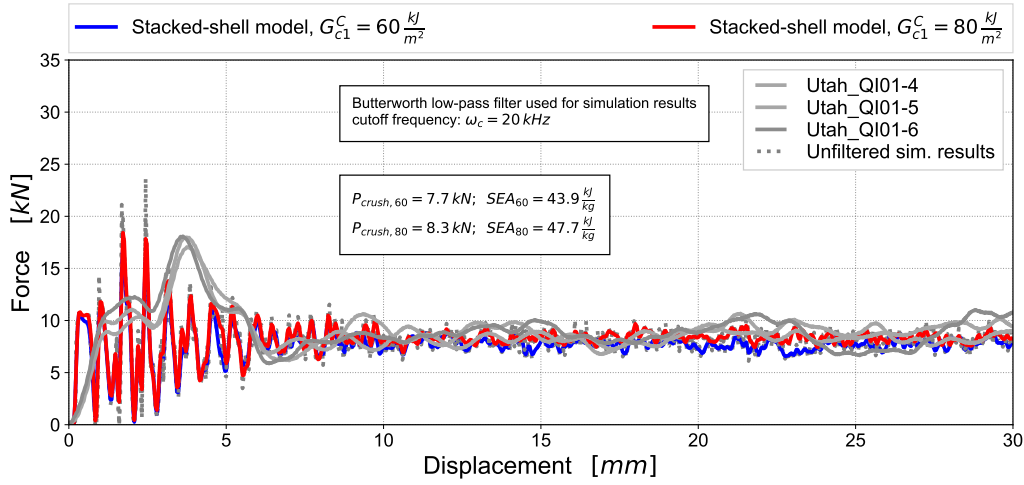
Figure 7.10: Force-displacement characteristic of the flat coupon simulation of laminate 'QI-01' $[90/\pm45/0]_{2s}$ using stacked-shell models with different compressive fibre fracture energy

mented into the model, with cohesive material input data taken directly from literature without further calibration (as shown in Table 3.2 and Table 3.3). Figure 7.11 highlights the stacked-shell modelling capability to present splaying and exemplarily compares the crush failure mode with the experiment of 'hard' laminate HL-01 with layup $[90_2/0_2/\pm45/0_2]_s$. For both, experiment and simulation, splaying of the outer layers can be seen whereas the inner layers fail in fragmentation. The extent of splaying and depth of delamination failure may change with a calibrated interface model. However, this proofs the model's capability to capture both relevant failure modes, fragmentation and splaying which absorb the majority of energy under progressive crushing. Furthermore, it is shown that the modelling approach developed in this work is capable to predict the experimental results without re-calibration of the material parameters.

7.3.4 Discussion and Conclusion of the Modelling Approach on the Prediction of Progressive Crushing

Since the multi-layered shell model is not capable to predict splaying, the specific energy absorption is generally over-predicted. This can be seen in Figure 7.12 in the force-displacement characteristics of the quasi-isotropic and 'hard' laminates. For all layups, the multi-layered shell models predict higher SEA as obtained in the experiments. Additionally, the multi-layered shell modelling approach is not capable to predict the influence of different layups on the SEA. In the state of the art, the present results of the flat coupon crush predictions would have lead to a recalibration of the material input, especially the fibre fracture energies. One could argue that this approach also models the influence of splaying by reducing the total absorbed energy of the laminate. However, this approach does not predict the crushing behaviour and also requires experimental results on the level of progressive crushing for calibration. Also, the influence of different layups is not predicted

a) Test Utah 'HL-01'; $[90_2/0_2/\pm 45/0_2]_s$ from [173]

b) Simulation 'HL-01'; $[90_2/0_2/\pm 45/0_2]_s$
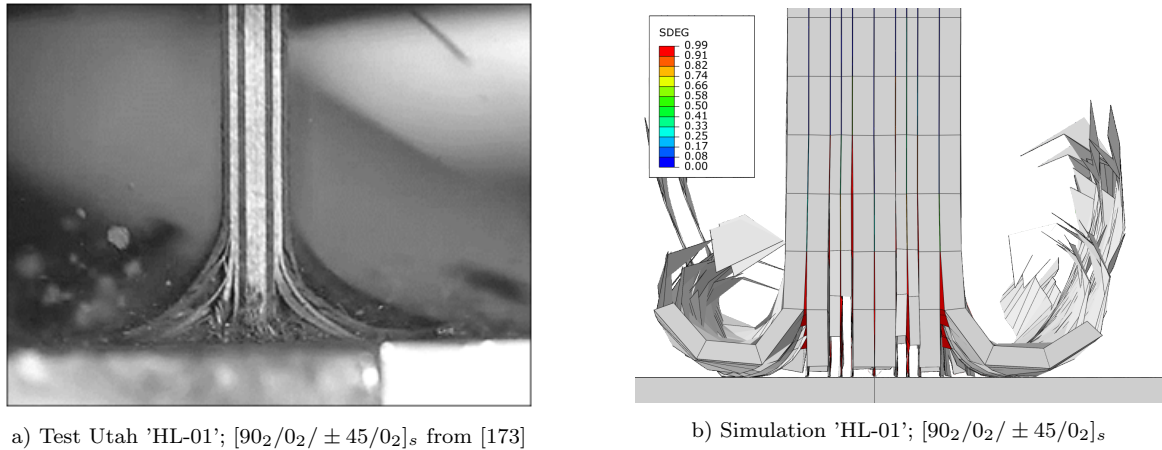
Figure 7.11: Side view of the flat coupon crush test from the high speed images and contour plot of cohesive damage (SDEG) of the simulation with stacked-shell model

a priori. From this it is concluded, that the modelling approach is predictive only if it captures all relevant failure modes of crushing.

Due to the capability of modelling the splaying failure mode, the stacked-shell model was identified to be capable to predict the influence of different layups. This is shown in Figure 7.12, where the force-displacement characteristics show good agreement with a range of experimental results of the quasi-isotropic and 'hard' laminates. The test/analysis correlation for layup 'QI-04' shows an outlier, the reasons for this are not clear. Since the gap height of this variant is the lowest of all tested layups, it is expected that splaying is less and the crushing behaviour is forced to a higher amount of fragmentation. This would result in higher mean crush force and SEA for this variant which would be in the range of layup 'QI-01' (the variant with the next higher gap height). The results of multi-layered shell models are also shown in comparison. For all simulated variants, the mean force level and SEA are higher compared to the experimental results. Also no significant influence of the layup is identified in the multi-layered shell simulation. Multi-layered shell simulation of layup 'QI-02' showed a catastrophic failure between crush distances of $15\,mm$ and $20\,mm$ due to the large gap height of $15\,mm$. Figure 7.13 quantitatively compares the SEA values of both multi-layered shell and stacked-shell simulations with the experimental results. The same tendency is shown: The influence of different layups is reasonably predicted by the stacked-shell simulations due to the capability to model both dominant crushing failure modes, fragmentation and splaying. The multi-layered shell modelling approach on the other hand is not able to predict the SEA and the influence of different layups.

Based on the outcomes of the flat coupon crush predictions, the conclusion is drawn that model capability of representing ply interface failure is essential although further complexity in the simulation model may lead to significant increase of resources in terms of simulation times and effort for the modelling setup.

Quasi-isotropic laminates

'QI-01'; $[90/\pm 45/0]_{2s}$; Gap height: $8.6\,mm$

'QI-02'; $[90_2/(\pm 45)_2/0_2]_s$; Gap height: $15\,mm$

'QI-03'; $[(\pm 45)_2/90_2/0_2]_s$; Gap height: $15\,mm$

'QI-04'$[\pm 45/90/0]_{2s}$; Gap height: $7.5\,mm$

'Hard' laminates

'HL-01'; $[90_2/0_2/\pm 45/0_2]_s$; Gap height: $14.5\,mm$

'HL-02'; $[90/+45/0_2/90/-45/0_2]_s$; Gap height: $14.5\,mm$
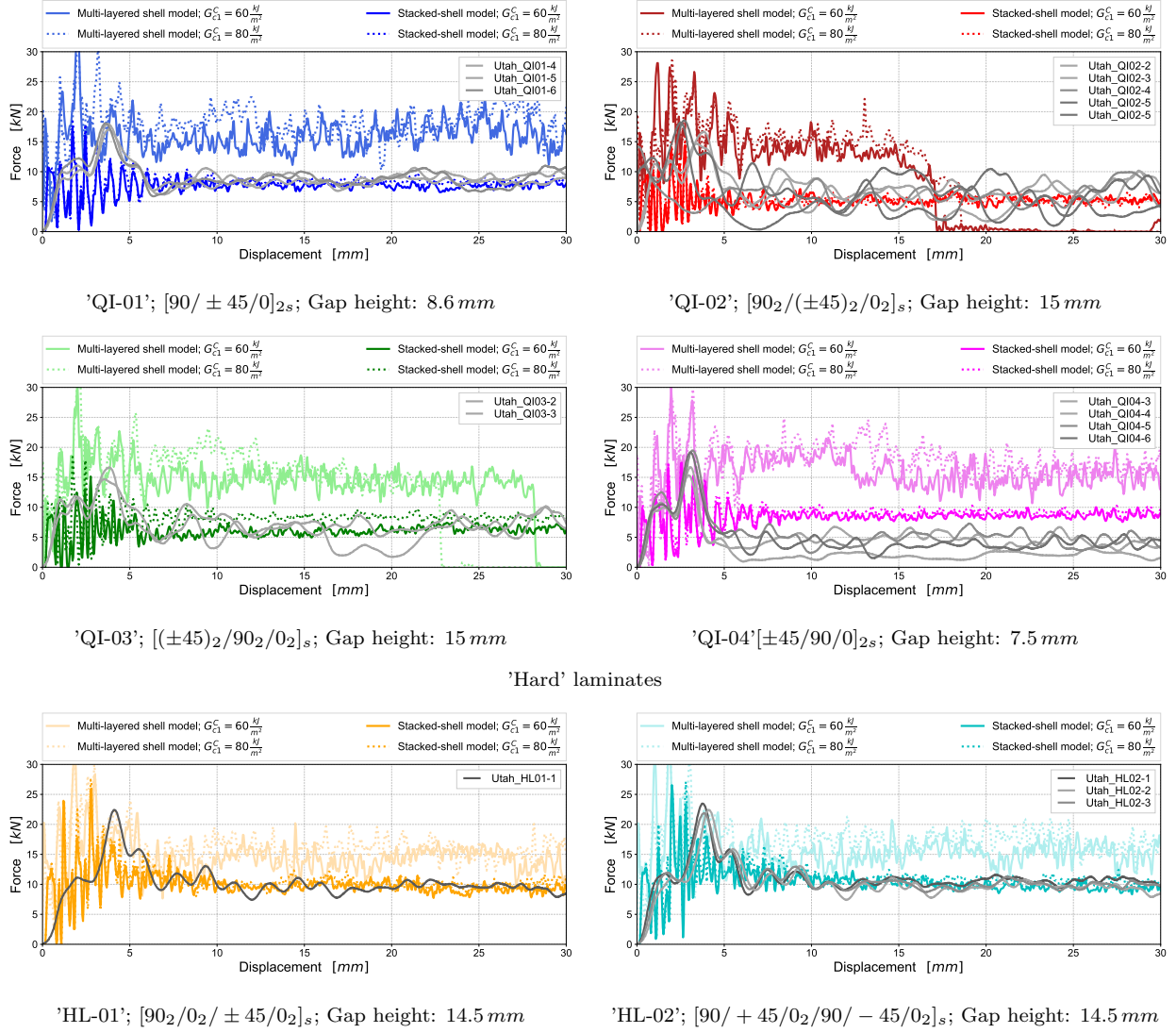
Figure 7.12: Force-displacement characteristics of different quasi-isotropic and 'hard' laminates simulation using both multi-layered shell and stacked-shell models. Comparison of simulations (coloured) and experimental results (grey)
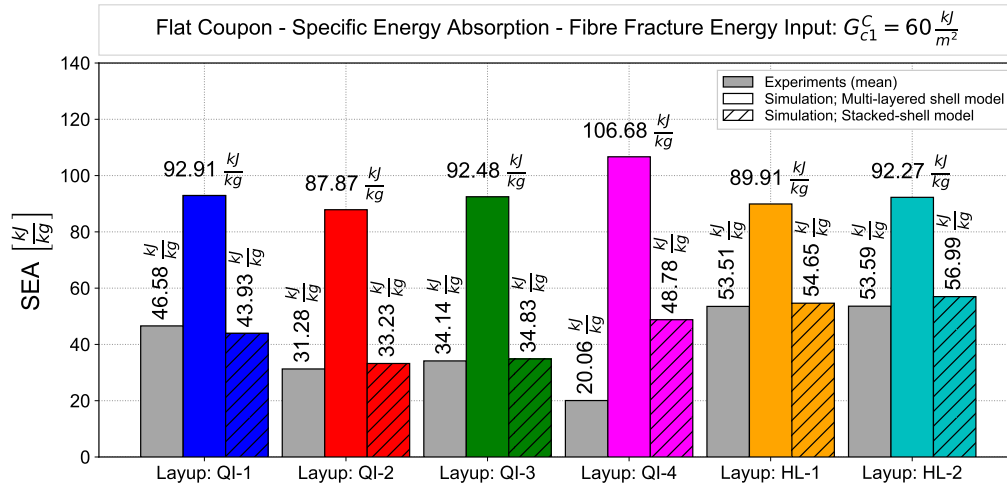
a) Fibre fracture energy input: $G_{c1}^C = 60 \frac{kJ}{m^2}$
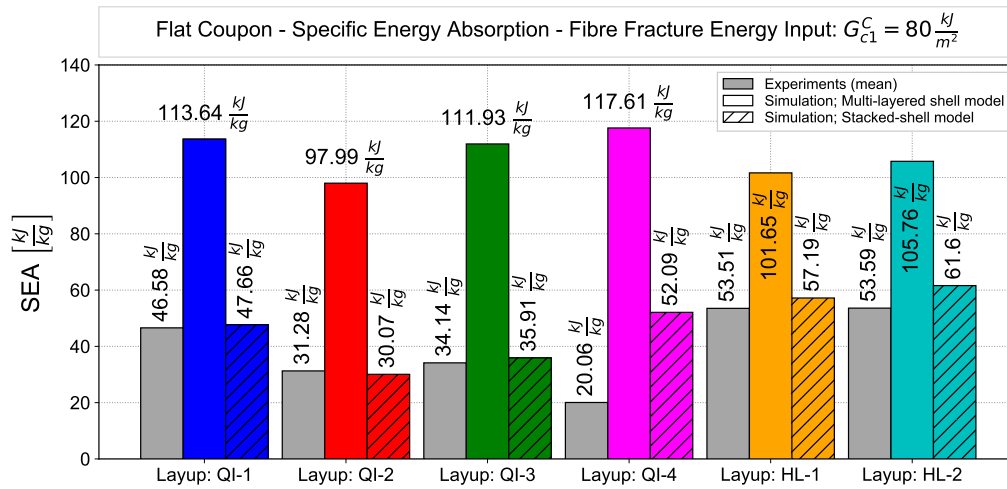
b) Fibre fracture energy input: $G_{c1}^C = 80 \frac{kJ}{m^2}$

Figure 7.13: Prediction of flat coupon crushing using both multi-layered shell and stacked-shell models. Specific energy absorption (SEA) of the simulations compared with the experimental results for fibre fracture energy input of a) $G_{c1}^C = 60 \frac{kJ}{m^2}$ and b) $G_{c1}^C = 80 \frac{kJ}{m^2}$

8 Conclusion, Contribution and Outlook

This chapter presents a summary of the main contributions and conclusions from this thesis. Topics for future potential research work are discussed based on encountered limitations of this work.

8.1 Summary, Conclusion and Contribution

Summary

Composite materials are being increasingly used in primary aircraft structures which are crucial for the structural integrity of the aircraft. The generally brittle behaviour of CFRP composites necessitates the implementation of specific crash concepts and energy absorbing devices to achieve the safety requirements in survivable crash events. Due to the high mass-specific energy absorption potential of CFRP materials, the imparted crash kinetic energy can largely be absorbed by progressive crushing of structures in the aircraft's sub-cargo floor region. Limited design guidelines on composite crashworthiness as well as the lack of accurate and efficient simulations tools led to the formation of the Crashworthiness Working Group of the Composite Materials Handbook (CMH-17) to address the development of guidelines and best practices for the numerical characterization of the energy absorbing capability and crash resistance of advanced composite structures. This dissertation aimed at the development of a simulation methodology to reliably predict the energy absorption of composite structures under crush loading. The research presented in this thesis was performed in the context of the international research collaboration 'DLR@UBC' of the German Aerospace Center (DLR) and the University of British Columbia (UBC), Canada. Also, part of this work was the contribution of DLR to the concise and comprehensive numerical Round Robin phase 3 campaign of the CMH-17 CWG.

A review and discussion of literature on crushing and energy absorption of composite structures identified the state of the art and revealed the research questions of this work:

- What levels of the building block are required to predict crushing of composite structures and which level requires experimental tests for calibration and validation of the methodology?

- How influence fibre softening options the damage process on different structural scales?

- How do discretization options influence the damage behaviour and how can mesh dependencies be avoided on different scales of the building block?
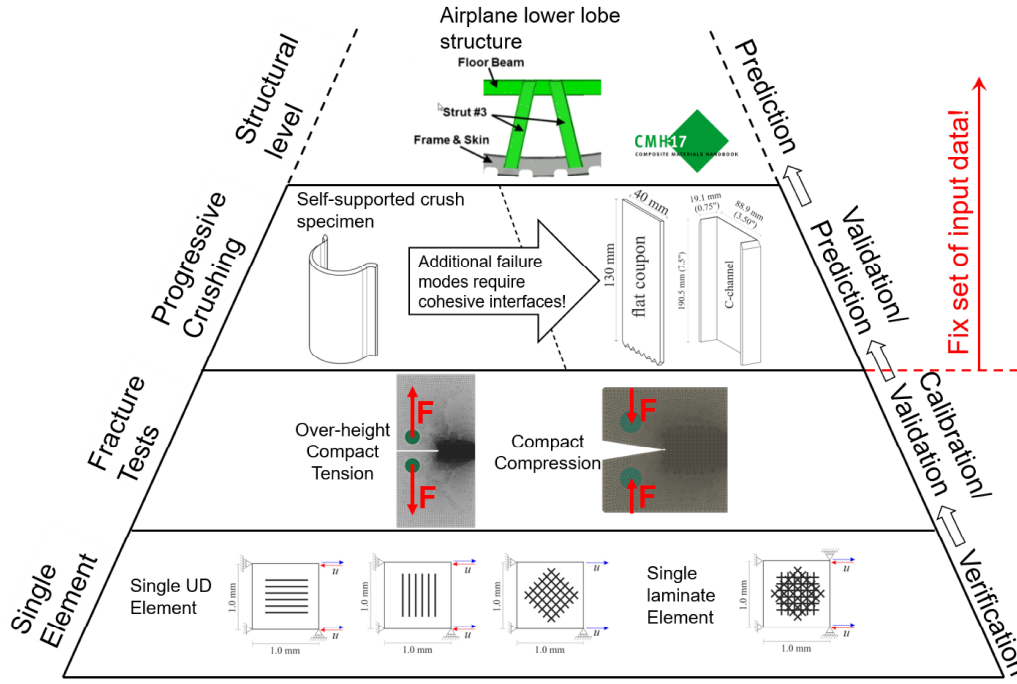
Figure 8.1: Building block approach used to predict progressive crushing of composite structures

- What level of detail in the model is required throughout the building block? Which modelling approach is required to reliably predict the complex failure behaviour of progressive crushing?

The methodology developed in this work is based on a meso-scale modelling approach focusing on the intralaminar behaviour of composite materials. It follows a building block approach from the definition of material inputs on ply-level up to the application of progressive crushing. Based on the outcomes of this thesis, the building block shown in Figure 8.1 could be developed.

The composite material system HEXCEL IM7/8552 was used consistently throughout this work. Relevant material parameters have been determined from open literature. Two versions of the material have been identified. A European version with an areal density of $134 \frac{g}{m^2}$ and a US-version with $192 \frac{g}{m^2}$. Both versions have been used in this work, dependent of the availability of the experimental results. Missing material parameters required for the simulation work have been identified and determined in material characterization tests in order to reduce assumptions in the simulations. The influence of the two material versions have been investigated and shown for each level of the building block. The fibre fracture energies have been identified as substantial material parameters of the modelling approach. Therefore, the influence of the fibre fracture energies has been investigated throughout the building block to identify the necessary levels for calibration and validation for different applications.

The numerical investigations in this work were performed using the intralaminar composite material

model ABQ_DLR_UD. Such a user-material model which enables access to the source code in order to adapt and extend was the key element to answer the research questions of this work. This explicit user-material model in the scope of continuum damage mechanics was implemented in the commercial FE-code Abaqus/Explicit and enhanced by the author. The material model describes the elementary ply by defining the behaviour of fibre and matrix. Fibre damage is based on fracture mechanics involving the fibre fracture energies. The fully accessible source code of the material model enabled the implementation and investigation of different fibre softening options within the same material model and FE-code which is novel in CDM material models. Also, the investigation of discretization options in order to answer the outlined research questions is possible.

Conclusions

The interpretation of the main results of this thesis contributes to the body of knowledge. The main conclusions of this work are:

- Simulations on the level of **single-element** models were identified as the basic level of the building block approach.

  - In a meso-scale modelling approach, single-element simulation of UD-laminates are suitable for user-material model verification. The influence of fibre fracture energy, element size, sensitivity of material parameters and fibre softening options on the stress-strain behaviour can be efficiently investigated. Already on this level, general tendencies valid for the entire building block can be identified.

  - As part of the user-material model verification, the following conclusions can be drawn at the single element level:

    * Due to the implemented crack band scaling approach, both the element size and fibre fracture energy scale the stress-strain curve of longitudinal (fibre) direction. With activated crack band scaling, mesh insensitive simulation results are achieved.

    * Single-element simulations of a UD-laminate verified that the different implemented fibre softening options obtained the same fibre fracture energies.

- **Single-laminate element** simulations were identified to be suitable to investigate the influence of a meso-scale modelling approach on the macroscopic laminate level. This level was defined as the fundamental level of the building block to compare meso- and macro-scale material models.

  - The numerical behaviour of a quasi-isotropic laminate under tension and compression is dominated by the fibre behaviour of the $0°$ and $\pm45°$ plies. Any change of behaviour in these plies, such as fibre softening option, fracture energy and element size directly influences the stress-strain characteristic of the laminate.

– A significant influence of the boundary conditions was identified on the single-laminate level in tension. Results of boundary conditions representing uni-axial strain and uni-axial stress, respectively, were compared and showed significant differences due to different damage behaviour of the $\pm45°$ plies. Since this effect is only relevant in meso-scale models, the boundary conditions have to be considered when results are compared to other modelling approaches. In addition, uni-axial strain vs. uni-axial stress should be considered and selected with respect to the later application of the considered modelling approach.

– The implied crack band scaling on ply-level governs the influence of element size and fracture energy on laminate level. A reduction of element size as well as an increase of fibre fracture energy results in an increase of the laminate ultimate strength. This is due to a higher energy release rate in the $0°$ and $\pm45°$ plies. Investigating the discretization of a quadratic tension/compression specimen revealed that mesh-independent results on this level were only achieved with active crack band scaling. From this it is concluded that crack band scaling is required on element level to avoid mesh sensitivities.

– The influence of different fibre softening options on the laminate stress-strain characteristic was identified due to different fibre damage growth in the $0°$ plies. A lower increase of fibre damage resulted in higher ultimate strength. Less growth in fibre damage is achieved by increasing the post-peak fibre stress-strain slope as in linear softening compared to exponential softening or by increasing the residual stress level in the brittle failure approach.

• The level of **fracture mechanic tests** of the building block was identified as a suitable level for calibration and validation of CDM models. Experimental results of OCT and CC specimens were used to calibrate the tensile and compressive fibre fracture energies, respectively. Numerical efficient multi-layered shell models can be used on this level since the damage was reported to be mainly intralaminar.

– The stress-strain response of the laminate which is dominated by the fibre behaviour directly influences both the force characteristic and crack propagation of the OCT and CC simulations. Effects of element size, fibre fracture energies and fibre softening options can be traced back to their influence on the stress-strain response on the meso- and macro-scale level.

– The influence of discretization options showed that crack band scaling is mandatory on the level of fracture mechanic tests to avoid mesh dependent results. This is due to the fact that damage in OCT and CC specimen is confined into a narrow band.

– The main impact of different fibre softening options on the level of fracture mechanic tests was identified in the strength obtained in OCT and CC simulations. Only minor influences were identified on the post-peak force level. Those effects were traced back

to the macro-scale level and the influence of the fibre softening options on the ultimate strength of the laminate.

– Fibre fracture energies in tension and compression showed a major impact on the global response of both OCT and CC simulations, respectively. The maximum force, post-peak force level and predicted laminate fracture energy increase with the fibre fracture energy input. The reasons were identified in an increase of both the ultimate laminate strength and post-peak stress on macro-scale level.

– Based on experimental results of OCT and CC tests, the tensile fibre fracture energy was validated as $G_{c1}^T = 120 \frac{kJ}{m^2}$. The compressive fibre fracture energy was validated to be in the range of $G_{c1}^C = 60 \frac{kJ}{m^2}$ to $80 \frac{kJ}{m^2}$ dependent on the material version of IM7/8552. With these calibrated fibre fracture energies, the material input data set in the developed modelling approach was fixed and no further calibration on higher levels of the building block was performed.

- At the building block level of **progressive crushing**, self-supported crush segments were identified as an ideal specimen for the validation of numerical methods for progressive crushing.

  – Test boundary conditions are simple and allow precise representation in the numerical models, and crush failure is dominated by intralaminar fragmentation.

  – A mesh dependency study is crucial in identifying proper discretization for simulation of progressive crushing. Investigation of different mesh types showed that structured meshes can lead to large force spikes which can eventually trigger catastrophic failure. A skewed or unstructured mesh type was identified as best practice in obtaining smooth force characteristic without unrealistic and mesh dependent force spikes.

  – Investigation of different mesh sizes confirmed that crack band scaling results in mesh-dependent damage prediction in progressive crushing. By definition, the crack band theory is only applicable where damage is confined into a narrow band. The application of crack band scaling in simulation of crushing led to severe mesh-dependent crush force predictions whereas simulations without crack band scaling revealed consistent force levels independent of the mesh size. From this it is concluded that crack band scaling in CDM-based material models is not applicable to simulations of axial crushing with fragmentation as major failure mode. Outcomes of the DLR@UBC collaboration revealed that the same trend was identified for multiple material models in different FE-codes. This indicates that this finding applies generally to all material models using CDM [22].

  – Multi-layered shell vs. stacked-shell modelling approach needs to be considered dependent on the individual application case for simulation of progressive crushing. The

multi-layered shell model capability showed major limitations and only pure fragmentation failure could be predicted. This resulted in an over-prediction of the crush force and specific energy absorption (SEA) when splaying occurs in the experiment. As splaying strongly depends on the layup, the single-shell modelling approach is not capable to identify the influence of different layups. In contrast, the stacked-shell modelling approach was identified to be capable to capture fragmentation and splaying. This results in good test/analysis correlation of the crush force and SEA for flat coupon specimens with different layups. However, significant increase of computational costs and efforts to build up the simulation model needs to be considered in the decision between multi-layered shell and stacked-shell modelling approach.

These conclusions lead to answering the leading research questions of this work and the simulation methodology to predict progressive crushing of composite materials:

- The required levels to reliably predict progressive crushing are the following:

  - The single element level as verification level. With simulation of single-UD and single-laminate elements, the main effects of continuum damage mechanics models can be verified and conclusion of the behaviour on higher levels can be drawn. No specific experimental tests expect for determination of material parameters are required. Also, fibre fracture energies can be calibrated and verified on macro-scale level using single-laminate element simulations when laminate fracture energies are known e.g. reported in open literature.

  - The level of fracture mechanic tests are suitable for calibration of fracture energies in case they are unknown for the material, and for validation if fibre fracture energies have been calibrated on single-element level. Experimental results of OCT and CC tests or similar fracture mechanic tests are required on this level. With a fixed set of material parameters, predictions on higher levels of the building block can be performed. Fracture mechanic test simulations such as OCT and CC simulations are suitable for validation of application cases with laminate fracturing as main failure mode.

  - For progressive crushing, self-supported crush segments such as the DLR crush segment were identified as a suitable validation case.

- Different fibre softening options with the same fracture energies on meso-scale level influence the global behaviour on all structural levels through affecting the ultimate strength and ultimate strain of the laminate. On the level of fracture mechanic tests, a higher ultimate strength of the laminate resulted in increased maximum force values whereas a lower ultimate strain of the laminate resulted in a higher increment of crack growth. On the level of progressive crushing, higher laminate strength resulted in higher force peaks. Higher ultimate strains however resulted in later element erosion and therefore more elements which are in contact with the impact plate increasing the crush force.

- Effects of discretization options on the different building block levels are dependent on the predominant damage behaviour. If the damage behaviour is crack like and confined into a narrow band, the crack band scaling approach is mandatory to avoid element size dependent results. In progressive crushing, where the total volume of the specimen is crushed down, the investigation of discretization options revealed two main effects: First, increasing the number of elements which are in contact with the impact plate reduces the force spikes and leads to a smoother force characteristic. This can be influenced by the mesh types such as the structured/skewed/unstructured mesh. Second, crack band scaling is not applicable in CDM-based simulations of progressive crushing and has to be disabled to avoid distinctive mesh dependencies.

- If intralaminar damage is the predominant failure mode, numerical efficient multi-layered shell models can be used. If interlaminar dominated damage like splaying plays an important role in the damage process, the model has to be able to capture this failure mode. Therefore, for the prediction of progressive crushing where the crush modes are unclear in advance, the stacked-shell modelling approach is recommended to reliably predict the crushing behaviour.

Contribution

The presented work was set out to develop a simulation methodology to numerically predict the energy absorption of composite structures under crash loading. The work contributes to the state of the art by defying a numerical building block approach to reliably predict the progressive damage and crushing behaviour of composite structures and to support the effective design of crashworthy composite components with reduced reliance on experiments. The simulation framework developed in this work enables the evaluation and selection of simulation approaches suitable for the respective case. This framework provides guidelines and best practices on the identification of appropriate input parameters and discretization methods. Within the objective research collaboration DLR@UBC it could be shown that this framework is suitable to compare different material models implemented in different FE-codes and that main effects were already identified on the basic level of the building block [17–22]. In the scope of the CMH-17 CWG, following this defined building block approach was identified as very helpful and a valuable strategy for the development of numerical methods by different analysis teams using different material models and FE-codes. This practice provides better objectivity and enables the identification of model- or FE-code-specific effects which otherwise could hardly be identified. The work provides important modelling guidelines for the successful and computationally-efficient simulation of composites under axial crushing and it could reduce the extend of experimental investigations. It is possible to conduct stable simulations which are able to predict the crushing behaviour without the need for validation on each individual level of the building block. Such a simulation methodology is extremely helpful to promote the approach of certification by analysis. It was shown that the crack band scaling commonly applied in state of the art CDM-based material models is not applicable to simulations of axial crushing

with fragmentation as major failure mode. Moreover, the detailed mesh type study revealed that state of the art structured meshes can lead to large force spikes which can result in catastrophic failure of the structure. The implementation of different fibre softening options in a user-material model enabled the investigation of this options in the same material model and FE-code. This possibility is not available in state of the art material models.

8.2 Limitations and Future Research

A few limitations were encountered during this work which guide the directions of future research on this field:

- Damage under transverse compressive loading was not considered in ABQ_DLR_UD according to the theory of Ladevèze and LeDantec. Failure was considered using a maximum stress criterion. However, in combination with modelling permanent strains due to plasticity, this may lead to unrealistic high failure strains and therefore higher energies absorbed by the matrix. Even if the behaviour of the fundamental ply is dominated by fibre behaviour, incorrect representation of the matrix compressive damage may influence the material behaviour on laminate level. In potential future work, the damage behaviour under transverse tensile loading based on the theory by Ladevèze and LeDantec can be adapted to compressive loading.

- The self-supported DLR crush segment was identified as a sufficient specimen for the validation of numerical simulation methods on the level of progressive crushing. Unfortunately, no experimental results for material system IM7/8552 were available and it was also not possible to conduct those tests in the scope of this work. However, it is strongly believed that these tests would round up the developed building block and further enhance the data base of IM7/8552 published in open literature.

- High fidelity FE-models like the stacked-shell modelling approach which are required to predict the complex crushing behaviour combining fragmentation and splaying result in significant high computational costs and efforts to build up the simulation model and are therefore not suitable for application in large scale structures. However, it is expected that further improvements in hardware and high-performance computing will help to overcome this issue. Nevertheless, the stacked-shell modelling approach can be applied to determine the force-displacement characteristics of sub-structural components which can be used as input for the simplified macro model approach [23, 38] in large structural models. Also, the application of this detailed approach can be applied for local crush zones in large structural models using multi model coupling. Detailed models can also be used for numerical extension of test programs and for understanding the complex phenomena in experimental tests by numerical simulation that allow better insight in effects.

- The cohesive parameters used in the stacked-shell approach were based on literature data. A building-block approach for interlaminar damage modelling similar to the approach presented in this work would help to identify relevant cohesive parameters and building block levels to calibrate and validate the cohesive parameters. An efficient procedure is outlined in [89].

- Strain-rate effects of the material was not considered in this work. As reported in [163, 175, 176], high-rate loading affects the material properties of IM7/8552. It is believed, that the use of strain-rate dependent material properties in the simulations of progressive crushing will have an influence. Especially strain-rate dependent cohesive parameters can significantly affect and change the crushing behaviour through influencing the amount of splaying in the model. In a first step, strain-rate dependent parameters can be used to investigate the effects. In a further step, intralaminar strain-rate dependent behaviour can be implemented directly in the material model through modifying the source code of ABQ_DLR_UD. This will enable the applicability of ABQ_DLR_UD on different loading rates. Implementation of strain-rate dependent cohesive behaviour in Abaqus/Explicit may require a cohesive user-material model.

8.3 Outlook

The simulation methodology developed in this work focused on the simulation of progressive axial crushing. However, the methodology and best practices for modelling different failure modes and the calibration and validation to predict the failure behaviour can also be applied to further energy absorbing mechanisms. A particular application case is energy absorption through progressive pin bearing failure. Progressive pin bearing was lately investigated in multiple cases covering a wide range of loading rates, geometrical influence of pin diameter and laminate thickness as well as different laminates for material system IM7/8552 with participation of the author of this work [52, 53, 156]. Since the material system is identical, the simulation methodology can be directly transferred to this energy absorbing case with a wide variety of experimental data for validation. Especially, the investigation of mesh type and mesh size influences may have a high potential since it is believed that the effects are directly comparable to progressive crushing. As outlined in other projects by the author [46, 48], mesh type and element sizes influence the predicted pin bearing behaviour in a similar manner as in progressive crushing. Meso-scale modelling of the pin bearing tests using a detailed stacked-shell modelling approach and fracture energy based CDM was performed and presented in [177]. However, mesh type and mesh size influences have not been investigated. Showing that crack band scaling is not applicable also on progressive pin-bearing would therefore help to identify further application cases and contribute to the base of knowledge. This will lead to the motivation for developing new approaches to overcome the mesh type and element size dependency.

A Appendix to Chapter 3 - HEXCEL IM7/8552 Material Properties

A.1 Material Characterization Tests for HexPly IM7/8552 (US-Version)

The material characterization tests for HexPly IM7/8552 is the contribution of DLR to the CMH-17 CWG. The tests described in this section are part of the CMH-17 CWG test documentation with the objective of establishing and documenting the numerous testing activities of the various team members. The CMH-17 CWG test document provides an overall summary of the coupon and element level tests conducted in an effort to provide input data for the numerical material models required for pre- and post-test simulations.

Purpose of this material characterization tests is to identify material input parameters for the ABQ_DLR_UD ply model developed by DLR which is used as user-material model in Abaqus/ Explicit (VUMAT). In detail, this test series concerned the identification of the matrix damage and plasticity parameters following the procedure by Ladevèze and LeDantec [108] as well as O'Higgins et al.[178].

A.1.1 Test Article Description

In the following tables, information about the test samples for material characterization of IM7/8552 (US-version, 190 $\frac{g}{m^2}$) are provided. In Table A.1, test samples of the $[\pm45]_{4s}$ cyclic tensile tests are listed. In Table A.2, test samples of the $[\pm67.5]_{4s}$ cyclic tensile tests are listed. Information about the length, width, thickness and mass of each specimen are provided. Additionally, strain gauge types for instrumentation are provided. Note that one test sample of each layup was monotonically loaded.

One specimen of each lay-up was subjected to quasi-static monotonous loading up to failure and five specimens of each layup were subjected to quasi-static cyclic loading with force control and then transferring to displacement control for the later cycles. The amplitude of force of the force controlled cycles was increased with each load/unload cycle whereas the displacement was constant for the displacement controlled cycles.

Table A.1: Test article description of $[\pm 45]_{4s}$ tests

| Code | Layup | Specimen Geometry | | | Instrumentation | Tensile Loading | |
		L [mm]	w [mm]	t [mm]	Mass [g]		Monotonous	Cyclic
CST_IM7_8552_45_4	$[\pm 45]_{4s}$	259	24.4	3.04	30.2	Biaxial rosette (FCA-6-11-1L)	X	
CST_IM7_8552_45_5	$[\pm 45]_{4s}$	259	24.4	3.06	30.2	Biaxial rosette (FCA-6-11-1L)		X
CST_IM7_8552_45_6	$[\pm 45]_{4s}$	259	24.4	3.06	30.2	Biaxial rosette (FCA-6-11-1L)		X
CST_IM7_8552_45_7	$[\pm 45]_{4s}$	259	24.4	3.06	30.3	Biaxial rosette (FCA-6-11-1L)		X
CST_IM7_8552_45_8	$[\pm 45]_{4s}$	259	24.4	3.07	30.0	Biaxial rosette (FCA-6-11-1L)		X
CST_IM7_8552_45_9	$[\pm 45]_{4s}$	259	24.4	3.04	29.3	Biaxial rosette (FCA-6-11-1L)		X

Table A.2: Test article description of $[\pm 67.5]_{4s}$ tests

| Code | Layup | Specimen Geometry | | | | Instrumentation | Tensile Loading | |
		L [mm]	w [mm]	t [mm]	Mass [g]		Monotonous	Cyclic
CST_IM7_8552_67.5_2	$[\pm 67.5]_{4s}$	261	24.7	2.96	29.8	Biaxial rosette (FCA-6-11-1L)	X	
CST_IM7_8552_67.5_3	$[\pm 67.5]_{4s}$	260	24.7	3.04	30.4	Biaxial rosette (FCA-6-11-1L)		X
CST_IM7_8552_67.5_5	$[\pm 67.5]_{4s}$	260.5	24.6	3.1	31	Biaxial rosette (FCA-6-11-1L)		X
CST_IM7_8552_67.5_7	$[\pm 67.5]_{4s}$	260.5	24.4	3.07	30.7	Biaxial rosette (FCA-6-11-1L)		X
CST_IM7_8552_67.5_8	$[\pm 67.5]_{4s}$	260.5	24.6	3.04	30.2	Biaxial rosette (FCA-6-11-1L)		X
CST_IM7_8552_67.5_9	$[\pm 67.5]_{4s}$	260.5	24.7	2.9	28.9	Biaxial rosette (FCA-6-11-1L)		X

Table A.3: Test matrix for identification of matrix damage and plasticity parameters

Code	Lay-up	Output	Monotonous	Cyclic	Total
CST_IM7_8552_45_#	$[\pm 45]_{4s}$	$Y_{120}, Y_{12c}, Y_{12s}, R_0, \beta, \mu$	1	5	6
CST_IM7_8552_67.5_#	$[\pm 67.5]_{4s}$	$Y_{20}, Y_{2c}, Y_{2s}, b, \alpha^2$	1	5	6

Cyclic tensile tests on $[\pm 45]_{4s}$ laminates were carried out to determine shear damage growth and plasticity parameters. In detail: the initial shear damage threshold parameter Y_{120}, the shear damage evolution parameter Y_{12s}, shear damage failure threshold Y_{12s}, the yield stress R_0, the plastic hardening law coefficient β and the the plastic hardening law exponent μ. Shear damage is characterized by the reduction of the shear modulus G_{12} with each loading/unloading cycle. Plasticity is characterized by the increase of the total plastic strain with each loading/unloading cycle.

Cyclic tensile tests on $[\pm 67.5]_{4s}$ laminates were used to identify the transverse damage master curves and shear-transverse damage and plasticity coupling parameters. In detail: the transverse damage initiation threshold Y_{20}, transverse damage failure threshold Y_{2s}, the transverse damage evolution parameter Y_{2c}, the shear-transverse damage coupling parameter b and the shear-transverse plasticity coupling parameter α. The one specimen of each lay-up which was tested under quasi-static monotonous tensile loading up to failure was used to determine the shear-stress-to-shear-strain and transverse-stress-to-transverse-strain master curves from which the maximum strains and load/unload points were derived. The test matrix is presented in Table A.3.

Test Methods

The geometry of the test specimens are based on guidelines given in ASTM D3039 [179] and ASTM D3518 [180]. The delivered plates of HexPly IM7/8552 in the US-Version [14, 16] (areal density: 190 $\frac{g}{m^2}$) with the $[\pm 45]_{4s}$ and $[\pm 67.5]_{4s}$ lay-ups and dimension of 30.5 x 30.5 mm were manufactured at the University of Utah and handed over to DLR. The plates were ultrasonic scanned prior to cutting and showed good uniformity. The specimens were cut using a diamond saw and details of each specimen are presented in Appendix A.1.1. Each test specimen was instrumented with one biaxial strain gauge rosette which was placed in the center of the specimen. Strain readings were taken from these strain gauges at a frequency of 10 Hz. Additionally, observable markers were painted on the specimen for strain measurement with an optical extensometer. Specimen surfaces were painted with a speckle pattern for strain field analysis. However, solely the strain gauge data were used for material characterization. Damage of the specimens initiated for all tests outside of the clamping region. The post-tested specimen showing the markers and speckle patterns are presented in Figure A.1. Five repeats were carried out for each lay-up. The free length in between the clamping was chosen to be larger than 150 mm (in detail: 154.2 mm) for all tests. All testing was performed at the German Aerospace Center (DLR) Institute of Structures and Design. All

testing was carried out on a ZwickRoell 1494 500 kN universal electromechanical testing machine. A 500 kN auxiliary load cell was used. The loading speed of each test was 0.033 mm/s and this includes both the loading and unloading cycles. All tests were performed at room temperature and dry conditions.

a) Post-test specimen of [±45]$_{4s}$ lay-up
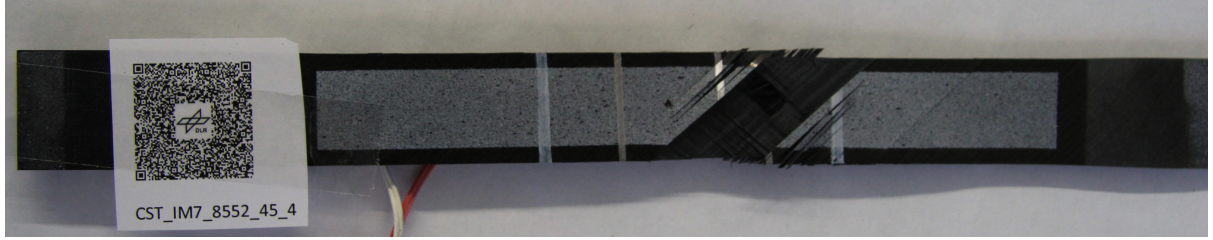
b) Post-test specimen of [±67.5]$_{4s}$ lay-up
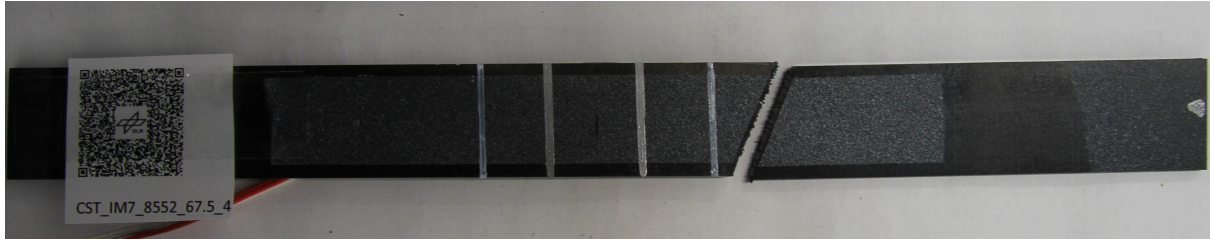
Figure A.1: Post-test specimen of the material characterization test programme; a) $[\pm45]_{4s}$ specimen; b) $[\pm67.5]_{4s}$ specimen

Identification of Shear Damage and Plasticity Parameters

Specimens with $[\pm45]_{4s}$ lay-ups were used to determine the shear damage and plasticity parameters. The specimens were cyclically loaded and unloaded in a combination of force and piston displacement control with increased force amplitude. Due to the low number of cycles, low-cycle fatigue phenomena is negligible. Details of the loading/unloading cycles are listed in Table A.4. The shear stress for each load/unload point was determined with the stress of the specimen at each load/unload point σ_i

$$\tau_{12i} = \frac{\sigma_i}{2} \tag{A.1}$$

The associated shear strain γ_{12i} was determined with the specimen longitudinal ε_{Li} and transverse ε_{Ti} strains determined from the biaxial strain gauges as:

$$\gamma_{12i} = \varepsilon_{Li} - \varepsilon_{Ti} \tag{A.2}$$

Table A.4: Details of loading/unloading cycles for $[\pm 45]_{4s}$ tests

Cycle	1	2	3	4	5	6	7	8
Load	5000 N	7500 N	10000 N	12500 N	7.5 mm	12.5 mm	17.5 mm	22.5 mm
Unload	1000 N	1000 N	1000 N	1000 N	1000 N	1000 N	1000 N	1000 N
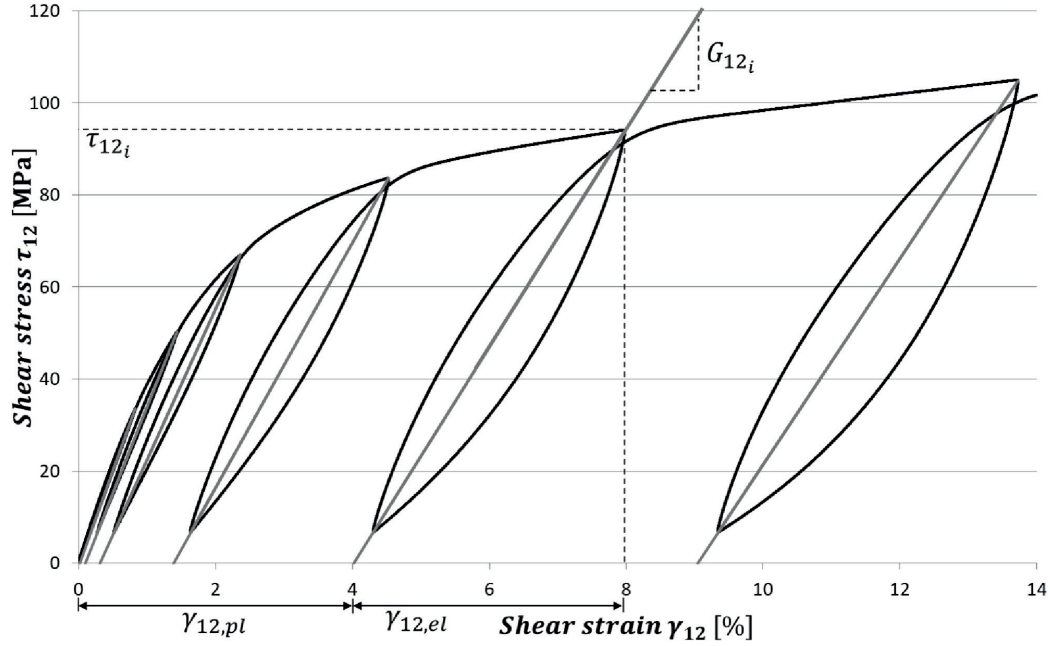
Figure A.2: Shear stress-shear strain curve of cyclic tensile test on a $[\pm 45]_{4s}$ specimen

From this, the shear modulus for each load/unload cycle is calculated with the elastic portion of the corresponding total strain $\gamma_{12,el}$ as shown in Figure A.2:

$$G_{12i} = \frac{\tau_{12i}}{\gamma_{12,el}} \tag{A.3}$$

By use of the initial, undamaged shear modulus, G_{12}^0, determined from the initial slope between 5 MPa and 20 MPa shear stress, the shear damage variable d_{12i} was then calculated from:

$$d_{12i} = 1 - \frac{G_{12i}}{G_{12}^0} \tag{A.4}$$

From the procedure outlined by Ladevèze and LeDantec [108], the damage evolution law $\underline{Y}_i$ was calculated:

$$\underline{Y}_i = \sqrt{Y_{12i}} = \frac{\tau_{12i}}{(1 - d_{12i})\sqrt{2 G_{12}^0}} \tag{A.5}$$

From this, the shear damage master curve of material system HexPly IM7/8552 (US-Version) is plotted in Figure A.3. In this plot, it is clear that good repeatability of the test results was obtained.

The $\underline{Y}$ - d_{12} behaviour is approximately linear up to a damage value of $d_{12} \sim 0.45$. According to Ladevèze and LeDantec [108], this linear relationship in Figure A.3 can also be expressed by:

$$d_{12} = \frac{\underline{Y} - Y_{120}}{Y_{12c}} \tag{A.6}$$

This linear relationship is also plotted in Figure A.3. The initial shear damage threshold parameter Y_{120} is the point at which d_{12} becomes zero and the shear damage evolution parameter Y_{12c} is the inverse of the slope. Additionally to the procedure proposed by Ladevèze and LeDantec [108], Schueler [90] and Schueler et al. [91] introduced the shear failure threshold Y_{12s} and transverse failure threshold Y_{2s}. From the linear relationship, the value of Y_{12s} was determined to be $Y_{12s} = 1.83\sqrt{MPa}$ which corresponds to the point where the shear damage master curve becomes non-linear in Figure A.3.

The plasticity development law parameters were also determined from $[\pm 45]_{4s}$ tests. According to Ladevèze and LeDantec[108], the plasticity threshold value, the sum of the yield stress R_0 and the plasticity development law parameter R_i at the i-th cycle were calculated from:

$$R_i + R_0 = \frac{\tau_{12i}}{1 - d_{12i}} \tag{A.7}$$

The accumulated plastic strain was calculated from Ladevèze and LeDantec[108]:

$$\tilde{p} = \int\limits_0^{\gamma_{12,pl}} (1 - d_{12i}) \, d\gamma \tag{A.8}$$

$\tilde{p}$ can be determined by plotting the plastic strain $\gamma_{12,pl}$ against $(1 - d_{12i})$ and calculating the area under this curve. With $R_i + R_0$ and $\tilde{p}$, the shear plasticity master curve for HexPly IM7/8552 as shown in Figure A.4 is plotted. A curve is fitted to the master curve using the power law

$$R(\tilde{p}) = \beta \tilde{p}^{\mu} \tag{A.9}$$

where β is the plastic hardening law coefficient and μ the plastic hardening law exponent.

The values for HexPly IM7/8552 (US-Version) determined from cyclic $[\pm 45]_{4s}$ tests are listed in Table A.5

Table A.5: Shear damage and plasticity parameters for material system HexPly IM7/8552 (US-Version)

Test	Y_{120} $(\sqrt{MPa})$	Y_{12c} $(\sqrt{MPa})$	Y_{12s} $(\sqrt{MPa})$	R_0 (MPa)	β (MPa)	μ $(-)$
$[\pm 45]_{4s}$	0.168	3.48	1.83	32.5	680	0.45
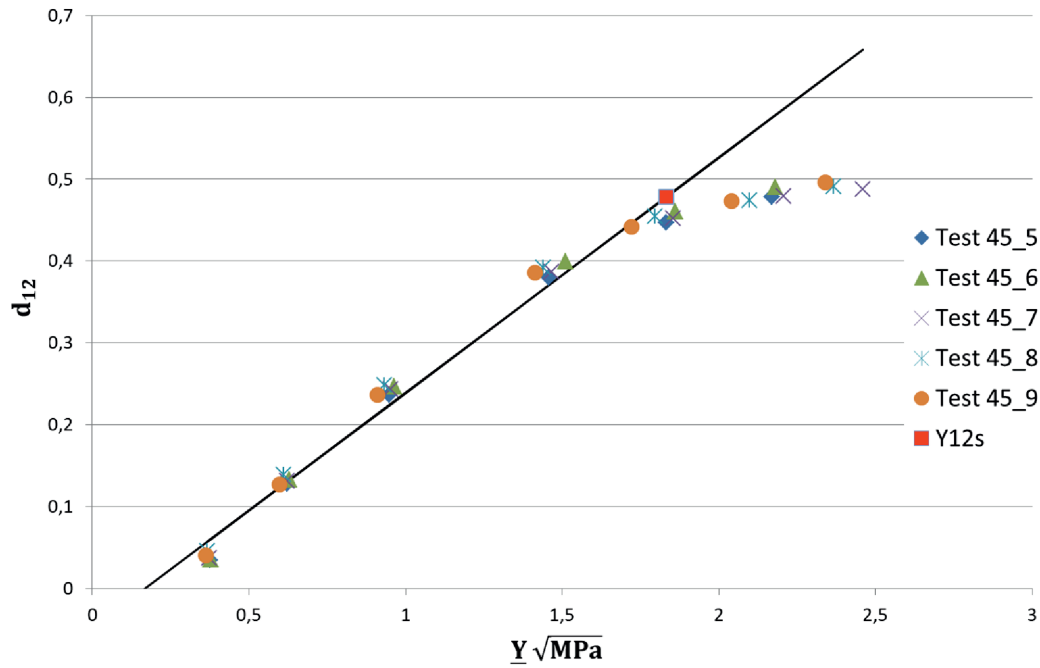
Figure A.3: Shear damage master curve of HexPly IM7/8552 (US-Version)
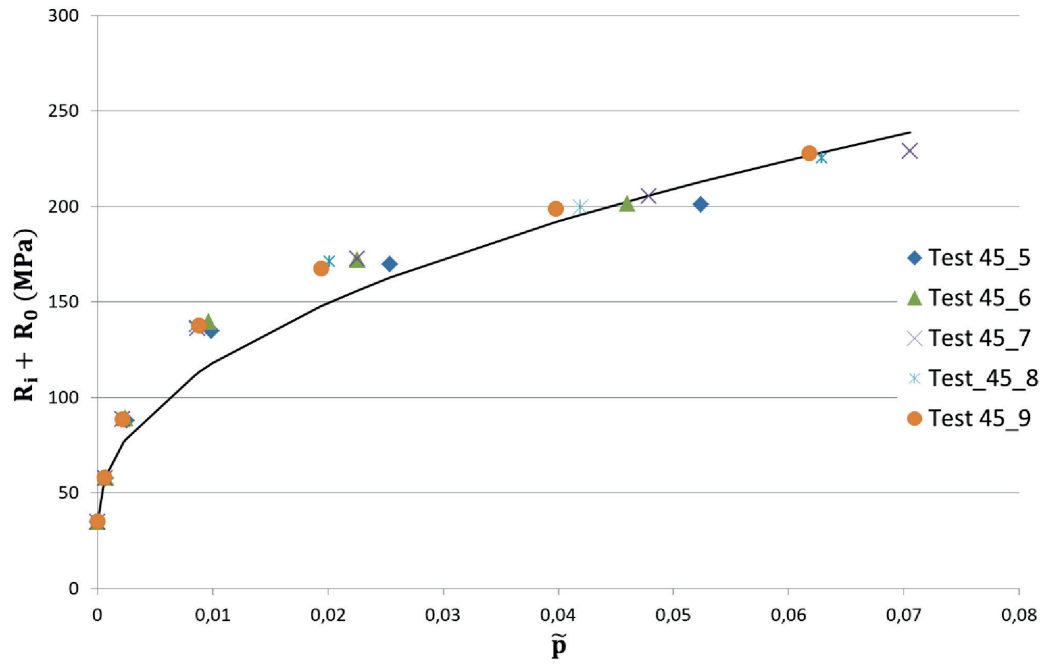
Figure A.4: Shear plasticity master curve of HexPly IM7/8552 (US-Version)

Identification of Transverse Damage and Coupling Parameters

Tests on laminates with $[\pm 67.5]_{4s}$ lay-ups were used to determine transverse damage parameters and the shear-transverse damage and plasticity coupling parameters as listed in Table A.3. The

specimens were cyclically loaded and unloaded in force control with increased force amplitude for the loading cycles as shown in Table A.6. To determine the shear-transverse damage and coupling parameters, the shear and transverse stresses were calculated using classical lamination theory as described in [181]:

$$\sigma_{22i} = (1 - B)\sigma_i \tag{A.10}$$

$$\tau_{12i} = \frac{-1}{2mn}(B(1 - 2m^2) + m^2)\sigma_i \tag{A.11}$$

with $m = \cos(67.5)$, $n = \sin(67.5)$ and the elastic material properties of HexPly IM7/8552 (US-Version) as reported in the NCAMP report [152] and used in the CMH-17 CWG, a value of $B = 0.207$ was calculated for $[\pm 67.5]_{4s}$ laminates. The principal lamina strains are:

$$\varepsilon_{22i} = n^2\varepsilon_{Li} + m^2 + \varepsilon_{Ti} \tag{A.12}$$

$$\gamma_{12i} = -2mn(\varepsilon_{Li} - \varepsilon_{Ti}) \tag{A.13}$$

From this, the cyclic behaviour of the $[\pm 67.5]_{4s}$ specimens can be plotted in terms of transverse stress-strain and shear-stress strain behaviour as shown in Figure A.5 and Figure A.6.

For each cycle, the transverse moduli E_{22i}, shear moduli G_{12i} and shear damage variables d_{12i} were determined as described in the previous section. The transverse damage variables for each cycle were calculated as:

$$d_{2i} = 1 - \left(\frac{E_{22i}}{E_{22}^0} \right) \tag{A.14}$$

With E_{22i} being the transverse modulus of the cycles in the principle material coordinate system and E_{22}^0 is the initial undamaged transverse modulus calculated for the initial linear slope between $1MPa$ and $4MPa$ transverse stress for each tested specimen. The initial shear modulus G_{12i}^0 was determined for the initial linear slope between $1MPa$ and $2MPa$ initial shear stress. With d_{2i} and d_{12i} the transverse and shear damage functions Y_{2i} and Y_{12i} were calculated following the procedure of Ladevèze and LeDantec [108]:

$$Y_{2i} = \frac{1}{2}\frac{\sigma_{22i}^2}{E_{22}^0(1 - d_{2i}^2)} \tag{A.15}$$

$$Y_{12i} = \frac{1}{2}\frac{\tau_{12i}^2}{G_{12}^0(1 - d_{12i}^2)} \tag{A.16}$$

Table A.6: Details of loading/unloading cycles for $[\pm 67.5]_{4s}$ tests

Cycle	1	2	3	4	5	6	7	8	9
Load	1250 N	2000 N	3000 N	3500 N	4000 N	4500 N	5000 N	5500 N	6000 N
Unload	100 N	100 N	100 N	100 N	100 N	100 N	100 N	100 N	100 N
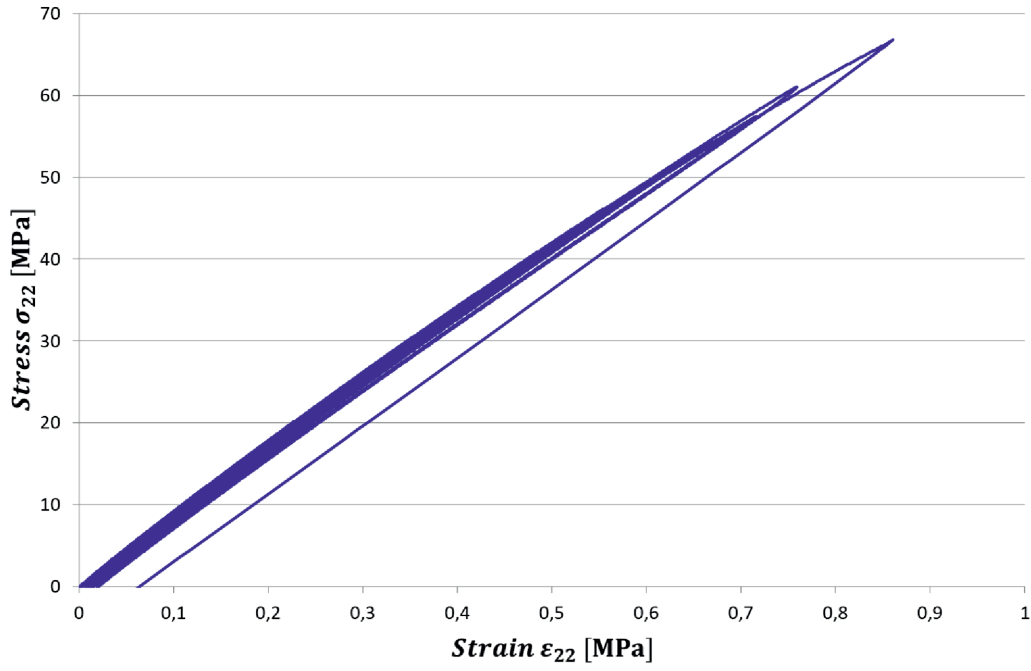
Figure A.5: Transverse stress-strain curve of cyclic tensile test on a $[\pm 67.5]_{4s}$ specimen
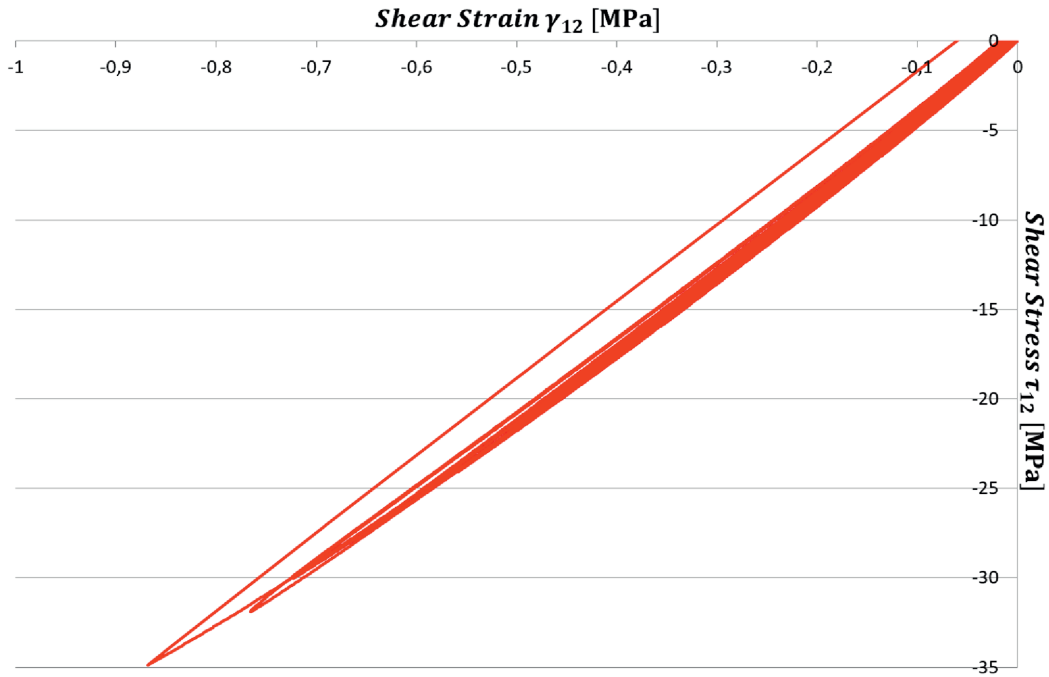
Figure A.6: Shear stress-shear strain curve of cyclic tensile test on a $[\pm 67.5]_{4s}$ specimen

and the coupling parameter b was calculated as:

$$b = \frac{(Y_{12c}d_{12i} + Y_{120})^2 - Y_{12i}}{Y_{2i}} \tag{A.17}$$
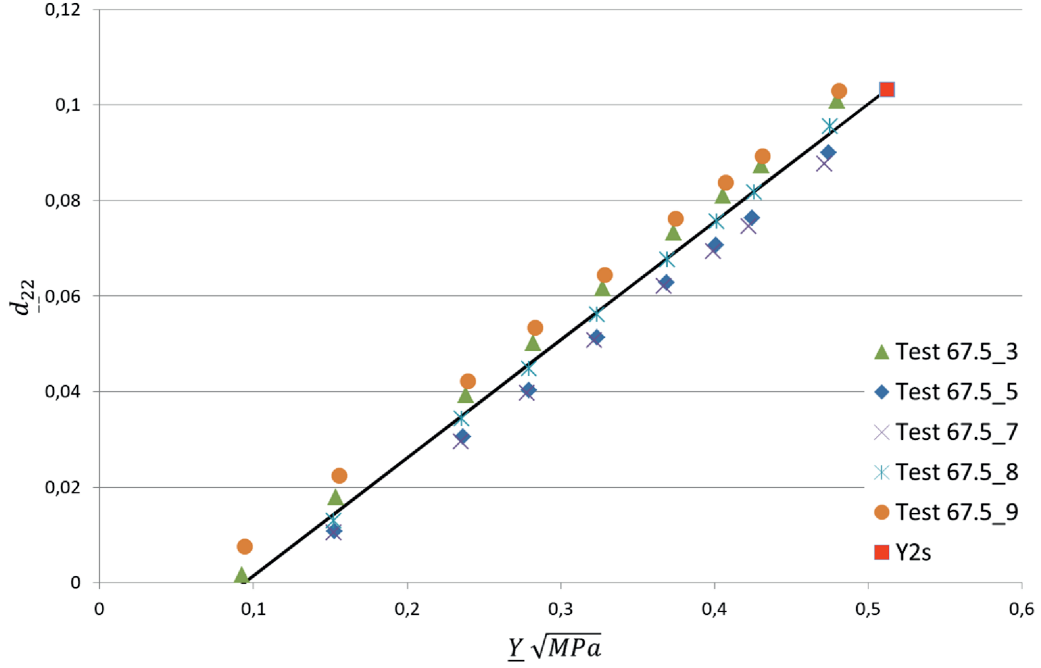
Figure A.7: Transverse damage master curve of HexPly IM7/8552 (US-Version)

with Y_{12c} and Y_{120} as determined in the previous section. As b is assumed to be a constant for material system HexPly IM7/8552, it can be found by plotting the lower term of Equation (A.17) against the upper term and the slope of the linear fit. The value of b was determined for Hex-Ply IM7/8552 (US-Version) to be $b = 0.465$. The transverse damage development law can be determined:

$$\underline{Y}_i = \sqrt{(Y_{12i} + bY_{2i})} \tag{A.18}$$

from which the transverse damage master curve is plotted in Figure A.7 and it is shown that good repeatability of the results could be achieved. As outlined by Ladevèze and LeDantec [108], the linear transverse damage master curve plotted in Figure A.7 can be expressed by:

$$d_{22i} = \frac{\underline{Y} - Y_{20}}{Y_{2c}} \tag{A.19}$$

The transverse damage threshold Y_{20} is the point at which d_{22} becomes zero and the transverse damage evolution parameter Y_{2c} is the inverse of the slope of the linear plot. The transverse failure threshold, Y_{2s} as introduced by Schueler [90, 91] was determined as $Y = 0.512\sqrt{MPa}$ which corresponds to the highest damage values seen in the tests. The shear-transverse plasticity coupling parameter α^2 was calculated following the procedure outlined in [108, 178]:

$$\alpha_i^2 = \frac{\varepsilon_{22pl,i}(1 - d_{2i}^2)\tau_{12i}}{\gamma_{12pl,i}(1 - d_{12i})^2\sigma_{22i}} \tag{A.20}$$

it is assumed that α^2 is a constant and can be determined by plotting the lower term of Equation (A.20) against the upper term for all tested specimens and applying a linear fit where $a^2 = 0.563$ is the slope.

Table A.7: Transverse damage and coupling parameters for material system HexPly IM7/8552 (US-Version)

Test	Y_{20} ($\sqrt{MPa}$)	Y_{2c} ($\sqrt{MPa}$)	Y_{2s} ($\sqrt{MPa}$)	b ($-$)	α ($-$)
$[\pm 67.5]_{4s}$	0.094	4.05	0.512	0.465	0.75

The values of HexPly IM7/8552 determined from cyclic $[\pm 67.5]_{4s}$ tests are listed in Table A.7

A.1.2 Interlaminar Fracture Toughness Parameters - Summary of Open Literature Data

In the scope of the CMH-17 CWG, Jusstuson et al. [182] provide information about DCB and ENF testes performed by Boeing on IM7/8552 and the plain-weave fabric SPG 196-PW/8552 in the scope of NASA's Advanced Composite Consortium (ACC) High Energy Dynamic Impact test programme (HEDI). Tests were performed using methods which vary to the ASTM D5528 and ASTM D7905 standards however with similar test fixtures used for DCB and ENF tests. Tests to determine the strain energy release rates G_{Ic} and G_{IIc} were performed by Boeing. G_{Ic} and G_{IIc} were calculated using:

$$G_{Ic} = G_{IIc} = \frac{\sum_{i=1}^{n}(P_{i+1} - P_i)L_i}{\alpha_f w} \tag{A.21}$$

P_i is the load at time step i, L_i is the initial length of the beam, α_f the crack length and w is the width of the DCB specimen. For IM7/8552 G_{Ic} was determined to be:

$$G_{Ic} = 0.324 \pm 0.012 \frac{kJ}{m^2} \tag{A.22}$$

which is slightly lower as the value of $G_{Ic} = 0.384\frac{kJ}{m^2}$ reported by Thorsson et al. [183] who simulated low velocity impact on specimen with the same material system using Abaqus/Explicit and cohesive elements to model delaminations. G_{IIc} was determined to be:

$$G_{IIc} = 0.778 \pm 0.063 \frac{kJ}{m^2} \tag{A.23}$$

Camanho et al. [157] used a continuum damage model to predict strength and size effects in notched carbon-epoxy laminates. The used material was IM7/8552 with a nominal ply thickness of 0.131 mm. To measure the components of the fracture toughness, double cantilever beam (DCB, using standard ASTM D 5528 [166]) and four-point bending end notched flexure (4-ENF, according to

[184]) were performed. The measured G_{Ic} and G_{IIC} values are:

$$G_{Ic} = 0.277 \pm 0.0246 \, \frac{kJ}{m^2} \tag{A.24}$$

$$G_{IIc} = 0.788 \pm 0.08 \, \frac{kJ}{m^2} \tag{A.25}$$

this shows that G_{Ic} as determined by Camanho et al. [157] is lower compared to the HEDI test data [182] whereas G_{IIc} is approximately equal for both tests.

Schoen et al. performed an extensive numerical and experimental investigation on the fracture mechanical properties of DCB [185] and ENF [186] specimens in accordance with standards defined by the European Structural Integrity Society (ESIS) [187]. Static and cyclic properties were studied for 0°/0°, 45°/45°, 90°/90° interfaces for several materials including IM7/8552 with a nominal ply thickness of 0.13 mm. For analysis of the test results, Schoen et al. used:

$$G_{Ic} = \frac{nP\delta}{2w\alpha} \tag{A.26}$$

where P is the applied load, δ is the crack-opening displacement at the point of the applied load, w is the width of the specimen and α is the crack-length. For IM7/8552, G_{Ic} was calculated for the 0°/0° interfaces as:

$$G_{Ic} = 0.22 \pm 0.01 \, \frac{kJ}{m^2} \tag{A.27}$$

For the 45°/45° and 90°/90° interfaces, damage initiation occurred at similar G_{Ic} values as for the 0°/0° interface [185]. Mode II fracture toughness was determined using ENF specimens [186]. The results for Mode II fracture toughness G_{IIc} for 0°/0°, 45°/45° and 90°/90° interfaces were presented in a bar diagram by Schoen et al. [186]. From this, the following values were derived:

$$\begin{aligned}
0°/0° \quad &\text{interface:} \quad G_{IIc} \sim 0.63 \, \frac{kJ}{m^2} \\
45°/45° \quad &\text{interface:} \quad G_{IIc} \sim 1.3 \, \frac{kJ}{m^2} \\
90°/90° \quad &\text{interface:} \quad G_{IIc} \sim 0.87 \, \frac{kJ}{m^2}
\end{aligned} \tag{A.28}$$

However, Andersons and Koenig [188] stated in their review paper the delamination cracks did not follow the intended interfaces for off-axis interfaces. Therefore, the values reported in [186] relate to complex inter- and intralaminar failure event rather than the mode II delamination along a give interface [188]. From the data reported by Schoen et al. [185, 186], G_{Ic} is lower compared to the HEDI test data by Jusstuson et al. [182]. whereas for 45°/45° and 90°/90° interfaces, G_{IIc} is higher compared to the HEDI test data.

Hiley [189] performed mode I, mode II and mixed-mode delamination tests between plies of different orientations (0°/0°, 0°/45°, 0°/90°) on IM7/8552 specimens. Mode I and Mode II strain energy

release rates G_{Ic} and G_{IIc} were determined using DCB and ENF tests in accordance to [187]. Mixed-mode tests were performed using 'Fixed-Ratio Mixed Mode' (FRMM) tests in accordance to [190]. The mode I fracture toughness G_{Ic} was calculated using:

$$G_{Ic} = \frac{3P\delta}{2w(\alpha + \Delta)})\frac{F}{N} \tag{A.29}$$

where P is the applied load, δ is the crack-opening displacement, w is the width of the specimen and α is the crack-length, Δ is a correction factor for the crack length. Corrections for large displacements F and end block effects N were also included but showed negligible effects [189]. G_{Ic} for IM7/8552 was determined for different interfaces as:

$$
\begin{aligned}
0°/0° \quad \text{interface:} \quad G_{Ic} &= 0.208 \, \frac{kJ}{m^2} \\
0°/45° \quad \text{interface:} \quad G_{Ic} &= 0.181 \, \frac{kJ}{m^2}
\end{aligned}
\tag{A.30}
$$

The mode II fracture toughness G_{IIc} was calculated using:

$$G_{IIc} = \frac{9\alpha^2 P^2 \delta}{2w(2L^3 + 3\alpha^3)} \tag{A.31}$$

where L is the half span width. The reported values for different interfaces (values for $0°/0°$ interfaces were not reported are:

$$
\begin{aligned}
0°/45° \quad \text{interface:} \quad G_{IIc} &= 0.941 \, \frac{kJ}{m^2} \\
0°/90° \quad \text{interface:} \quad G_{IIc} &= 0.727 \, \frac{kJ}{m^2}
\end{aligned}
\tag{A.32}
$$

Compared to the HEDI test data, G_{Ic} is slightly lower whereas the mode II fracture toughness G_{IIc} is higher for $0°/45°$ interfaces and slightly lower for $0°/90°$ interfaces.

Hansen and Martin [191] performed DCB, 4-ENF and Mixed Mode Bending (MMB) tests on IM7/8552 under both quasi-static and fatigue loading. The mode I fracture toughness was determined using DCB tests in accordance to ASTM D5528 [166] and was determined as:

$$G_{Ic} = 0.208 \pm 0.0085 \, \frac{kJ}{m^2} \tag{A.33}$$

Mode II fracture toughness was determined using 4-ENF tests performed on a standard four-point bend fixture [191] and was reported as:

$$G_{IIc} = 1.334 \pm 0.293 \, \frac{kJ}{m^2} \tag{A.34}$$

The mixed-mode bending tests were performed on a test fixture suggested by Draft ASTM MMB

standard. The fracture toughness under mixed-mode bending G_c was determined for ratios $\frac{G_{II}}{G_{tot}} = 0.33$ and 0.66. The reported values are:

$$
\begin{aligned}
\frac{G_{II}}{G_{tot}} = 0.33 : \qquad G_c = 0.298 \pm 0.042 \, \frac{kJ}{m^2} \\
\frac{G_{II}}{G_{tot}} = 0.66 : \qquad G_c = 0.374 \pm 0.109 \, \frac{kJ}{m^2}
\end{aligned}
\tag{A.35}
$$

Compared to the HEDI test data, G_{Ic} is lower but is the same as for $0°/0°$ interfaces reported in [189]. The value of G_{IIc} is significantly higher compared to the HEDI test data but is in the same range as the reported value for $45°/45°$ interfaces in [186]. No mixed mode bending was performed in the HEDI test programme.

Conclusion and Final Interlaminar Fracture Toughness data

IM7/8852 was widely used and results for fracture toughness in mode I, mode II and mixed-mode bending were published in literature. Mode I fracture toughness was mostly determined using DCB tests and most of the reported tests procedures followed ESIS [187] and ASTM [166] standards. The results of mode I fracture toughness G_{Ic} published in literature based on the ESIS/ASTM standards are lower compared to the fracture toughness reported in the HEDI test report following a Boeing-preferred test standard[182]. For mode II fracture toughness G_{IIc}, the values reported in literature showed a strong dependency on the fibre orientation of the interface.

Based on the large range of fracture toughness values reported in literature following the ASTM standards, the literature data will be used as basis for CMH-17 CWG ongoing material models for crash modelling efforts.

B Appendix to Chapter 4 - Numerical Modelling of Composite Materials

B.1 Hard- and Software

In this section, the hard- and software used for this work are presented which are constant for all simulations.

Hardware

Solution were carried out on a computing cluster with 14 nodes in total. 12 nodes (beo-1 to beo-12) equipped with 2 quadcore 64-bit Intel-Xeon E5540 processors and 2.53 GHz. Each node has 96 GB (beo-01 to beo-02) or 24 GB (beo-03 to beo-12) of RAM. Solutions were carried out on nodes beo-13 and beo-14 equipped with 2 octocore 64-bit Intel Xeon E5-2667 processors and 3.2 GHz. Each node has 512 GB RAM. Post-processing was conducted on a standard workstation running Windows. All interaction with the computing cluster was done using the remote client *Putty*.

Software

The user-material model ABQ_DLR_UD is written in the Fortran language. Compilation was performed within the framework of Abaqus/Explicit Version 2016 using the Intel Fortran Compiler 12.1.0. Simulations of this work were carried out using Abaqus/Explicit Version 2020 and the compiled files of VUMAT ABQ_DLR_UD were transferred to the newer version of the solver.

Pre-Processing on single-element level was carried out directly in the input text file in the framework of Abaqus/Explicit. Pre-processing on the higher level of the building block was done using Abaqus/CAE version 2020.

Solution The simulation files were transferred to the computing cluster and the simulations were performed using the following job settings:

- $1 - 16$ CPUs in shared memory processing mode. Detailed information on the used number of CPUs is provided in chapters Appendix D and **??**. For the single-element level one single CPU was used.

- Double precision mode was used consistently.

Post-processing was performed using the Abaqus/Explicit output database file (.odb files) including the time history outputs. Python scripts of version 2.7 were used to automatically extract the data using Abaqus/CAE version 2020. The simulation data were plotted using Python scripts and the Python libraries *numpy*, *matplotlib*, and *pyplot*. Contour plots were evaluated interactively using Abaqus/CAE version 2020.

B.2 List of Solution Dependent Variables

This sections provides an overview of the Solution Dependent Variables (SDV) of ABQ_DLR_UD, see Table B.1. The SDVs are used to store state dependent variables throughout the analysis process. The SDVs are stored in the output data base file (.odb) in Abaqus/Explicit and can be used to plot analysis results for pre-defined section points in post-processing.

B.3 Influence of Fibre Strain-Softening Options

In this section the fibre softening options are verified on single-element level. Stress-strain and the development of fibre and transverse damage variables are presented for linear softening, brittle failure with residual stress level and linear softening with residual stress level under longitudinal and compressive loading. Influence of different residual stress plateaus is presented exemplarily for 20 % and 80 % of the tensile or compressive strength.

Table B.1: Solution dependent variables (SDV) of ABQ_DLR_UD

SDV	Output Variable	Description
SDV1	ε_1^{el}	Elastic strain, long. direction
SDV2	ε_2^{el}	Elastic strain, trans. direction
SDV3	ε_{12}^{el}	Elastic strain, shear
SDV4	d_1^T	Fibre tensile damage
SDV5	d_1^C	Fibre compressive damage
SDV6	d_2^T	Matrix tensile damage
SDV7	d_2^C	Matrix compressive damage
SDV8	d_{12}	Shear damage
SDV9	$\underline{Y}$	Transverse damage energy release rate
SDV10	p	Equivalent plastic strain
SDV11	-	not in use
SDV12	-	not in use
SDV13	-	not in use
SDV14	-	not in use
SDV15	r_{1t}	Fibre tensile damage threshold
SDV16	r_{1c}	Fibre compressive damage threshold
SDV17	r_{2t}	Matrix tensile damage threshold
SDV18	r_{2c}	Matrix compressive damage threshold
SDV19	G_{c1}^T	Fibre tensile fracture energy - calibrated ($l^* > l_{max}^*$)
SDV20	G_{c1}^C	Fibre compressive fracture energy - calibrated ($l^* > l_{max}^*$)
SDV21	-	not in use
SDV22	-	not in use
SDV23	$Status$	Material point status
SDV24	l^*	Characteristic element length
SDV25	$\underline{Y}_2$	Transverse tensile energy release rate
SDV26	Y_{12}	Shear energy release rate
SDV27	-	not in use
SDV28	ε_2^{pl}	Plastic strain
SDV29	$fail_1^T$	Failure flag, long. tension ($\varepsilon_1 \geqslant \varepsilon_{sat,1}$)
SDV30	$fail_1^C$	Failure flag, long. compression ($\varepsilon_1 \leqslant \varepsilon_{sat,1}$)
SDV31	$fail_2^T$	Failure flag, trans. tension ($\underline{Y} > Y_{12s}$ or $\underline{Y}_2 > Y_{2s}$)
SDV32	$fail_2^C$	Failure flag, trans. compression ($\sigma_2 > Y_C$)
SDV33	$fail_{12}$	Failure flag, shear $\underline{Y} > Y_{12s}$ or $\underline{Y}_2 > Y_{2s}$
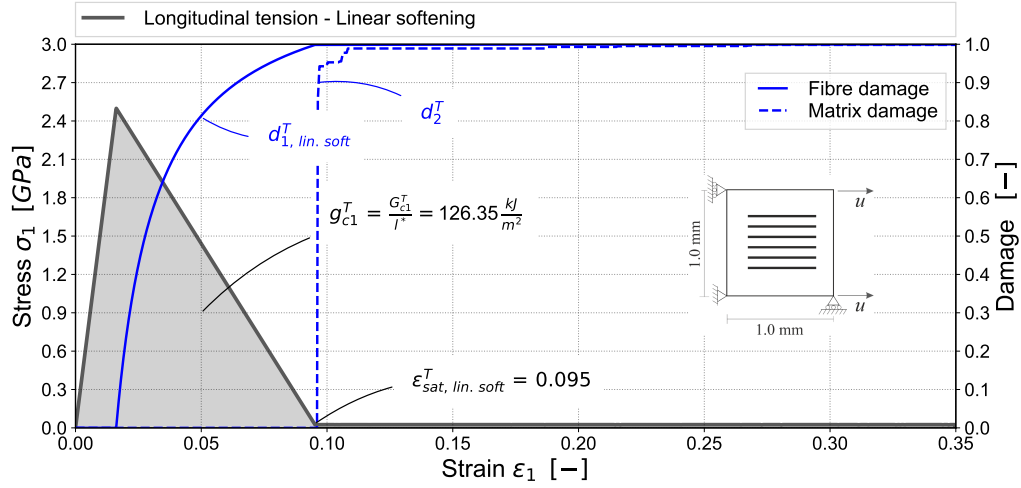
a) Longitudinal tensile loading
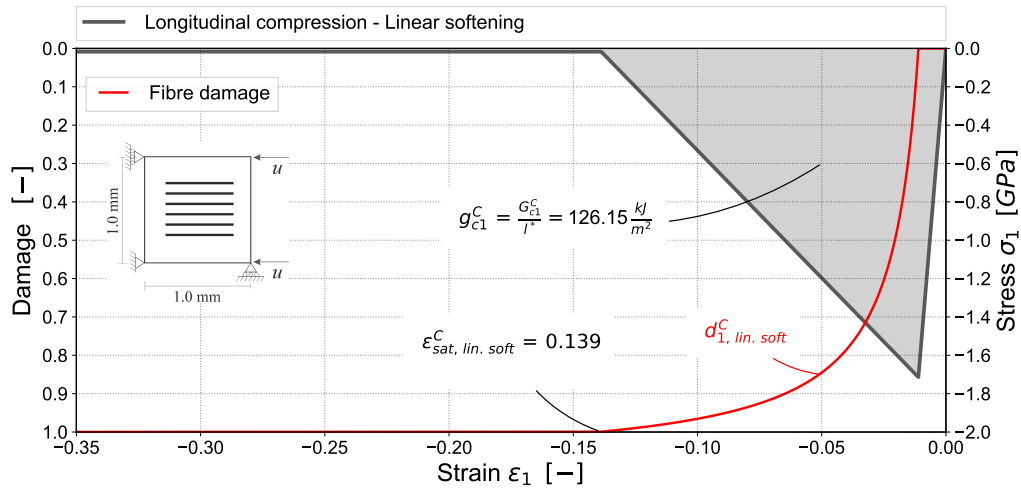
b) Longitudinal compressive loading

Figure B.1: Single-element simulation - Stress-strain characteristic of a) longitudinal tensile loading, b) longitudinal compressive loading with linear strain softening. Evolution of fibre tensile and compressive damage variables d_1^T, d_1^C and a) transverse tensile damage d_2^T and shear damage d_{12} variables; Material properties of IM7/8552 EU-Version and IM7/8552 US-Version
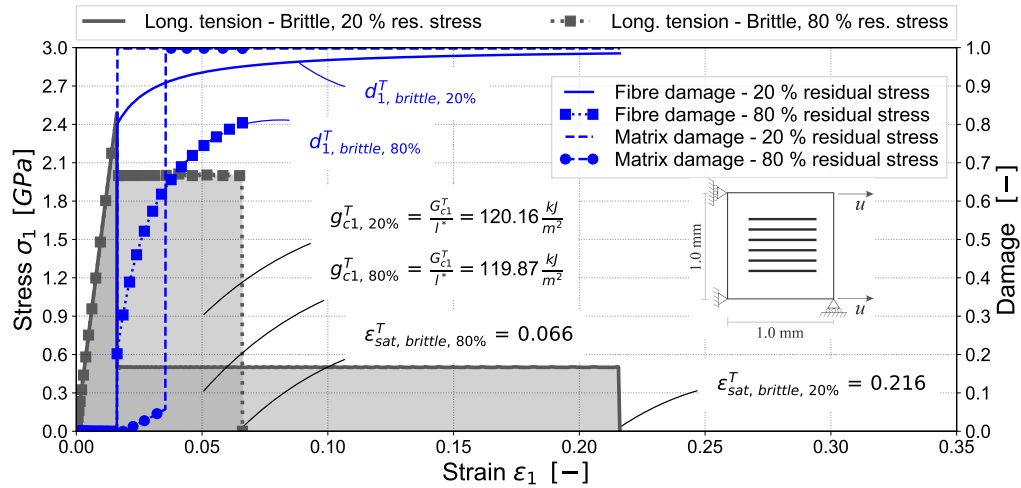
a) Longitudinal tensile loading
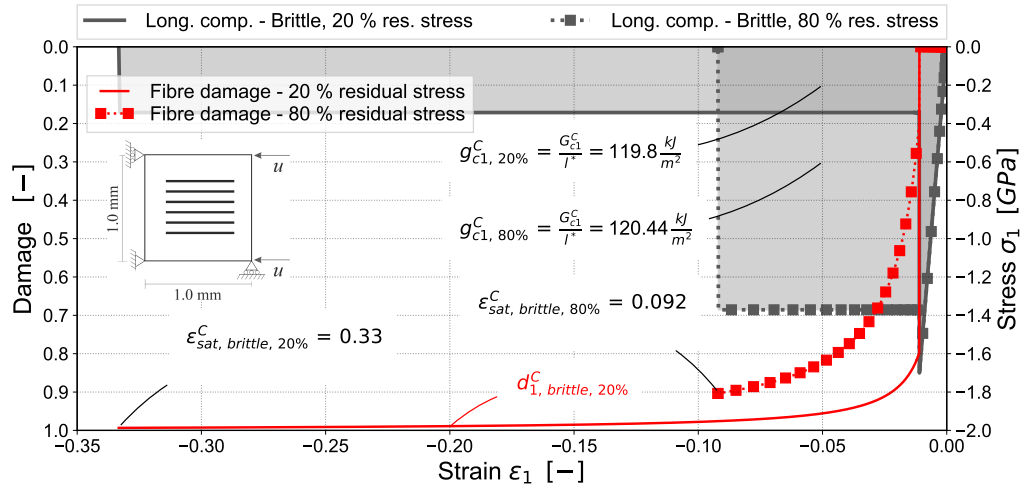
b) Longitudinal compressive loading

Figure B.2: Single-element simulation - Stress-strain characteristic of a) longitudinal tensile loading, b) longitudinal compressive loading with brittle failure with residual stress. Evolution of fibre tensile and compressive damage variables d_1^T, d_1^C and a) transverse tensile damage d_2^T and shear damage d_{12} variables; Residual stress level of 20% and 80% of the strength. Material properties of IM7/8552 EU-Version and IM7/8552 US-Version
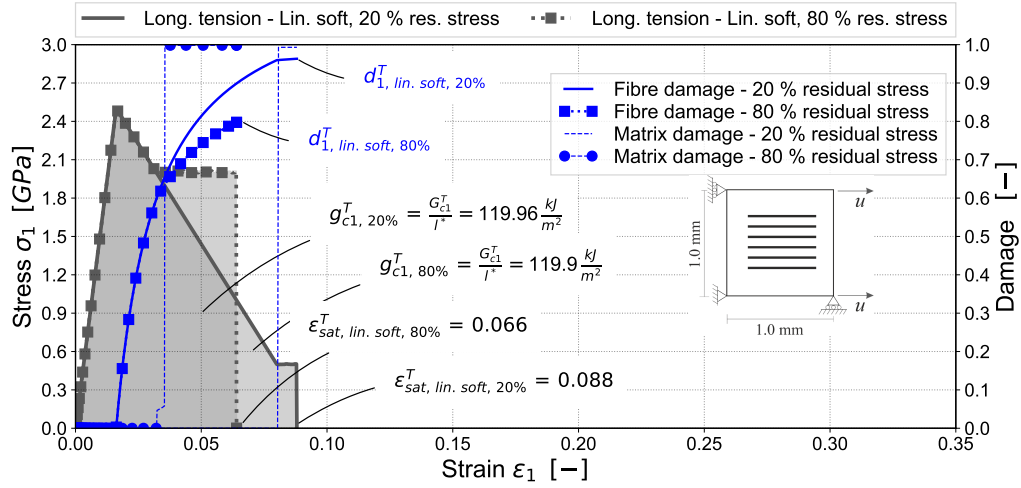
a) Longitudinal tensile loading
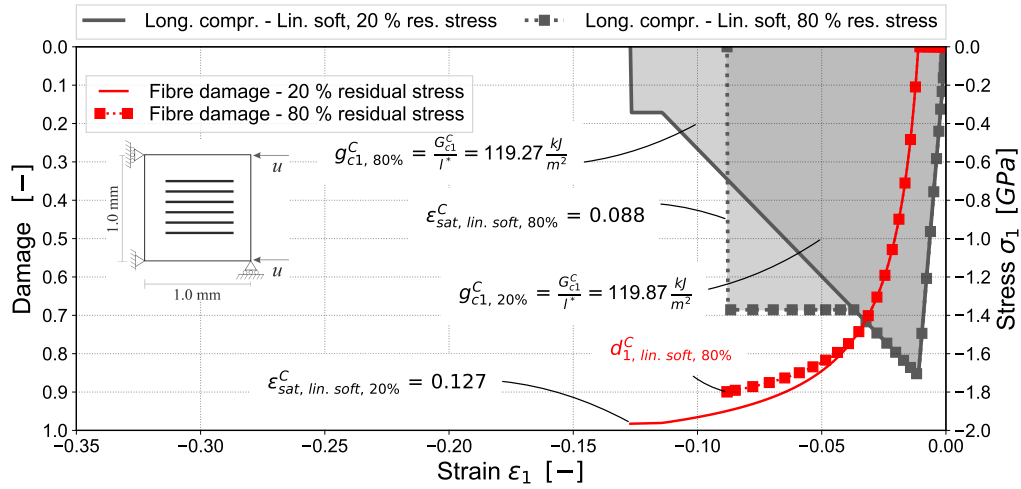
b) Longitudinal compressive loading

Figure B.3: Single-element simulation - Stress-strain characteristic of a) longitudinal tensile loading, b) longitudinal compressive loading with linear softening with residual stress. Evolution of fibre tensile and compressive damage variables d_1^T, d_1^C and a) transverse tensile damage d_2^T and shear damage d_{12} variables; Residual stress level of 20% and 80% of the strength. Material properties of IM7/8552 EU-Version and IM7/8552 US-Version

C Appendix to Chapter 5 - Behaviour at the Laminate Level

C.1 Influence of Fibre Softening Options - Evolution of Damage in the Individual Plies

In the following, the evolution of fibre and transverse damage in the individual plies under tensile and compressive loading are presented for the different fibre softening options linear softening, brittle failure with residual stress and linear softening with residual stress are presented. Influence of the residual stress levels are exemplarily presented for 20 % and 80 % residual stress level.

a) Compressive loading
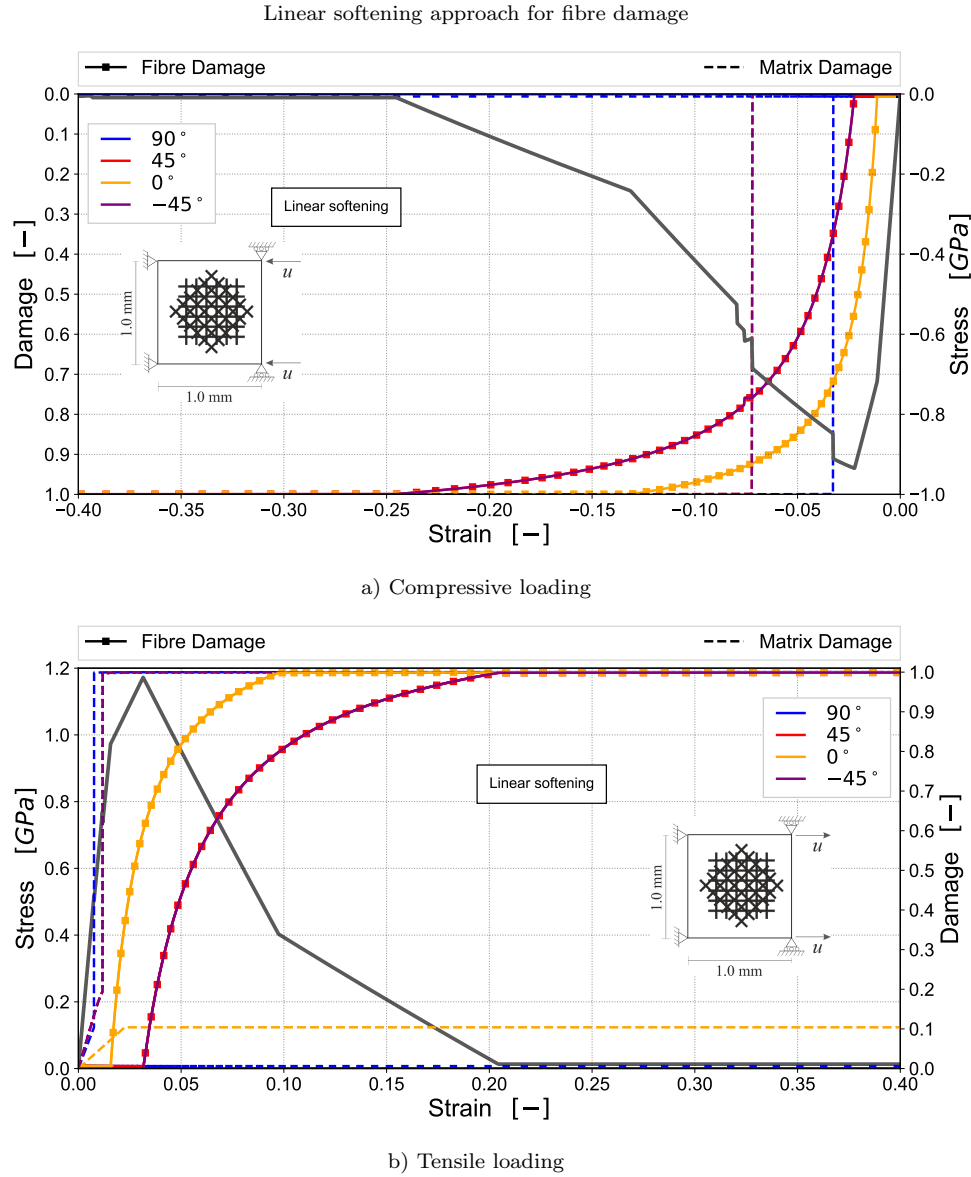
b) Tensile loading

Figure C.1: Single-laminate element simulation of layup $[90/45/0/-45]_{4s}$ - Stress-strain characteristic of a) compressive loading and b) tensile loading with linear softening approach. Evolution of damage parameters in the individual plies. Material properties of IM7/8552 EU-Version

Brittle failure with 20% residual stress plateau

a) Compressive loading

b) Tensile loading

Brittle failure with 80% residual stress plateau

a) Compressive loading
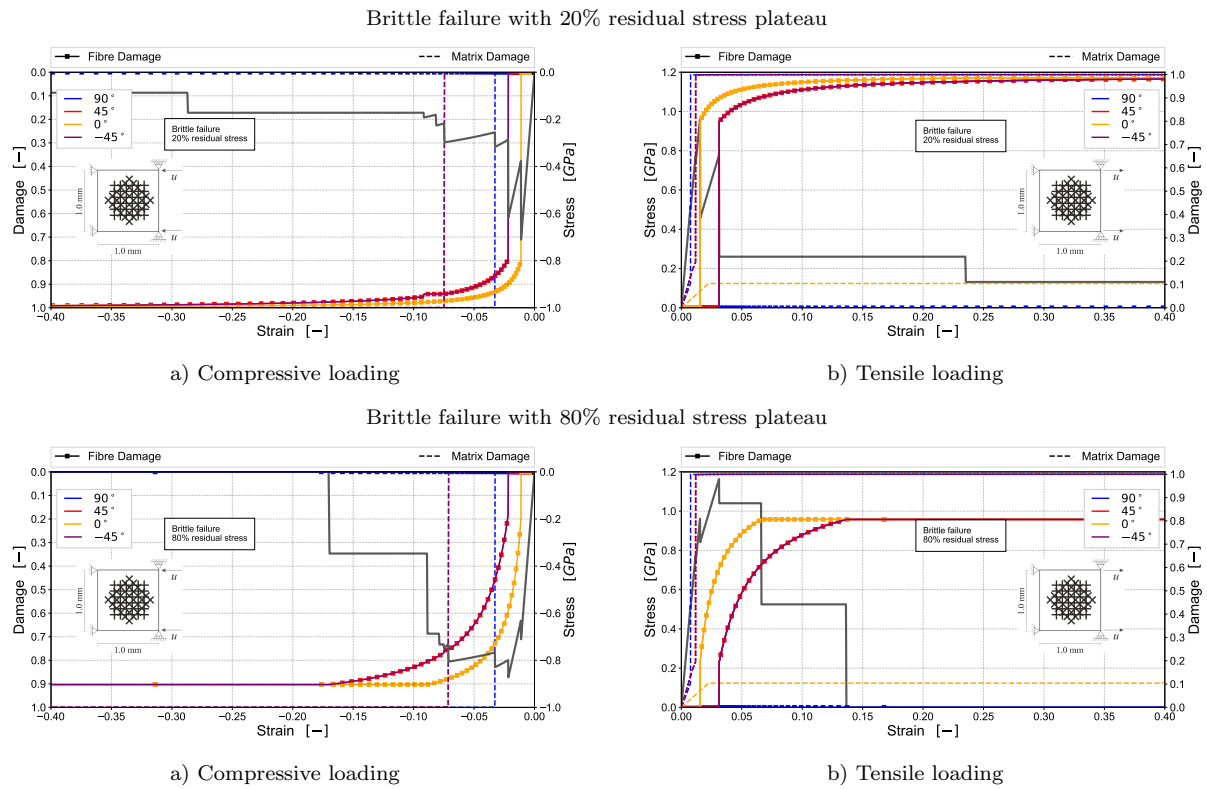
b) Tensile loading

Figure C.2: Single-laminate element simulation - Stress-strain characteristic of a) compressive loading and b) tensile loading with brittle failure with residual stress. Evolution of damage parameters in the individual plies. Material properties of IM7/8552 EU-Version

Linear softening with 20% residual stress plateau

a) Compressive loading

b) Tensile loading

Linear softening with 80% residual stress plateau

a) Compressive loading
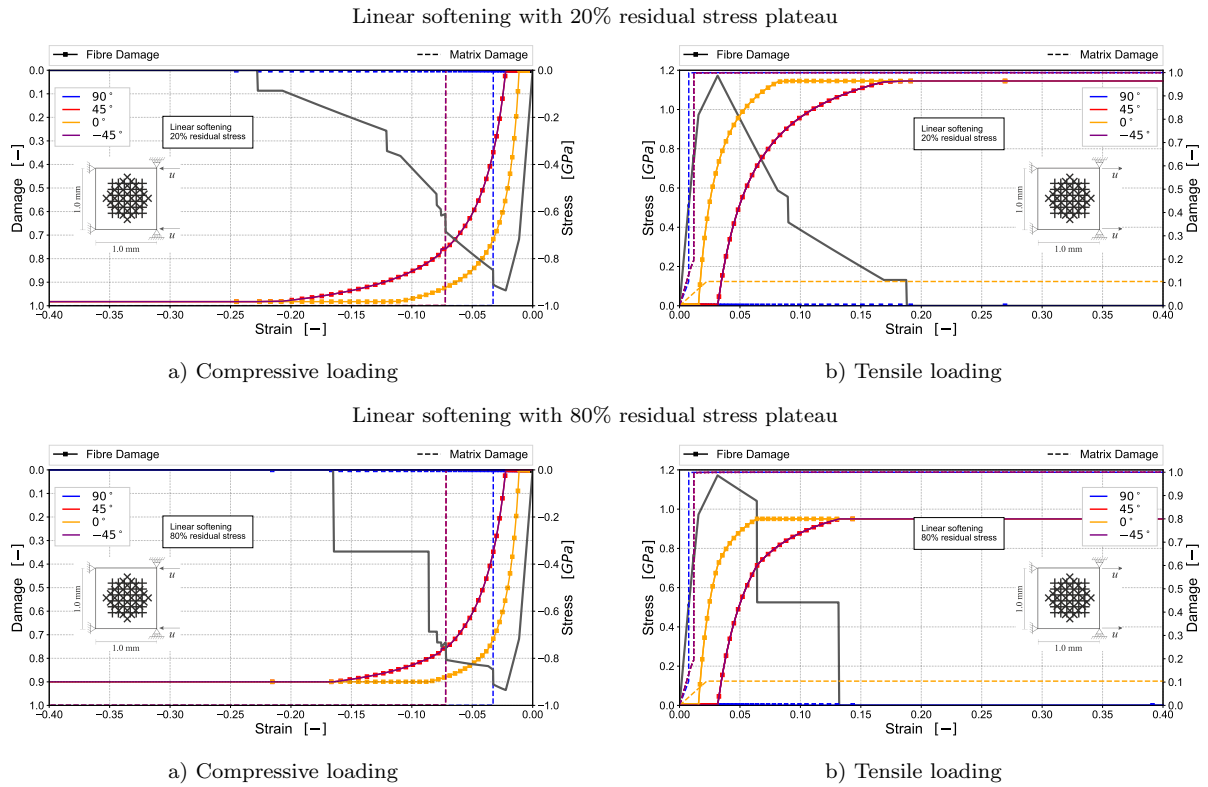
b) Tensile loading

Figure C.3: Single-laminate element simulation - Stress-strain characteristic of a) compressive loading and b) tensile loading with linear softening with residual stress. Evolution of damage parameters in the individual plies. Material properties of IM7/8552 EU-Version

D Appendix to Chapter 6 - Numerical Analysis and Validation of Fracture Mechanic Tests

D.1 Simulation Details

In the following tables, information about the simulation models, number of elements, initial time increment and wall-clock times are given for the OCT and CC models. The tables list information for the major model types of different element size and the stacked-shell model. All simulations performed for OCT or CC used one of these models. Note that initial time increment, CPU and wall-clock time may differ for the individual simulations. No mass-scaling of the initial time increment was performed in the simulations.

Table D.1: OCT simulation details

Over-height Compact Tension simulation details						
Model	Element size	No. of Elements	Initial time increment	CPU	Simulation time	Wall-clock time (hh:mm:ss)
OCT, $0.5\,mm$	$0.5\,mm$	27008	$3.68 \cdot 10^{-5}\,ms$	16	$20\,ms$	11:45:10
OCT, $1.0\,mm$	$1.0\,mm$	14770	$4.03 \cdot 10^{-5}\,ms$	4	$20\,ms$	14:05:50
OCT, $2.0\,mm$	$2.0\,mm$	12312	$3.82 \cdot 10^{-5}\,ms$	4	$20\,ms$	13:18:46
OCT, stacked-shell	$1.0\,mm$	221550	$1.79 \cdot 10^{-5}\,ms$	4	$20\,ms$	45:57:13

D.2 Simulation of Compact Compression Tests without Contact Modelling

In the following sections, the CC-simulation results are presented for the model without contact. The simulations are identical to Section 6.3. Also, the main findings outlined in Section 6.3 are also valid for the simulations without contact.

Table D.2: CC simulation details

Compact Compression simulation details						
Model	Element size	No. of Elements	Initial time increment	CPU	Simulation time	Wall-clock time
CC, $0.5\,mm$	$0.5\,mm$	11327	$4.74 \cdot 10^{-5}\,ms$	4	$20\,ms$	11:20:25
CC, $1.0\,mm$	$1.0\,mm$	4528	$7.25 \cdot 10^{-5}\,ms$	4	$20\,ms$	03:15:08
CC, stacked-shell	$1.0\,mm$	66233	$1.98 \cdot 10^{-5}\,ms$	4	$20\,ms$	05:23:13

D.2.1 Validation of Compressive Fibre Fracture Energies without Contact Modelling

D.2.2 Effects of Fibre Softening Options in Compact Compression Simulations without Contact

D.2.3 Validation of Stacked-Shell Modelling Approach
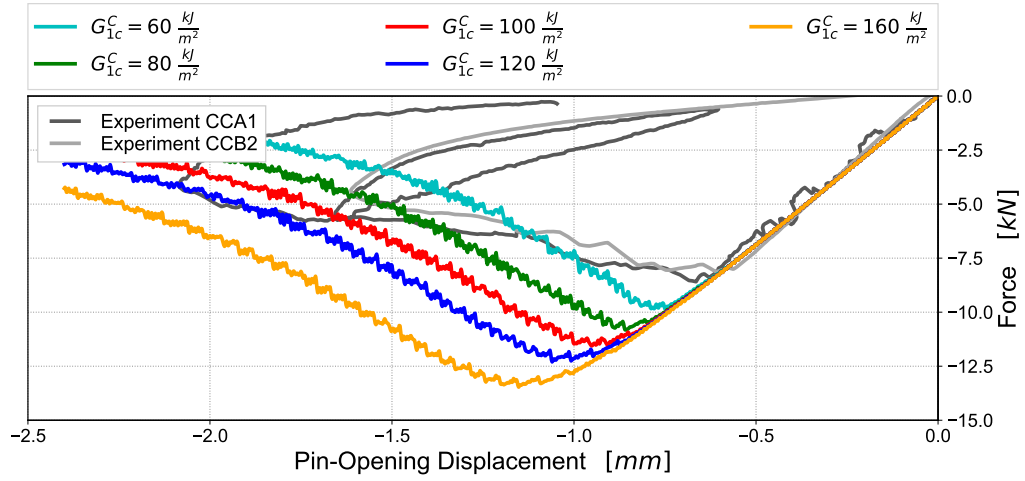
a) Force vs. pin-opening displacement characteristic
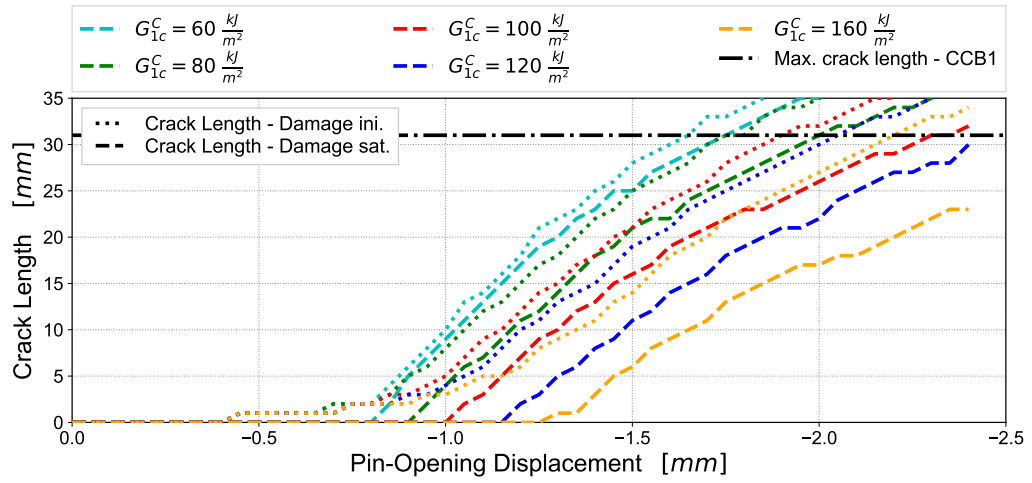
b) Crack length vs. pin-opening displacement

Figure D.1: OCT simulation - Validation of tensile fibre fracture energy; a) Force-displacement characteristics, b) crack length vs. pin-opening displacement
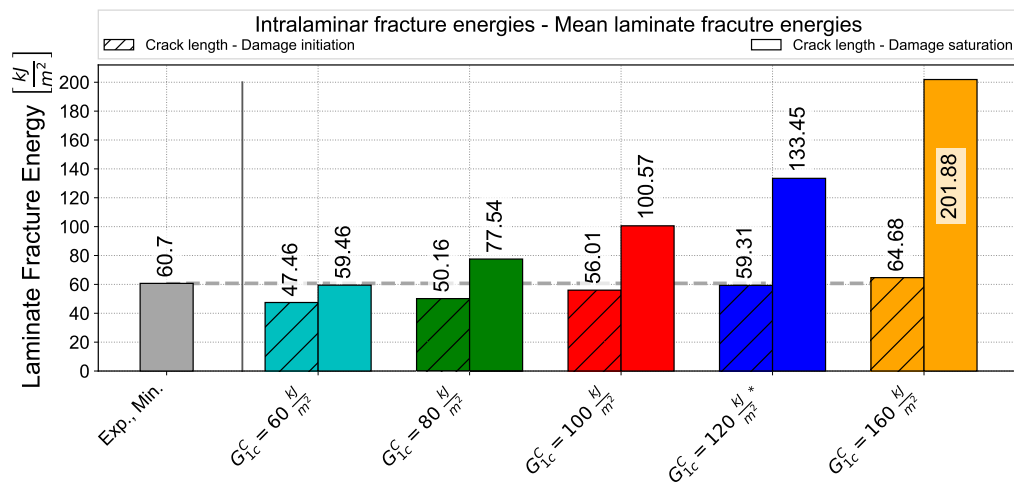
Figure D.2: Laminate fracture energies predicted from CC simulations using different fibre compressive fracture energies

Force vs. pin-opening displacement characteristic · Crack length vs. pin-opening displacement

a) Linear softening

b) Brittle failure with residual stress

c) Linear softening with residual stress
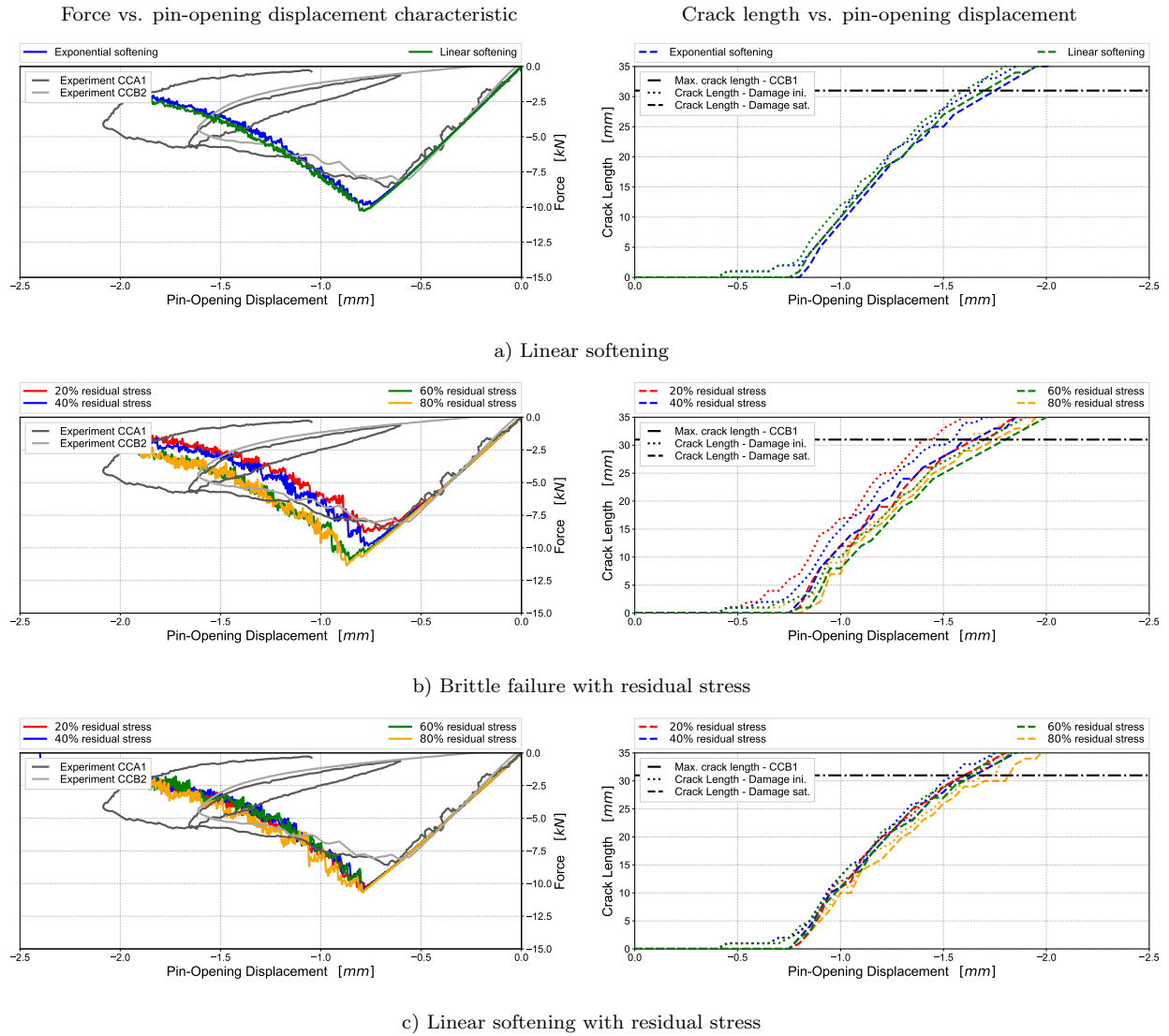
Figure D.3: CC simulation - Effects of fibre softening options; a) Force-displacement characteristics, b) crack length vs. pin-opening displacement
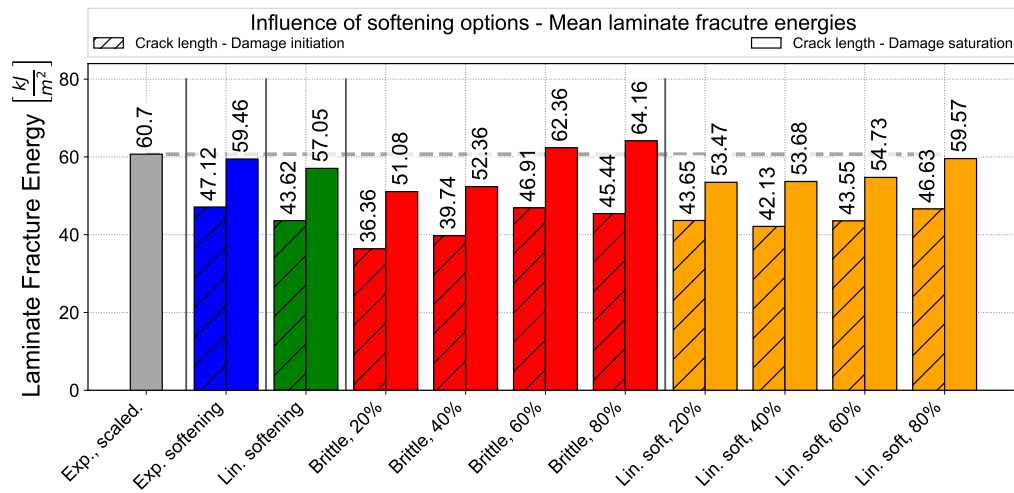
Figure D.4: Laminate fracture energies predicted from CC simulations using different fibre softening options
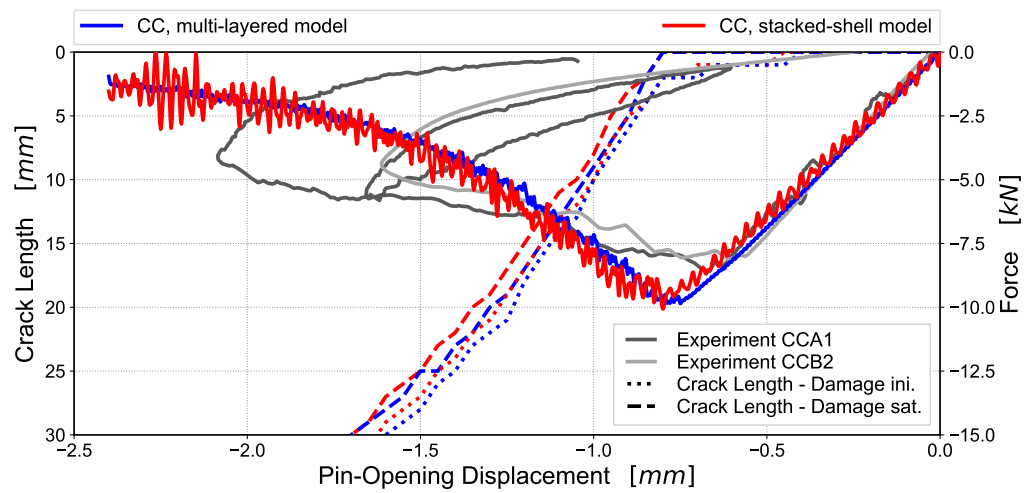
a) CC - Force vs. pin-opening displacement characteristic and crack length
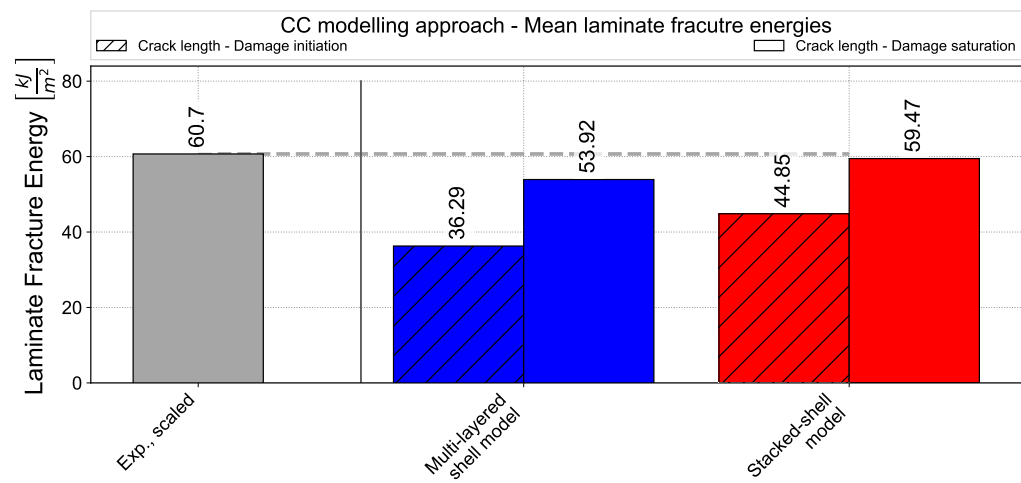
b) CC - Predicted laminate fracture energies

Figure D.5: Comparison of CC results obtained with multi-layered shell and stacked shell models

E Appendix to Chapter 7 - Numerical Analysis of Progressive Crushing

E.1 Simulation Details

In the following tables, information about the simulation models, number of elements, initial time increment, simulation times and wall-clock times are given for the self-supported DLR crush segment, flat coupon and C-channel segment simulations. The tables list information for the major model types of different element size, multi-layered and stacked shell models. In the study of the fibre softening options on the DLR crush segment, the skewed mesh type with $1.0\,mm$ element size was used. This model is highlighted in red in Table E.1. The simulations of different layups of the flat coupon specimen with multi-layered shell model were performed on the skewed mesh with $1.0\,mm$ element size. The model is highlighted in red in Table E.2. Note that the time increment is not constant during the simulation. Evolution of the time increment is dependent on the deformation and erosion of elements due to damage and therefore dependent on different settings in the material model like fibre softening option and fibre fracture energy. The evolution of the time increments directly influences the wall-clock times. No mass scaling was used in the simulations.

E.2 Mesh Type and Element Size Study on Flat Coupon Specimens

In this study, the influence of mesh type and element size on the flat coupon crushing behaviour is investigated. This study is identical to the study on the self-supported DLR crush segment in Section 7.2.2. The flat coupon specimen is meshed with the same mesh types and element sizes. The study on the flat coupon specimen confirms the results and findings obtained from the DLR segment. However, the element size influence in the skewed mesh type are more distinct for the flat coupon simulation compared to the DLR segment simulation.

E.3 Influence of Fibre Softening Options on Flat coupon crushing

The influence of fibre softening options is investigated on the flat coupon specimen. The study is identical to the one performed on the self-supported DLR-segment in Section 7.2.3. The results are

Table E.1: DLR crush segment simulation details

DLR crush segment simulation details						
Model	Element size	No. of Elements	Initial time increment	CPU	Simulation time	Wall-clock time (hh:mm:ss)
Structured mesh type						
Structured mesh	$0.5\,mm$	25578	$6.68 \cdot 10^{-5}\,ms$	4	$10\,ms$	06:46:22
Structured mesh	$1.0\,mm$	7823	$1.33 \cdot 10^{-4}\,ms$	4	$10\,ms$	00:48:01
Structured mes	$2.0\,mm$	3356	$2.62 \cdot 10^{-4}\,ms$	4	$10\,ms$	00:07:29
Skewed mesh type						
Skewed Mesh	$0.5\,mm$	27378	$3.25 \cdot 10^{-5}\,ms$	4	$10\,ms$	12:51:54
Skewed Mesh	$1.0\,mm$	7472	$2.65 \cdot 10^{-5}\,ms$	4	$10\,ms$	01:50:43
Skewed Mesh	$2.0\,mm$	3749	$5.71 \cdot 10^{-5}\,ms$	4	$10\,ms$	00:14:14
Unstructured mesh type						
Unstructured Mesh	$0.5\,mm$	30397	$1.71 \cdot 10^{-5}\,ms$	4	$10\,ms$	23:08:50
Unstructured Mesh	$1.0\,mm$	8945	$3.89 \cdot 10^{-5}\,ms$	4	$10\,ms$	02:24:08
Unstructured Mesh	$2.0\,mm$	3813	$8.71 \cdot 10^{-5}\,ms$	4	$10\,ms$	00:20:08

shown in Figure E.2. It is shown that the influence of different fibre softening options is identical to the effects observed for the DLR crush segment simulations. From this it is concluded that the results and explanations obtained for the DLR crush segment are also valid for flat coupon crushing.

Table E.2: Flat coupon simulation details

Flat coupon crushing simulation details						
Model	Element size	No. of Elements	Initial time increment	CPU	Simulation time	Wall-clock time (hh:mm:ss)
Multi-layered shell model						
Mesh type study - Structured mesh						
Structured mesh	$0.5\,mm$	21508	$2.92 \cdot 10^{-5}\,ms$	4	$10\,ms$	05:57:56
Structured mesh	$1.0\,mm$	6088	$5.49 \cdot 10^{-5}\,ms$	4	$10\,ms$	00:43:25
Structured mes	$2.0\,mm$	2456	$1.06 \cdot 10^{-4}\,ms$	4	$10\,ms$	00:09:25
Mesh type study - Skewed mesh						
Skewed Mesh	$0.5\,mm$	22447	$3.22 \cdot 10^{-5}\,ms$	4	$10\,ms$	07:37:33
Skewed Mesh	$1.0\,mm$	6192	$7.58 \cdot 10^{-5}\,ms$	4	$10\,ms$	00:46:40
Skewed Mesh	$2.0\,mm$	2167	$1.39 \cdot 10^{-4}\,ms$	4	$10\,ms$	00:07:29
Mesh type study - Unstructured mesh type						
Unstructured Mesh	$0.5\,mm$	26791	$2.75 \cdot 10^{-5}\,ms$	4	$10\,ms$	14:41:41
Unstructured Mesh	$1.0\,mm$	7339	$6.28 \cdot 10^{-5}\,ms$	4	$10\,ms$	01:31:50
Unstructured Mesh	$2.0\,mm$	2485	$1.30 \cdot 10^{-4}\,ms$	4	$10\,ms$	00:13:00
Stacked-shell model						
Layup 'QI-01'	$1.0\,mm$	164250	$4.42 \cdot 10^{-5}\,ms$	4	$10\,ms$	23:44:58
Layup 'QI-02'	$1.0\,mm$	83030	$4.42 \cdot 10^{-5}\,ms$	4	$10\,ms$	05:46:11
Layup 'QI-03'	$1.0\,mm$	83030	$4.42 \cdot 10^{-5}\,ms$	4	$10\,ms$	04:39:17
Layup 'QI-04'	$1.0\,mm$	170718	$4.42 \cdot 10^{-5}\,ms$	4	$10\,ms$	18:58:09
Layup 'HL-01'	$1.0\,mm$	101769	$4.42 \cdot 10^{-5}\,ms$	4	$10\,ms$	05:20:58
Layup 'HL-02'	$1.0\,mm$	123013	$4.42 \cdot 10^{-5}\,ms$	4	$10\,ms$	07:02:09

a) Structured mesh

b) Skewed mesh

c) Unstructured mesh
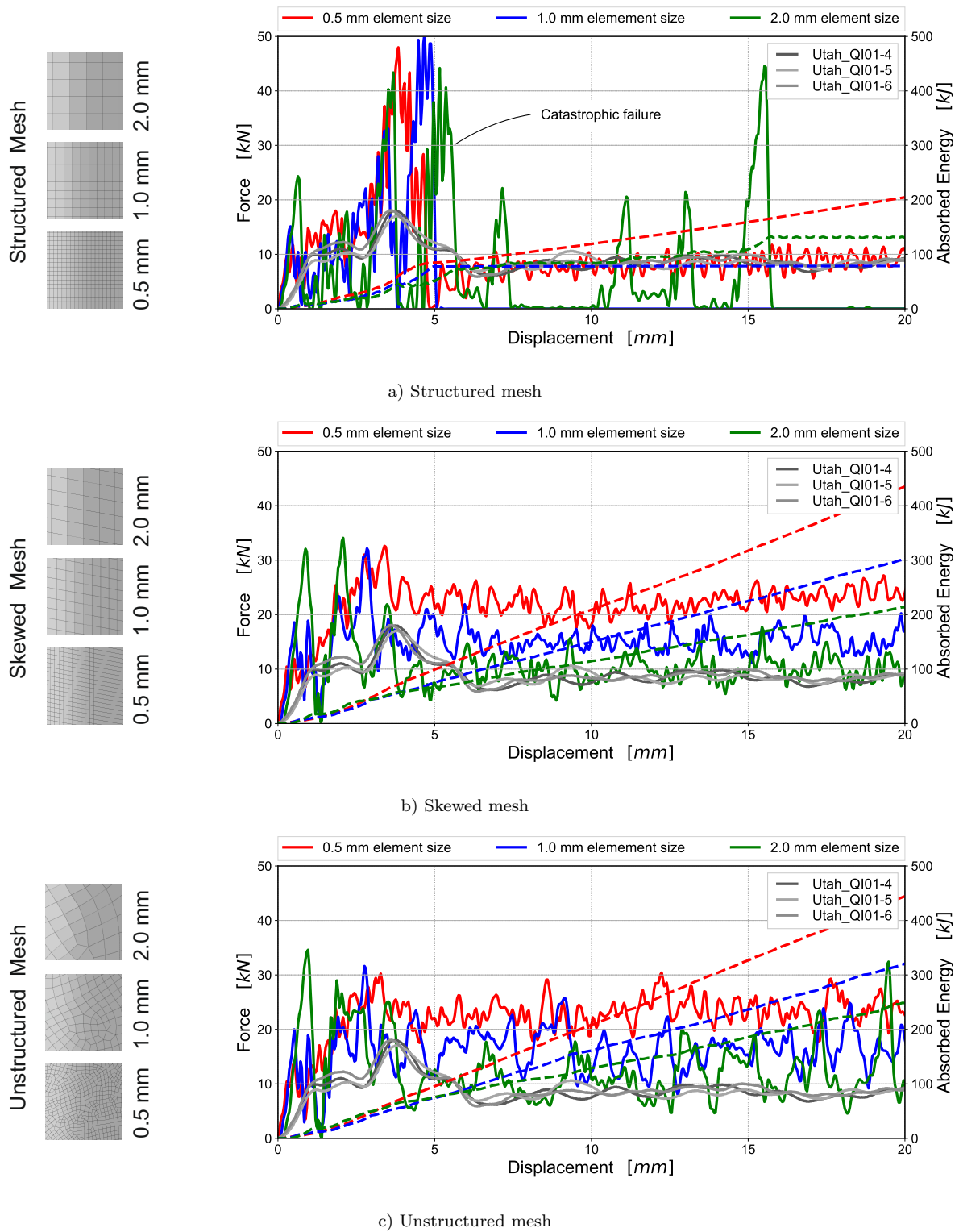
Figure E.1: Mesh type and element size study on the flat coupon specimen. Investigation of three mesh types: Structured mesh, skewed mesh and unstructured mesh and three element sizes, $0.5\,mm$, $1.0\,mm$ and $2.0\,mm$. Force-displacement characteristic and evolution of absorbed energy
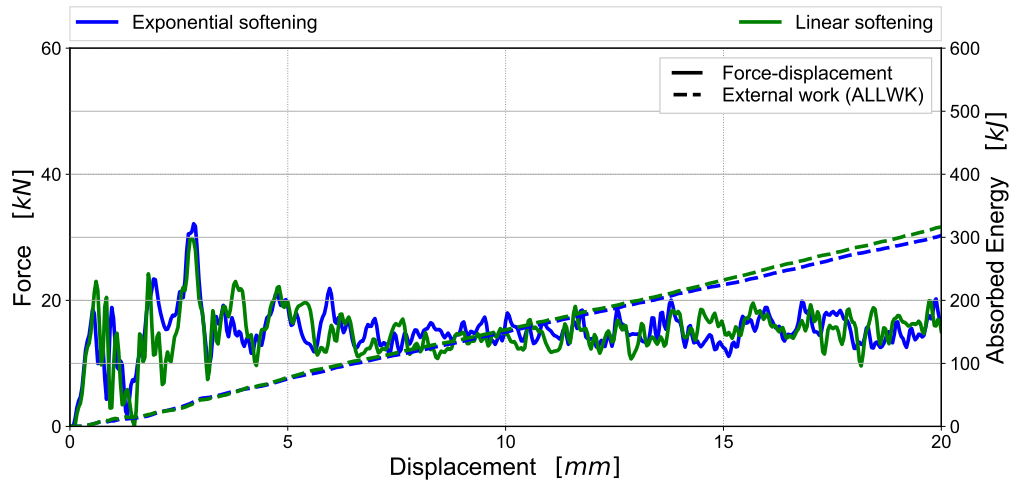
a) Linear softening
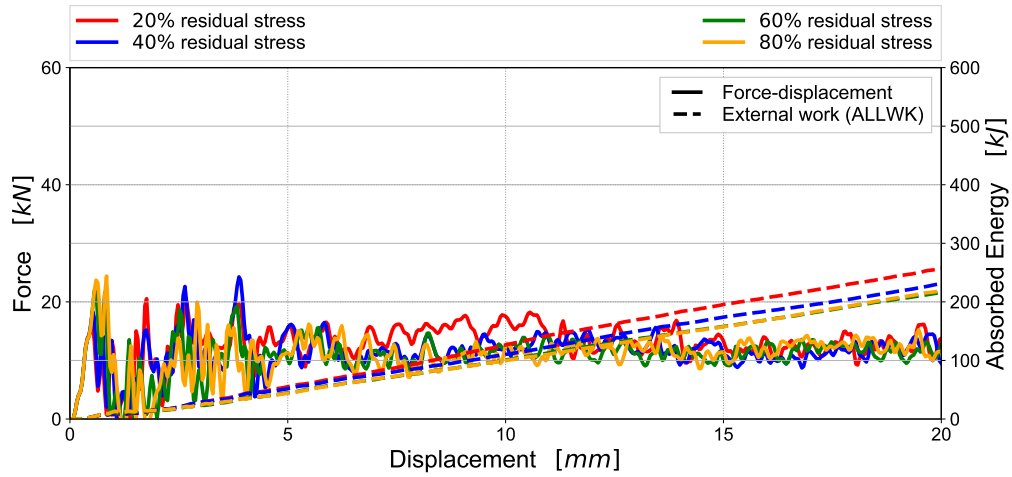
b) Brittle failure with residual stress
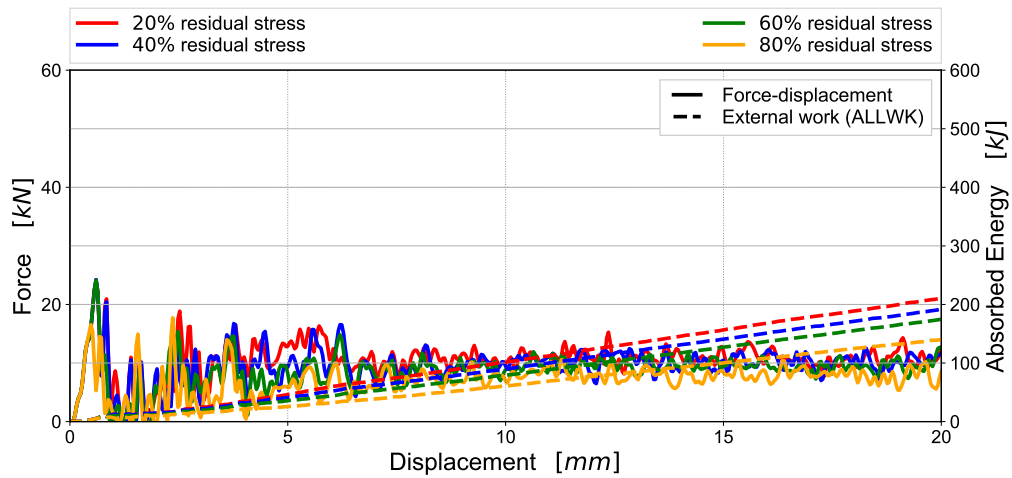
c) Linear softening with residual stress

Figure E.2: Numerical study of a flat coupon crushing - Influence of fibre softening options in progressive crushing; Force-displacement characteristic and evolution of absorbed energy
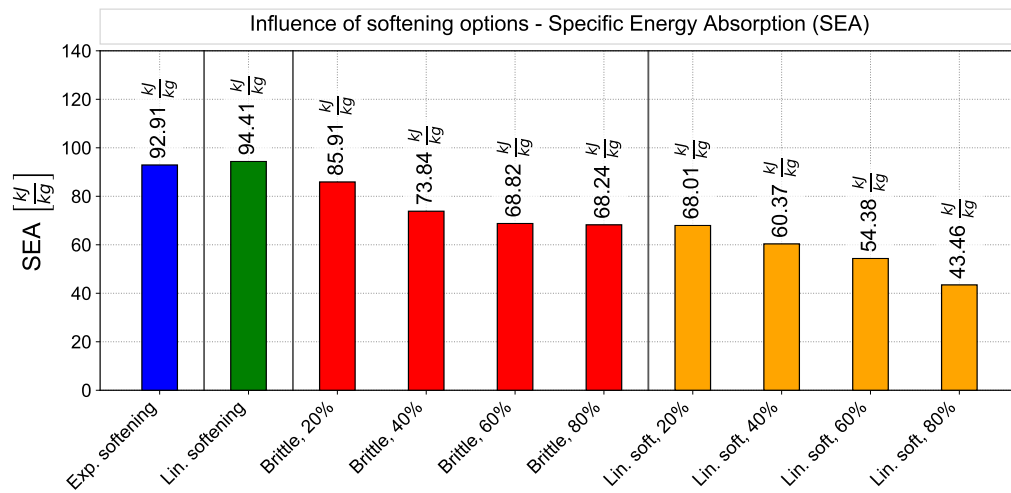
Figure E.3: SEA of Flat coupon crushing predicted using different fibre softening options

List of Figures

List of Tables

Bibliography

1. Hale J. Boeing 787 from the Ground Up. AERO Magazine 2006;QTR_04.06:17–23.

2. Hellard G. Composites in Airbus. A Long Story of Innovations and Experiences. In: *EADS Global Investor Forum, Sevilla, Spain.* 2008.

3. Federal Aviation Administration (FAA). Special Conditions: Boeing Model 787-8 Airplane; Crashworthiness; Docket No. NM368 Special Conditions No. 25-07-05-SC. Government Document. US Federal Register, 2007.

4. Federal Aviation Administration (FAA). Special Conditions: Airbus, A350-900 Series Airplane; Crashworthiness - Emergency Landing Conditions; Docket No. FAA-2013-0892; Notice No. 25–13–21–SC. Government Document. US Federal Register, 2014.

5. LePage F and Carciente R. A320 fusealge section vertical drop test - Part 2 test results. CEAT test report S95 5776/2. Europen Community funded research project 'Crashworthiness for commercial aircarft', 1995.

6. Farley G. Energy Absorption of Composite Materials. Journal of Composite Materials 1983;17:267–27.

7. Bolukbasi A, Baxter T, Nguyen T, et al. United States Patent No. US 8,376,275 B2. 2013.

8. Ostrower J. Boeing faces hurdles, opportunities on the road to an on-time 787 entry into service. 2007. URL: https://flightblogger.blogspot.com (visited on 06/12/2020).

9. Wichita State University. Composite Materials Handbook CMH-17. 2013. URL: https://www.cmh17.org/HOME.aspx (visited on 06/12/2020).

10. ASTM International. Committee D30 on Composite Materials. 2020. URL: https://www.astm.org/COMMITTEE/D30.htm (visited on 06/12/2020).

11. Davies G and Olsson R. Impact on composite structures. The Aeronautical Journal (1968) 2004;108:541–63.

12. Guida M, Marulo M, and Abrate S. Advances in crash dynamics for aircraft safety. Progress in Aerospace Sciences 2018;98:106–23.

13. Olivares G, Acosta J, Yadav V, Keshavarayana S, and Abramowitz A. Crashworthiness of Composites-Certification by Analysis. In: *JAMS Workshop Technical Review.* 2011.

14. Hexcel Corporation. HexTow IM7 Carbon Fiber. Product Data Sheet CTA351 JA20. Hexcel Corporation, 2020.

15. Hexcel Corporation. HexPly 8552. Epoxy matrix (180°C / 356°F curing matrix). Product Data Sheet FTA-072-MY20. Hexcel Corporation, 2020.

16. Hexcel Corporation. HexPly 8552. Mid-toughened, high strength, damage-resistant, structural epoxy matrix. Product Data Sheet FTA-072-2-MY20. Hexcel Corporation, 2020.

17. Reiner J, Zobeiry N, Vaziri R, et al. Prediction of Damage Progression in Notched Tensile Specimens: Comparison Between Two Intra-laminar Damage Models. In: *VI ECCOMAS Thematic Conference on the Mechanical Response of Composites COMPOSITES 2017*. Eindhoven, Netherlands, 2017.

18. Feser T, Waimer M, Schüler D, et al. Simulation of Dynamic Crushing of Composite Structures using two Intra-Laminar Damage Models Implemented in LS-DYNA and ABAQUS/Explicit. In: *Aerospace Structural Impact and Dynamics International Conference (ASIDIC)*. Wichita, USA, 2017.

19. Feser T, Reiner J, Vaziri R, Waimer M, Schueler D, and Toso-Pentecote N. Simulation of Axial Crushing of Flat Coupon Specimens using two Intra-Laminar Damage Models Implemented in LS-Dyna and Abaqus/Explicit. In: *13th World Congress in Computational Mechanics (WCCM 2018)*. New York, USA, 2018.

20. Reiner J, Feser T, Schueler D, Waimer M, and Vaziri R. Comparison of two progressive damage models for studying the notched behavior of composite laminates under tension. Composite Structures 2019;207:385–96.

21. Feser T, Reiner J, Waimer M, and Vaziri R. A Study on Crashworthiness of CFRP Laminates: Comparison of two Finite Element Models in LS-DYNA and ABAQUS/Explicit. In: *Aerospace Structural Impact and Dynamics International Conference (ASIDIC) 2019*. Madrid, Spain, 2019.

22. Reiner J, Feser T, Waimer M, Poursartip A, Voggenreiter H, and Vaziri R. Axial Crush Simulation of Composites Using Continuum Damage Mechanics: FE Software and Material Model Independent Considerations. Submitted to Composites Part B - under review 2021.

23. Waimer M. Development of a Kinematics Model for Assessment of Global Crash Scenarios of a Composite Transport Aircraft Fuselage. PhD Thesis. University of Stuttgart, 2013.

24. Preston G and Pesman G. Accelerations in Transport-Airplane Crashes. report NACA-TN-4158. National Advisory Committee for Aeronautics (NACA), 1958.

25. Reed W, Robertson S, Weinberg L, and Tyndall L. Full-scale dynamic crash test of a Douglas DC-7 aircraft. FAA-ADS-37. Federal Aviation Administration, 1965.

26. Reed W, Robertson S, Weinberg L, and Tyndall L. Full-scale dynamic crash test of a Lockheed Constellation model 1649 aircraft. FAA-ADS-38. Federal Aviation Administration, 1965.

27. Williams M and Hayduk R. Vertical drop test of a transport fuselage section located forward of the wing. Technical Memorandum TM85679. National Aeronautics and Space Administration (NASA), 1983.

28. Fasanella E and Alfaro-Bou E. Vertical drop test of a transport fuselage section located aft of the wing. Technical Memorandum TM89025. National Aeronautics and Space Administration (NASA), 1986.

29. Williams M and Hayduk R. Vertical drop test of a transport fuselage center section including the wing wells. Technical Memorandum TM85706. National Aeronautics and Space Administration (NASA), 1983.

30. Horton TW and Kempel RW. Flight Test Experience and Controlled Impact of a Remotely Piloted Jet Transport Aircraft. Technical Memorandunm 4084. National Aeronautics and Space Administration (NASA), 1988.

31. Hashemi R. Sub-component quasi-static tests on an Airbus A320 rear fuselage. Sub-task 2.4 of the European Community funded research project 'Crashworthiness for commercial aircaft'. Cranfield Impact Centre Limited, 1994.

32. Hashemi R. Sub-component dynamic tests on an Airbus A320 rear fuselage. Sub-task 2.4 of the European Community funded research project 'Crashworthiness for commercial aircaft'. Cranfield Impact Centre Limited, 1994.

33. Meade D. NASA Drops a Fokker Full of Dummies for Science. 2019. URL: `https://www.nasa.gov/langley/fokker-f28-crash-test-nasa` (visited on 06/13/2020).

34. Wikipedia contributors. Controlled Impact Demonstration — Wikipedia, The Free Encyclopedia. 2019. URL: `https://en.wikipedia.org/w/index.php?title=Controlled_Impact_Demonstration&oldid=928775835` (visited on 06/13/2020).

35. Federal Aviation Administration. Federal Aviation Regulations, Part 25: Airworthiness Standards: Transport Category Airplanes. 1997.

36. Kindervater CM. Energy Absorption of Composites as an Aspect of Aircraft Structural Crash-Resistance. In: *Developments in the Science and Technology of Composite Materials: Fourth European Conference on Composite Materials September 25–28, 1990 Stuttgart-Germany.* Ed. by Füller J, Grüninger G, Schulte K, Bunsell AR, and Massiah A. Springer Netherlands, 1990:643–51.

37. Kindervater C and Georgi H. Composite strength and energy absorption as an aspect of structural crash resistance. Structural crashworthiness and failure 1993:189–235.

38. Waimer M, Kohlgrüber D, Keck R, and Voggenreiter H. Contribution to an improved crash design for a composite transport aircraft fuselage—development of a kinematics model and an experimental component test setup. CEAS Aeronautical Journal 2013;4:265–75.

39. Woodson MB, Johnson ER, and Haftka RT. Optimal design of composite fuselage frames for crashworthiness. International Journal of Crashworthiness 1996;1:369–80.

40. Heimbs S, Strobl F, Middendorf P, and Guimard J. Composite crash absorber for aircraft fuselage applications. Structures Under Shock and Impact XI 2010:3–14.

41. Heimbs S, Strobl F, and Middendorf P. Integration of a Composite Crash Absorber in Aircraft Fuselage Vertical Struts. International Journal of Vehicle Structures & Systems 2011;3:87–95.

42. Pein M, Krause D, Heimbs S, and Middendorf P. Innovative energy-absorbing concept for aircraft cabin interior. 2007.

43. Heimbs S, Vogt D, Hartnack R, Schlattmann J, and Maier M. Numerical simulation of aircraft interior components under crash loads. International Journal of Crashworthiness - INT J CRASHWORTHINESS 2008;13:511–21.

44. Pein M. Entwicklungsmethode für Hochleistungswerkstoffe am Beispiel von Energieabsorbern für Flugzeugkabinen. Thesis. 2009.

45. Waimer M, Kohlgrüber, D. K, H. Hachenberg D, and Margull L. Connection Arrangement and Structure. European Patent EP 2881319 A1. 2015.

46. Waimer M, Feser T, Schatrow P, and Schueler D. Crash concepts for CFRP transport aircraft–comparison of the traditional bend frame concept versus the developments in a tension absorbers concept. International Journal of Crashworthiness 2018;23:193–218.

47. Heimbs S, Hoffmann M, Waimer M, Schmeer S, and Blaurock J. Dynamic testing and modelling of composite fuselage frames and fasteners for aircraft crash simulations. International Journal of Crashworthiness 2013;18:406–22.

48. Feser T and Waimer M. Numerical simulation of progressive bearing failure of bolted joints in CFRP aircraft structures. In: *First international conference on impact loading of structures and materials. Turin, Italy.* 2016.

49. Heimbs S and Bergmann T. Bearing Mode Absorber – On the Energy Absorption Capability of Pulling a Bolt through a Composite or Sandwich Plate. Procedia Engineering 2014;88:149–56.

50. Bergmann T. Beitrag zur Charakterisierung und Auslegung zugbelasteter Energieabsorberkonzepte mittels experimenteller, analytischer und numerischer Methoden. PhD. Technische Universität Kaiserslautern, 2016.

51. Portemont G, Berthe J, Deudon A, and Irisarri FX. Static and dynamic bearing failure of carbon/epoxy composite joints. Composite Structures 2018;204:131–41.

52. Hassan J, Feser T, O'Higgins RM, et al. Energy absorption capability of composite bolted joints undergoing extended bearing failure. Composite Structures 2020;237:111868.

53. Feser T, Hassan J, Waimer M, et al. Effects of transient dynamic loading on the energy absorption capability of composite bolted joints undergoing extended bearing failure. Composite Structures 2020;247:112476.

54. Crashworthiness of Aircraft Composites Structures (Invited Talk). Vol. Transportation: Making Tracks for Tomorrow's Transportation. ASME International Mechanical Engineering Congress and Exposition. 2002:31–40.

55. CRASURV. Commercial aircraft - Design for crash survivability. EU FP4 RTD Project IMT AREA 3 (3A5.6), 1996-1999.

56. Kohlgrueber D. CRASURV - D.1.1.1 Initial Materials Data of Carbon and Aramid Fabric Materials. DLR-report IB 435-97/24. DLR Institute of Structures and Design, 1997.

57. Kohlgrueber D.and Weissinger H. Crash behaviour of composite sub-floor components - final report on component tests. DLR-report IB 435-97/38. DLR Institute of Structures and Design, 1998.

58. Kohlgrueber D.and Weissinger H. Crash behaviour of composite commuter sub-floor components - report on dynamic tests. DLR-report IB 435-98/21. DLR Institute of Structures and Design, 1998.

59. Kohlgrueber D.and Weissinger H. Results of dynamic tests of composite sub-floor boxes - final report. DLR-report IB 435-98/22. DLR Institute of Structures and Design, 1998.

60. AC20-107B. Advisory circular on composite aircraft structure. AC20-107B. Federal Aviation Administration. 2010.

61. Jackson A, Dutton S, Gunnion A, and Kelly D. Investigation into laminate design of open carbon–fibre/epoxy sections by quasi–static and dynamic crushing. Composite Structures - COMPOS STRUCT 2011;93:2646–54.

62. David M. Experimental and Numerical Investigation of Polymer Composite Energy Absorbers under Dynamic Loading. Thesis. 2015.

63. David M, Johnson AF, and Voggenreiter H. Analysis of Crushing Response of Composite Crashworthy Structures. Applied Composite Materials 2013;20:773–87.

64. David M and Johnson AF. Effect of strain rate on the failure mechanisms and energy absorption in polymer composite elements under axial loading. Composite Structures 2015;122:430–9.

65. Herrmann R. MAAXIMUS - More Affordable Aircraft through Extended, Integrated and Mature Numerical Sizing. Springer International Publishing, 2020. URL: https://books.google.de/books?id=y3M7vgAACAAJ.

66. Waimer M, Kohlgrüber D, Hachenberg D, and Voggenreiter H. Experimental study of CFRP components subjected to dynamic crash loads. Composite Structures 2013;105:288–99.

67. Delsart D, Portemont G, and Waimer M. Crash Testing of a CFRP Commercial Aircraft Sub-Cargo Fuselage Section. Procedia Structural Integrity 2016;2. 21st European Conference on Fracture, ECF21, 20-24 June 2016, Catania, Italy:2198–205.

68. Bolukbasi, A.O. and Laananen, D.H. Energy absorption in composite stiffeners. Composites 1995;26:291–301.

69. Feraboli P. Development of a Corrugated Test Specimen for Composite Materials Energy Absorption. Journal of Composite Materials 2008;42:229–56.

70. Feraboli P, Garattoni F, and Deleo F. TOWARD THE DEVELOPMENT OF A TEST STANDARD FOR CHARACTERIZING THE ENERGY ABSORPTION OF COMPOSITE MATERIALS: PART II. 6th Annual SPE Automotive Composites Conference 2006 2006;2.

71. Thornton P. Energy Absorption in Composite Structures. Journal of Composite Materials 1979;13:247–62.

72. Hull D. A unified approach to progressive crushing of fibre-reinforced composite tubes. Composites Science and Technology 1991;40:377–421.

73. Keal R. Post failure energy absorbing mechanisms of filament wound composite tubes. PhD Thesis. University of Liverpool, 1983.

74. Berry J. Energy absorption and failure mechanisms of axially crushed GRP tubes. PhD Thesis. University of Liverpool, 1984.

75. Mamalis A, Robinson M, Manolakos D, Demosthenous G, Ioannidis M, and Carruthers J. Analysis of failur mechanisms observed in axial collapse of thin-walled circular fibreglass composite tubes. Thin-Walled Structures 1997:335–52.

76. Farley GL. Effect of Specimen Geometry on the Energy Absorption Capability of Composite Materials. Journal of Composite Materials 1986;20:390–400.

77. Farley GL and Jones RM. Energy-Absorption Capability of Composite Tubes and Beams. Technical Memorandum TM 101934. NASA, 1989.

78. Farley GL and Jones RM. Crushing Characteristics of Continuous Fiber-Reinforced Composite Tubes. Journal of Composite Materials 1992;26:37–50.

79. Farley GL and Jones RM. Predicition of the Energy-Absorption Capability of Composite Tubes. Journal of Composite Materials 1992;26:388–404.

80. Sen JK and Dremann CC. Design development tests for composite crashworthy helicopter fuselage. SAMPE Q.; (United States) 1985.

81. M. KC. Quasi-Static and Dynamic Crushing of Energy Absorbing Materials and Structural Components with the Aim of Improving Helicopter Crashwhiness, in: *Proceedings of 7th European Rotorcraft and Powered Lift Aircraft Forum*. Paper No. 66. Deutsche Gesellschaft für Luft- und Raumfahrt (DGLR). Garmisch-Partenkirchen, 1981.

82. Forghani A, Shahbazi M, Zobeiry N, Poursartip A, and Vaziri R. 6 - An overview of continuum damage models used to simulate intralaminar failure mechanisms in advanced composite materials. In: *Numerical Modelling of Failure in Advanced Composite Materials*. Ed. by Camanho PP and Hallett SR. Woodhead Publishing Series in Composites Science and Engineering. Woodhead Publishing, 2015:151–73.

83. Reiner J and Vaziri R. 8.4 Structural Analysis of Composites With Finite Element Codes: An Overview of Commonly Used Computational Methods. In: *Comprehensive Composite Materials II*. 2018:61–84. DOI: `10.1016/b978-0-12-803581-8.10050-5`.

84. Xia Z, Chen Y, and Ellyin F. A meso/micro-mechanical model for damage progression in glass-fiber/epoxy cross-ply laminates by finite-element analysis. Composites Science and Technology 2000;60:1171–9.

85. Zhang Y, Xia Z, and Ellyin F. Viscoelastic and Damage Analyses of Fibrous Polymer Laminates by Micro/meso-mechanical Modeling. Journal of Composite Materials 2005;39:2001–22.

86. Grufman C and Ellyin F. Numerical modelling of damage susceptibility of an inhomogeneous representative material volume element of polymer composites. Composites Science and Technology 2008;68:650–7.

87. Ladevèze P, Allix O, Deü JF, and Lévêque D. A mesomodel for localisation and damage computation in laminates. Computer Methods in Applied Mechanics and Engineering 2000;183:105–22.

88. Mamalis A, Manolakos D, Ioannidis M, and Papapostolou D. The static and dynamic axial collapse of CFRP square tubes: Finite element modelling. Composite Structures 2006;74:213–25.

89. Waimer M, Siemann M, and Feser T. Simulation of CFRP components subjected to dynamic crash loads. International Journal of Impact Engineering 2017;101:115–31.

90. Schueler D. Effects of Static Preloads on the High Velocity Impact Response of Composite Structures. Thesis. 2017.

91. Schueler D, Toso-Pentecôte N, and Voggenreiter H. Simulation of High Velocity Impact on Composite Structures - Model Implementation and Validation. Applied Composite Materials 2016;23:857–78.

92. Sebaey T, Costa J, Maimí P, Batista Y, Blanco N, and Mayugo J. Measurement of the in situ transverse tensile strength of composite plies by means of the real time monitoring of microcracking. Composites Part B: Engineering 2014;65. Damage Mechanics:40–6.

93. Williams KV and Vaziri R. Application of a damage mechanics model for predicting the impact response of composite materials. Computers & Structures 2001;79:997–1011.

94. McGregor CJ, Vaziri R, Poursartip A, and Xiao X. Simulation of progressive damage development in braided composite tubes under axial compression. Composites Part A: Applied Science and Manufacturing 2007;38:2247–59.

95. McGregor C, Vaziri R, and Xiao X. Finite element modelling of the progressive crushing of braided composite tubes under axial impact. International Journal of Impact Engineering 2010;37:662–72.

96. McGregor C, Zobeiry N, Vaziri R, Poursartip A, and Xiao X. Calibration and validation of a continuum damage mechanics model in aid of axial crush simulation of braided composite tubes. Composites Part A: Applied Science and Manufacturing 2017;95:208–19.

97. Xiao X, McGregor C, Vaziri R, and Poursartip A. Progress in braided composite tube crush simulation. International Journal of Impact Engineering 2009;36:711–9.

98. Xiao X. Modeling Energy Absorption with a Damage Mechanics Based Composite Material Model. Journal of Composite Materials 2009;43:427–44.

99. Fish J and Yu Q. Multiscale damage modelling for composite materials: theory and computational framework. International Journal for Numerical Methods in Engineering. 52:161–91.

100. Ladevèze P. Multiscale modelling and computational strategies for composites. International Journal for Numerical Methods in Engineering 2004;60:233–53.

101. Kachanov L. Introduction to continuum damage mechanics. Mechanics of Elastic Stability. Springer Netherlands, 1986.

102. Matzenmiller A, Lubliner J, and Taylor R. A constitutive model for anisotropic damage in fiber-composites. Mechanics of Materials 1995;20:125–52.

103. Davila CG, Camanho PP, and Rose CA. Failure Criteria for FRP Laminates. Journal of Composite Materials 2005;39:323–45.

104. Tsai SW and Wu EM. A General Theory of Strength for Anisotropic Materials. Journal of Composite Materials 1971;5:58–80.

105. Hashin Z. Failure Criteria for Unidirectional Fiber Composites. Journal of Applied Mechanics 1980;47:329–34.

106. Chang FK and Chang KY. A Progressive Damage Model for Laminated Composites Containing Stress Concentrations. Journal of Composite Materials 1987;21:834–55.

107. Puck A and Schürmann H. FAILURE ANALYSIS OF FRP LAMINATES BY MEANS OF PHYSICALLY BASED PHENOMENOLOGICAL MODELS. Composites Science and Technology 1998;58:1045–67.

108. Ladeveze P and LeDantec E. Damage modelling of the elementary ply for laminated composites. Composites Science and Technology 1992;43:257–67.

109. Johnson A, Pickett A, and Rozycki P. Computational methods for predicting impact damage in composite structures. Composites Science and Technology 2001;61:2183–92.

110. Iannucci L. Progressive failure modelling of woven carbon composite under impact. International Journal of Impact Engineering 2006;32:1013–43.

111. Iannucci L and Willows M. An energy based damage mechanics approach to modelling impact onto woven composite materials—Part I: Numerical models. Composites Part A: Applied Science and Manufacturing 2006;37:2041–56.

112. Iannucci L and Ankersen J. An energy based damage model for thin laminated composites. Composites Science and Technology 2006;66:934–51.

113. Bazant Z and Oh B. Crack Band Theory for Fracture of Concrete. Matériaux et Constructions 1983;16:155–77.

114. Bazant Z and Planas J. Fracture and Size Effect in Concrete and Other Quasibrittle Materials. 2019.

115. Maimí P, Camanho P, Mayugo J, and Dávila C. A continuum damage model for composite laminates: Part I – Constitutive model. Mechanics of Materials 2007;39:897–908.

116. Maimí P, Camanho P, Mayugo J, and Dávila C. A continuum damage model for composite laminates: Part II – Computational implementation and validation. Mechanics of Materials 2007;39:909–19.

117. Pinho S, Dávila C, Camanho P, Iannucci L, and Robinson P. Failure Models and Criteria for FRP Under In-Plane or Three-Dimensional Stress States Including Shear Non-Linearity. 2005.

118. Allix O and Ladevèze P. Interlaminar interface modelling for the prediction of delamination. Composite Structures 1992;22:235–42.

119. Turon A, Camanho P, Costa J, and Dávila C. A damage model for the simulation of delamination in advanced composites under variable-mode loading. Mechanics of Materials 2006;38:1072–89.

120. Dugdale D. Yielding of steel sheets containing slits. Journal of the Mechanics and Physics of Solids 1960;8:100–4.

121. Barenblatt G. The Mathematical Theory of Equilibrium Cracks in Brittle Fracture. In: ed. by Dryden H, von Kármán T, Kuerti G, van den Dungen F, and Howarth L. Vol. 7. Advances in Applied Mechanics. Elsevier, 1962:55–129. DOI: https://doi.org/10.1016/S0065-2156(08)70121-2. URL: https://www.sciencedirect.com/science/article/pii/S0065215608701212.

122. Shet C and Chandra N. Analysis of Energy Balance When Using Cohesive Zone Models to Simulate Fracture Processes. Journal of Engineering Materials and Technology-transactions of The Asme - J ENG MATER TECHNOL 2002;124.

123. Turon A, Camanho PP, Soto A, and González EV. Analysis of Delamination Damage in Composite Structures Using Cohesive Elements. In: *Comprehensive Composite Materials II*. Ed. by Beaumont PWR and Zweben CH. Elsevier, 2018:136–56. DOI: `10.1016/B978-0-12-803581-8.10059-1`.

124. Lin Ye. Role of matrix resin in delamination onset and growth in composite laminates. Composites Science and Technology 1988;33:257–77.

125. Camanho PP, Davila CG, and Moura MF de. Numerical Simulation of Mixed-Mode Progressive Delamination in Composite Materials. Journal of Composite Materials 2003;37:1415–38.

126. Benzeggagh M and Kenane M. Measurement of mixed-mode delamination fracture toughness of unidirectional glass/epoxy composites with mixed-mode bending apparatus. Composites Science and Technology 1996;56:439–49.

127. Mi Y, Crisfield MA, Davies GAO, and Hellweg HB. Progressive Delamination Using Interface Elements. Journal of Composite Materials 1998;32:1246–72.

128. Harper PW and Hallett SR. Cohesive zone length in numerical simulations of composite delamination. Engineering Fracture Mechanics 2008;75:4774–92.

129. Turon A, Dávila C, Camanho P, and Costa J. An engineering solution for mesh size effects in the simulation of delamination using cohesive zone models. Engineering Fracture Mechanics 2007;74:1665–82.

130. Dassault Systemes Simulia. Abaqus 2020 Analysis User's Guide. Selecting material parameters in Abaqus for cohesive elements defined in terms of traction-separation. Manual. Providence, Rhode Island, USA: Dassault Systemes Simulia Corp., 2020.

131. Heimbs S. Bird Strike Simulations on Composite Aircraft Structures. In: *SIMULIA Customer Conference, Barcelona, Spain*. 2011.

132. Hauptmann R and Schweizerhof K. A systematic development of 'solid-shell' element formulations for linear and non-linear analyses employing only displacement degrees of freedom. International Journal for Numerical Methods in Engineering. 42:49–69.

133. Fiolka M and Matzenmiller A. Berechnung fortschreitender Risse in Laminaten. In: 2005.

134. Siemann M. Numerische Simulation dynamischer Stauchtests an CFK-Absorbern. Diploma thesis. TU Dresden, 2011.

135. Feser T. Numerische Simulation dynamischer Stauchtests an CFK-Absorbern. Diploma thesis. University of Stuttgart, 2013.

136. McCarthy MA, Harte CG, Wiggenraad JFM, Michielsen ALPJ, Kohlgrüber D, and Kamoulakos A. Finite element modelling of crash response of composite aerospace sub-floor structures. Computational Mechanics 2000;26:250–8.

137. Kohlgrueber D and Kamoulakos A. Validation of Numerical Simulation of Composite Helicopter Sub-floor Structures Under Crash Loading. In: *American Helicopter Society*. 54. 1998.

138. Aktay L. Improved Simulation Techniques for Modelling Impact and Crash Behaviour of Composite Structures. PhD Thesis. University of Stuttgart, 2008.

139. Aktay L and Johnson AF. FEM/SPH Coupling Technique for High Velocity Impact Simulations. In: *Advances in Meshfree Techniques*. Ed. by Leitão VMA, Alves CJS, and Armando Duarte C. Dordrecht: Springer Netherlands, 2007:147–67.

140. Aktay L, Kröplin BH, Toksoy A, and Güden M. Finite element and coupled finite element/smooth particle hydrodynamics modeling of the quasi-static crushing of empty and foam-filled single, bitubular and constraint hexagonal- and square-packed aluminum tubes. Materials & Design 2008;29:952–62.

141. Boria S, Obradovic J, and Belingardi G. Experimental and numerical investigations of the impact behaviour of composite frontal crash structures. Composites Part B: Engineering 2015;79:20–7.

142. Cherniaev A, Butcher C, and Montesano J. Predicting the axial crush response of CFRP tubes using three damage-based constitutive models. Thin-Walled Structures 2018;129:349–64.

143. Zhu G, Sun G, Li G, Cheng A, and Li Q. Modeling for CFRP structures subjected to quasi-static crushing. Composite Structures 2018;184:41–55.

144. Ren Y, Jiang H, Ji W, Zhang H, Xiang J, and Yuan FG. Improvement of Progressive Damage Model to Predicting Crashworthy Composite Corrugated Plate. Applied Composite Materials 2018;25:45–66.

145. Ren Y, Jiang H, Gao B, and Xiang J. A progressive intraply material deterioration and delamination based failure model for the crashworthiness of fabric composite corrugated beam: Parameter sensitivity analysis. Composites Part B: Engineering 2018;135:49–71.

146. Dalli D, Varandas L, Catalanotti G, Foster S, and Falzon B. Assessing the current modelling approach for predicting the crashworthiness of Formula One composite structures. Composites Part B: Engineering 2020;201:108242.

147. McGregor C, Vaziri R, Poursartip A, and Xiao X. Axial crushing of triaxially braided composite tubes at quasi-static and dynamic rates. Composite Structures 2016;157:197–206.

148. Kaddour A, Hinton M, Smith P, and Li S. Mechanical properties and details of composite laminates for the test cases used in the third world-wide failure exercise. Journal of Composite Materials 2013;47:2427–42.

149. Kaddour A, Hinton M, Smith P, and Li S. The background to the third world-wide failure exercise. Journal of Composite Materials 2013;47:2417–26.

150. Soden P, Kaddour A, and Hinton M. Recommendations for designers and researchers resulting from the world-wide failure exercise. Composites Science and Technology 2004;64. Failure criteria in fibre reinforced polymer composites Part C: Additional theories conclusions and recommendations:589–604.

151. Daghia F and Ladeveze P. Identification and validation of an enhanced mesomodel for laminated composites within the WWFE-III. Journal of Composite Materials 2013;47:2675–93.

152. Marlett K. Hexcel 8552 IM7 unidirectional prepregs 190 gsm & 35% RC qualification material property data report. Report. National Institute for Aviation Research, 2011.

153. Lee J and Soutis C. Measuring the notched compressive strength of composite laminates: Specimen size effects. Composites Science and Technology 2008;68:2359–66.

154. Zobeiry N. Extracting the strain-softening response of composites using full-field displacement measurement. PhD thesis. 2010.

155. Zobeiry N, Vaziri R, and Poursartip A. Characterization of strain-softening behavior and failure mechanisms of composites under tension and compression. Composites Part A: Applied Science and Manufacturing 2015;68:29–41.

156. Hassan J, O'Higgins RM, Feser T, et al. Influence of layup, stacking sequence and loading rate on energy absorption of tension-absorber joints. Composite Structures 2021;261:113327.

157. Camanho P, Maimí P, and Dávila C. Prediction of size effects in notched laminates using continuum damage mechanics. Composites Science and Technology 2007;67:2715–27.

158. Camanho P, Bessa M, Catalanotti G, Vogler M, and Rolfes R. Modeling the inelastic deformation and fracture of polymer composites – Part II: Smeared crack model. Mechanics of Materials 2013;59:36–49.

159. Zhou S, Sun Y, Chen B, and Tay TE. Progressive damage simulation of open-hole composite laminates under compression based on different failure criteria. Journal of Composite Materials 2017;51:1239–51.

160. Laffan M, Pinho S, Robinson P, Iannucci L, and McMillan A. Measurement of the fracture toughness associated with the longitudinal fibre compressive failure mode of laminated composites. Composites Part A: Applied Science and Manufacturing 2012;43:1930–8.

161. Catalanotti G, Camanho P, Xavier J, Dávila C, and Marques A. Measurement of resistance curves in the longitudinal failure of composites using digital image correlation. Composites Science and Technology 2010;70:1986–93.

162. Pinho S, Robinson P, and Iannucci L. Fracture toughness of the tensile and compressive fibre failure modes in laminated composites. Composites Science and Technology 2006;66:2069–79.

163. Kuhn P, Catalanotti G, Xavier J, Camanho P, and Koerber H. Fracture toughness and crack resistance curves for fiber compressive failure mode in polymer composites under high rate loading. Composite Structures 2017;182:164–75.

164. Zobeiry N, Reiner J, and Vaziri R. Theory-guided machine learning for damage characterization of composites. Composite Structures 2020;246:112407.

165. Kongshavn I and Poursartip A. Experimental investigation of a strain-softening approach to predicting failure in notched fibre-reinforced composite laminates. Composites Science and Technology 1999;59:29–40.

166. ASTM D 5528 - 13. Standard Test Method for Mode I Interlaminar Fracture Toughness of Unidirectional Fiber-Reinforced Polymer Matrix Composites. West Conshohocken, PA: ASTM International, 2013. URL: www.astm.org.

167. ASTM D 7905 - 94a. Standard Test Method for Determination of the Mode II Interlaminar Fracture Toughness of Unidirectional Fiber-Reinforced Polymer Matrix Composites. West Conshohocken, PA: ASTM International, 2019. URL: www.astm.org.

168. Hassan J, O'Higgins RM, McCarthy CT, Toso N, and McCarthy MA. Mesoscale modelling of extended bearing failure in tension-absorber joints. International Journal of Mechanical Sciences 2020;182:105777.

169. Hallett SR, Green BG, Jiang WG, and Wisnom MR. An experimental and numerical investigation into the damage mechanisms in notched composites. Composites Part A: Applied Science and Manufacturing 2009;40:613–24.

170. Ehrich F. Low Velocity Impact on Pre-Loaded Composite Structures. PhD Thesis. London, Imperial College, 2013.

171. Li X, Hallett SR, Wisnom MR, Zobeiry N, Vaziri R, and Poursartip A. Experimental study of damage propagation in Over-height Compact Tension tests. Composites Part A: Applied Science and Manufacturing 2009;40:1891–9.

172. Hobbs JM and Adams DO. Laminate Design for Crashworthiness of Carbon/Epoxy Composites. In: *2nd Aerospace Structural Impact and Dynamics International Conference (ASIDIC)*. Seville, Spain, 2015.

173. Perl M and Adams D. Phase III Flat Coupon Crush Test Results. CMH-17 Crashworthiness WG Presentation. Presentation. University of Utah, 2017.

174. Perl M and Adams D. Phase III Flat Coupon Crush Test Results. Private conversation. University of Utah, 2018.

175. Koerber H and Camanho P. High strain rate characterisation of unidirectional carbon–epoxy IM7-8552 in longitudinal compression. Composites Part A: Applied Science and Manufacturing 2011;42:462–70.

176. Koerber H, Xavier J, and Camanho P. High strain rate characterisation of unidirectional carbon-epoxy IM7-8552 in transverse compression and in-plane shear using digital image correlation. Mechanics of Materials 2010;42:1004–19.

177. Hassan J, O'Higgins RM, McCarthy CT, Toso N, and McCarthy MA. Mesoscale modelling of extended bearing failure in tension-absorber joints. International Journal of Mechanical Sciences 2020;182:105777.

178. O'Higgins RM, McCarthy CT, and McCarthy MA. Identification of Damage and Plasticity Parameters for Continuum Damage Mechanics Modelling of Carbon and Glass Fibre-Reinforced Composite Materials. Strain 2011;47:105–15.

179. ASTM D3039 / D3039M-17. Standard Test Method for Tensile Properties of Polymer Matrix Composite Materials. West Conshohocken, PA: ASTM International, 2017. URL: www.astm.org.

180. ASTM D3518 / D3518M-18. Standard Test Method for In-Plane Shear Response of Polymer Matrix Composite Materials by Tensile Test of a ±45° Laminate. West Conshohocken, PA: ASTM International, 2018. URL: www.astm.org.

181. Herakovich CT. Mechanics of Fibrous Composites. Vol. 1. WILEY, 1997.

182. Justusson B, Pang J, Molitor M, et al. Composite Coupon Test Data in Support of CMH-17 Crashworthiness Working Group. report. NASA ACC, 2018.

183. Thorsson SI, Yoshimura A, Waas AM, and Rassaian M. Prediction of Low-Velocity Face-on Impact Response of Composite Laminates using High-Fidelity Finite Element Modeling Techniques. In: *57th AIAA/ASCE/AHS/ASC Structures, Structural Dynamics, and Materials Conference.*

184. Martin R, Elms T, and Bowron S. Characterisation of mode II delamination using the 4 ENF. In: *4 th European Conference on Composites: Testing and Standardisation.* 1998:161–70.

185. Schön J, Nyman T, Blom A, and Ansell H. A numerical and experimental investigation of delamination behaviour in the DCB specimen. Composites Science and Technology 2000;60(2):173–84.

186. Schön J, Nyman T, Blom A, and Ansell H. Numerical and experimental investigation of a composite ENF-specimen. Engineering Fracture Mechanics 2000a;65:405–33.

187. ESIS. European Structural Integrity Society, Polymer and Composite Task Force. Protocol for interlarninar fracture testing Nos. 1 and 2. 1992.

188. Andersons J and König M. Dependence of fracture toughness of composite laminates on interface ply orientations and delamination growth direction. Composites Science and Technology 2004;64:2139–52.

189. Hiley M. Delamination between multi-directional ply interfaces in carbon-epoxy composites under static and fatigue loading. In: *Fracture of Polymers, Composites and Adhesives.* Ed. by Williams J and Pavan A. Vol. 27. European Structural Integrity Society. Elsevier, 2000:61–72.

190. Kinloch A, Wang Y, Williams J, and Yayla P. The mixed-mode delamination of fibre composite materials. Composites Science and Technology 1993;47:225–37.

191. Hansen P and Martin R. DCB, 4ENF and MMB Delamination Characterisation of S2/8552 and IM7/8552. AD-a368 672. 1999.

Curriculum Vitae

Personal data

Name	Thomas Feser
Date of Birth	October 10, 1986
Place of Birth	Herrenberg, Germany
Nationality	German

Education

2003 – 2006	Technical secondary school, Gottlieb-Daimler-Schule I, Sindelfingen, Germany Graduation: Abitur
2007 – 2013	Diplom-Ingenieur, Aerospace Engineering, Faculty of Aerospace Engineering and Geodesy, University of Stuttgart *Diploma thesis: "Numerical simulation of dynamic crush tests on CFRP energy absorbers"* *Institute of Aircraft Design, University of Stuttgart and Institute of Structures and Design, German Aerospace Center (DLR), Stuttgart*
2016 – 2021	Doctoral Candidate, Institute of Structures and Design, German Aerospace Center (DLR), Stuttgart

Professional Experience

2013 – 2020   Research Scientist, Institute of Structures and Design, German Aerospace Center (DLR), Stuttgart

Investigation and development of numerical methods to predict the crushing behaviour and energy absorption of CFRP energy absorbers of transport aircraft structures within industrial and publicly funded research projects:

2013 - 2015: TP123 WP4 'PAX floor tension'
Development of FE modelling methods to precisely analyse the energy absorption of progressive bearing failure (industrial research project with AIRBUS)

2014 - 2017: Collaborative Project 'SCHACH'
Development of a detailed FE modelling approach to capture the failure behaviour of composite bolted joints (National funded research project)

2016 - 2020: Research collaboration 'DLR@UBC'
Development of a robust simulation framework to support the effective design of crashworthy/impact-resistant components with reduced reliance on experiments (International research collaboration)

2016 - 2020: Participation in the CMH-17 CWG
Definition of guidelines and best practices for the numerical prediction of crashworthy structures in commercial FE codes (International research collaboration)

2017 - 2020: Joint research project with the University of Limerick, Ireland
Investigation of the energy absorption capability of composite bolted joints in extended bearing failure under quasi-static and dynamic loading (International research project)

since 2020   Research Scientist, Institute of Vehicle Concepts, German Aerospace Center (DLR), Stuttgart
Development and simulation of innovative materials for future vehicle applications under consideration of manufacturing processes